UNIVERSITY OF Southampton

FACULTY OF ENGINEERING AND PHYSICAL SCIENCE

ENERGY TECHNOLOGY RESEARCH GROUP

Gold-based Electro Catalysts on Titanate nanotubes Support for Direct Oxidation of Borohydride

by

Recep Dag

Orcid ID: 0009-0002-4561-4121

Thesis for the degree of Doctor of Philosophy

June 2024

Abstract

Fuel cells offer a higher specific energy density compared to the traditional batteries and can convert stored chemical energy directly into electricity, not requiring any combustion or mechanical convertor such as turbines. Direct borohydride fuel cells offer higher specific energy output among the existing fuel cell systems. Moreover, sodium borohydride being used in aqueous solution to feed the cell system eases fuel storage and handling, simplifying direct borohydride fuel cell design in terms of engineering perspective. However, there are remaining challenges –mainly arising from anode catalyst development— which prevent commercialization of direct borohydride fuel cells. These are: 1) hydrolysis of borohydride, 2) high cost of anode catalyst due to high dependency on noble metal usage, 3) fuel crossover, and 4) stability of anode catalyst.

In this study, titanate nanotubes, highly stable catalyst support in alkaline or acidic medium, was synthesized by wet chemical method. The deposition of gold, nickel, cobalt, and copper onto titanate nanotubes was conducted separately using the ion-exchange deposition-reduction method. The results revealed that the maximum weight percentages of gold, nickel, cobalt, and copper deposited on the titanate nanotubes were 17.28%, 2.11%, 3.65%, and 4.00% respectively. This method allowed for the determination of adsorption isotherms for each metal, which were then used to establish a correlation between catalyst loading and the initial concentration of metal solutions. By utilizing this correlation, gold-metal composite catalysts (Au-Ni/TiNT, Au-Co/TiNT, and Au-Cu/TiNT) were synthesized on the surface of titanate nanotubes at different molar ratios, resulting in a total metal loading of 4% by weight. Cyclic voltammetry (CV), linear sweep voltammetry (LSV), and chronoamperometry (CA) were used to test the borohydride oxidation by these synthesized composited catalysts.

The cyclic voltammetry results for the developed catalysts, Au100 TiNT, Au-Ni/TiNT, Au-Co TiNT, and Au-Cu TiNT, show that there is a single oxidation peak during the forward scan, indicating the direct oxidation of borohydride. However, during the reverse scan, an additional oxidation peak is observed, which is believed to be caused by the oxidation of adsorbed intermediates such as BH_3OH^-.

Linear sweep voltammetry used to determine kinetic parameters and diffusion coefficient number for the developed catalysts. Diffusion coefficient number for borohydride ions in 2 M $NaBH_4$ found to be 1.77×10^{-5} cm^2 using gold rotating disc electrode. This determined diffusion coefficient number was used in determination of developed catalysts of Au-Ni/TiNT, Au-Co/TiNT, and Au-Cu/TiNT. Transferred electron numbers and apparent rate constant for the developed catalyst were calculated at different potentials.

Chronoamperometry was deployed to investigate further catalytic activities and stabilities of developed catalysts.

Keywords: borohydride oxidation, gold-nickel composite catalyst, gold-cobalt composite catalyst, gold-copper composite catalyst, titanate nanotubes, TiNT, borohydride fuel cell.

CONTENT

List of Figures

List of Tables

Research Thesis: Declaration of Authorship

I, Recep Dag, declare that the thesis entitled

Gold-based Electro Catalysts on Titanate nanotubes Support for Direct Oxidation of Borohydride

and the work presented in the thesis are both my own and have been generated by me as the result of my own original research. I confirm that:

- this work was done wholly or mainly while in candidature for a research degree at this University;
- where any part of this thesis has previously been submitted for a degree or any other qualification at this University or any other institution, this has been clearly stated;
- where I have consulted the published work of others, this is always clearly attributed;
- where I have quoted from the work of others, the source is always given. With the exception of such quotations, this thesis is entirely my own work;
- I have acknowledged all main sources of help;
- where the thesis is based on work done by myself jointly with others, I have made clear exactly what was done by others and what I have contributed myself;
- None of this work has been published before submission

Signature: Date:

Acknowledgements

I am deeply grateful to my supervisor, Dr. Dmitry Bavykin, for his unwavering support, guidance, and invaluable insights throughout my PhD journey. His supervision and constant assistance have been instrumental on both academic and personal levels, for which I am profoundly thankful. I also extend my gratitude to my supervisory team, Professor Carlos Ponce de Leon Albarrán and Dr. Zheng Jiang, for their unwavering help and support during my PhD.

I am immensely indebted to the Republic of Turkey and its respectful, peaceful, and generous people for providing me with the opportunity to pursue my PhD at the University of Southampton. Without their financial and spiritual support, my PhD journey would not have been possible.

Above all, I owe an immeasurable debt of gratitude to my family. Throughout my PhD journey, their unwavering spiritual support has been my rock. I am deeply thankful to each and every one of them. I am especially grateful to my beloved wife, Elif Ceyda, and my sons, Alperen Berat and Hamza Cagri, who have stood by me and supported me unconditionally, even in my absence during my PhD pursuit. Their love and encouragement have been my greatest source of strength and motivation.

Chapter 1: INTRODUCTION

1.1 Motivation and Background for DBFC

The main energy demand in industry and our daily life is supplied from fossil fuels. Dependence on carbon-based fuels for energy leads to release high amount of carbon dioxide gas to the atmosphere. Having greenhouse effect in the atmosphere, large amount of CO_2 emission is believed the main reason for global worming besides the other greenhouse gases such as methane, nitrous oxide, chlorofluorocarbon, and other volatile hydrocarbons. To diminish CO_2 emission, energy demand of the world needs to be supplied from clean, sustainable, and carbon free energy sources. Hydropower, wind power, solar power, bioenergy, and geothermal energy can be given as renewable energy source and nuclear power as sustainable energy source. However, it is not possible to have a continuous energy flow in the case of most renewable sources. Due to this, energy storage is an important factor to get a continuous energy flow when the energy is supplied from renewable energy sources. There are several methods to store energy when the energy supply is more than its consumption. Superconducting magnetic energy storage, super capacitor energy storage, compressed air energy storage, flywheel energy storage, pumped hydro energy storage, thermal energy storage, battery energy storage, flow battery energy storage, hydrogen energy storage, and synthetic fuels can be given as examples to these storage methods [1].

Among the energy storage methods mentioned above, hydrogen energy storage seems an attractive way to store energy because hydrogen has a considerably high gravimetric energy density, 33.3 kW h kg^{-1}, which is almost three times of those of gasoline, 12.2 kW h kg^{-1} [2], [3]. Another important reason which makes hydrogen energy storage attractive is that of the possible usage of hydrogen and hydrogen compounds in fuel cell systems to directly convert stored chemical energy into electricity. In theory, conversion efficiency of fuel cells much higher than those of based on combustion of fossil fuels which use thermal cycle for energy conversion. According to the second law of thermodynamics, these systems which are restricted by Carnot limit (max. efficiency = $(T_{hot} - T_{cold}) / T_{hot}$). Typically, these systems exhibit efficiencies ranging from 20 to 50 percent, with an average around 30 percent. In many instances, the end products of fuel cells are free from carbon dioxide emission being clean and environmentally friendly energy sources. This makes them favourable alternatives to limit CO_2 emission. Hydrogen can be stored in several ways. In **Figure 1.1**, the storage technologies can be seen for hydrogen in different forms.

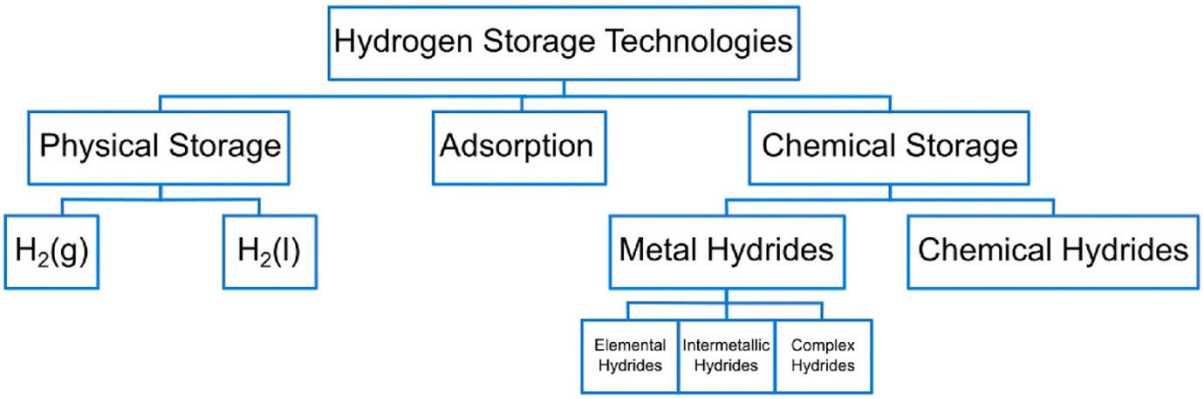

Figure 1.1: Technologies for hydrogen storage, adapted from ref. [4]

Hydrogen can be directly used in a H_2/O_2 fuel cell, the most developed fuel cell type, in the case of physical hydrogen storage. Yet, there are several remaining challenges related to usage of highly flammable hydrogen gas which can be categorized as supply, storage, and safe handling (especially for mobile applications) [5], [6]. Requiring large storage volume per kg fuel and high pressure, hydrogen gas has a low volumetric density, 7.8 kg m^{-3} at 100 bar (10 MPa) and 20 ^{o}C [3]. This value is almost ten times lower than liquid hydrogen storage value, 70 kg m^{-3} at 1 bar and -253 ^{o}C. For example, to achieve a vehicle a range of 500 km, it is required 5-6 kg hydrogen on board the vehicle, with a required pressurized tank volume about 180 litter at 35 MPa [3]. Moreover, hydrogen is a highly volatile and flammable gas which requires careful handling, not to cause any harmful accident.

However, to overcome the problems originated from the use gaseous fuel in a fuel cell, it is required to replace gaseous fuel with liquid fuels as hydrogen carrier. Besides, solving the problems caused by gaseous fuel in a fuel cell, replacement of gaseous fuel with liquid one simplifies the engineering aspect of the cell, hence lower the system complexity, and thereby minimize the overall cost of the cell. Methanol, ethanol, and formic acid are examples of liquid fuels, in the form of chemical hydride storage for hydrogen, as replacement of H_2 gas in a fuel cell. The use of the mentioned liquid fuels has limitations that restrict their usage, including low open circuit potential (OCP), a high rate of fuel crossover, insufficient fuel oxidation, and catalyst poisoning caused by carbon monoxide [6]. In addition, using carbon-based fuels release CO_2 gas as end-product which appears as another disadvantage of these fuels. Metal hydrides, on the other hand, are considered as suitable and highest amount of hydrogen carriers. Due to large hydrogen content, the borohydrides (M-BH_4, M = metal) compounds have a very high energy storage capacity. Among the borohydrides, liquid solutions of $LiBH_4$, $NaBH_4$, and KBH_4 can be feed into a direct borohydride fuel cell to convert stored hydrogen energy into

electricity. Gravimetric hydrogen content of $LiBH_4$, $NaBH_4$ and KBH_4 borohydrides are 18.4 wt. %, 10.6 wt. % and 7.4 wt. %, respectively. Despite sodium borohydride containing less hydrogen than lithium borohydride per unit weight, it is favoured over lithium borohydride due to its ease of handling, stability, the possibility of operation at ambient temperature, and relatively lower cost, as well as the widespread availability of sodium metal [5]. In addition, $NaBH_4$ salt can be transported as white crystal form or 30% aqueous solution, not requiring expensive transportation equipment. In both case, sodium borohydride provides easy handling, not being explosive when contact with water or air, and being insensitive to shock [7].

Compared to methanol, ethanol, formic acid, and H_2/O_2 fuel cells, sodium borohydride fed fuel cells offer higher theoretical cell voltage. This is mainly due to the different half-cell potential of reactions taking place in the anode and cathode compartments, as well as the pH difference between these two compartments. Moreover, end products of a DBFC consist of only water and borate ions. Borate is considered as environmentally acceptable material and potentially can be recycled back to borohydride by hydrogenating under suitable conditions. These facts prioritize DBFCs among its counterparts. Some of the selected fuel cell systems are represented in **Table 1.1**. As represented in **Table 1.1**, the maximum theoretical cell voltage and power density belongs $NaBH_4$ fuel cell systems.

Table 1.1: Theoretical cell potential and energy densities of selected fuel cell at 25 ^oC and 1 atm [8], [9], [10].

Fuel	oxidant	Theoretical cell voltage, V	Theoretical energy density, kW h kg^{-1}
Formic acid ($HCOOH$)	O_2	1.48	1.72
H_2	O_2	1.23	32.8
Methanol (CH_3OH)	O_2	1.21	6.08
Ethanol (C_2H_5OH)	O_2	1.15	8.04
$NaBH_4$	O_2	1.64	9.3
$NaBH_4$	H_2O_2	3.02	17

1.2 Aims and Objectives

The main aim of this research is to develop gold-based electrocatalysts using titanate nanotubes as catalyst support and determine their kinetic parameters for borohydride oxidation. The main goal is to elevate the electroactivity of gold in borohydride electrooxidation, achieve a reduction in total gold loading to lower catalyst costs, and fortify the long-term durability of

electrocatalysts during the direct oxidation reaction of borohydride. This research aimed to achieve the following objectives:

- In addition to its large surface area per mass and excellent durability at extreme acidic or basic conditions, titanate nanotubes have been synthesized and utilized as catalyst support materials to enhance the durability of electrocatalysts for potential use in direct borohydride fuel cells.
- To increase catalytic activity of gold catalyst, gold is deposited on titanate nanotubes with transition metals, namely Nickel (Ni), Cobalt (Co), and Copper (Cu). It is expected that using gold with inexpensive metals will not only improve the catalytic activity of gold, but also reduce the catalyst cost by replacing some of the gold content with inexpensive metals in the catalyst structure.
- Gold and gold-metal co catalysts were synthesised. These synthesised catalysts, coated on a glassy carbon (GC) electrode surface, were used as working electrode to test the electrochemical characterization of these synthesized catalysts in borohydride oxidation by cyclic voltammetry, linear sweep voltammetry, chronoamperometry.
- Kinetic parameters of developed catalysts in borohydride oxidation, such as transferred electron numbers and apparent rate constant, are determined.

Chapter 2: LITERATURE REVIEW

The literature investigation was conducted to uncover achievements, deficiencies and remaining challenges related to direct borohydride fuel cells. Additionally, a detailed review was conducted about each compartment of the direct borohydride fuel cell. Specifically, the anode part was examined more comprehensively. Furthermore, catalyst support for the active catalyst materials reviewed in this chapter.

2.1 Borohydride Fuel Cells

Fuel cells are becoming increasingly important for our future, playing a key role in powering portable devices, stationary systems, and transportation. This is mainly because of their potential of efficient energy conversion, where fuel undergoes direct electrooxidation in fuel cell applications, eliminating the need for traditional fuel combustion [7], [11]. Among the existing fuel cell systems, direct borohydride fuel cell has one of the highest theoretical power outputs because of high hydrogen content of borohydride ions. However, there are still some obstacles to overcome for DBFC for its widespread commercialization: high cost, low performance, and long-term durability.

The first DBFC configuration was introduced by Indig and Snyder [12] at the beginning of 1960s, but fully designed of a DBFC that employed an ion exchange membrane as separator, an air breathing cathode, and 97% Au-3% Pt particles finely divided on carbon cloths as anode was deployed by Amendola and co-workers for the first time [13]. In recent years, there has been a growing interest in DBFC systems, particularly after the 2000s [7].

Borohydride fuel cells can be categorized in two types, depending on cathode oxidants used in cathode compartment, namely oxygen (or air) and hydrogen peroxide. These fuel cells are called direct borohydride fuel cell (DBFC) and direct borohydride hydrogen peroxide fuel cell (DBHFC) depending on used oxidant types. Sometimes DBFC abbreviation is used for both types of borohydride fuel cells. In this paper DBFC covers both fuel cell configuration as well, unless otherwise stated. The reactions taking place in anode compartment are the same for both types of fuel cells. These two fuel cells differ from each other in terms of the reaction mechanisms taking place at cathode and overall cell potentials of the cells. In terms of DBFC, anode and cathode half-cell reactions are as follows for a complete $8e^-$ and $4e^-$ transfer taking place at the anode and cathode, respectively:

$$BH_4^- + 8OH^- \rightarrow BO_2^- + 6H_2O + 8e^- \quad E^0_{anode} = -1.24\ V\ vs.\ SHE \tag{2.1}$$

$$O_2 + 2H_2O + 4e^- \rightarrow 4OH^- \quad E^0_{cathode} = 0.40\ V\ vs.\ SHE \tag{2.2}$$

By combining half-cell reactions given in Eq. (2.1) and Eq. (2.2), the overall cell reaction and theoretical cell potential can be obtained as given by Eq. (2.3):

$$BH_4^- + 2O_2 \rightarrow BO_2^- + 2H_2O \quad E^0_{cell} = 1.64\ V\ vs.\ SHE \tag{2.3}$$

On the other hand, when hydrogen peroxide is in the acidic medium, overall cell potential and power density of the cell can be higher than those of DBFC one's [14]. The cathode reaction for a complete $2e^-$ transfer in a DBHFC and overall cell reaction are given by Eq. (2.4) and Eq. (2.6), respectively.

$$H_2O_2 + 2H^+ + 2e^- \rightarrow 8H_2O \quad E^0_{cathode} = 1.77\ V\ vs.\ SHE \tag{2.4}$$

$$BH_4^- + 8OH^- \rightarrow BO_2^- + 6H_2O + 8e^- \quad E^0_{anode} = -1.24\ V\ vs.\ SHE \tag{2.5}$$

$$BH_4^- + 4H_2O_2 \rightarrow BO_2^- + 6H_2O \quad E^0_{cell} = 3.01\ V\ vs.\ SHE \tag{2.6}$$

However, both systems have their own advantages and drawbacks. When one designs a borohydride fuel cell, he must pay attention the requirements of the intended application. For example, DBHFC facilitates cell design by replacing gaseous oxidant by a liquid one.

Table 2.1: Selected DBHF configuration from the literature. Here, symbols represent the following terms: P is the power density, j is the current density, S is the geometric active surface are of the working electrode, and T is the operating temperature.

Ref.	Anode composition	Cathode composition	Anolyte composition	Catolyte composition	separator	T (°C)	S (cm^2)	j (mA cm^{-2}) [P (mW cm^{-2})
[15]	$Au_{0.65}Zn_{0.35}$/C on stainless steel gauze (4.5 $mg_{catalyst}$ cm^{-2}, 0.9 mg_{metal}) + Nafion®	Au/C cathode	1 M $NaBH_4$ + 3 M NaOH	2 M H_2O_2 + 0.5 M H_2SO_4	N117	20	N/A	60 [39.5]
[14]	$Pt_{67}Zn_{33}$/C (0.9 mg metal cm^{-2}) on stainless steel gauze (4.5 $mg_{catalyst}$, 0.9 mg_{metal})	Pt/C (0.9 mg Pt cm^{-2})	1 M $NaBH_4$ + 3 M NaOH	2 M H_2O_2 + 0.5 M H_2SO_4	N117	25	N/A	79.5 [79.9]
[16]	Bulk zinc metal	Bulk Pt (0.5 cm^{-2})	1 M NaBH4 + 4 M NaOH	35% H_2O_2 in 1 M H_2SO_4, v/v 1:2.5	N117	22	N/A	426 [470]
[17]	$Au_{45}Co_{55}$/C with 10% metal loading	Au/C cathode	1 M $NaBH_4$ + 3 M NaOH	2 M H_2O_2 + 0.5 M H_2SO_4	N117	25	NA	85 [66.5]
[18]	Porous nickel electrodes, (167 mg_{metal} cm^{-2})	Pt/C, or Ag/C; 1 mg_{metal} cm^{-2}	5 wt. % $NaBH_4$ + 6 M NaOH	Air	NRE211	25	6	80 [40]
[19]	AuCo/TiO_2-NTs (0.022 mg_{au} cm^{-2})	Pt sheet	1 M $NaBH_4$ + 4 M NaOH	2 M H_2O_2 + 0.5 M H_2SO_4	N117	25	1	255 [177]
[20]	Pd_2Zn/NPC (4.5 mg_{metal} cm^{-2})	Pt/C	1 M $NaBH_4$ + 3 M NaOH	2 M H_2O_2 + 0.5 M H_2SO_4	N117	25		100 [103.9]
[21]	$Pd_{50}Cu_{50}$ on carbon cloth (0.5 mg_{metal} cm^{-2})	Pt/C (0.5 mg cm^{-2})	1 M $NaBH_4$ in 6 M NaOH at a 3 cm^3 min^{-1} flow rate	Humidified O_2 at 0.2 L min^{-1}	N115	60	25	223 [98]

[1] N117 are types of Nafion® cation-exchange membranes (DuPont).

2.1.1 Cathode

Cathode catalysts selection has an important role to play on DBFC performance [6], [5], [22]. In most DBFC research, Pt based cathode catalysts used due to its high activity towards oxygen reduction, considerable chemical stability, and high electrical conductivity [6]. Cheng and co-workers prepared different cathode catalysts to unearth the cathode compartment effect on DBFC performance [22]. In their study, a Nafion 117 membrane was used as separator, Au/C as anode (with 2 mg Au cm^{-2} loading), 5 wt.-% $NaBH_4$ in 10 wt.-% NaOH solution as fuel and O_2 as oxidant (at ambient pressure, 200 cm^3 min^{-1}); Pt, Ni and Ag as cathode catalysts supported on carbon with a 2 mg cm^{-2} metal loading for each catalyst. The authors highlighted that Pt/C cathode outperformed those of Ni/C and Ag/C at the same conditions with a ca. 72 mW cm^{-2} power density. However, Pt is an expensive noble metal which restricts its competitiveness in the market; therefore, replacing Pt with non-precious catalysts such as manganese oxide-based catalysts could reduce cost of the cathode catalyst thereby total cost of the fuel cell.

Feng and co-workers developed a carbon supported MnO_2-catalyzed air cathode and Au-catalyzed anode to investigate catalytic activities of cathode catalysts in a DBFC configuration, with a 20 wt. % MnO_2 loading [23]. They reported that MnO_2 showed significant electrocatalytic activity towards oxygen reduction while it exhibited negligible catalytic activities for both electrooxidation and hydrolysis of BH_4^- ions. The authors defended that these virtues of MnO_2 can eliminate performance deterioration causing from crossover of BH_4^- ions and the use of expensive Pt catalyst. In their report, the I-V polarization curves of blank solution (6 mol/L KOH) and with BH_4^- solution (1 mol/L KBH4 + 6 mol/L KOH) at 25 ^oC shows almost identical patterns, suggesting that presence of BH_4^- ions has no negative impact on catalytic activities of MnO_2 catalyst for O_2 reduction. In addition, XRD data obtained before and after immersing BH_4^- solution for 48 hours shows similar shapes for cathode catalyst MnO_2, which it was interpreted as evidence of catalyst stability. Besides advantages using MnO_2 as cathode, the authors also mentioned its drawback that MnO_2-catalyzed reduction of O_2 at the cathode suffers from slow kinetics.

In another study conducted by Grimmer and co-workers, electrocatalytic activities of MnO_2 and Pt were compared [24]. The researchers developed carbon supported MnO_2 cathode catalyst with a 13 mg cm^{-2} MnO_2 loading and purchased carbon supported Pt catalyst with a 0.50 mg loading of Pt to test them in O_2 reduction. They observed that Pt shows better catalytic activity than MnO_2 in O_2 reduction under ideal condition such as absence of BH_4^-, but manganese oxide outperformed Pt in the presence of BH_4^- ions. The maximum power density

obtained using Pt based anode and manganese oxide cathode reported as 38 mW cm^{-2}, which is considerably low for practical application.

As a result, using catalysts which are abundant, cheap, and less active towards both hydrolysis and oxidation of borohydride such as MnO_2, iron tetramethoxy phenyl porphyrin, cobalt phthalocyanine, or iron phthalocyanine as cathode catalyst may help to reduce overall fuel cell cost at a certain point if the catalytic activities of these catalysts improved further [6].

2.1.2 Anode

In this section, problems, advancements, and remaining challenges related to catalyst materials used as anode in DBFC were investigated. Moreover, the most utilized catalysts reported in the literature for direct borohydride fuel cell were summarized. Catalysts which were used metal oxides as support materials were specifically in the focus of the investigation. Pd, Pt and Ni are very active catalyst materials towards both borohydride oxidation reaction (BOR) and its hydrolysis reaction [25], [26]. Most of the active catalysts for BH_4^- oxidation reported in the literature are also active for its hydrolysis such catalysts mentioned above. Therefore, using these catalysts yields high power output but low columbic efficiencies, due to hydrolysis of borohydride ions accompanies to its electro oxidation at the anode and lowering theoretical 8e- transfer per BH_4^- ion. In addition, besides heterogeneous hydrolysis of borohydride ions on the electrode surface, homogenous hydrolysis of BH_4^- ions may take place in anolyte solution at lower pH (pH < 12). Reactions given by Eq. (2.1) and Eq. (2.7) are the complete oxidation and hydrolysis of BH_4^- ions, respectively. Bearing in mind reaction (2.1) and (2.7) which occur in parallel on the anode surface, a more general oxidation reaction can be written as represented Eq. (2.8) [26].

$$BH_4^- + 2H_2O \rightarrow BO_2^- + 4H_2 \tag{2.7}$$

$$BH_4^- + xOH^- \rightarrow BO_2^- + (x-2)H_2O + (4-(0.5)x)H_2 + xe^- \tag{2.8}$$

Here, x represents the transferred electron numbers per BH_4^- ion oxidised. It can be interpreted from Eq. (2.8) that when $x = 0$, only hydrolysis reaction take place, and when $x = 8$ only oxidation reaction occurs on the anode. There are only few metals considered as solely active for BOR, but these catalysts such as Au and Ag suffer from slow kinetics towards borohydride oxidation. The existing catalysts do not satisfy both essentials, which are low catalytic activity

for the hydrolysis of borohydride and high activity for its oxidation [14]. As a result, it is crucial to develop an anode catalyst for DBFC that meets both requirements simultaneously.

There are several barriers to commercialization of DBFC. First, finding highly active catalysts for the direct oxidation of BH_4^- with no activity towards hydrolysis of BH_4^- ions or minimal activity is one of the most critical obstacles to tackle. Catalysts such as Pt, Pd, and Ni which are active towards BH_4^- electrooxidation are also active for BH_4^- hydrolysis. On the other hand, having a little activity BH_4^- ions, gold could be a good candidate if its activity can be increased for BH_4^- direct oxidation pathway. Second, stability of anode catalyst in alkaline medium is another problem to be addressed. Carbon black, used widely as support material, degrades during cell operation reducing cell lifetime. To deal with this problem, metal oxide-based support materials could be chosen because metal oxides are in their higher oxidation states.

Pt, Au, Pd, Ag, are the most used noble catalysts either stand alone, or with support material or a combination of with other metals for anode materials in DBFC [27]. Because of the high cost of these noble and precious metals, minimization use of these catalysts materials is essential. Alloying noble metals with transition metals is one way to reduce noble metal loading in anode composition thereby total catalyst cost. In terms of improved activity, selectivity, and stability; intrinsic properties of binary or ternary metal combinations may function different from the parent metals [28]. Alloying precious metals with transition metals not only decrease catalyst cost but may also improve the catalytic activities. Ni, Co, Zn, Fe, Sn, and Cu are some examples of these transition metals alloyed with noble metals.

Preventing hydrolysis of BH_4^- and facilitating its oxidation pathway is still one of the most important obstacles, preventing DBFC from commercialization. Dissociation of borohydride to H_2 gas is not only lowers ideal $8e^-$ transfer thereby reduces anodic fuel efficiency but also raises practical issues, causing instabilities in pressure and preventing liquid fuel transport to electrode surface. To solve the hydrolysis problem of BH_4^- and increase the fuel utilization rate, several approaches were reported in literature: using inhibitors such as thiourea, finding catalysts less active for hydrolysis meanwhile more active towards oxidation for BH_4^- ions such as Au and Ag, and using catalysts active for hydrogen adoption thereby hydrogen oxidation reaction (HOR) such as Pt and Pd are some of these approaches.

Borohydride ions oxidation reaction can be catalysed by on a vast majority of electrode materials. Oxidation of borohydride releases a theoretical maximum $8e^-$ in alkaline medium according to the Eq. (2.1). One of the main problems related to borohydride oxidation taking

place at the anode is spontaneous hydrolysis of BH_4^- ions to form $BH_3(OH)^-$ intermediate as given Eq. (2.9) which is further oxidizes liberating $3e^-$ and hydrogen gas in accordance with Eq. (2.10), or hydrolyses completely to form H_2 gas given by Eq. (2.11). [29]. It is accepted that hydrolysis of borohydride competes with borohydride oxidation reaction at low and moderate pH (pH<12) [30]. To suppress the hydrolysis of borohydride, it gains importance to use concentration ratio of $[OH^-]/[BH_4^-]$ higher than 4.4 [31], [30]. Lower than this value of $[OH^-]/[BH_4^-]$ ratio, BH_4^- hydrolysis is favourable, forming $BH3(OH)^-$ intermediate. This fact necessitates to use ratios $[OH^-]/[BH_4^-]$ higher than 4.4. However, it was reported that hydrolysis of BH_4^- ions may happen even at pH 14, depending on the anode catalysts used to catalyse the oxidation reaction of borohydride [32], [7].

$$BH_4^- + H_2O \rightarrow BH_3(OH)^- + H_2 \text{ (partial hydrolysis)} \quad (2.9)$$

$$BH_3(OH)^- + 3OH^- \rightarrow BO_2^- + \frac{3}{2}H_2 + 2H_2O + 3e^- \quad (2.10)$$

$$BH_3(OH)^- + H_2O \rightarrow BO_2^- + 3H_2 \quad (2.11)$$

It was reported in the literature that the first stage of borohydride oxidation on gold includes three steps: electrochemical oxidation (E) followed by chemical hydrolysis (C) and again electrochemical oxidation (E) shown in Eq. (2.12), Eq. (2.13) and Eq. (2.14) [31],[33]. It has been suggested that remaining $6e^-$ in BH_3 release in fast reaction with OH^- [33].

$$\text{(E) } BH_4^- \leftrightarrow BH_4^{\bullet} + e^- \quad (2.12)$$

$$\text{(C) } BH_4^{\bullet} + OH^- \leftrightarrow BH_3^- + H_2O \text{ (very fast)} \quad (2.13)$$

$$\text{(E) } BH_3^- \leftrightarrow BH_3 + e^- \quad (2.14)$$

Gyenge observed two peaks on the forward scan of cyclic voltammogram curve of borohydride oxidation on Pt disc electrode, conducted using 0.03 M $NaBH_4$ + 2 M NaOH anolyte solution [31]. The first peak was attributed to hydrolysis of BH_4^- yielding H_2 gas followed by its electrooxidation between -0.9 and -0.7 V potential range *vs* KCl saturated Ag/AgCl. He stated that hydrogen evolution involves either Tafel-Volmer or Heyrovsky-Volmer steps as shown in **Figure 2.1**. The second peak was interpreted as the direct oxidation of BH_4^- ions at more positive potentials (between -0.15 and -0.05 V *vs* KCl saturated Ag/AgCl) [29], [31]. Due to hydrogen

formation taking place on the electrode surface by slow chemical dissociation of BH_4^- ions, formed hydrogen from this dissociation can be oxidized immediately with a complete $8e^-$ transfer if it stays on the surface for a sufficient time, giving first oxidation peak aforementioned [34] according to the Eq.(2.15) [35]. Finkelstein and co-workers stated a similar mechanism for borohydride electrooxidation on Pt, chemical hydrolysis of BH_4- shown Eq. (2.9) followed by electrooxidation of H_2 seen as in Eq. (2.15), and chemical hydrolysis of $BH_3(OH)^-$ shown Eq. (2.10) [32]. Complete oxidations of BH_4^- to BO_2^- includes stepwise mechanism, forming intermediates which can be either hydrolysed to H_2 gas or undergone electrochemical oxidations. This difference in reaction pathway for BH_4^- oxidation is resulted in a variation in utilized electron numbers per borohydride ion.

$$H_2 + 2OH^- \rightarrow 2H_2O + 2e^- \quad E^0_{anode} = -0.828\ V\ vs\ SHE \tag{2.15}$$

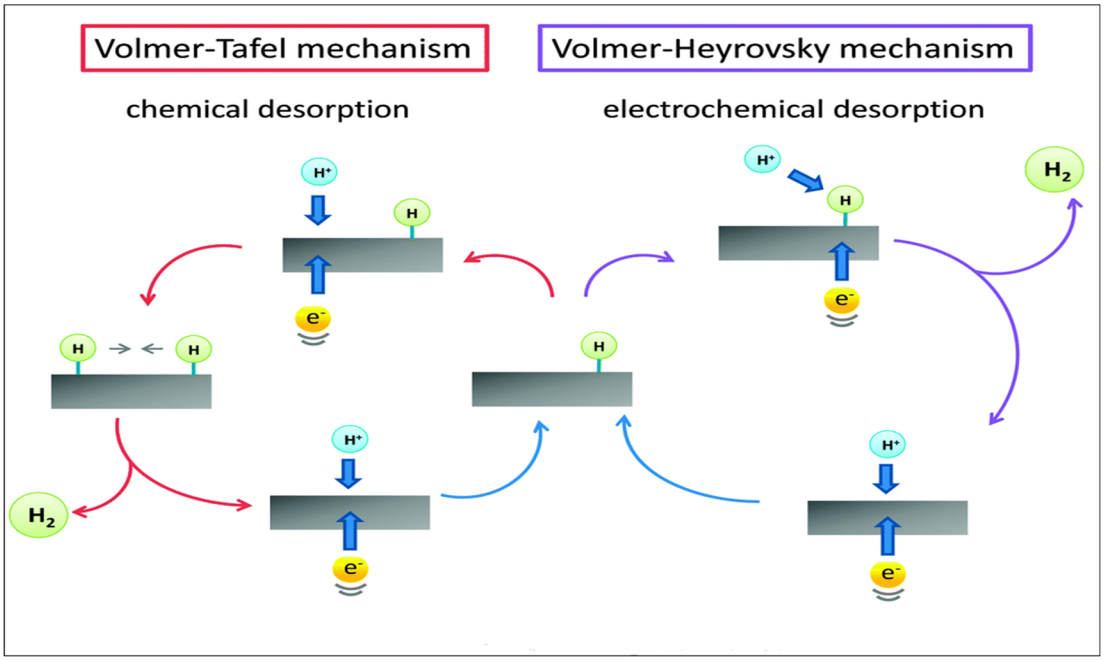

Figure 2.1: Representation of hydrogen evolution mechanisms involving Volmer-Tafel and Volmer-Heyrovsky steps, adapted from ref. [36].

Despite the suggested reaction mechanisms for borohydride direct oxidation and hydrolysis taking place on different electro-catalysts, these suggested reaction mechanisms and reaction pathway of borohydride oxidation are not yet fully understood and open to speculation. The reason for this uncertainty is that electrochemical behaviour of borohydride ions is very complex due to multiple electron transfer.

2.1.2.1 Gold

Gold is extensively studied as an anode electrocatalyst for BH_4^- electrooxidation due to its capability to release approximately 8 electrons during the borohydride oxidation reaction [30], [37], [38]. It has been reported in the literature that gold (Au) exhibits significant activity in BH_4^- electrooxidation while demonstrating minimal activity for BH_4^- hydrolysis [31], [37], [39]. However, Chatenet and co-workers [40] argued that their experimental results, obtained using online mass spectrometry to detect H_2 generation during BH_4^- electrooxidation on a sputtered gold electrode, are not negligible. Nevertheless, this study has not been corroborated by any other researchers. Çelikkan and co-workers, on the other hand, studied Au, Pt, Ag, Pd, and Ni towards borohydride electrooxidation [37]. Authors defended in this study that Au shows the best electro-catalytic activities for direct oxidation of borohydride among the studied catalysts. A similar observation reported by Cheng and co-workers who compared catalytic activities of carbon supported Au, Pt, Pd, Ag, and Ni and suggested that Au is the best electrocatalyst for borohydride oxidation for a long-term operation [41]. Feng and co-workers [23], Chatenet and co-workers [39], and Amendola and co-workers have reported transferred electron numbers of 7.4, 7.5, and 6.9, respectively, in the case of using gold as the anode. These transferred electron number are close to those of possible $8e^-$ per BH_4^- ions, indicating that Au based anode catalysts have a good faradic efficiency. However, gold has a low catalytic activity towards borohydride oxidation which needs to be improved for practical applications of DBFCs. Alloying gold with other metals may lead to improve catalytic activities of gold. In this regard, based on solely gold and Au-M (M = metal or metals alloyed with gold) anode materials for DBFC were investigated to unearth the effect of different metals alloyed with gold on direct borohydride oxidation.

He and co-workers tested carbon supported gold-zinc bimetallic catalysts prepared by reverse microemulsion method as anode material in a DBFC [15]. The cathode catalyst used in this study was carbon supported Au, donated as Au/C. They used different atomic ratio of zinc and gold in anode catalysts composition, namely Au/C, $Au_{0.8}Zn_{0.2}$/C, $Au_{0.65}Zn_{0.35}$/C, and $Au_{0.5}Zn_{0.5}$/C. $Au_{0.65}Zn_{0.35}$/C was reported the most active catalyst among these prepared electro-catalyst towards direct oxidation of borohydride, with 60 mA cm^{-2} peak current density at 0.67 V *vs* Ag/AgCI and 39.5 mW peak power density. It was also observed that none of the prepared catalysts were active towards hydrolysis of borohydride ions, which is very important for a better fuel utilization and safer cell operation. Moreover, the authors reported that Zinc improved the catalytic activity of gold. Furthermore, to reveal the short-term fuel cell stability,

they monitored the cell voltage change during the galvanostatic discharge of 5 mA cm^{-2} of the cell for 30 hours. This experiment result revealed that $Au_{0.65}Zn_{0.35}$/C had a better stability and higher cell voltage than that of Au/C. However, the authors did not provide any information about long term stability of these catalysts. Due to this, long term stability of these catalysts is open to the speculation. Lastly, they reported the size of bimetallic Au-Zn nanoparticles varied from 3 to 6 nm. This size range is below than 10 nm which is reported in the literature that gold catalyst is more active when its particle size below than 10 nm [42]. In another study, He and co-workers used Au-M (M = Zn, Fe, Co, Ni, and Cu) bimetallic catalysts prepared by a reverse micelle method as anode catalysts with ca. 1:1 atomic ratio for each bimetallic catalysts [43]. Among these prepared electro-catalysts, Au-Zn/C, Au-Fe/C and Au-Cu/C were reported as inactive catalysts towards borohydride hydrolysis. While Au-Ni/C and Au-Co/C caused partial hydrolysis of borohydride, the former reported more active than the later for hydrolysis reaction of borohydride. **Table 2.2** shows the transferred electron numbers calculated by He and co-workers in the oxidation reaction of borohydride for different electro-catalysts [43].

Table 2.2: Transferred electron numbers of bimetallic electro-catalysts reported in ref. [43]

electrocatalyst	n	Anolyte	Sweep rate (mV s^{-1})	T (^{o}C)
Au-Zn/C	7.3	0.05 M $NaBH_4$ + 3 M NaOH	10	20
Au-Cu/C	6.3			
Au-Ni/C	6.8			
Au-Co/C	6.5			
Au-Fe/C	5.7			

As it can be seen in this table, transferred electron numbers for Au-Zn/C, Au-Ni/C and Au-Co/C are close to theoretical 8 electron transfer number for electrooxidation of borohydride. The authors highlighted that being capable of $7.3e^-$ transfer, having an optimum electrochemical surface area (ECSA) and long-term running stability among the prepared Au-M/C catalysts, Au-Zn/C could be a suitable electro-catalyst for particle application of DBFC if the kinetic of the BH_4^- oxidation on Au-Zn/C is improved further.

Pei and co-workers prepared Au-Co polymetallic electrocatalysts supported on Vulcan XC-72R carbon by reverse microemulsion method and tested them in a direct borohydride-hydrogen peroxide fuel cell system. Obtained results showed that the most active catalyst was $Au_{45}Co_{55}$/C among the prepared catalysts in this research, with a 66.5 mW cm^{-2} peak power

density. This value is nearly double that of Au/C anode electrocatalyst performance, which was 28.2 mW cm^{-2} on borohydride oxidation, and higher than that of Co/C anode catalyst, which was 47.4 mW cm^{-2}. A similar study was conducted by Yi and co-workers, using Au-Cu bimetallic electrocatalysts supported on carbon. Providing 51.8 mW cm^{-2} peak power density at 69.5 mA cm^{-2} current density and 20 ºC, $Au_{67}Cu_{33}$/C showed the highest electrocatalytic activities [44]. In this study, peak power performance of Au/C was reported 22.1 mW cm^{-2}. In both studies, the authors defended that performance of bimetallic gold electrocatalysts in borohydride electrooxidation were higher than carbon supported monometallic gold catalysts.

Geng and co-workers synthesized two different Pt-modified gold nanoparticles supported on carbon with a mass ratio of Pt and Au as 1:9 in both case [45]. The catalysts were prepared by co-reduction of Au and Pt on carbon donated as A-AuPt/C, and step-by-step chemical reduction of Au followed by Pt reduction on carbon donated as B-AuPt/C. The researchers also prepared carbon supported Au nanoparticles by chemical reduction method (Au/C) to compare the electrocatalytic activities with the first two catalysts. As can be seen in **Figure 2.2**, B-AuPt/C outperformed the other two electrocatalysts performance with a maximum power density of 112 mW cm^{-2} at 40 ºC. In addition, the authors stated that apparent number of transferred electrons were 6.4 in 1M $NaBH_4$ and 7.2 in 0.5M $NaBH_4$ in the case of employment B-AuPt/C as anode, showing slight addition of Pt improved catalytic activity of Au.

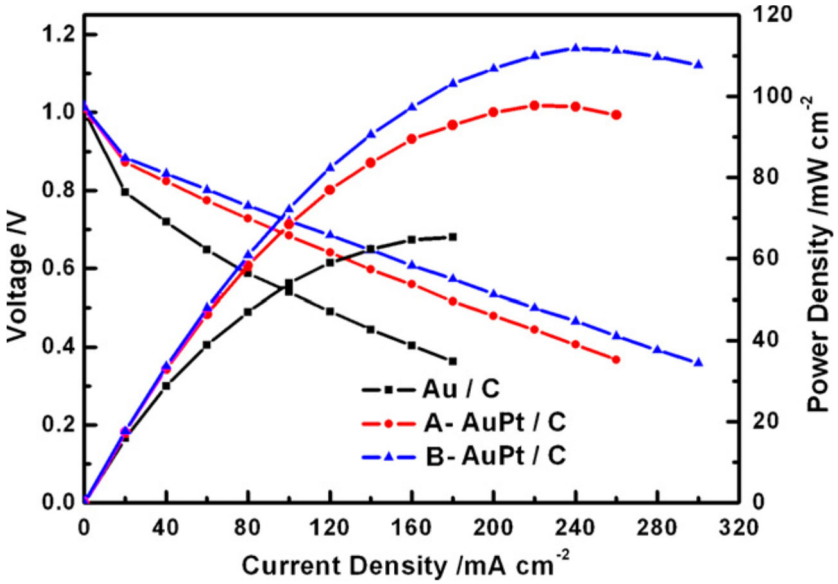

Figure 2.2: Performance data for DBFCs utilizing 0.5 mg cm^{-2} Pt supported on carbon as cathode and three different anode catalysts with 1 mg cm^{-2} metal load at 40 ºC. Anolyte was 1 M $NaBH_4$ + M NaOH, oxidant was dry O_2 at 0.1 L min^{-2} at 2 atm. from ref. [45]

2.1.2.2 Platinum

Yi and colleagues synthesized carbon-supported Pt-Zn bimetallic catalysts at various ratios and assessed their electrochemical performance for borohydride electrooxidation [14]. According to their fuel cell tests, conducted at 25°C, the maximum current densities and corresponding maximum power densities achieved using $Pt_{67}Zn_{33}$/C and Pt/C electrodes were 79.5 mA cm^{-2} (79.9 mW cm^{-2}) and 39.6 mA cm^{-2} (42.8 mW cm^{-2}), respectively. The authors attributed this increase in current and power densities to the synergistic effect of bimetallic combination Pt and Zn nanoparticles. In addition, they measured that open circuit potential (OCP) for a single direct borohydride-hydrogen peroxide cell was 1.7 V in the case of $Pt_{67}Zn_{33}$/C anode and Pt/C cathode usage.

Liu and co-workers tested several metals as anode electrode, namely Pt, Au, Cu, Pd, Ni, and Raney Ni [26]. In terms of OCP, the following order was examined Ni = Raney Ni > Cu > Au > Pd > Pt, from more negative to less negative. The measured OCPs were less negative than equilibrium open circuit potentials for each catalyst yet higher than hydrogen oxidation potential. The shift from equilibrium OCPs to less negative OCPs were attributed to intermediate products of oxidation reaction. Their results showed that oxidation of borohydride on Ni, Raney Ni and Cu followed $4e^-$ transfer pathway, while exchange electron number on Pd and Pt found to be close to $8e^-$ under certain conditions: low BH_4^- concentration (< 1.5 M), low temperature and high current densities (between 250 mA cm^{-2} and 400 mA cm^{-2}). Surprisingly, they stated that exchange electron number on Au was close to 4.5 under the same conditions. The authors did not clarify the reason behind this observation. However, they concluded that using high concentration of borohydride (<1.5 M) almost ceases hydrogen generation on carbon supported Pt and Pd electrocatalysts.

2.1.2.3 Palladium

Palladium has been reported as a catalytically active catalyst for both hydrolysis and electrooxidation of borohydride, providing considerably high anodic currents and high coulombic efficiencies at low borohydride concentrations [5]. Electrooxidation of borohydride on carbon supported Pd has been examined and found that oxidation process has a 75% faradic efficiency, liberating $6e^-$ in this process according to Eq. (2.16) [26].

$$BH_4^- + 6OH^- \rightarrow BO_2^- + 4H_2O + H_2 + 6e^- \quad (2.16)$$

However, Cheng and colleagues compared the electrocatalytic activities of carbon supported Au, Pt, Pd, Ag, and Ni [41]. The maximum power density (89.6 mW cm^{-2} at 85 ºC) was

achieved using Pd/C anode, but it was reported that this value did not sustain due to low stability of Pd/C electrode. The stability tests demonstrated that Pt/C and Au/C showed the most stable performance, while Ag/C exhibited moderate stability and stability performance of Ni/C was the lowest after Pd/C. The authors summarized that Pd was not suitable catalysts due to its unstable nature in DBFC conditions. Celik and co-workers reported a peak power density of ca. 12.7 mW cm^{-2} at 25 ^{o}C, deploying Pd/C anode and Pt/C cathode separated by a Nafion membrane [46]. The anolyte was composed of 1 M $NaBH_4$ in 20 wt. % NaOH and oxidant was humidified air. When they shifted Pd loading from 0.3 to 1.08 mg cm^{-2}, maximum power density increased to 19.4 mW cm^{-2} as expected. Replacement of oxidant to H_2O_2 could have yielded a higher power output.

The high cost and relative instability of using mono-metallic forms of Pd as a catalyst in DBFC configurations have prompted researchers to explore alloying Pd with other catalyst materials for further investigation into borohydride oxidation. Liu and co-workers prepared nanoporous carbon (NPC) supported bimetallic Pd-Zn/NPC electrocatalysts with different molar ratios (1:1, 2:1 and 3:1) and Pd/NPC as anode catalysts for DBFC employing H_2O_2 as oxidant [20]. The measurements of electrochemically active surface area (ECSA) revealed that Pd_2Zn/NPC has the largest ECSA among the prepared electrocatalyst. The experimenters observed that all Pd-Zn/NPC catalysts showed better catalytic activity and stability than Pd/NPC electrocatalyst. Pd_2Zn/NPC exhibited the highest peak power density (103.3 mW cm^{-2} at 25 ^{o}C) as expected due to having the largest ECSA. The authors argued that alloying Pd with Zn enhances catalytic activities and reduces the cost of the catalyst by substituting non-precious Zn for Pd. Behmenyar and co-workers investigated carbon supported Pd-Cu bimetallic electrocatalyst with different compositions with a total metal loading of 20 wt. % of the catalyst composition [21]. The results obtained with different Pd-Cu catalysts are shown in **Figure 2.3**. As illusturated, alloying Pd with Cu improved its catalytic activities toward borohydride oxidation. Ponce de Leon and co-workers investigated hydrogen evolution and BH_4^- oxidation on Pd-Ir bimetallic anode catalysts and showed that alloying Pd with Ir favours oxidation of borohydride rather than its hydrolysis compared to pure Pd anode [47]. It is evident that alloying Pd with other metals alters stability and activity in DBFC.

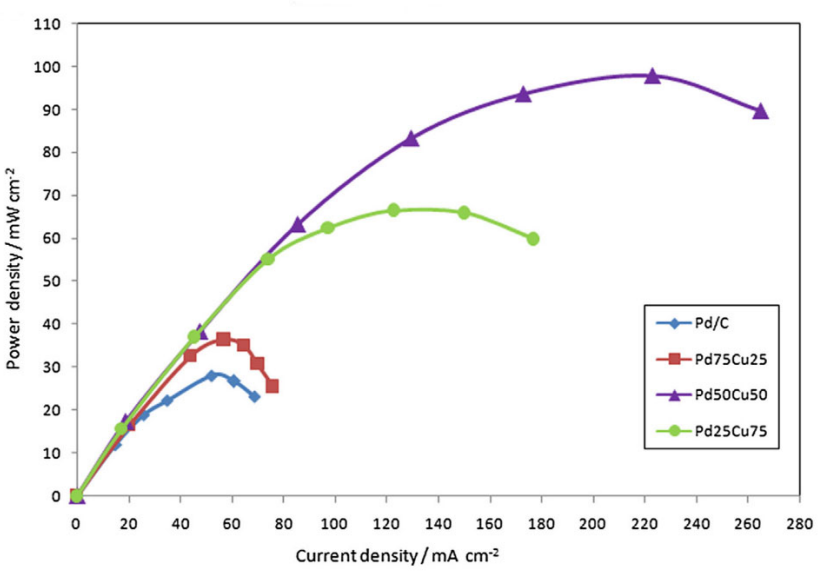

Figure 2.3: Power density curves of DBFC employing Pd-Cu/C electrocatalyst as anode with 0.5 mg_{metal} cm^{-2}, Pt/C as cathode with 0.5 mg_{metal} cm^{-2}, 3 ml min^{-1} 1 M $NaBH_4$ in 6 M NaOH and humidified O_2 at 0.2 L min^{-1}, from ref. [21]

2.1.2.4 Silver

Silver has been tested as an anode catalyst for DBFC in some research studies [18], [41]. Chatenet and co-workers and Sanli and colleagues reported that liberated electron numbers during electrooxidation of borohydride on Ag electrocatalyst has been found to be ca. 8 and $6e^-$, respectively, and Sanli and co-workers proposed reaction mechanism for BH_4^- oxidation on Ag which involves $6e^-$ transfer as shown in Eq. (2.17) [48], [49]. Cheng and co-workers used different anode materials including Ag to reveal the effect of anode catalyst on DBFC performance [41]. Compared to Au, Ag was reported to have a lower electrocatalytic activity toward borohydride oxidation by the last reference. Chatenet and co-workers reported exchanged electron number to be $7.5e^-$ in electrooxidation of borohydride on carbon supported Ag catalyst [39]. They also defended that Ag/C showed the best catalytic activity among the all studied catalyst materials towards BH_3OH^- ions oxidation, which is an intermediate of BH_4^- hydrolysis, whereas showed poor activity towards BH_4^- electrooxidation. However, even though Ag shows relatively low catalytic activity in comparison to Au in the electrooxidation of borohydride, low price of Ag makes it a good candidate for anode catalyst in DBFC, with a relatively good power density (ca. 50 mW cm^{-2}) obtained using carbon supported Ag [41].

$$Ag_2O + BH_4^- + 6OH^- \rightarrow 2Ag + BO_2^- + 5H_2O + 6e^- \quad (2.17)$$

Feng and co-workers fabricated Ag and AgNi (wt. ratio of 1:1) bimetallic electrocatalyst supported on carbon to investigate their performance towards borohydride electrooxidation

[50]. The results revealed that discharge voltage and capacity of DBFC deploying AgNi/C as anode was higher than those Ag deploying as anode and exchanged electron numbers was more than $7e^-$ in AgNi/C catalysed electrooxidation of $BH4^-$, which has been reported $4e^-$ on Ni [18]. This enhancement has been attributed to collective effect of effective surpassing characteristic of Ag for BH_4^- hydrolysis and electrocatalytic activity of Ni toward BH_4^- oxidation [50].

2.1.2.5 Nickel

Ni has been the most investigated non-precious transition metal as anode catalyst for DBFC, either in monometallic form or combined other metals, and its coulombic efficiency for borohydride oxidation has been reported to be 50%, yielding $4e^-$ in the electrooxidation of borohydride [18], [51], [52]. Liu and co-workers reported that Ni and Raney nickel has the most negative open circuit potential (-1.03 V *vs* SHE) among the tested six anode materials using the anodic fuel composition of 2.4 M $NaBH_4$ in 6 M NaOH [26]. In another study of Liu and co-workers which was investigated short and long term stability of Ni anode and Pt cathode catalysts under passive conditions, it was found that anodic polarization increased gradually due to oxide formation on the Ni anode surface, reducing catalytic activity of the anode at a great extent [53]. Cheng and co-workers tested carbon supported Ni as anode in DBFC deploying O_2 as oxidant at 1 atm and 200 cm^3 min^{-1}, 5 wt. % $NaBH_4$ in 10 wt. % NaOH at 10 cm^3 min^{-1} as fuel, and a Nafion 117 membrane as separator [41]. The researchers achieved peak power density of 40.5 mW cm^{-2} at 165 mA cm^{-2} using 2 mg cm^{-2} Ni loading at the anode and 2 mg cm^{-2} Pt at the cathode. They also observed a performance reduction of DBFC over the time, in which Ni was used as anode. This performance reduction was attributed to NiO formation on the anode surface. However, some publications which bimetallic form of Ni investigated have been reported that dealloying Ni with other metals (mainly precious metals) could improve DBFC performance and lower the catalyst price [50], [53], [54], [55], [56], [57], [58].

2.1.2.6 Copper

Copper is another non-precious metal tested as anode catalyst in DBFC. Behmenyar and Akin tested carbon-supported Pd and bimetallic Pd-Cu anode catalysts prepared by polyol technique [21]. They reported that $Pd_{50}Cu_{50}/C$ gives 4.3 times higher current density than Pd/C, being 223 and 52 A cm^{-2} at 60 ^oC, respectively.

2.1.2.7 Zinc

Zinc could be a suitable anode material for a DBFC due to its suppressing effect on hydrogen evolution in alkaline medium thereby high fuel utilization rate and high open-circuit potential [14]. Santos and co-workers investigated bulk zinc metal as anode catalyst [16]. Their work revealed that using zinc anode resulted in high power density and high cell voltage.

2.1.3 Effect of Other Variables on Anode Performance

Beside anode catalyst selection, there are other variables which influence anode performance in DBFCs. These parameters need to be considered to obtain optimum cell operation condition. In this respect, the following parameters were investigated.

2.1.3.1 Anode Composition

Composition and design of the anode can play an important role on the DBFC performance, besides selection of different anode electrocatalysts [59]. A common preparation procedure of catalyst ink is to mix binder (Nafion or PTFE) and catalyst powder in isopropyl alcohol, water, methyl pyrrolidone, ethanol, or in a combination of these solvents [43], [54], [60],[61]. Prepared ink is then applied on a conductive substrate to fabricate anode. Due to the nature of Nafion binder, it has both hydrophilic and hydrophobic properties while PTFE has only hydrophobic features. Considering these properties, using Nafion as binder improves interaction between aqueous fuel and anode surface; while PTFE usage as binder can facilitate generated H_2 release at the anode, but its hydrophobic nature increases undesirable resistance for diffusion of aqueous reducer to the anode surface. In addition, it has been reported that addiction of Nafion improves ion conductivity in the DMFC and PEFC electrodes [6]. Park and co-workers reported that an increase in PTFE content in the anode catalyst resulted in a dramatic decrease in cell performance [62]. Liu and co-workers studied the effect of different binders on anode catalyst performance and observed that the current increased greatly when Nafion was used as binder rather than PTFE [63]. Kim and co-workers investigated Nafion content to unearth its effect on the anode performance by varying percentage of 10 to 30 wt. % [64]. The researchers reported that increase of Nafion content in anode catalyst improved cell performance up to a certain percentage (25 wt. %), reducing the interfacial resistance between anode and the aqueous fuel. Further increase in Nafion percentage resulted in a decrease in fuel cell performance as can be seen clearly in **Figure 2.4**. This decrease was explained that further increase above the optimum level of Nafion amount in the catalyst structure lowers the electrical conductivity of the electrode, due to the electrical insulator effect of Nafion.

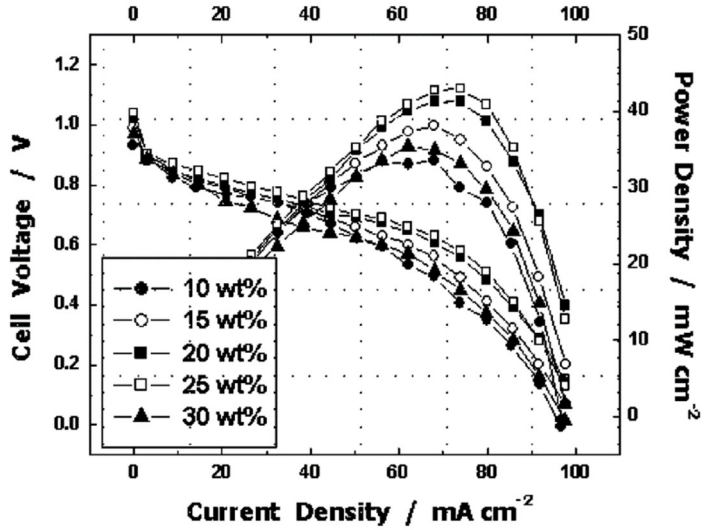

Figure 2.4: Effect of Nafion content on DBHF performance, with air-berthing cathode configuration of DBFC that deploy unsupported platinum on both anode and cathode with a Pt loading of 5.92 mg cm^{-2}, 0.5 M $NaBH_4$ in 6 M KOH as fuel at room temperature [64].

2.1.3.2 Catalyst Loading

Catalyst loading is an important parameter in investigation of DBFC performance. An increase in catalyst loading would lead to an improvement in power output of the cell. However, the rise in catalyst loading and corresponding power density increase has been found to be not proportional [22]. Cheng and co-workers researched cathode catalyst loading effect on power output of DBFC, using different Pt loading (1, 2 and 5 mg Pt cm^{-2}) [22]. They demonstrated that there was a 16% increase in power density when Pt loading shifted from 1 to 2 mg cm^{-2}. Further increase in Pt loading from 2 to 5 mg cm^{-2} led only 8% rise in power density. This was attributed to the negative impact of thick catalyst layer on cell resistance and mass transport. In the same study, gold loading in the anode was investigated as well, utilizing different Au loading values. When Au loading was doubled, only a 15% increase was obtained in peak power density. Further increase in Au loading from 2 to 5 mg cm^{-2} resulted in only 6% in power density. In another study, Liu and colleagues investigated the effect of catalyst loading on DBFC performance, and they found that an almost fivefold increase in Pt loading on the cathode resulted in only a 20% rise in power density [18]. They concluded that an optimum catalyst loading would be applied to obtain an optimized cell performance while avoiding excessive usage of precious catalyst materials. Therefore, it is noteworthy that optimum catalyst loading would help to obtain a maximum power output and lower the cost by using less catalyst materials in the anode and cathode. **lues in** the anode and cathode.

Table 2.3 illustrates the corresponding power densities obtained using different loading values in the anode and cathode.

Table 2.3: Effect of anode and cathode catalysts loading on power density [22]

catalyst	Catalyst loading, mg_{metal} cm^{-2}	P_{peak}, mW cm^{-2}	% increase in P_{peak}
Anode, Au/C	1	61.2	-
	2	72.2	15
	5	77.4	6
Cathode, Pt/C	1	60.5	-
	2	72.2	16
	5	78.6	8

2.1.3.3 Borohydride Concentration

The effect of BH_4^- ions concentration on DBFC performance has been reported in the literature [65], [46], [66]. It has been monitored that an increase in borohydride concentration generally leads to a rise in current and power density, increasing transportation of fuel to the electrode surface and enhancing reaction kinetics of fuel oxidation. An increase in fuel crossover and its hydrolysis has also been observed in response to a rise in borohydride concentration in the cell, resulting in a loss of coulombic efficiency, a reduction in OCV, and activation losses at the cathode catalyst [67]. Boyacı San and co-workers reported that an increase in borohydride concentration was useful at low temperatures (<50 ºC), whereas it caused detrimental effects at high temperatures (>50 ºC) due to increasing borohydride hydrolysis and crossover [66]. However, Kim and his team observed a decrease in power density with further increase than 0.5 M $NaBH_4$ concentrations in 6 M KOH at room temperature [64]. The downward trend in power density with the rise of fuel concentration was explained by the enhanced fuel crossover at higher fuel concentrations, which was believed to cause deactivation of the cathode catalyst and thereby a decrease in cell voltage. The authors summarized that optimum fuel concentration in 6 M KOH was 0.5 M $NaBH_4$. Geng and colleagues observed an enhancement in power density with the rise of borohydride concentration until a certain level [45]. When concentration of BH_4^- was shifted from 0.2 to 0.5 M, peak power density increased dramatically; and when it was shifted from 0.5 to 1 M, power density climbed from 92 to 112 mW cm^{-2}. Further increase in borohydride concentration had barely influence on peak power density, as shown in **Figure 2.5**.

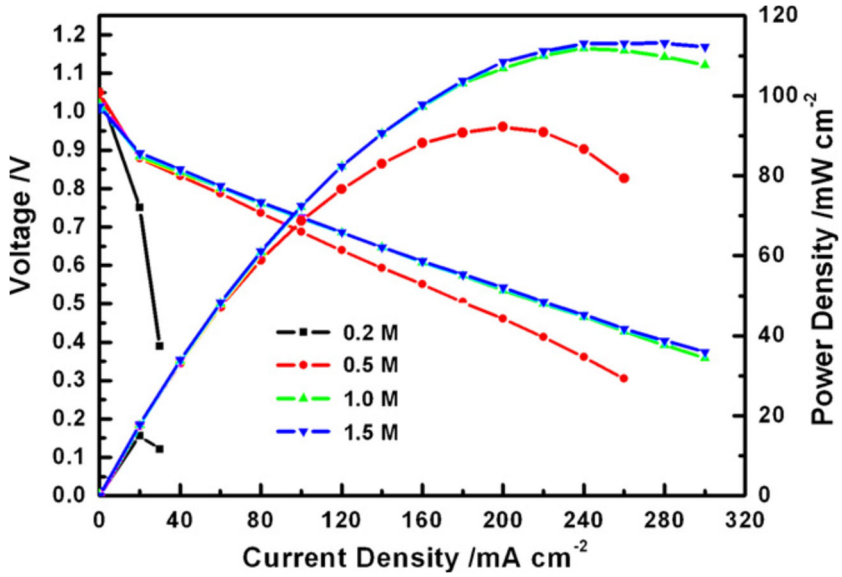

Figure 2.5: Borohydride concentration effect on power output of DBFC. AuPt/C anode, Pt/C cathode, at 40 ºC, and constant NaOH concentration of 2 M, from ref. [45].

As a summary, a common agreement about the optimized borohydride concentration in DBFC operation was reported to be between 10 and 30 wt. % [7], [64], [45].

2.1.3.4 Concentration of Hydroxide Ions

NaOH and KOH are the most utilized bases in preparation of supporting electrolyte in DBFCs and concentration of these MOH has been reported to be in the range between 10 and 40 wt. % to obtain an optimized fuel cell performance [7]. Strong alkaline medium is required to keep borohydride ions stable, and it has been reported that $[OH^-]/[BH_4^-]$ ratio must be above 4.4 to achieve this goal [31], [30]. Hydroxide concentration was found to have a limited effect on DBFC performance compared to those of borohydride concentration [46], [66], [67]. Cheng and co-workers observed a slight increase in sustained current density and power density with the increase of NaOH concentration up to 10 wt. % and further increase was found to be detrimental effect on the cell performance as shown in **Figure 2.6** [67]. These enhancements resulted from hydroxide concentration rise has been reasoned to the improved ionic conductivity of the anolyte solution with the rise of NaOH concentration. Deterioration of cell performance caused from the further increase of NaOH concentration above 10 wt. % has been addressed to the increased viscosity of the anolyte solution, which limits BH_4^- movement towards anode surface and Na^+ ions to the membrane. In addition, the authors stated that an increase in NaOH leads to sodium carbonate formation on cathode surface in the presence of atmospheric CO_2 in the oxidant, deactivating cathode at some extend and considered as another reason for cell performance loss with the further increase of NaOH concentration.

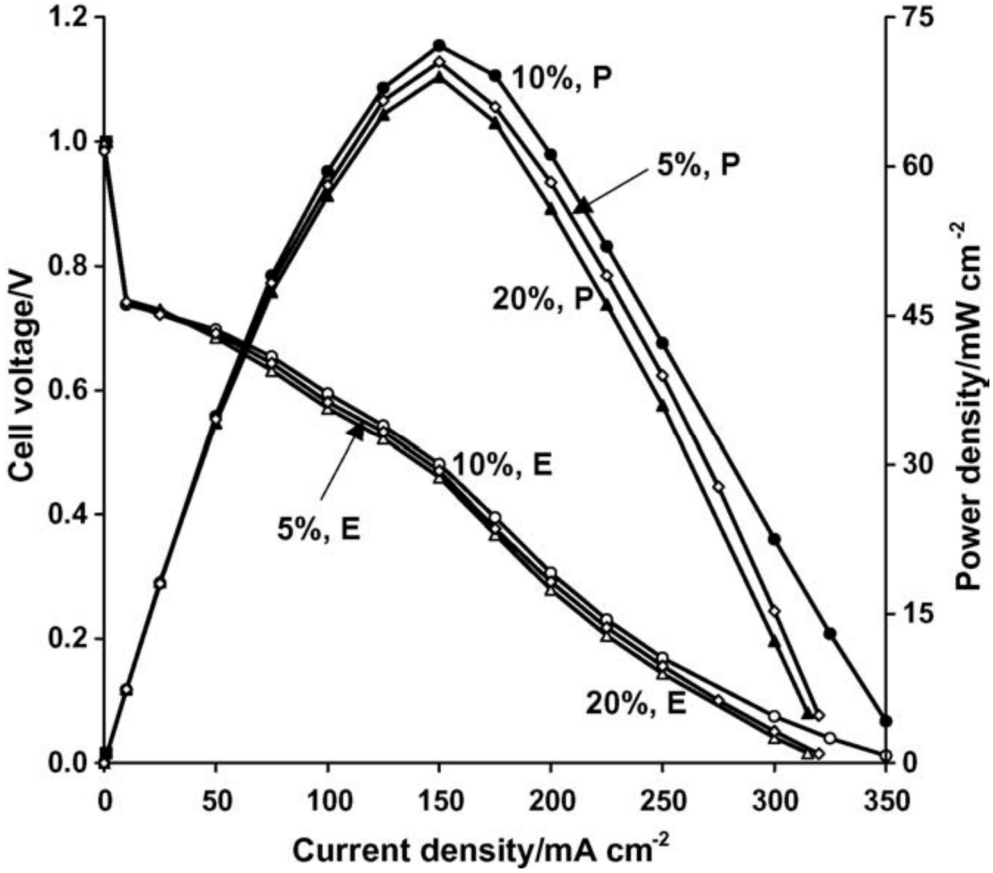

Figure 2.6: Effect of NaOH concentration on DBFC performance. Conducted using 5, 10 and 20 wt. % NaOH and 5 wt. % $NaBH_4$ solution, from ref. [67]

Celik and co-workers and Geng and co-workers observed a similar relation between NaOH concentration increase and DBFC performance with those of Cheng and co-workers [46], [45]. As a result, it has been emphasized in the literature that an optimized hydroxide concentration of around 20 wt.% needs to be chosen to achieve better DBFC performance.

2.1.3.5 Anolyte Inhibitors Used to Minimize H_2 Generation

Jamard and co-workers, tested thiourea to inhibit hydrolysis of borohydride using Pt based anode catalyst [57]. They found out that using thiourea as inhibitor helps to alter practical fuel utilization capacity from 18% to 64% of theoretical one. However, their findings demonstrate that adding 10^{-4} M thiourea into anolyte solution (2 M $NaBH_4$ + 1 M NaOH) lowers peak power density from 200 mW cm^{-2} to ca. 90 mW cm^{-2}, poisoning the active sites of hydrogen adsorption. The authors concluded that fuel optimization and catalyst loading could be more beneficial rather than adding TU to achieve a high fuel utilization rate. A similar study conducted by Gyenge to investigate thiourea effect on borohydride ions hydrolysis [31]. In his work, he used gold and platinum (non-catalytic and catalytic catalysts, respectively) for BH_4^- hydrolysis reaction. In the case of Pt catalyst usage, he tested thiourea to suppress BH_4^-

hydrolysis accompanied by H_2 evolution. His experimental results conducted with Pt catalyst that in the presence of 1.5×10^{-3} M thiourea shows that there was no hydrolysis peak on cyclic voltammetry curve which was interpreted as evidence of prevention of BH_4^- ions hydrolysis. The author highlighted the long-term usage of thiourea could reduce the anode performance and affect stability of the catalyst by poisoning its active sites. Martins and co-workers tested thiourea as inhibitor in one-compartment cell [68]. In this study it was also reported that thiourea effectively suppressed H_2 generation and led to $8e^-$ oxidation on Pt anode electrocatalyst. Their results conducted with different thiourea concentrations (0.3 and 0.6 M) and keeping fuel concentration constant at 0.5 M NaBH4 in 3 M NaOH revealed that an increase in inhibitor concentration greatly reduced the current density. This could be deactivation effect of thiourea on electrocatalyst active sites which reported by Gyenge and Jamard and co-workers [31], [57].

Consequently, although thiourea has positive effect on surpassing H_2 generation, it was reported in the literature that addiction of thiourea in the anolyte causes power loss [31], [57] [68].

2.1.4 Separators

Cathode catalysts which are active for borohydride oxidation or its hydrolysis, such as Pt, could be deactivated by forming carbonate on the electrode surface in the presence of CO_2 if fuel cross-over is not prevented [18]. In addition, fuel cross-over would reduce fuel utilization besides causing deactivation of cathode. Serving as a selective ion exchange tool between anode and cathode compartments thereby maintaining charge balance between the compartments, separators have an important role on DBFC performance. Conductivity, thickness, composition, ion exchange capacity, equilibrium water content, and mechanical strength can be considered as some properties to evaluate membranes. In general, there are two main types of membranes deployed in DBFC configuration, namely cationic and anionic membranes. In the case of anion-exchange membrane deployment, the main charge carriers are hydroxyl ions [OH^-] transported from the cathode compartment to anode. These types of membranes could be ideal selection for a DBFC to maintain alkaline pH of the anolyte at intended level hence ensuring a stable medium for BH_4^- ions. However, these types of membranes suffer from high rate of BH_4^- cross-over beside OH^- transportation.

In most DBFCs reported in the literature, a cation exchange membrane was used to separate anode and cathode compartment, allowing Na^+ ions transportation as charge carrier from anode to cathode compartment [6], [59]. Then, Na^+ ions combine with OH^- ions at the cathode forming

NaOH under cell operation, which this means that displacement of NaOH from anode to cathode compartment raise an undesirable condition at the anode for BH_4^- ions. **Figure 2.7** shows the main ion movements between anode and cathode for both types of membranes.

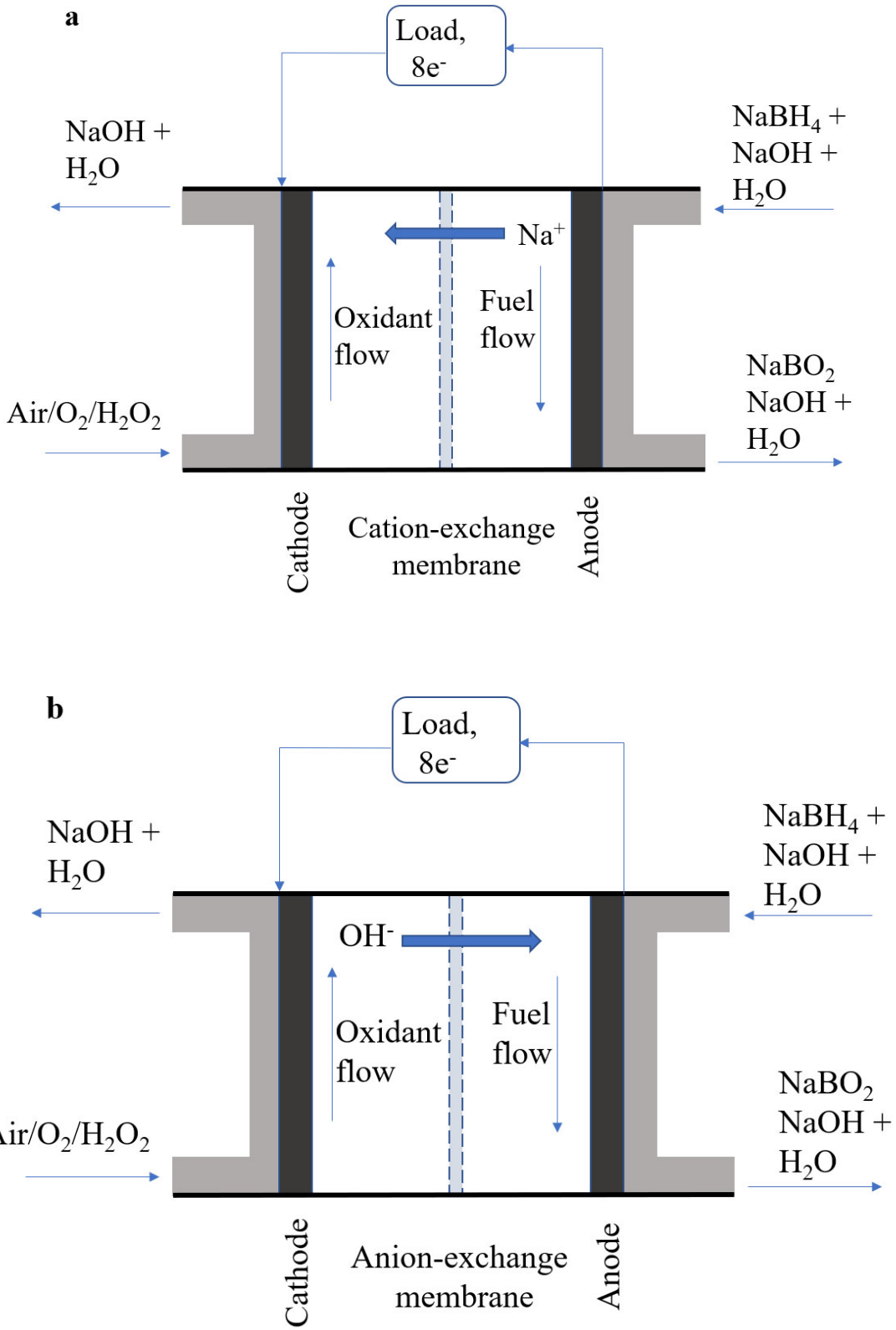

Figure 2.7: Schematic illustration of DBFC configurations deployed different types of membranes: a) cation-exchanged membrane, and b) anion-exchanged membrane.

As can be seen in **Table 2.1**, most of the cationic membranes used in DBFCs are Nafion-based, belonging to the perfluorinated membrane group. This is because these types of membranes possess beneficial properties such as good ionic conductivity, high chemical stability, low fuel crossover, and high mechanical strength [18]. It is important to mention that these types of membranes rely heavily on water for cation transfer, and therefore, the preferred operating temperature is generally below then 90 ^{o}C [6].

Liu and co-workers compared effectiveness of cation and anion-exchange membranes in a micro DBFC [18]. Their results showed that cation-exchange membrane (Nafion 115) performance was better than those of anion-exchange membrane (Asahikasei A-501SB), which can be clearly seen on the cell polarizations curves obtained under same condition only changing membranes as illustrated in **Figure 2.8**.

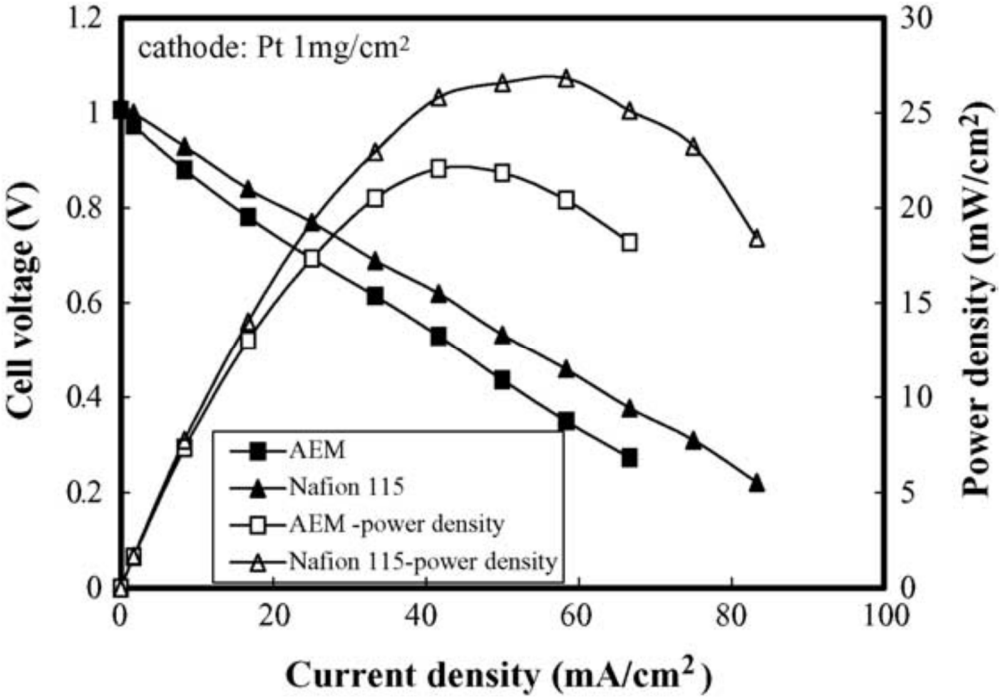

Figure 2.8: Cell polarization curves obtained by deploying a Nafion 115 and an anion-exchage membranes at 25 ^{o}C. Porous nickel anode and Pt/C were deployed, obtained from ref. [18].

Apart from the mentioned membranes above, some researchers attempted to develop more efficient membranes for a DBFC. Choudhury and co-workers developed a Na_2HPO_4-based ionically cross-linked chitosan hydrogel membrane electrolytes (ICCSHMEs) and reported that 810 mW cm^{-2} peak power density was achieved at 70 ^{o}C [69]. To the best knowledge of the authors, this value was the highest peak power density reported in the literature. Yet, the maximum current density at 30 ^{o}C was ca. 200 mW cm^{-2} in the same study. To note that

temperature has considerable effects on membrane. Increase in temperature improves membrane conductivity thus enhances the power density [69], but increase in temperature causes a decrease in water content inside the membrane, resulting in higher ionic resistance through the membrane thereby decreases cell performance [6].

Due to the high cost of ion-exchange membranes, complexity in cell design resulting from deployment of these membranes, and unwanted fuel crossover, it requires to find a replacement to these membranes. Using cathode catalysts which inactive for BH_4^- ions could eliminate the usage of these expensive separators. Feng and co-workers reported an undivided membrane-less DBFC, which MnO_2 used as cathode catalyst and Au/C as anode [23]. The authors claimed that this replacement simplified the cell construction and lowered the cell cost.

2.1.5 Effect of Operation Variables on DBFC Performance

2.1.5.1 Operation Temperature

It was reported that power density of a DBFC increased with the temperature, or vice versa [6], [59], [46], [67], [70]. Cheng and co-workers performed experiments to investigate operation conditions on DBFC performance and evaluated their DBFC at 25, 50, 70, and 85 ºC [67]. They reported that DBFC employing Au/C anode (2 mg_{Au} cm^{-2}), Pt/C cathode (2 mg_{Pt} cm^{-2}), a Nafion 117 membrane, 5wt. % $NaBH_4$ in 10 wt. % NaOH as fuel (10 cm^{-3} min^{-1}), and O_2 (1 atm. pressure, 200 cm^3 min^{-1}) as oxidant was capable to deliver high power density at 25 ºC. Based on their observation, there was almost fifth fold increase in power density when temperature was shifted from 25 to 85 ºC. A similar observation was reported by Choudhury and co-workers who tested a membrane prepared ionically cross-linked chitosan (CS) hydrogel at 30, 40, 50, 60, and 70 ºC (see **Figure 2.9**) [71]. In this study, when the tempeture was increased form 30 to 70 ºC, the power density was altered from 238 to 810 mW cm^{-2}, increasing by almost 2.5 fold. These enhencement in power density with the rise of temperature were atributed to improved mass transport of the electro-active species toward electrode surface, enhenced conductivity of the eletrolyte and faster oxidation of borohyride at higher temperature [71], [67]. However, an increase in temperature could be detrimental, increasing BH_4^- crossover, cell resistance resulted by patrialy drying of the membrane, and hydrolysis of borohydride [46]. As a result, an optimum operation temperature is required to obtain more efficent fuel cell operation.

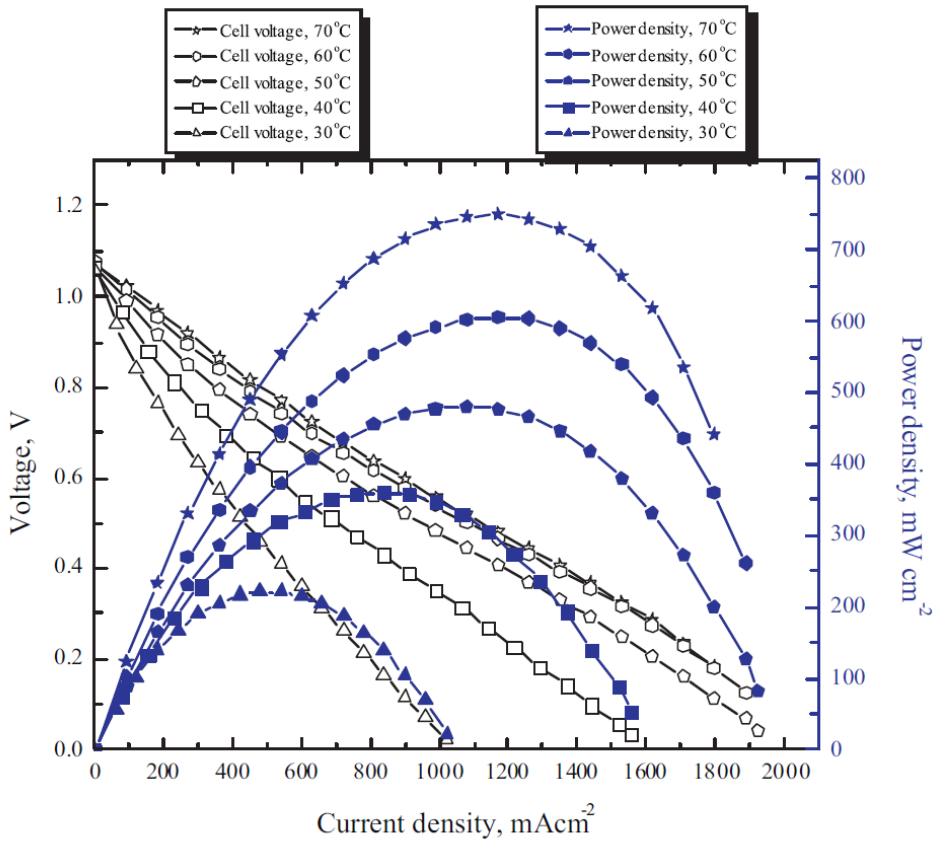

Figure 2.9: Temperature effect on DBFC performance employing a Na_2HPO_4-based ionically cross-linked chitosan hydrogel membrane electrolytes , from ref. [71]

2.1.5.2 Flow Rate of Anolyte and Oxidant

Flow rate and flow direction of fuel and oxidant have been reported to have an influence on DBFC performance [46], [66], [67]. It is expected that using high flow rate of fuel minimizes possible channel blocking problems caused from hydrogen evolution and removes the end products formed at the anode surface due to the improved mass transport of the fuel at high flow rate [6]. Cheng and co-workers observed 5 % improvement in power output when they altered fuel flow rate from 5 to 10 mL min^{-1} [67]. A further increase from 10 to 100 mL min^{-1} resulted in only 3.5 % rise in power output. Using high fuel flow rate could have negative impact on cell operation, increasing risk of fuel leakage, fuel crossover, flooding problem at the cathode compartment in the case of gas oxidant employment [66]. To avoid these risks, fuel flow rate is needed to be optimized, providing maximum power as possible as at the optimized flow rate of the cell or the cell stack. Taking into account that a small contribution comes from increase of anolyte flow rate, operating the cell at low fuel flow rate would be more economical [6].

Air, pure oxygen, and hydrogen peroxide have been reported as the main oxidants used in DBFC [5], [6], [59], [46], [67], [70]. Keeping the other variables constant and changing only the oxidant type, the maximum power density has been observed as to be the highest to the lowest in the following order: hydrogen peroxide > pure oxygen > air [22], [67]. Theoretically, H_2O_2 oxidant-based DBFC can deliver up to 30% more specific energy than oxygen-based one [70]. H_2O_2 type oxidant might be advantageous when air or O_2 supply is limited such as underwater or space applications. However, being freely available, air could be advantageous as oxygen source where air is available. It is noteworthy that in the case of usage of air as oxidant source CO2 enters has been reported that forms sodium carbonate, reacting with Na^+.

2.2 Titanium Oxide as Catalyst Support

Long-term durability of the electrocatalyst is desirable and necessary for an intended period of fuel cell operation because electrochemical degradation of support materials and aggregation of metal nanoparticles leads to a decrease in electrocatalytic activities of the electrocatalyst [72]. Carbon black is the most used catalyst support in fuel cell applications, but it degrades rapidly during the operation, especially under impermanent load and on/off operation conditions, leading a decrease in cell performance [73]. This could lead a decrease in total operational time of a catalyst during fuel cell operation and needs to be deal with by replacing carbon black with more durable support materials. Compared to carbon black, metal oxide supports exhibit higher stability being in the highest oxidation state and not easily lose electron for further oxidation states [11]. In this regard metal oxides looks a promising choice due to their abundance sources, high chemical and electrochemical stability, low cost, high stability in extreme acidic and basic media, and good interaction with metal nanoparticles [11]. Having a large surface area per unit weight (252 $m^2\ g^{-1}$) which is an important factor for fine dispersion and high exploitation of precious catalysts nanoparticles on support materials [74], titanate nanotubes (TiNT) has become prominent among the metal oxide catalyst supports. In addition, TiNT has some other important virtues besides its large specific surface area such as high stability in acidic and basic medium, easily controllable size and morphology, low cost, and non-toxicity nature [72].

One of the main advantages of TiNT as catalyst support is the strong interaction between TiNT and metal nanoparticles, preventing agglomeration of metal nanoparticles dispersed on the support [75]. Secondly, TiNT has a high specific surface area (250 $m^2\ g^{-1}$) compared to Vulcan XC-72 (240 $m^2\ g^{-1}$) which is widely used as support material in catalyst preparations [70].

Finally, TiNT can possibly support a catalyst metal loading up to 10 wt. % with an evenly distribution. Ponce de Léon and co-workers prepared a catalyst by ion exchange deposition followed by chemical reduction of gold precursors on TiNT support surface for a DBFC, with ca. 4 nm diameter of evenly distributed spherical gold nanoparticles [76]. Their results demonstrated that Au nanoparticles deposited on TiNT carried almost two times higher electrical charge than those of Au/C in the oxidation of borohydride. Wolf and co-workers, prepared different electrocatalysts deposited gold nanoparticles different support materials for CO oxidation, namely Au/TiO_2, Au/Co_3O_4, Au/Al_2O_3 and Au/ZrO_2 [77]. Among these, Au/TiO_2 was more active than the others. The authors stated that besides gold particle size impact on catalytic activity, interaction between support materials and metal nanoparticles could also have an important effect on catalytic activity of the prepared catalysts. Although, TiNT supported electrocatalysts show some electrocatalytic activities, poor electro conductivity of titanium oxide makes it necessary to improve its electro conductivity to obtain satisfactory results.

Mixing TiNT with carbon black or carbon nanotubes is a simple and effective way to increase electro conductivity of the TiNT to facilitate charge transfer from catalyst to current collector, improving catalyst effectiveness. In the present study, metal and metal alloys deposited TiNT catalyst have been mixed with carbon black prior to catalyst ink preparation.

2.3 Titanate Nanotubes as Catalyst Support in DBFCs

There are several attempts which deployed titanate nanotubes as catalyst support in DBFCs. Most of the published studies used anodized titanate nanotubes rather than prepared by wet chemical method.

Ponce de Léon and co-workers tested gold nanoparticles deposited on titanate nanotubes prepared by alkaline hydrothermal treatment of TiO_2 anastate with 10 M NaOH solution at 140 ^oC as the anode catalyst supported on a carbon plate [78]. In their study, they used three different anode catalysts to compare their electrocatalytic activities for borohydride oxidation, namely: gold nanoparticles deposited on titanate nanotubes Au/NT with 0.1 mg cm^{-2} Au loading, a commercial gold deposited on Vulcan carbon Au/C with 0.5 mg cm^{-2} Au loading, and an Au foil bulk gold electrode. In this study, the peak current densities obtained from borohydride oxidation experiments using these three electrodes are as follows: 5 mA cm^{-2} for Au/NT, 15 mA cm^{-2} for Au/C, and 9 mA cm^{-2} for gold foil. These results show that Au/NT electrocatalyst shows a comparable electro activity towards borohydride electro oxidation,

even with a five times lower Au loading than Au/C. The authors also defended that during the borohydride oxidation gold nanoparticles deposited on nanotubular titanate carries nearly 2 times higher electrical charge than those of gold particles dispersed on carbon black electrode.

Santos and co-workers synthesized titania nanotubes via anodic oxidation of a titanium metal plate and formed Co and Au-Co alloys on it by electroless deposition of Co followed by Au displacement with different Au loadings as anode catalyst in a direct borohydride/hydrogen peroxide fuel cell arrangement and a Pt sheet as cathode [19]. Namely, they prepared Co/TiO_2-NTs and AuCO/TiO_2-NTs (with 0.0100, 0.0222, and 0.0594 mg cm-2 Au loading) anode catalysts and tested their catalytic activities at four different temperatures (25, 35, 45, and 55 ^oC). Using AuCo/TiO_2-NTs as anode with a gold loading of ca. 0.06 mg cm^{-2} Au showed remarkable power output (283 mW cm^{-2}) at 55 ^oC. This value almost three times higher than Co/TiO_2-NTs gained under same condition, indicating that alloying Co with Au helps to improve its catalytic activity in BH_4^- oxidation. The authors did not provide any information about fuel utilization efficiency and fuel cross-over in their report.

To the best knowledge of the author, titanate nanotubes prepared by wet chemical method has not been investigated as catalyst support in DBFC, and thereby has a potential to be explored.

Chapter 3: EXPERIMENTAL STUDIES: METHODOLOGY

This chapter outlines the materials and methodologies employed to study the oxidation of BH_4^- on various electrocatalysts utilized in this study.

3.1 Utilized Chemicals

All the chemicals and reagents were used as received, without any further purification: chloroauric acid (48% Au based, Fluka), sodium borohydride (96% purity, Sigma-Aldrich), sodium hydroxide (97% purity, Fisher Scientific), zinc chloride (98% purity, Acros Organics), nickel (II) nitrate (98% purity, Sigma-Aldrich), cobalt chloride (97% purity, Sigma-Aldrich), titanium dioxide (anastate, 99.7 purity, Sigma-Aldrich) cupper (II) nitrate hydrate (99.9 purity, Sigma-Aldrich), lead nitrate (99 purity, Alfa Easar), iron (II) sulphate heptahydrate (99 purity, Sigma-Aldrich), 5 wt. Nafion solution (Sigma-Aldrich), ethylenediamine (99 purity, Sigma-Aldrich), Nafion® 115 membrane.

3.2 Instruments

A Gamry interface 1000 potentiostat/galvanostat controlled by a computer with Gamry Echem Analyst computer program, A Pt rotating disc electrode (Metrohm), an Au rotating disc electrode (Metrohm), and glassy carbon electrode (Metrohm) were used.

3.3 Electrochemical Measurements

3.3.1 Half-cell Studies

Cyclic voltammetry (CV), linear sweep voltammetry (LSV), and chronoamperometry (CA) methods were employed to investigate the electrochemical characterization of the prepared anode catalysts in the reaction of borohydride electrooxidation. Borohydride oxidation studies were recorded between -1.10 V and 0.50 V *vs* SCE at 0.01 V s^{-1} scan rate by using a Gamry interface 1000 potentiostat/galvanostat controlled by a computer with Gamry Echem Analyst computer program. Liner sweep voltammograms (LSV) were obtained at rotation rates between 400 and 2000 rpm. The geometrical surface area of the working electrode was used to determine current densities. For the reproducibility of the reported data, each experiment was repeated three times. A traditional three-electrode glass cell of 80 mL volume, thermostated at 20 ^oC, was used to conduct electrochemical measurements of the borohydride oxidation reaction. In this setup, a KCl-saturated calomel electrode (SCE) was used as the reference electrode, and a Pt coil served as the counter electrode. The working electrode was rotation

controlled Autolab Rotating Disc Electrodes (RDEs). Counter electrode and working electrode compartments were separated by a proton exchange Nafion® 115 membrane. All measurements were performed using a 0.03 M $NaBH_4$ anolyte in 2 M NaOH supporting electrolyte solution, unless stated otherwise. The cell setup is illustrated in **Figure 3.1**. Pt and Au RDEs were polished to a mirror finish using 0.3 μm and 0.05 μm alumina solution, and ultrasonicated for 5 minutes before each use.

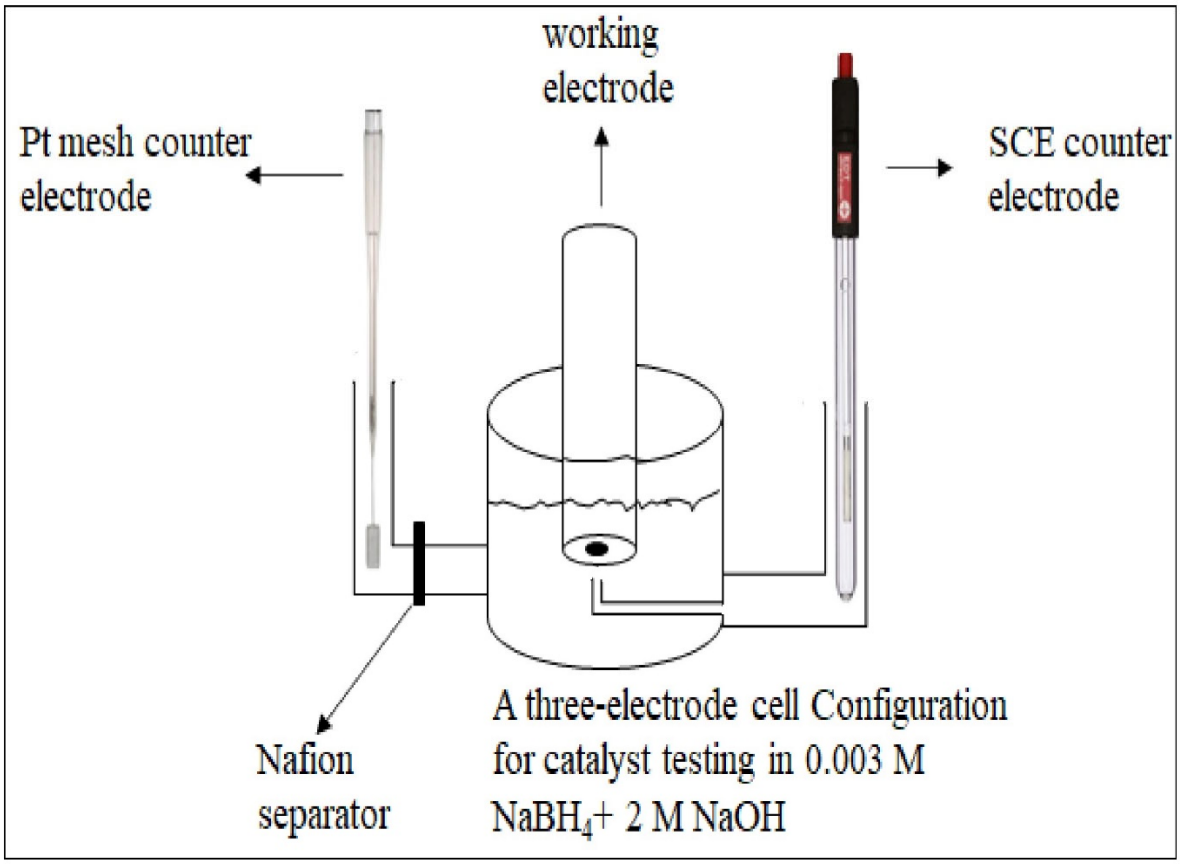

Figure 3.1: A three-electrode cell setup is illustrated: a Pt gauze counter electrode; a glassy carbon rotating disc electrode coated with developed electrocatalysts; a saturated calomel reference electrode (SCE); a Nafion 115 separator.

3.4 Preparation of Titanate Nanotubes and Anode Catalysts

Preparation of titanate nanotubes and titanate nanotubes supported metal nanoparticles prepared based on publications by Bavykin and colleagues [74], [79]. A brief description of the synthesis of titanate nanotubes and the preparation of the catalysts is provided below.

3.4.1 Titanate Nanotubes (TiNT)

There are three main methods for preparing titanate nanotubes: anodic oxidation, the template method, and the wet chemical method [74]. In this research, the wet chemical method was

employed to synthesize TiNT. This method was well explained elsewhere [74]. Briefly, 110 g titanium oxide (anatase grade) was added to 550 mL of NaOH solution in a PTFE beaker and mixed vigorously for 30 minutes. Then, the well mixed solution was placed in an autoclave at a set temperature of 140 ºC for 24 hours. At the end of this period the heater was turned off, and system cooled down naturally to ambient temperature. Following this, resulted white titanate nanotubes was washed with deionized water many times until to get pH 10.6. To lower the pH of the washed TiO_2 solution further, it was washed with 0.05 M H_2SO_4 solution followed by deionized water wash many times, achieving final pH 7.2. Finally, white powder was separated from the solution by filtering the final solution and dried at ambient conditions.

3.5 Deposition of Metals on Titanate Nanotubes

Ion-exchange deposition-reduction method was employed to achieve an evenly distributed deposition of metal nanoparticles on titanate nanotubes. Initially, metal ions were deposited onto the titanate nanotubes, followed by electrochemical reduction using a 0.2 M sodium borohydride solution.

3.5.1 Gold Deposition on Titanate Tanotubes

To determine Au loading on titanate nanotubes, 0.1 gram of titanate nanotubes was added into 5 mL of six different diethylenediamine gold trichloride $[Au(en)_2]CI_3$ solutions. When the white titanate nanotubes powder came into contact with the yellow gold solution, it turned yellow, and solution became lighter yellow in colour. The concentration of $[Au(en)_2]CI_3$ solution were 2, 4, 8, 16,32, and 64 mM. These solutions were prepared from 0.1 M $HAuCI_4$ stock solution by mixing the required amount of ethylenediamine (en) and deionized water given in **Table 3.1**

Table 3.1: required amounts of each component to prepare 2, 4, 8, 16, 32, and 64 M gold-diethylenediamine complex solutions.

Molarity, mM	0.1 M $HAuCI_4$, mL	Ethylenediamine, µL	Deionized water, mL
2	0.1	10.1	4.9
4	0.2	20.2	4.8
8	0.4	40.1	4.6
16	0.8	82.8	4.2
32	1.6	160.5	3.4
64	3.2	320.9	1.8

After 18 h vigorous stirring with magnetic stirrer to achieve ion-exchange deposition equilibrium, solutions were centrifuged at with 4000 rpm for 10 minutes to separate

diethylenediamine gold $[Au(en)_2]^{3+}_{(aq)}$ complex adsorbed titanate nanotubes powder from rest of the solution. Following that, collected powder was filtered and washed with adequate water and reduced with 20 mL of 0.2 M sodium borohydride solution for 5 minutes, and dried at 80 ^oC overnight. During the reduction step, yellow titanate nanotubes powder immediately turned into dark violet colour. Remaining solutions collected after centrifugation process were analysed by UV-visible spectroscopy, revealing that the amount of gold deposited on the titanate nanotubes was approximately 2, 3.67, 7.15, 11.98, 15.15, and 17.28 wt% for the concentrations mentioned above.

3.5.2 Nickel Deposition on Titanate Nanotubes

Deposition of nickel on titanate nanotubes was carried out in the same procedure with gold deposition on titanate nanotubes. Using 0.1 M $Ni(NO_3)_2$ stock solution, different concentration of $[Ni(en)_3](NO_3)_2$ ligand complex were prepared by mixing $Ni(NO_3)_2$, ethylenediamine (en), and deionized water given in the **Table 3.2** to obtain a 25 mL final volume.

Table 3.2: required amounts of each component to prepare desired nickel-triethylenediamine complex concentrations.

Molarity, mM	0.1 $Ni(NO_3)_2$, mL	Ethylenediamine, µL	Deionized water, mL
2	0.5	50	24.45
4	1.0	100	23.90
8	2.0	200	22.80
16	4.0	400	20.60
32	8.0	800	16.20
64	16	1600	7.40

0.5 g titanate nanotubes powder were added to these prepared 25 mL nickel-triethylenediamine metal complex solutions and stirred for 18 hours to reach ion-exchange deposition equilibrium on titanate nanotubes surface. Then, each solution was centrifuged, and separated metal ion deposited titanate nanotubes from the rest of the solutions. Collected powder was filtered and wash with water. Following that pink nickel-triethylenediamine complex deposited nano powder was reduced with 20 mL of 0.2 M of $NaBH_4$ solution for 20 mins under vigorous stirring. When light pink powder contact with the reducer, its colour turned from pink to grey. Finally, reduced metal deposited powder filtered, washed with water, and dried at 80 ^oC overnight. The collected solution after the centrifugation process was evaluated by UV-visible spectroscopy to determine quantity of adsorbed metal on titanate nanotubes. The findings show that the percentage of metal deposition on titanate were the following order for the studied concentration given in **Table 3.2** 0.74, 1.17, 1.27, 1.66, and 2.11 wt. %.

3.5.3 Co-deposition of Gold-nickel (Au-Ni)

The same deposition method was applied as was done for Au and Ni deposition on titanate, as mentioned above. 50 mL of metal ligands which includes $[Au(en)_2]^{3+}_{(aq)}$ and $Ni(en)_3]^{2+}_{(aq)}$ cationic ions were prepared by mixing ethylenediamine, deionized water, and the required amounts metal solutions from 0.1 M $HAuCI_4$ and 0.1 M $Ni(NO_3)_2$ stock solutions in an 80 mL beaker. To prepare composite catalysts at the desired molar ratios, an exact amount of each component was provided in **Table 3.3**. 1 g of titanate nanotubes powder were added to each beaker which contain prepared solutions and stirred for 18 h, allowing the metal ligands to reach ion-exchange deposition equilibrium on titanate nanotubes. After this period, the same procedure was followed as described in gold and nickel deposition sections. Due to low adsorption of $Ni(en)_3]^{2+}_{(aq)}$ complex on titanate nanotubes surface, total metal loading on the resulted titanate nanotubes kept at 4 wt. %, to achieve the desired molar ratio of each metal. During co-deposition of gold and nickel on titanate nanotubes, it was assumed that adsorption of $[Au(en)_2]^{3+}_{(aq)}$ and $Ni(en)_3]^{2+}_{(aq)}$ ligands did not affect each other on titanate nanotubes surface.

Table 3.3: required amounts of each component to prepare Au-Ni composite catalysts at aimed molar ratios.

Catalyst	0.1 M $HAuCI_4$, mL	0.1 $Ni(NO_3)_2$, mL	Ethylenediamine, mL	Deionized water, mL
Au_{100}/TiNT	2.00	0	0.20	47.80
$Au_{80}Ni_{20}$/TiNT	1.89	2.02	0.39	45.69
$Au_{60}Ni_{40}$/TiNT	1.75	3.65	0.54	44.06
$Au_{40}Ni_{60}$/TiNT	1.56	8.78	1.04	38.62
$Au_{20}Ni_{80}$/TiNT	1.30	37.00	3.84	7.86

3.5.4 Cobalt Deposition on Titanate Nanotubes

Using the same deposition method mentioned under nickel deposition section, cobalt deposition on titanate nanotubes was carried out. Different concentrations of $[Co(en)_3](NO_3)_2$ ligand complex were formed by mixing $Co(NO_3)_2$ from 0.1 M stock solution, ethylenediamine (en), and deionized water given in **Table 3.4** to get a 25 mL final volume. Then, 0.5 g titanate nanotubes was added to each solution prepared as 25 mL and left to stir for 18 hours to reach ion-exchange deposition equilibrium on titanate nanotubes surface. Remaining steps for cobalt deposition were the same mentioned in nickel deposition section. When the collected powder was reduced with 0.2 M sodium borohydride, its purple colour turned to grey immediately. After analysing the results for cobalt adsorption on titanate nanotubes, the following adsorption

percentage obtained for measured concentrations shown in **Table 3.4**; 0.58, 1.15, 1.73, 2.29, 2.70, 2.92, 3.65 wt. %.

Table 3.4: required amounts of each component to prepare desired cobalt-triethylenediamine complex concentrations.

Molarity, mM	0.1 $Co(NO_3)_2$, mL	Ethylenediamine, µL	Deionized water, mL
2	0.5	50	24.45
4	1.0	100	23.90
6	1.5	150	23.35
8	2.0	200	22.80
12	3.0	300	21.70
16	4.0	400	20.60
32	8.0	800	16.20

3.5.5 Co-deposition of Gold-cobalt (Au-Co)

Co-deposition of gold-cobalt metal couples were carried out for different molar ratios of each metal, resulting in a final 4 wt. % of combined total metal loading on titanate nanotubes. To achieve the intended molar ratio for each of the five electrocatalysts, the required amounts of $HAuCI_4$, $Co(NO_3)_2$, ethylenediamine, and deionized water were combined to a final volume of 50 mL in an 80 mL beaker, as shown in **Table 3.5**. After adding 1 g of titanate nanotubes to each beaker, they were left to stir for 18 hours. Then, the same procedure was followed as described for gold deposition in section **3.5.1**.

Table 3.5: required amounts of each component to prepare Au-Co composite catalysts at intended molar ratios.

Catalyst	0.1 M $HAuCI_4$, mL	0.1 $Co(NO_3)_2$, mL	Ethylenediamine, mL	Deionized water, mL
Au_{100}/TiNT	2.00	0	0.20	47.80
$Au_{80}Co_{20}$/TiNT	1.89	0.81	0.27	47.03
$Au_{60}Co_{40}$/TiNT	1.75	1.13	0.29	46.82
$Au_{40}Co_{60}$/TiNT	1.56	1.87	0.34	46.22
$Au_{20}Co_{80}$/TiNT	1.30	4.26	0.56	43.88

3.5.6 Copper Deposition on Titanate Nanotubes

To investigate copper deposition on titanate nanotubes, six different solutions were prepared using the required amount of 0.1 M $Cu(NO_3)_2$ stock solution, ethylenediamine, and deionized water, as shown in **Table 3.6**. 0.5 g titanate nanotubes powder was added to each of these prepared 25 mL copper-diethylenediamine metal complex solutions and stirred for 18 hours to reach ion-exchange deposition equilibrium on titanate nanotubes surface. Remaining steps were the same as described in nickel deposition section **3.5.2**. When the collected powder

treated with 0.2 M sodium borohydride reducer, its purple colour turned into black. After evaluating copper adsorption on titanate nanotubes, the percentages of adsorbed metal were calculated as follows, from low to high concentration: 1.06, 2.27, 2.63, 3.06, 3.44, and 3.99 wt. %.

Table 3.6: required amounts of each component to prepare desired cupper-triethylenediamine complex concentrations.

Molarity, mM	0.1 M $Cu(NO_3)_2$, mL	Ethylenediamine, µL	Deionized water, mL
4	1.0	100	23.9
8	2.0	200	22.8
12	3.0	300	21.7
16	4.0	400	20.6
32	8.0	800	16.2
64	16	1600	7.4

3.5.7 Co-deposition of Gold-copper (Au-Cu)

Co-deposition of gold-copper metal couples was conducted for different molar ratios of each metal, resulting in a final 4 wt. % combined total metal loading on titanate nanotubes. To achieve for the intended molar ratio for five electrocatalyst, required amount of $HAuCl_4$, $Cu(NO_3)_2$, ethylenediamine and deionized water, were combined with a final 50 mL volume in a 80 mL beaker as shown in **Table 3.7**. Afterward 1 g of titanate nanotubes to each beaker, they left to stir for 18 h. After then, the same procedure was followed as done for gold deposition in section **3.5.1**

Table 3.7: required amounts of each component to prepare Au-Cu composit catalysts at aimed molar ratios.

Catalyst	0.1 M $HAuCl_4$, mL	0.1 $Cu(NO_3)_2$, mL	Ethylenediamine, mL	Deionized water, mL
Au_{100}/TiNT	2.00	0	0.20	47.80
$Au_{80}Cu_{20}$/TiNT	1.89	0.67	0.26	47.19
$Au_{60}Cu_{40}$/TiNT	1.75	1.01	0.28	46.98
$Au_{40}Cu_{60}$/TiNT	1.56	1.82	0.34	46.30
$Au_{20}Cu_{80}$/TiNT	1.30	4.67	0.60	43.45

3.5.8 Evaluation of the Adsorption Isotherm of Metals

Determination of gold, nickel, cobalt, and copper metal complex adsorption isotherm on titanate nanotubes were carried out at room temperature (21 ºC, ±1) by measuring the remaining metal concentration of the solutions after ion-exchange deposition of metal complex on titanate nanotubes using UV-visible spectroscopy. Using the Eq. (3.1), the relative amount of deposited metal complex, denoted as a [mol(M)×mol $(TiO_2)^{-1}$], was determined:

$$a = \frac{80 \times (C_0 - C^*) \times V}{m} \quad (3.1)$$

Here *m* is mass of nanotubes powder added to the solution, V is final volume of solution, C_o is initial concentration of solution, and C^* is remaining concentration of the solution after deposition process take place.

After determining C^* and knowing the volume of solution, adsorbed metal mass can be calculated with the following formula:

$$m\,(metal) = (C_0 - C^*) \times MW(metal) \times V \quad (3.2)$$

Here *m* is mass of adsorbed metal, and *MW* is molecular weight of the metal studied. Considering the added titanate nanotubes powder mass in the studied solution, it allows us to determine weight percentage of the metal adsorbed on titanate nanotubes powder added to the solution. This can be calculated with the formula as shown below:

$$adsorbed\ metal\ wt.\% = \frac{m\,(metal)}{m\,(metal) + m(TiNT)} \times 100 \quad (3.3)$$

3.6 Fabrication of Anode Catalysts

To increase the electrical conductivity of titanate nanotubes supported electrocatalysts, carbon black (Vulcan XC 72R) was mixed with synthesized electrocatalysts with a mass ratio of 1:9. The catalytic ink was prepared by mixing 200 mg catalyst powder (180 mg metal nanoparticle adsorbed titanate nanotubes and 20 mg carbon black), 2 mL of 5 wt. % nafion solution, and 1 mL of deionized water. Then, the mixture blended using shear blade mixer for 1 hour at 7000 rpm to obtain a well suspended catalyst powder in catalyst ink. Nafion solution was used to bind the electrocatalyst powder to the surface of 3 mm diameter conductive glassy carbon electrode. Following that 1.5 µL resulted catalyst ink was drop casted on conductive surface of the glassy carbon electrode using a 10 µL micropipette and dried naturally overnight. One of the catalyst ink drop-casted glassy carbon electrode surface is shown in **Figure 3.2** under 25X magnification. It is evident here that the 3 mm electrode surface is evenly covered by the electrocatalyst ink. All the drop-casting electrode coverage were kept similar on glassy carbon electrode.

Resulted active metal catalyst loading was ca. 0.051 mg_{metal} cm^{-2}. Metal-adsorbed titanate nanotubes are denoted as Au/TiNT, Au_aNi_b/TiNT , Au_aCo_b/TiNT, and Au_aCu_b/TiNT (here a and b is atomic ratios of each metals) with a total metal loading of 4 wt. %. After adding Nafion and carbon black into the catalyst composition to prepare the catalyst ink, these catalysts are

represented as Au/TiNT-C, Au_aNi_b/TiNT-C, Au_aCo_b/TiNT-C, and Au_aCu_b/TiNT-C with a total metal loading of 2.51 wt. %.

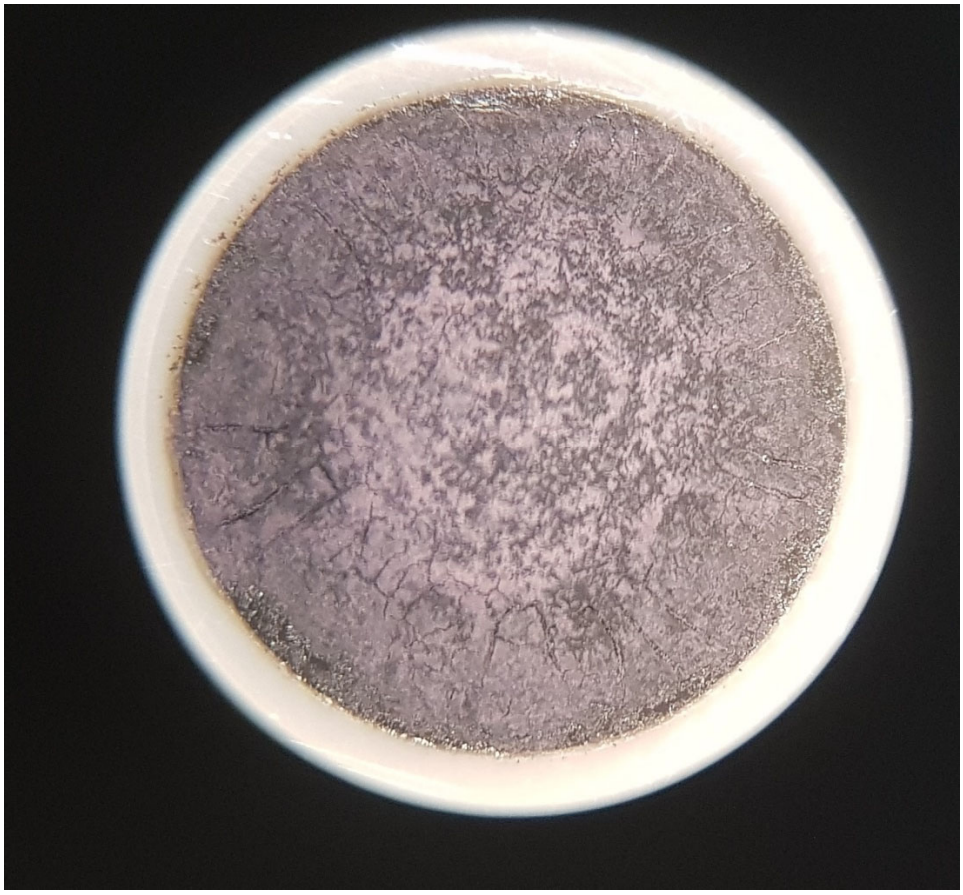

Figure 3.2: Photo of catalyst ink drop-casted glassy carbon electrode surface under 25X magnification.

3.7 Catalyst Loading Calculation

This section gives a detailed explanation about how catalyst loading calculated.

Amount of each component which used to prepare 3 mL of catalyst ink:

deionized water = 1 mL

5 wt. % nafion solution (d=0.847 g mol^{-1}) = 2 mL ➔ $2\,mL \times 0.874\,\frac{g}{mL} \times \frac{10^3\,mg}{1\,g} \times \frac{5}{100} =$ 87.4 mg Nafion

4 wt. % metal decorated TiNT = 180 mg

Carbon black (Vulcan XC 72R) = 20 mg

Total dried mass of 3 mL catalyst ink = (87.4+180+20) = 287.4 mg

Percentage of Nafion in catalyst mixture = $\frac{87.4}{287.4} \times 100 = 30.41\,wt\,\%$

Percentage of 4 wt. % metal decorated TiNT in catalyst mixture = $\frac{180}{287.4} \times 100 = 62.63\,wt\,\%$

Percentage of carbon black in catalyst mixture = $\frac{20}{287.4} \times 100 = 6.96\,wt\,\%$

Density of 3 mL catalyst ink = $\frac{287.4\ mg}{3\ mL} = 95.8 \frac{mg}{mL}$

Applied catalyst ink on glassy carbon (GC) electrode = 1.5 µL.

Resulted total catalyst amount on GC = $1.5\ \mu L \frac{1\ mL}{10^3\ \mu L} \times 95.8 \frac{mg}{mL} = 0.1437 mg$ catalyst (including Nafion+TiNT+CB)

Area of GC electrode (with 3 mm diameter) = $\pi \times \left(\frac{3}{2} mm \times \frac{1}{10} cm\right)^2 = 0.070686\ cm^2$

Total catalyst loading = $\frac{0.1437}{0.070686} \frac{mg}{cm^2} = 2.033 \frac{mg}{cm^2}$

Metal based catalyst loading = $2.033 \frac{mg}{cm^2} \times (0.6263) \times (0.04) = 0.051\ mg_{metal}\ cm^{-2}$

This is TiNT percentage in catalyst texture

this is adsorbed metal percentage on TiNT

.

Weight percentage of active metals in catalyst texture = $\frac{0.051}{2.033} \times 100 = 2.51\ wt.\%$

3.8 Catalyst Characterisation

The main approach for synthesis of bi-metallic alloy nanoparticles is to saturate TiNT structure with cations of the metal precursor Au(III) and Ni(II)) followed by their reduction with an excess of $NaBH_4$. The high local concentration of the metal precursor on the surface of TiNT and the uniform distribution of Au(III) and Ni(II) atoms can provide suitable conditions for effective mixing and the formation of Au-Ni alloy nanoparticles on the surface of titanate nanotubes, as illustrated with crossed path in **Figure 3.3**.

The electron microscopy analysis, however, prove that instead of alloy nanoparticles on the surface of TiNT, the application of the two steps method results in formation of the mixed composite on the surface of nanotubes. **Figure 3.4** shows HRTEM image of titanate nanotubes decorated with Au-Ni nanostructures and EDX analysis for 3 different spots labelled A, B and C. Atomic ratio of Au:Ni was 60:40 and the catalyst loading with 4 wt. % (total metal mass). According to EDX data, the dark spherical object (label A) is attributed to pure gold nanoparticles, whereas nickel is distributed evenly over the free surface of titanate nanotubes without forming structures with identifiable morphology (see schematics in **Figure 3.3**). Despite the fact that the above approach didn't result in formation of metallic alloy nanoparticles, obtained composites have better catalytic properties towards reaction of BH_4^- oxidation compare to pure gold nanoparticles on the surface of TiNT.

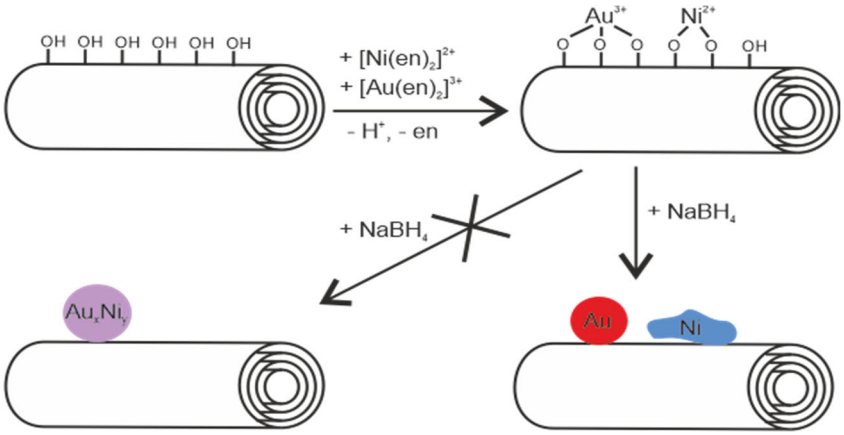

Figure 3.3: Schematic representaion of the two-steps approach for decoration of TiNT with An-Ni nanostructures. Crossed arrow shows possible but not realised path for Au-Ni alloys.

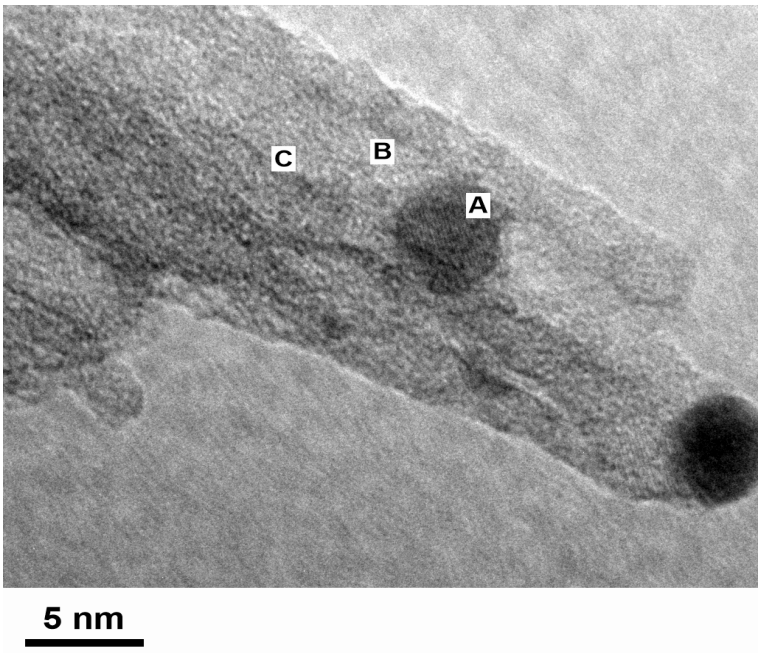

a)

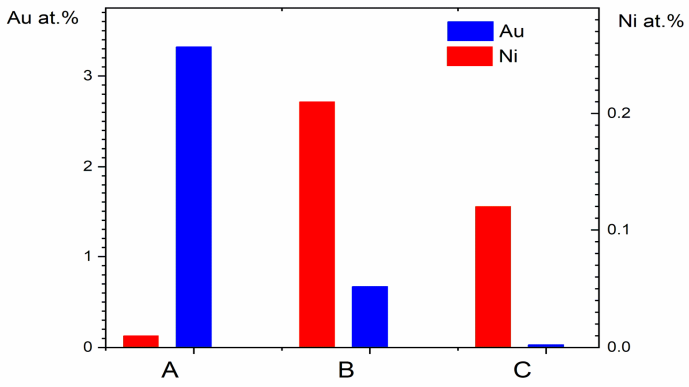

b)

Figure 3.4: (a) HRTEM image of Ni-Au/TiNT for 4 wt% metal loading and Ni:Au atomic ratio 40:60. (b) EDX atomic percentage of Au and Ni for points A, B, and C.

Chapter 4: ELECTROCATALITIC OXIDATION OF BOROHYDRIDE BY GOLD-NICKEL COMPOSITE CATALYSTS

Under this chapter, a detailed explanation of deposition method, quantitative analysis of catalyst loading, electrochemical characterisation of developed catalysts will be provided.

4.1 Quantitative Analysis: Metal Deposition Determination

To decorate a nonconductive surface, such as titanate nanotubes, with metal nanoparticles, several well-established techniques have been reported in literature. These techniques include wetness impregnation, electron-beam lithography, vacuum vapour deposition techniques, spin-coating, vesicle mediated deposition (employing micro-emulsion solutions or reverse micelles), and deposition-reduction (based on anionic or cationic adsorption) [80], [81], [77]. In this study, the cationic deposition-reduction method was chosen, involving the deposition of cationic metal ions followed by reduction with a reducing agent (here, $NaBH_4$), to deposit metal nanoparticles on the surface of titanate nanotubes. This method ensures the even distribution of metal nanoparticles on the surface of titanate nanotubes, with sizes ranging between 2 to 10 nm [78]. Additionally, this method is a simple and inexpensive technique for preparing electrocatalysts. UV-visible spectroscopy was utilized to quantitatively evaluate metal deposition.

4.1.1 Gold Deposition on Titanate Nanotubes

Based on Lambert-Beer Law, concentration of an unknown solution can be quantitatively calculated by measuring light absorption of the solution and placing it in Eq. (4.1). To do this, it is necessary to establish a calibration curve by performing UV-visible spectroscopy on several standard solutions. For this purpose, 7 standard solutions of diethylenediamine gold trichloride $[Au(en)_2]CI_3$ were prepared, ranging from 0.0005 to 0.0011 M. Subsequently, absorbance of these solutions was measured in 190 to 500 nm spectrum range using a quartz cuvette in the spectrophotometer, and calibration line was constructed.

$$A = \varepsilon . c . l \tag{4.1}$$

where:

ε: is extinction coefficient, in L/(cm.mol)

c: is sample concentration, in mol/L

d: is path length of the cuvette which light beam pass through, in cm

As it can be seen in **Figure 4.1,** absorbance of $[Au(en)_2]CI_3$ solutions reach a maximum peak value at around 305 nm. Considering these absorbance values at 305 nm, calibration line was plotted as seen in **Figure 4.2**. Later, this calibration curve was used to quantify metal adsorption on titanate nanotubes. As provided in **Figure 4.2**, extinction-coefficient which equals to the slope of the calibration line has a large value (1705 L cm^{-1} mol^{-1}) for gold solution. This enables to detect even the smaller concentration changes in determination of metal adsorption process.

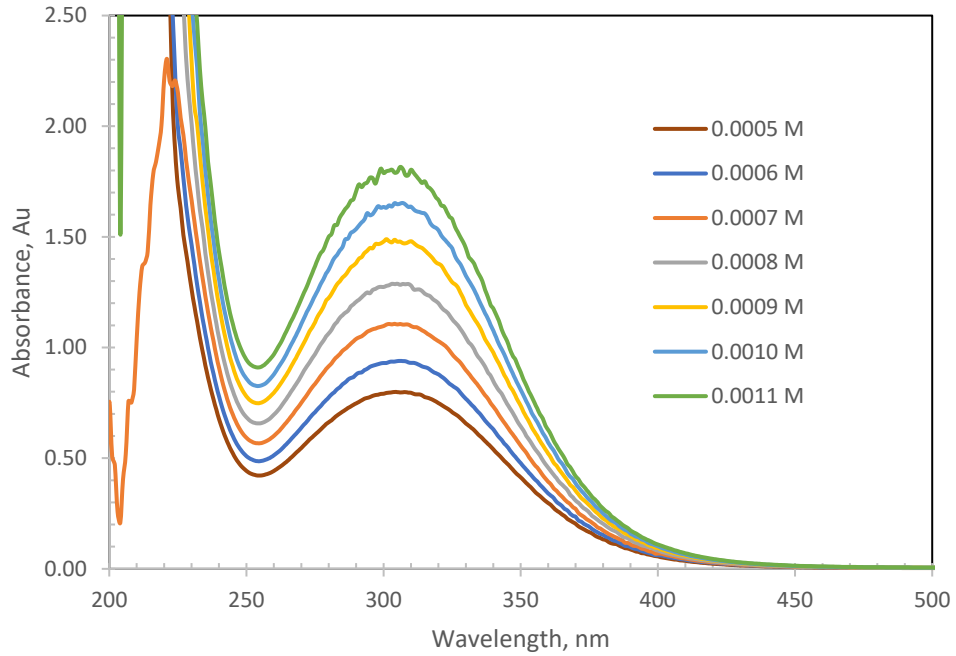

Figure 4.1: Absorbance spectrum of diethylenediamine gold trichloride $[Au(en)_2]CI_3$ solutions measured at 22 °C

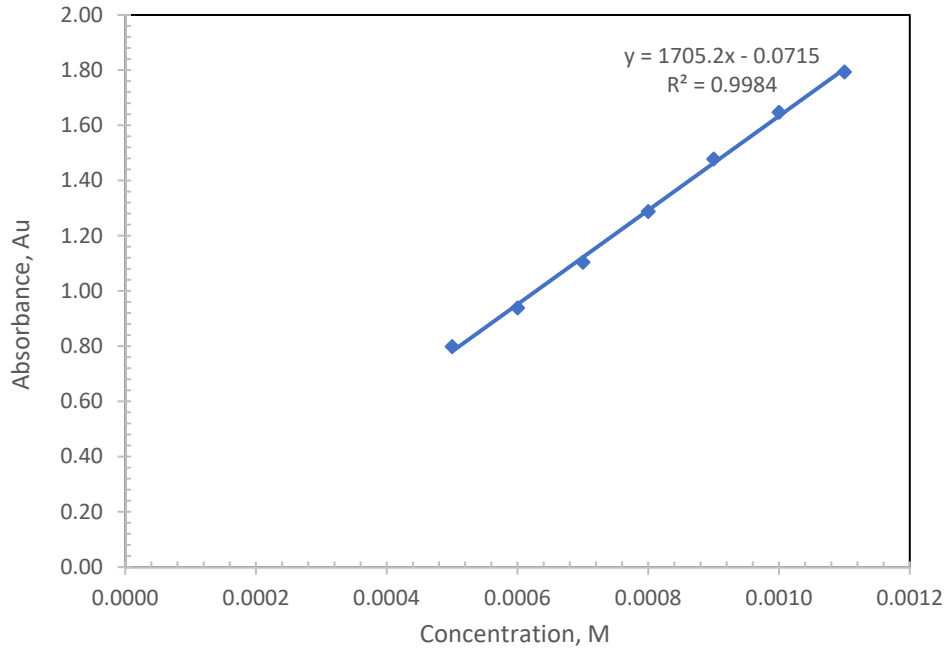

Figure 4.2: Calibration curve obtained at 305 nm for $[Au(en)_2]CI_3$ solution.

The quantitative analysis of Au deposition on titanate nanotubes included several steps. First, ion-exchanged deposition of $[Au(en)_2]^{3+}_{(aq)}$ cations was carried out in 25 mL solutions adding 0.5 g titanate. Following that absorbance of remaining solution measured by spectrophotometer to detect remaining metal concentration. Finally, measured absorbance of remaining solution was placed on **Figure 4.2** to find remaining metal concentration after deposition. **Figure 4.3** provide a detailed schematic explanation of these steps.

The relative amount of deposited metal complex *a* [mol(M)×mol $(TiO_2)^{-1}$] can be determined by the following formula:

$$a = \frac{80 \times (C_0 - C^*) \times V}{m} \quad (4.2)$$

Here m is mass of added TiO_2 nanotubes powder. Calculating *a* value can be beneficial to understand how many mol metal can be adsorbed by per mol of titanate nanotubes powder from the solution.

Table 4.1 includes all the data collected from colorimetric measurements. These data were used to calculate gold adsorption isotherm which can be seen in **Figure 4.4**. On this figure, ion-exchange molar ratio, a, did not change at a considerable level for $[Au(en)_2]^{3+}_{(aq)}$ adsorption from 0.072 to 0.085 mol (Au) / mol (TiNT), even with an increase in initial concentration from 32 to 64 mmol L^{-1}. When initial concentration increased from 32 to 64 mmol L^{-1}, corresponding gold loading enhanced only ca. 2 percent by rising from 15.15 to 17.28. As a result, it could better not to exceed an initial concentration of 32 mmol L^{-1} for practical applications.

Table 4.1: Initial and remaining concentration of $[Au(en)_2]^{3+}_{(aq)}$ with the data obtained based on these two measurements.

Initial $[Au(en)_2]^{3+}_{(aq)}$ concentration, mmol dm^{-3}, C_o	Remaining $[Au(en)_2]^{3+}_{(aq)}$ concentration, mmol dm^{-3}, C^*	Ion-exchange molar ratio / mol (Au) mol^{-1} (TiNT), a	wt. %
4	0.015	0.015	3.67
8	0.027	0.031	7.15
16	1.782	0.055	11.97
32	13.515	0.072	15.15
64	42.577	0.085	17.28

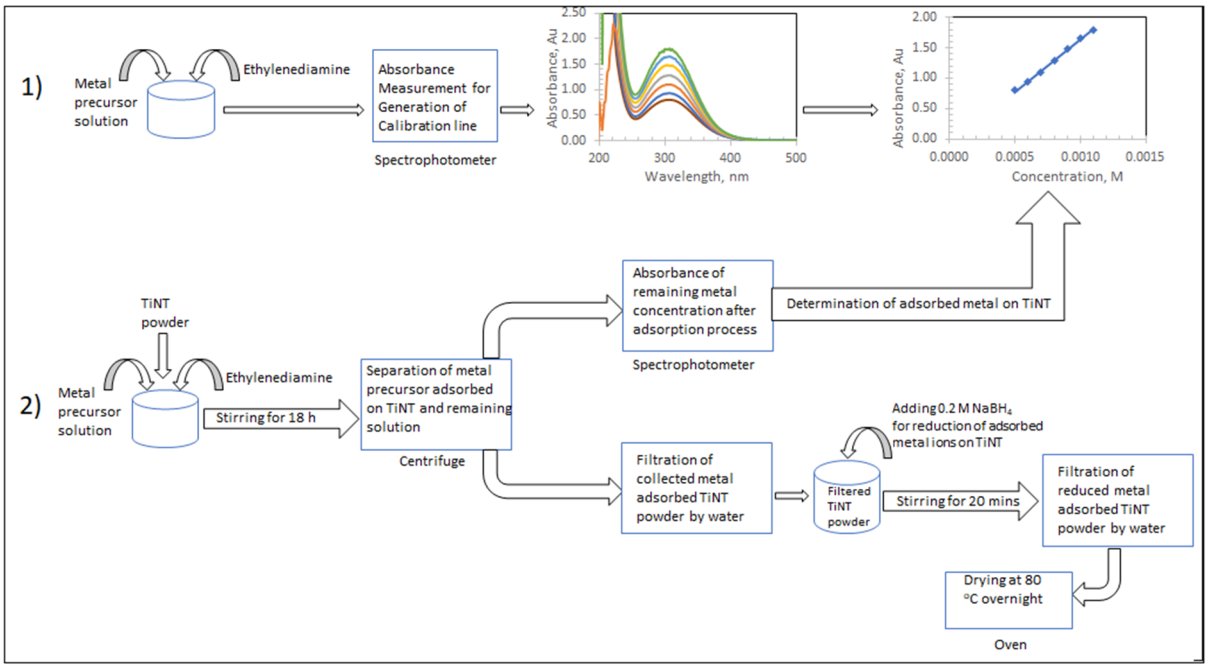

Figure 4.3: Schematic illustration of deposition procedure of metals on TiNT via ion-exchange deposition-reduction method.

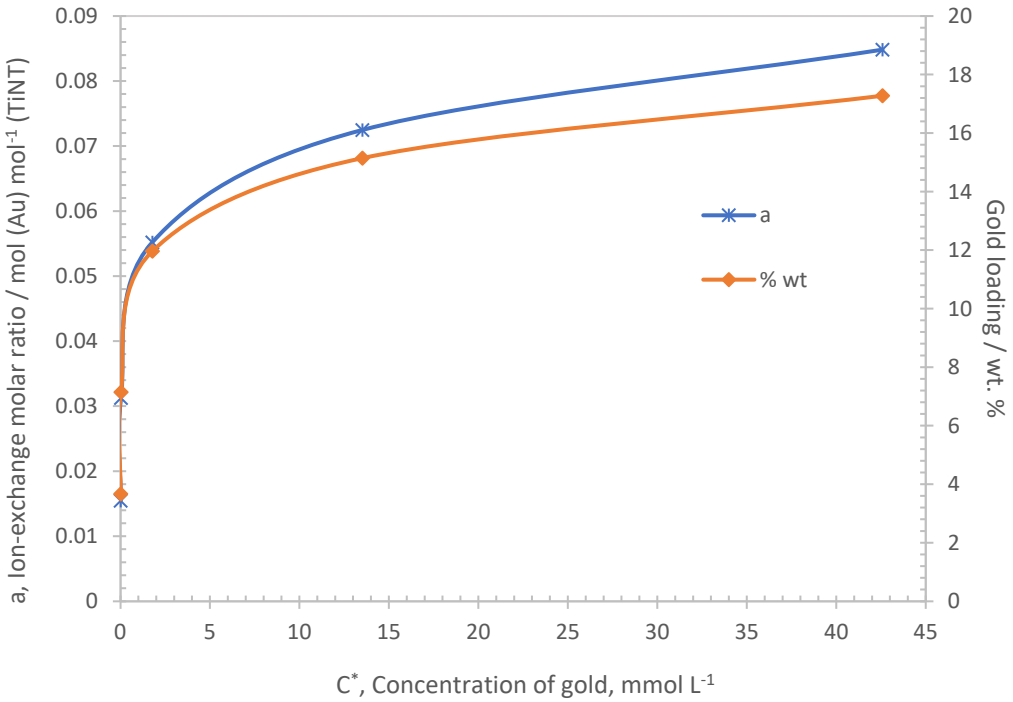

Figure 4.4: Isotherm of $[Au(en)_2]^{3+}_{(aq)}$ cation adsorption on titanate nanotubes in water suspension at 20 ºC (±1 ºC) and responding wt. % gold loading.

4.1.2 Nickel Deposition on Titanate Nanotubes

The same procedure was followed for nickel deposition as was done for gold. Briefly, ten different standard solution of $[Ni(en)_3](NO_3)_2$ were prepared to measure absorbance and generate the calibration line, ranging between 0.001 to 0.091 M. Absorbance of these solutions was measured in 190 to 700 nm spectrum range. As illustrated in **Figure 4.5**, $[Ni(en)_3](NO3)_2$ gives three characteristic absorbance peaks which appear at, 300, 340, and 544 nm. The peak that appears at 544 nm was chosen to plot calibration line for $[Ni(en)_3](NO3)_2$ solution shown in **Figure 4.6**.

Deposition of nickel on titanate nanotubes has several steps. Initially, the process involved the ion-exchanged deposition of $[Ni(en)_3]^{2+}_{(aq)}$ cations in 25 mL solutions by adding 0.5 g titanate. Subsequently, the spectrophotometer was used to measure the absorbance of the remaining solution. Finally, the measured absorbance of the remaining solution was placed on **Figure 4.6** to ascertain the concentration of metal that remained after deposition. All the data collected from colorimetric measurements are included in **Table 4.2**. These data were used to calculate the nickel adsorption isotherm, which can be observed in **Figure 4.7**. When this figure is examined, the ion-exchange molar ratio, a, increase relatively slowly for $[Ni(en)_3]^{2+}_{(aq}$ adsorption on titanate nanotubes. While Ni loading is 0.74 percent at 8 mmol L^{-1}, it is 2.11 percent at 64 mmol L^{-1}.

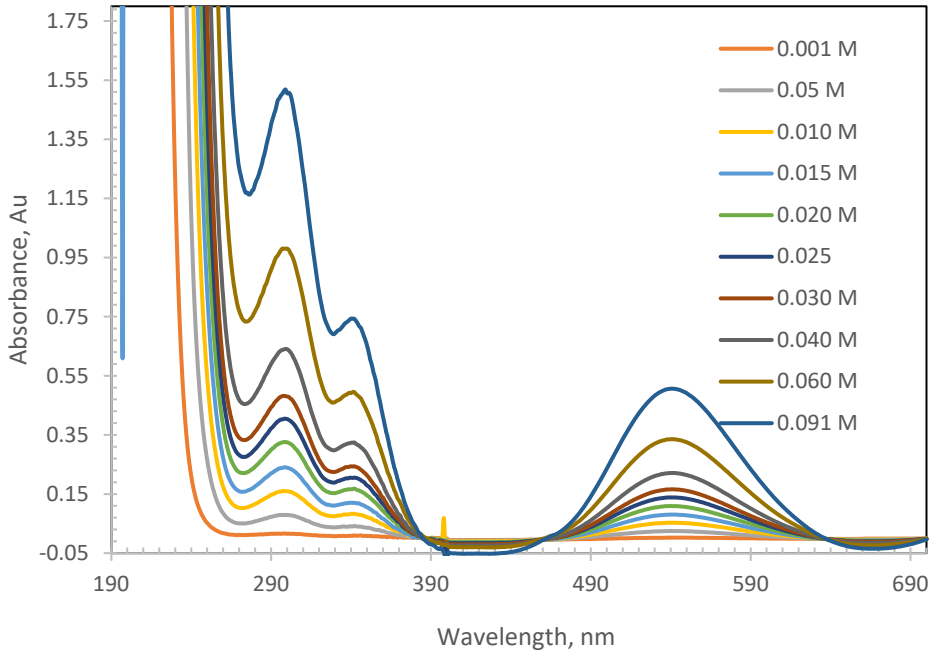

Figure 4.5: Absorbance spectrum of triethylenediamine nickel (II) nitrate $[Ni(en)_3](NO3)_2$ solutions measured at 22 °C

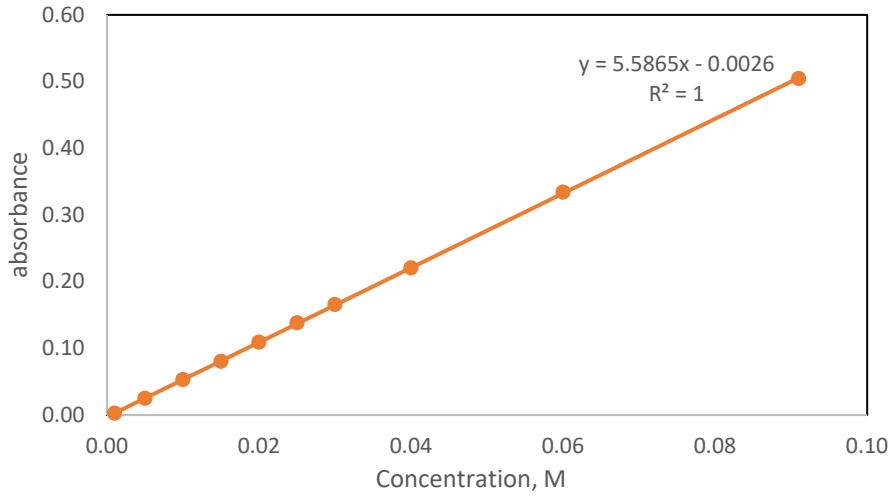

Figure 4.6: Calibration curve obtained at 544 nm for triethylenediamine nickel (II) nitrate $[Ni(en)_3](NO3)_2$ solutions.

Table 4.2: Initial and remaining concentration of $[Ni(en)_3]^{2+}$ with the data calculated based on these two measurements.

Initial $[Ni(en)_3]^{2+}_{(aq)}$ concentration, mmol L^{-1}, C_o	Remaining $[Ni(en)_3]^{2+}_{(aq)}$ concentration, mmol L^{-1}, C^*	Ion-exchange molar ratio / mol (Ni) mol^{-1} (TiNT), a	wt. %
8	5.44	0.010	0.74
16	11.95	0.016	1.17
18	13.62	0.017	1.27
32	26.26	0.023	1.66
64	56.64	0.029	2.11

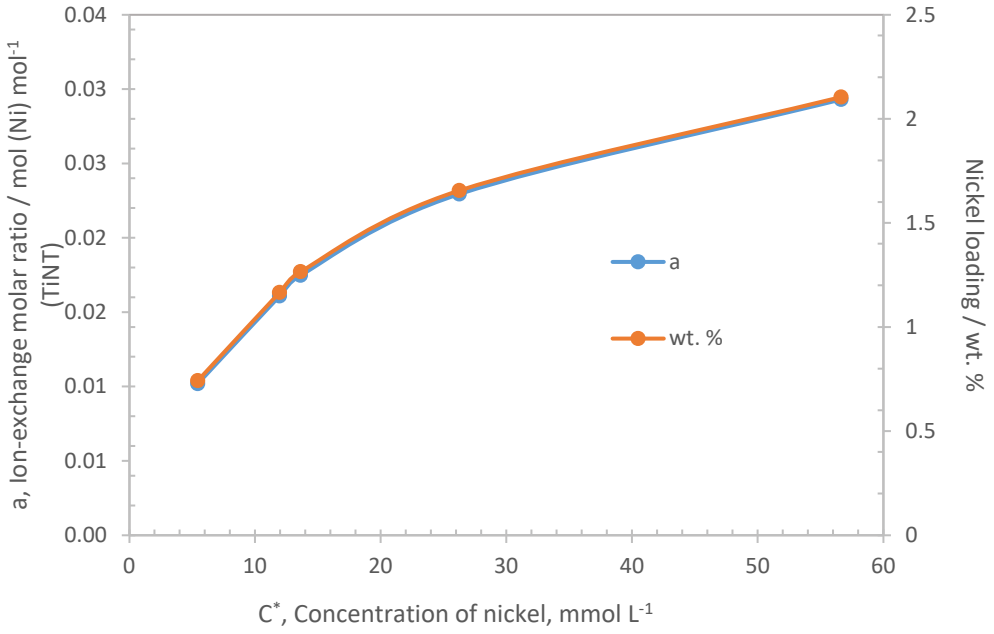

Figure 4.7: Adsorption isotherm of $[Ni(en)_3]^{2+}_{(aq)}$ cation on titanate nanotubes in water suspension at 20 °C (±1 °C) and responding wt. % nickel loading.

4.1.3 Co-deposition of Gold-nickel (Au-Ni)

To calculate weight percentage of adsorbed metals, a value provided by Eq. (3.1) were converted into g (metal) g^{-1} (TiO2) as expressed with Eq. (4.3):

$$a\,[g\,(metal)\,g^{-1}\,(TiO_2)] = a \times \frac{MW_{metal}}{MW_{TiO_2}} \tag{4.3}$$

After converting 'a' value into g (metal) g-1 (TiO2) for all the studied concentrations, weight percentage of adsorbed metal were calculated by Eq. (4.4):

$$wt.\% = \frac{g_{metal}}{g_{TiO_2} + g_{metal}} \times 100 \tag{4.4}$$

Exploiting initial concentration versus weight percentage of adsorbed metal, the correlation between adsorbed metal percentage and its required initial concentration to reach this percentage were provided as function of natural logarithm as seen in **Figure 4.8** and **Figure 4.9**. Intended a final 4 wt. % catalyst loadings were determined with different molar ratios of metals on titanate nanotubes surface. In **Table 4.3**, required metal weight percentages for the intended molar ratio of gold:nickel was provided. To obtain the weight percentage of each metal shown in **Table 4.3**, required amount of metal solutions were determined by using functions provided in **Figure 4.8** and **Figure 4.9**. For instance, to get a Au:Ni weight percentages ratio of (3.72):(0.28) out of 4 wt. % catalyst loading on 1 g TiNTs, which corresponds a 80:20 Au:Ni molar ratio, it was calculated that 1.89 mL of $HAuCI_4$ solution from its 0.1 M stock solution and 2.02 mL of $Ni(NO_3)_2$ from its 0.1 M stock solution are required.

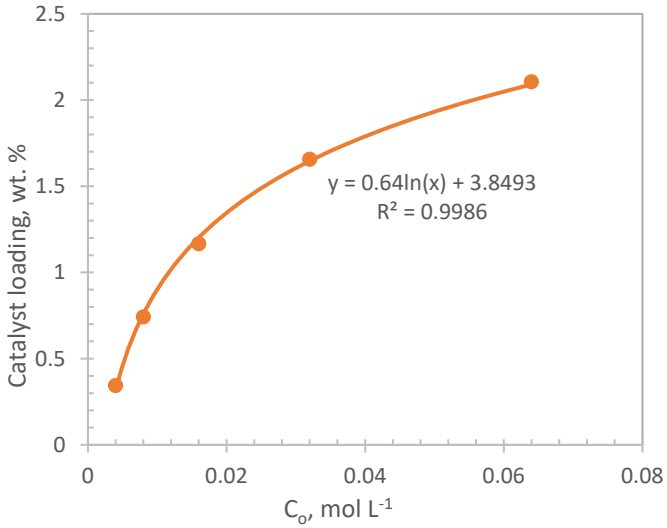

Figure 4.8: Correlation of Catalyst loading (wt. %)-initial concentration of $Ni(en)_3]^{2+}{}_{(aq)}$.

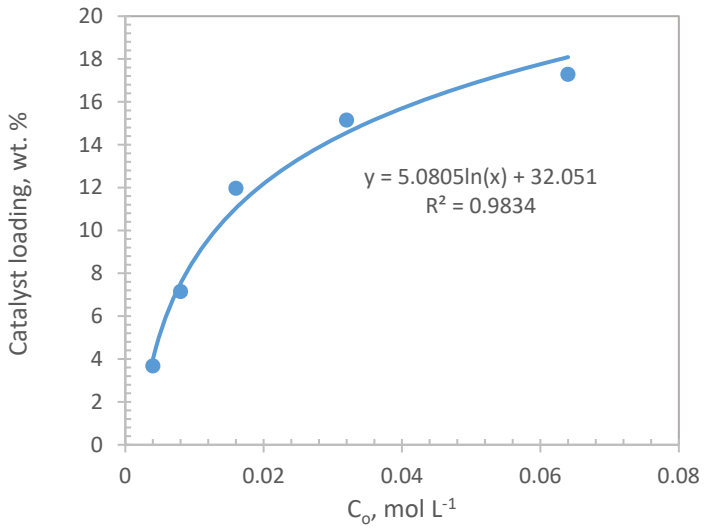

Figure 4.9: Correlation of Catalyst loading (wt. %)-initial concentration of $[Au(en)_2]^{3+}{}_{(aq)}$.

Table 4.3: Calculated molar ratios between gold and nickel with a total catalyst loading on TiNT

	Molar ratio of Au:Ni, %		Weight to weight percentage of Au:Ni, wt. %		
Catalyst	Au	Ni	Au	Ni	Total
Au_{100}/TiNT	100	0	4	0	4
$Au_{80}Ni_{20}$/TiNT	80	20	3.72	0.28	4
$Au_{60}Ni_{40}$/TiNT	60	40	3.33	0.67	4
$Au_{40}Ni_{60}$/TiNT	40	60	2.75	1.25	4
$Au_{20}Ni_{80}$/TiNT	20	80	1.8	2.2	4

4.2 Electrochemical Measurements

4.2.1 Cyclic Voltammetry

Borohydride electrooxidation on Au/TiNT-C, Au_aNi_b/TiNT-C (here a and b are atomic ratios of each metal), Au rotating disc electrode, and Pt rotating disc electrode have been investigated by cyclic voltammetry method. The scanned potential range was between -1.1 and +0.5 V *vs* SCE. The studies conducted with Pt disc electrode have revealed that oxidation of borohydride on Pt follows a complicated route and included multi electron transfer steps, appearing as multi-oxidation peaks on CV curve as shown in **Figure 4.10**. The peak a_1 appeared at around -1 V is attributed to the oxidation of intermediates e.g. H_2 resulted from borohydride hydrolysis on Pt electrode according to the reactions given by Eq. (4.5) and (4.6) [31], [32], [57]. Peak a_2 appeared at -0.15 V is associated the oxidation of BH_4^-, and peak c_1 appeared on reverse scan at -0.38 V is proposed oxidation of adsorbed intermediates, such as BH_3OH^- [31].

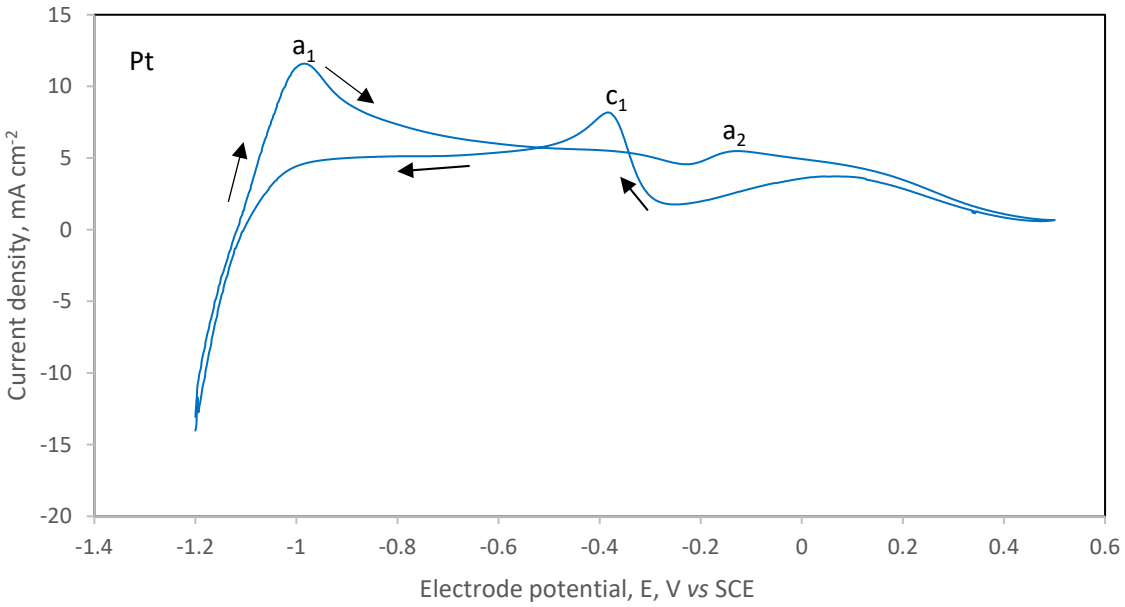

Figure 4.10: CV curve of Pt disc electrode. Counter electrode: Pt; electrolyte: 0.03 M $NaBH_4$ + 2 M NaOH; scan rate:10 mV s^{-1}; at ambient temperature (20 ºC ±1).

$$BH_4^- + H_2O \rightarrow BH_3(OH)^- + H_2 \text{ (partial hydrolysis)} \quad (4.5)$$

$$H_2 + 2OH^- \rightarrow 2H_2O + 2e^- \quad (4.6)$$

Contrary to the Pt rotating disc electrode, the oxidation peak appeared around -0.8 V, which is associated with H_2 oxidation, does not appear on Au rotating disc CV curve, as illustrated in **Figure 4.11**. In the literature, this has been interpreted that gold does not have reactivity toward borohydride hydrolysis, thereby no H_2 oxidation peak appeared on CV curve [31]. The first peak appeared at -0.40 V on CV curves during forward scan was linked direct oxidation of borohydride ions. A broad peak was observed at +0.25 V on Au rotating disc electrode CV curve which associated intermediates oxidation. The peaks c_1 on reverse scan have been originated to the oxidation of adsorbed intermediates, such as BH_3OH^- [43].

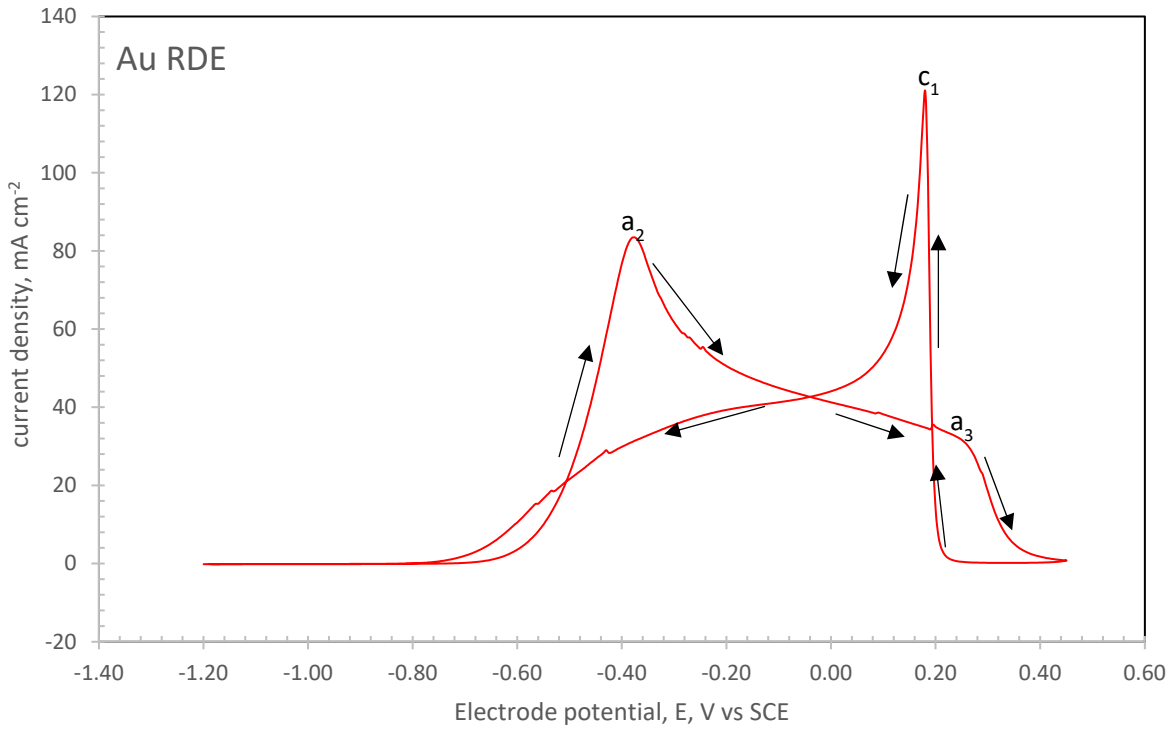

Figure 4.11: CV curve of Au disc electrode. Counter electrode: Pt; electrolyte: 0.03 M $NaBH_4$ + 2 M NaOH; scan rate:10 mV s^{-1}; at ambient temperature (20 °C ±1)

A broad oxidation peak (a_2) appeared on the forward scan of Au/TiNT-C and $Au_{40}Ni_{60}$/TiNT-C as shown in **Figure 4.12** and **Figure 4.13**, respectively. When these curves are examined, these peaks formed at around +0.10 V for Au/TiNT-C and -0.05 V for $Au_{40}Ni_{60}$/TiNT-C, shifting 0.15 V to more negative potentials which makes $Au_{40}Ni_{60}$/TiNT-C preferable over Au/TiNT-C for direct oxidation of borohydride. These peaks have been mainly attributed to direct oxidation of borohydride as shown in Eq. (4.7) [16], [78]. The other CV curves which obtained for $Au_{80}Ni_{20}$/TiNT-C, $Au_{60}Ni_{40}$/TiNT-C, $Au_{20}Ni_{80}$/TiNT-C were provided in **Appendix A**.

$$BH_4^- + 8OH^- \rightarrow BO_2^- + 6H_2O + 8e^- \quad E^0_{anode} = -1.24\ V\ vs.\ SHE \tag{4.7}$$

.

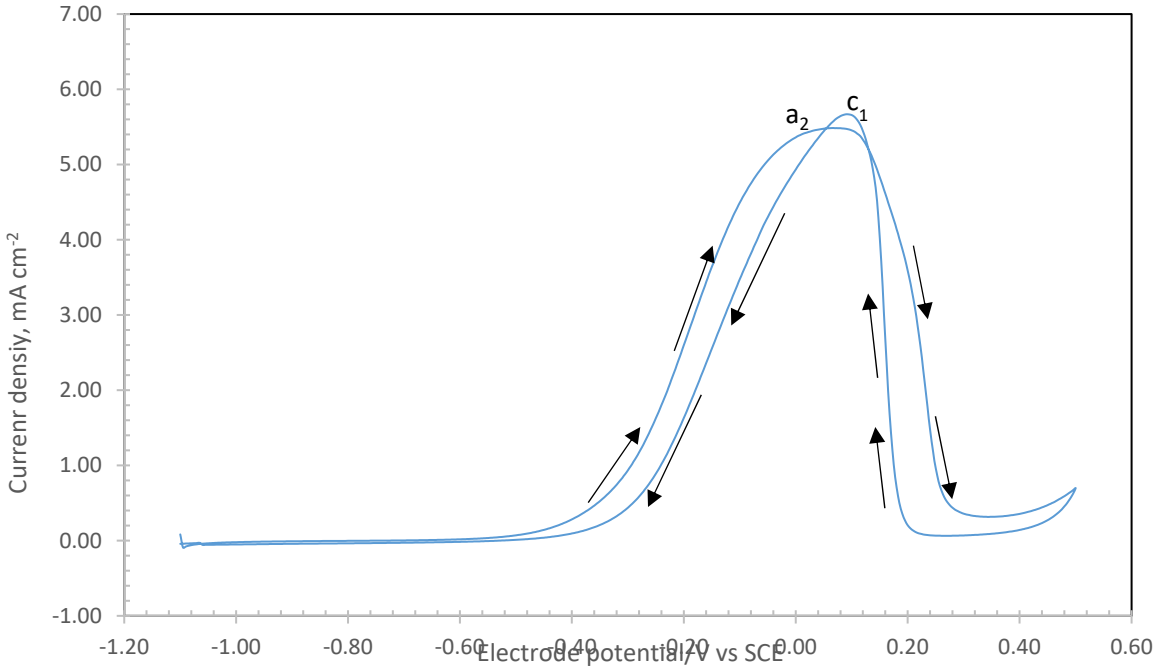

Figure 4.12: CV curve of Au/TiNT-C electrocatalyst coated on glassy carbon electrode. Counter electrode: Pt; electrolyte: 0.03 M $NaBH_4$ + 2 M NaOH; scan rate:10 mV s^{-1}; disc rotation 400 rpm; at ambient temperature (20 ^oC ±1)

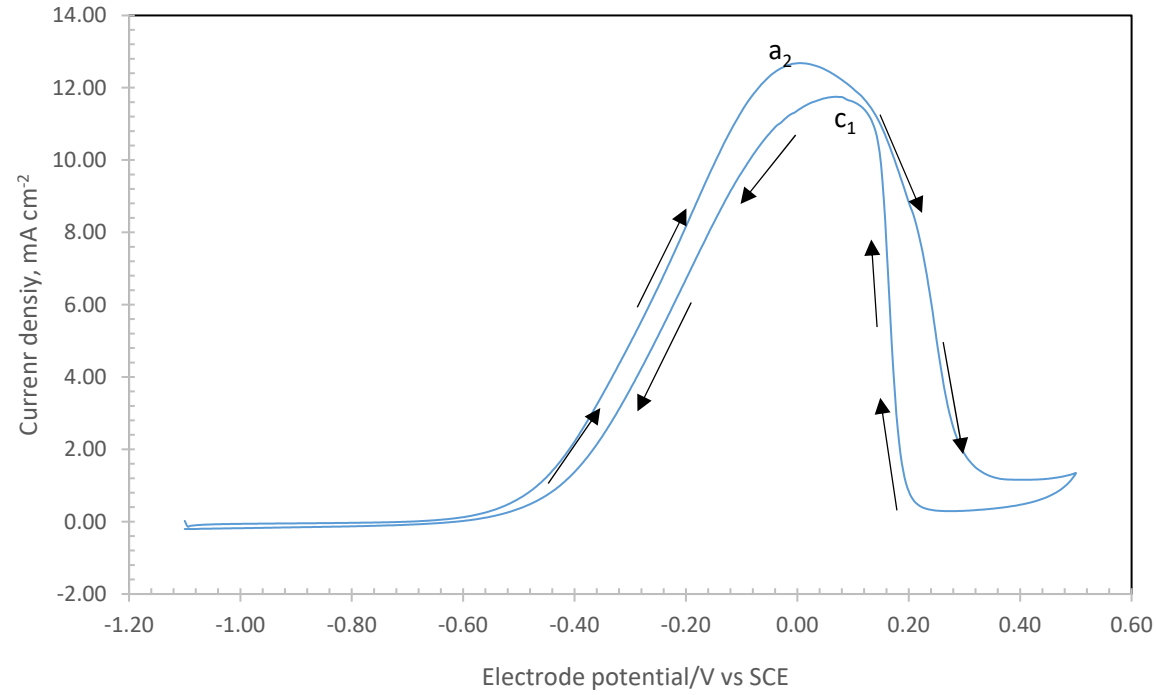

Figure 4.13: CV curve of $Au_{40}Ni_{60}$/TiNT-C C electrocatalyst coated on glassy carbon electrode. Counter electrode: Pt; electrolyte: 0.03 M $NaBH_4$ + 2 M NaOH; scan rate:10 mV s^{-1}; disc rotation 400 rpm; at ambient temperature (20 ^oC ±1)

4.2.2 Linear Sweep Voltammetry

Linear sweep voltammetry curves for Au rotating disc electrode obtained at five different rotation rates is shown in **Figure 4.14**. Current density starts to increase rapidly after -0.6 V until it begins to level off due to mass transport limitations to the electrode surface. Below the voltage value of -0.6 V, there was not considerable increase in current densities, where the current density is totally controlled by kinetics of electron transfer [30]. An increase in current densities can be observed by increasing rotation rates from 400 up to 2000 rpm.

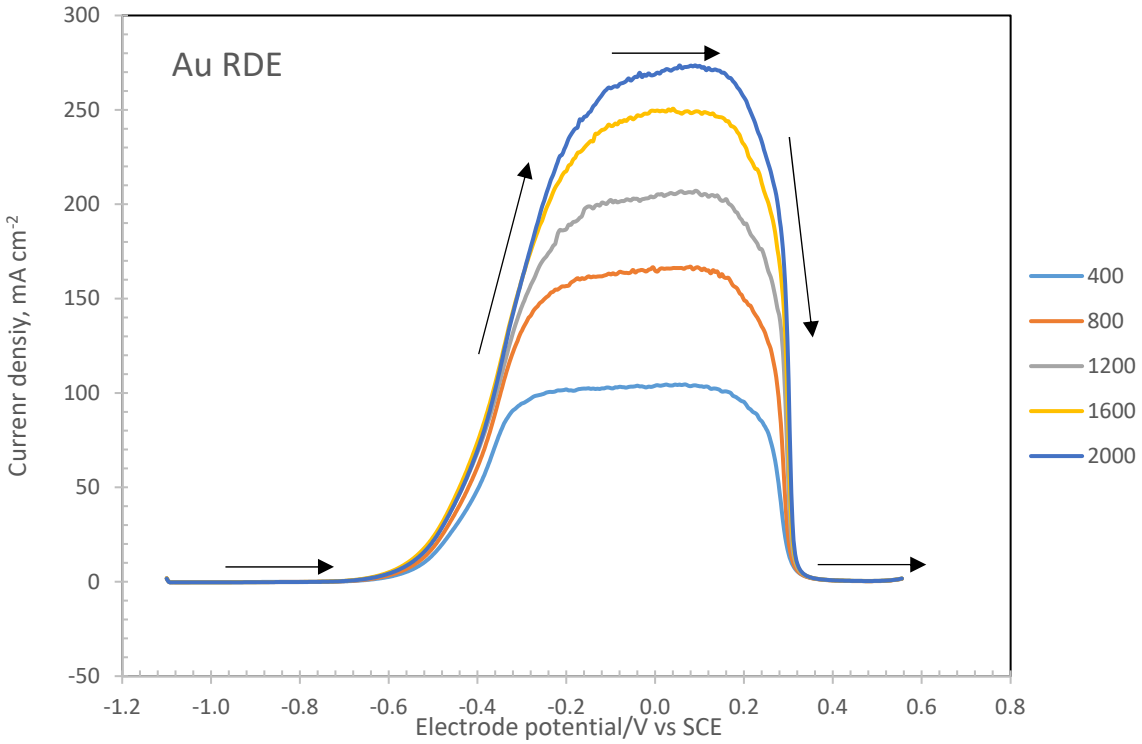

Figure 4.14: Linear sweep voltammograms of rotating Au disc electrode at different rotation rates. Counter electrode: Pt; electrolyte: 0.03 M $NaBH_4$ + 2 M NaOH; scan rate:10 mV s^{-1}; at 20 ºC (±1 ºC)

Figure 4.15 shows the polarization curves of Au_{100}/TiNT-C coated glassy carbon disc electrodes at five different rotation rates. When this figure compared with linear sweep voltammograms of Au rotating disc electrode given in **Figure 4.14**, a similar tendency can be examined in terms of peak current appearance place on the voltammograms. Oxidation reaction starts at slightly more positive voltage on Au_{100}/TiNT-C (ca. -0.5 V). This could be due to low gold loading.

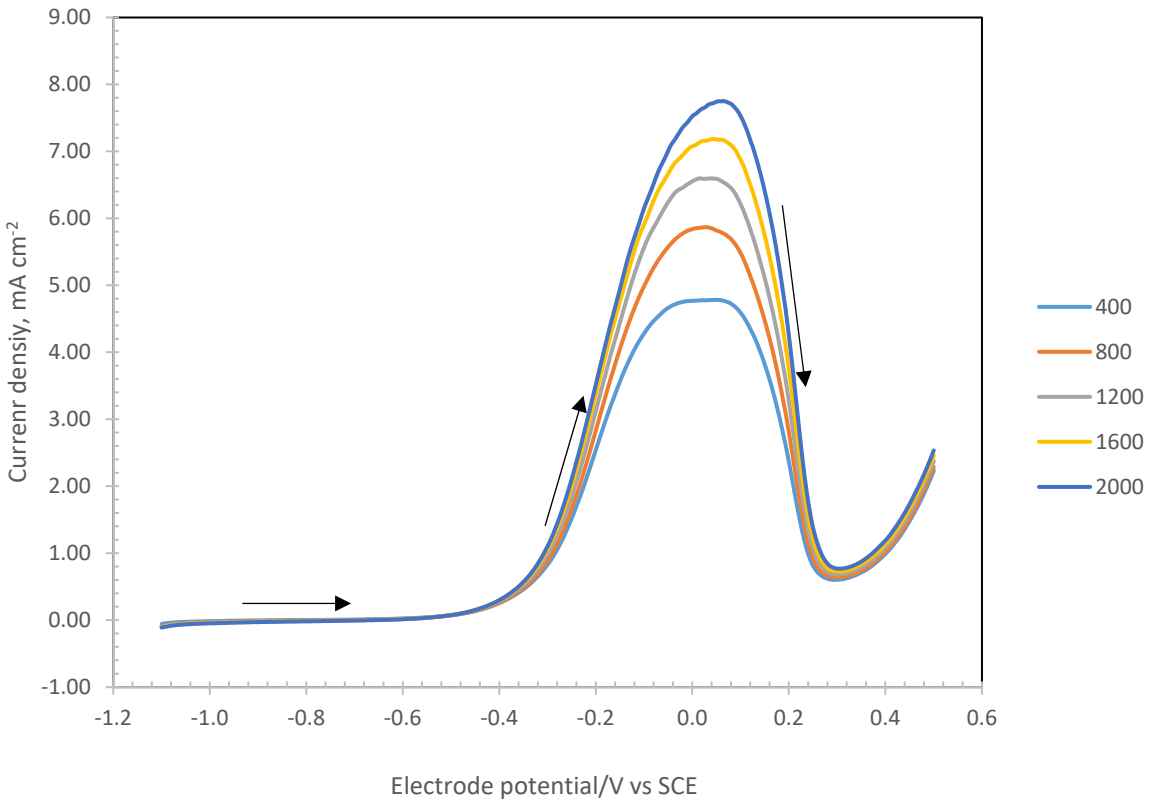

Figure 4.15: Linear sweep voltammograms (LSV) of Au_{100}/TiNT-C coated glassy carbon disc electrode at different rotation rates. Counter electrode: Pt; electrolyte: 0.03 M $NaBH_4$ + 2 M NaOH; scan rate:10 mV s^{-1}; at 20 ºC (±1 ºC)

However, when gold combined with nickel, oxidation of borohydride starts at ca. -0.6 V which is nearly the same potential with gold rotating disc electrode. This shift can be clearly seen in **Figure 4.16** which obtained for $Au_{40}Ni_{60}$/TiNT-C coated glassy carbon disc electrode. Most importantly, all studied Au_aNi_b/TiNT-C binary metal composite catalysts in this study surpassed the performance of Au_{100}/TiNT-C in borohydride oxidation. This can be clearly seen in **Figure 4.17** that obtained at 2000 rpm for Au_{100}/TiNT-C, $Au_{80}Ni_{20}$/TiNT-C, $Au_{60}Ni_{40}$/TiNT-C, $Au_{40}Ni_{60}$/TiNT-C, and $Au_{20}Ni_{80}$/TiNT-C.

Figure 4.18 was plotted to compare peak current densities versus gold content percentage in the composite catalysts, clarifying the improvement in current densities. The gold weight content in percentage was the following order: 2.51, 2.33, 2.09, 1.72, and 1.13 % for Au_{100}/TiNT-C, $Au_{80}Ni_{20}$/TiNT-C, $Au_{60}Ni_{40}$/TiNT-C, $Au_{40}Ni_{60}$/TiNT-C, and $Au_{20}Ni_{80}$/TiNT-C, respectively.

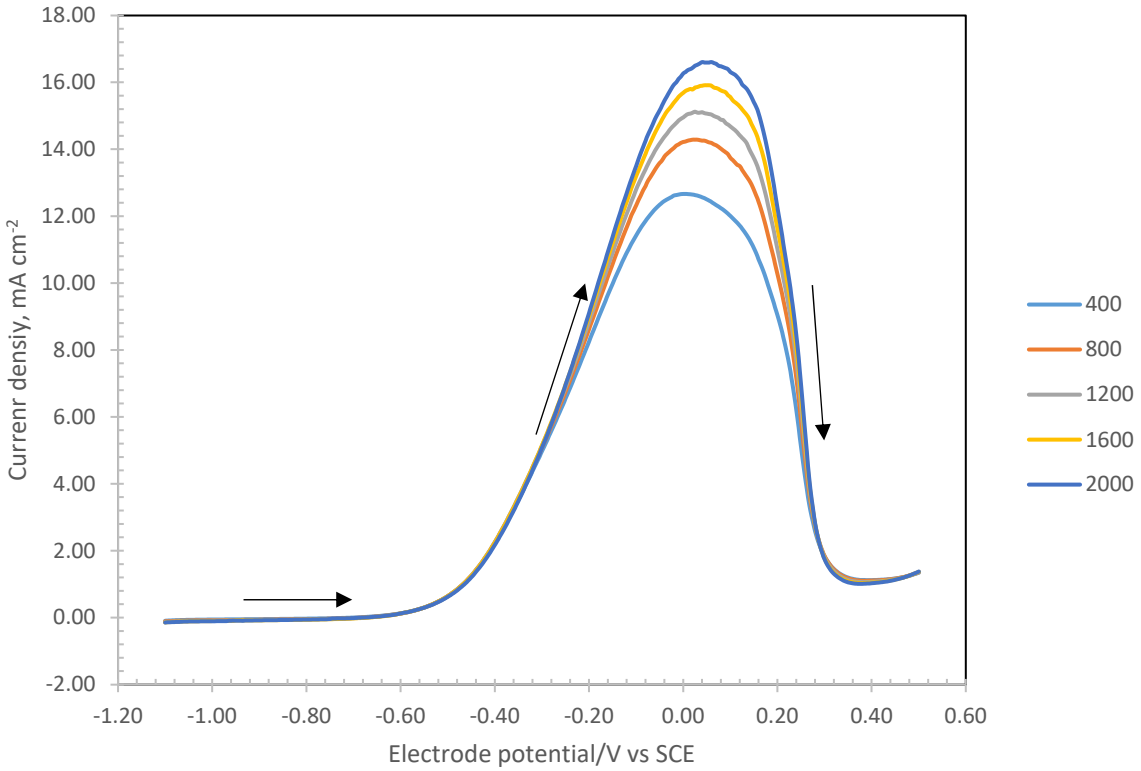

Figure 4.16: Linear sweep voltammograms of $Au_{40}Ni_{60}$/TNT-C coated glassy carbon disc electrode at different rotation rates. Counter electrode: Pt; electrolyte: 0.03 M $NaBH_4$ + 2 M NaOH; scan rate:10 mV s^{-1}; at 20 ^oC (±1 ^oC)

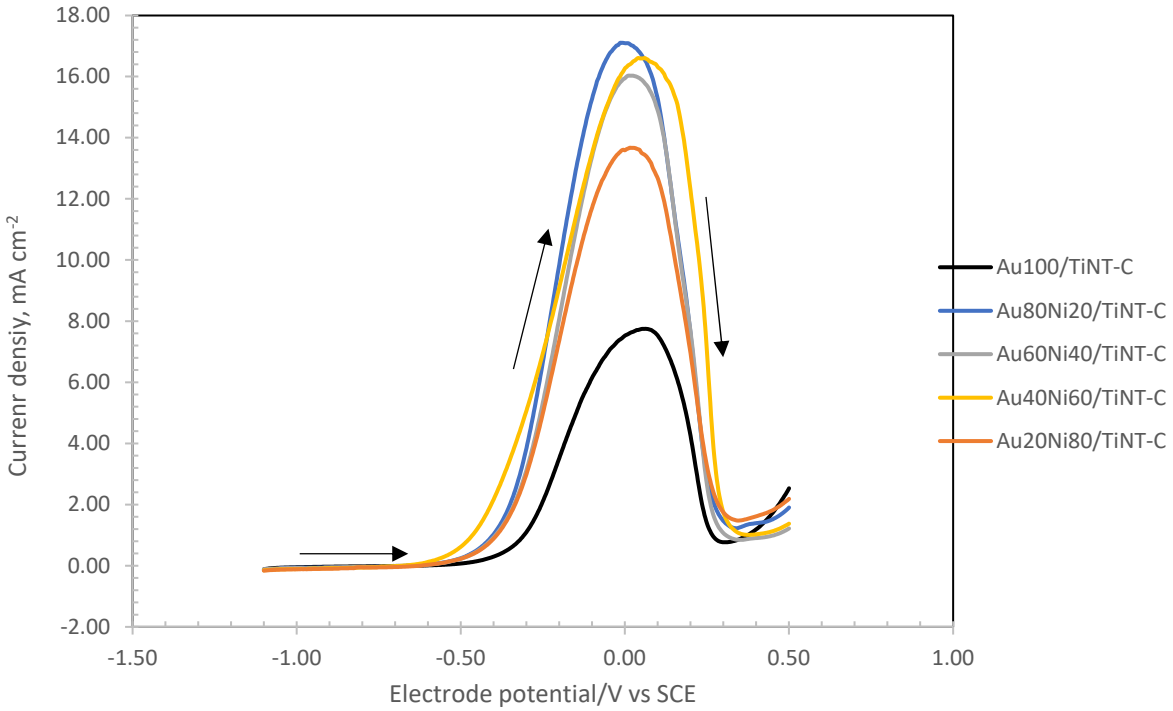

Figure 4.17: Comparison of linear sweep voltammogram peak current densities measured for Au_{100}/TiNT-C, $Au_{80}Ni_{20}$/TiNT-C, $Au_{60}Ni_{40}$/TiNT-C, $Au_{40}Ni_{60}$/TiNT-C, and $Au_{20}Ni_{80}$/TiNT-C at 2000 rpm. Counter electrode: Pt; electrolyte: 0.03 M $NaBH_4$ + 2 M NaOH; scan rate:10 mV s^{-1}; at 20 ^oC (±1 ^oC)

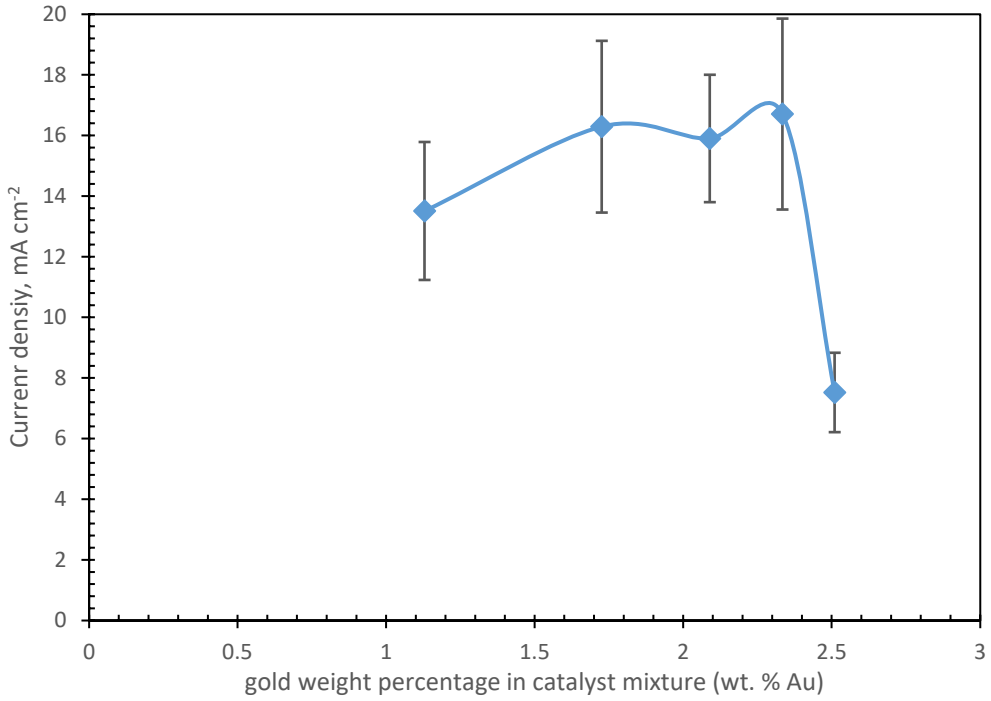

Figure 4.18: Comparison of maximum current densities versus gold weight percentage in the catalyst mixture for the developed catalysts: Au_{100}/TiNT-C, $Au_{80}Ni_{20}$/TiNT-C, $Au_{60}Ni_{40}$/TiNT-C, $Au_{40}Ni_{60}$/TiNT-C, and $Au_{20}Ni_{80}$/TiNT-C, obtained at 2000 rpm.

Among the Au-Ni composite catalysts, $Au_{80}Ni_{20}$/TiNT-C shows the best performance in terms of maximum current generation in borohydride oxidation. These performance improvements can be expressed as percentage for a better understanding in comparison of Au_{100}/TiNT-C with Au_aNi_b/TiNT-C composite catalysts. When the performance of $Au_{80}Ni_{20}$/TiNT-C, $Au_{60}Ni_{40}$/TiNT-C, $Au_{40}Ni_{60}$/TiNT-C, and $Au_{20}Ni_{80}$/TiNT-C are compared whit those of Au_{100}/TiNT-C at 2000 rpm, composite catalysts show the following improvements in percentage: 122.0, 111.3, 116.5, and 79.5, respectively. As expressed, all composite catalysts show at least 80% more catalytic activity than Au_{100}/TiNT-C. Even a small amount of nickel addition to the catalyst structure has a great role to play in catalytic activity increase when $Au_{80}Ni_{20}$/TiNT-C and Au_{100}/TiNT-C are compared. This increase in catalytic activity of $Au_{80}Ni_{20}$/TiNT-C is 2.22 times higher than those of Au_{100}/TiNT-C. Meanwhile, when Au_aNi_b/TiNT-C composite catalysts compared with each other, $Au_{80}Ni_{20}$/TiNT-C and $Au_{40}Ni_{60}$/TiNT-C show a similar catalytic activity toward borohydride oxidation, having 2.22 and 2.11 times higher catalytic activity than those of Au_{100}/TiNT-C, respectively.

Active catalyst mass based catalytic activity comparison is a useful method to reveal catalyst performance. In this regard, **Table 4.4** was generated to compare catalytic performance of developed catalysts in borohydride oxidation. There are several important results to discuss on

this table. First, being active metal catalyst loading 0.051 mg cm^{-2}, it is considerably low compared to the anode catalysts developed for DBFC in the literature reviewed by P.-Y. Olu and co-workers [59]. In most paper in that review, precious metal loading, such as Au, Pt, Pd etc., were more than 0.13 mg cm^{-2} and total metal loading were above 1 mg cm^{-2}. Second, when **Table 4.4** is examined, interestingly, Au mass based current density of $Au_{20}Ni_{80}$/TiNT-C outperform the other catalysts, being ca. 4 time higher than those of Au_{100}/TiNT-C. Third but not least, there was an inverse proportion between maximum Au-based current density and Au content in the catalyst mixture.

Table 4.4: Maximum current density and Au mass-based current density comparison of developed Au_{100}/TiNT-C and Au_aNi_b/TiNT-C catalysts.

Catalyst	Weight percentage of Au (wt. % Au)	Au loading mg cm^{-2}	Weight percentage of Ni (wt. % Ni)	Ni loading mg cm^{-2}	Max. current density at 2000 rpm, mA cm^{-2}	Au mass based current density mA mg^{-1}
Au_{100}/TiNT-C	2.51	0.051	0	0.00	7.53	147.57
$Au_{80}Ni_{20}$/TiNT-C	2.33	0.047	0.18	0.004	16.71	355.48
$Au_{60}Ni_{40}$/TiNT-C	2.09	0.042	0.42	0.009	15.90	378.60
$Au_{40}Ni_{60}$/TiNT-C	1.72	0.035	0.79	0.016	16.29	465.44
$Au_{20}Ni_{80}$/TiNT-C	1.13	0.023	1.38	0.028	13.51	587.41

Another important test is to check only gold adsorbed titanate nonotubes catalysts for borohydride oxidation, excluding nickel in the catalyst texture. For this purpose, Au_{100}/TiNT-C, Au_{80}/TiNT-C, Au_{60}/TiNT-C, Au_{40}/TiNT-C, and Au_{20}/TiNT-C were prepared. LSV performance of these catalyst at 2000 rpm is illustrated in **Figure 4.19**. From this figure, it can be seen that performance of Au_{100}/TiNT-C, Au_{80}/TiNT-C, and, Au_{40}/TiNT-C are close to each other, generating similar peak currents. On the other hand, Au_{60}/TiNT-C outperform the other catalys performance with a 9.68 mA cm^{-2} peak current density, and Au_{20}/TiNT-C shows the lowest performance by generating only 2 mA cm^{-2} peak current. Weight percentage of gold in catalyst mixture and corresponding peak current densities appears on **Figure 4.19** can be found on **Table 4.5**.

When this table is examined, current density increases from 2.00 to 9.68 mA cm^{-2} when gold percentages rise from 1.13 to 2 .09 wt. %. By increasing gold percentage in catalyst texture from 2.09 to 2.33, peak current density goes down from 9.68 to 7.5 mA cm^{-2}. This relation between gold percentage and peak current densities can be see clearly on **Figure 4.20**. It can be concluded that 2 wt. % might be ideal to use for practical applications.

Table 4.5: Maximum current density and Au mass-based current density comparison of developed Au_{100}/TiNT-C, Au_{80}/TiNT-C, Au_{60}/TiNT-C, Au_{40}/TiNT-C, and Au_{20}/TiNT-C catalysts.

Catalyst	Weight percentage of Au (wt. % Au)	Au loading mg cm^{-2}	Max. current density at 2000 rpm, mA cm^{-2}	Au mass based current density mA mg^{-1}
Au_{100}/TiNT-C	2.51	0.051	7.53	147.57
Au_{80}/TiNT-C	2.33	0.047	7.15	152.13
Au_{60}/TiNT-C	2.09	0.042	9.68	230.48
Au_{40}/TiNT-C	1.72	0.035	7.27	207.71
Au_{20}/TiNT-C	1.13	0.023	2.00	86.96

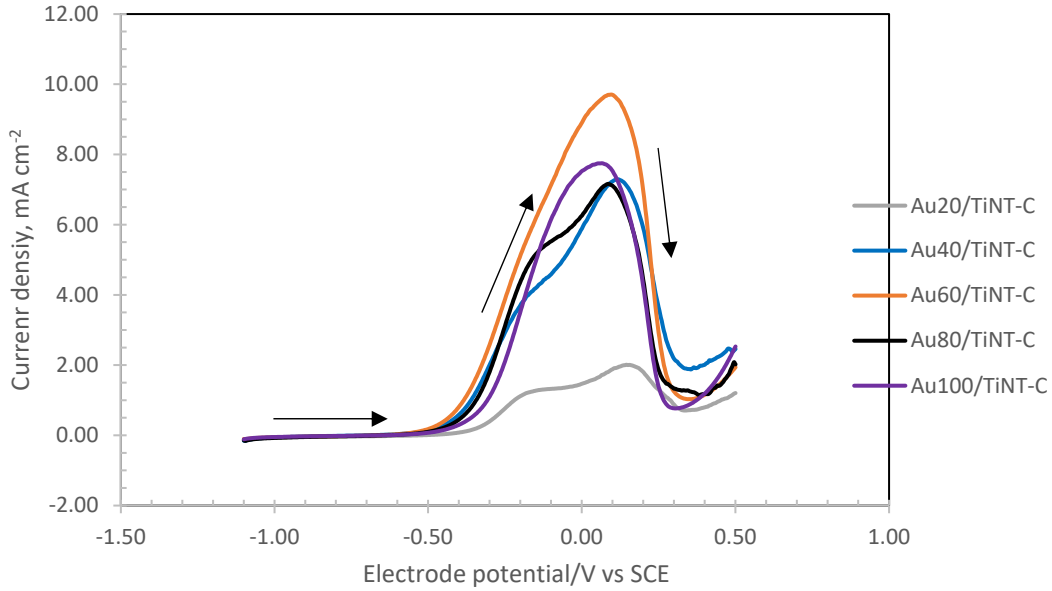

Figure 4.19: Comparison of linear sweep voltammogram peak current densities measured for Au_{100}/TiNT-C, Au_{80}/TiNT-C, Au_{60}/TiNT-C, Au_{40}TiNT-C, and Au_{20}/TiNT-C at 2000 rpm. Counter electrode: Pt; electrolyte: 0.03 M $NaBH_4$ + 2 M NaOH; scan rate:10 mV s^{-1}; at 20 ºC (±1 ºC)

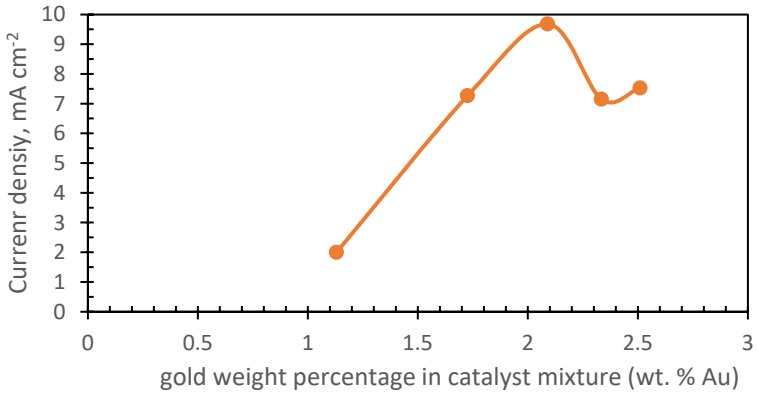

Figure 4.20: Comparison of maximum current densities versus gold weight percentage in the catalyst mixture for the developed catalysts: Au_{100}/TiNT-C, Au_{80}/TiNT-C, Au_{60}/TiNT-C, Au_{40}/TiNT-C, and Au_{20}/TiNT-C, obtained at 2000 rpm.

4.2.3 Determination of D, *k*, and *n*

Using a rotating disc electrode (RDE) configuration, diffusion coefficient number, D, can be obtained in an electrochemical reaction at a preferred potential using Levich equation given by Eq. (4.8) [30].

$$I_L = -0.62nFAD^{\frac{2}{3}}C_b v^{-\frac{1}{6}}\omega^{1/2} \quad (4.8)$$

Where, I_L is limiting current (A cm^{-2}), n is transferred electron number (n was assumed to be 8), A is geometric area of working electrode (cm^2), F is Faraday constant (96485 C mol^{-1}), D is diffusion coefficient of the electro active species (cm^2 s^{-1}), C_b is bulk concentration of borohydride (mol cm^{-3}), v is kinematic viscosity of the solution (cm^2 s^{-1}), and ω is the angular velocity of the rotating disc (radians s^{-1}). Regarding the data given in **Figure 4.14** and using the Eq. (4.8), the plot of limiting current density of disc electrode (j_L) versus square root of angular velocity of the disc ($\omega^{1/2}$) must be linear and pass through the origin, obeying only mass-transport limitation at all rotation rates. However, some intermediates form (BH_3OH^- or B_2H_6) in irreversible electrooxidation reaction of borohydride, causing the deviation of the intercept point from the origin to a different value, as shown in **Figure 4.21** [30]. By means of the slope of the **Figure 4.21**, diffusion coefficient number, D, was calculated to be 1.77×10^{-5} cm^2 s^{-1}. This calculated D value matches with those of D values reported for similar conditions in the literature (D = 1.80×10^{-5} cm^2 s^{-1}) for borohydride ions diffusion [82], [83]. In all calculations which include D values in it, this measured D (1.77×10^{-5} cm^2 s^{-1}) value was used.

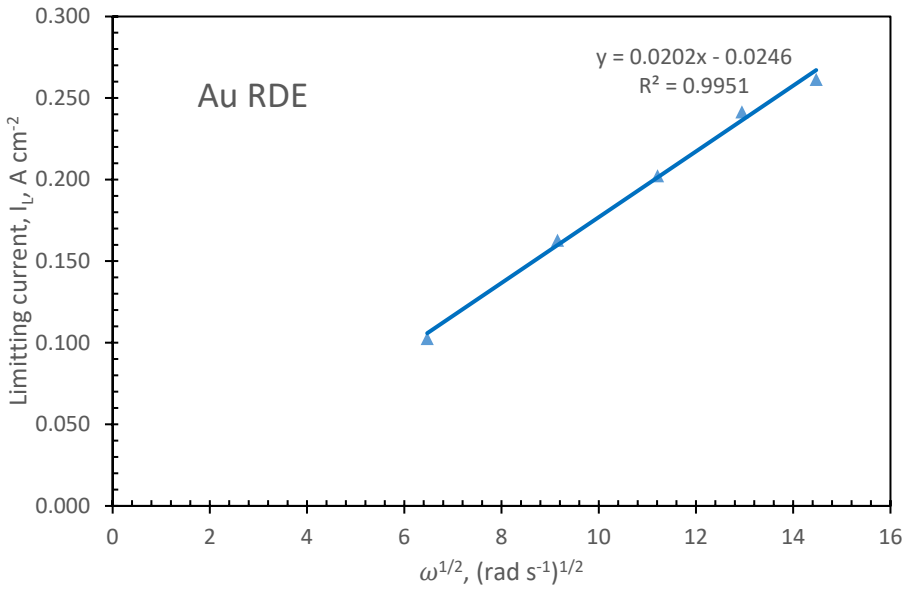

Figure 4.21: Levich plot of Au rotating disc electrode, the parameters were the same as shown **Figure 4.14.**

To calculate transferred electron number, n, and apparent rate constant, k, the Koutecky-Levich equation was used given by Eq. (4.9) [32].

$$\frac{1}{j} = \frac{1}{nFkC_b} + \frac{1}{0.62nFD^{2/3}C_b v^{-1/6}\omega^{1/2}} \quad (4.9)$$

Where, j is disc current density (A cm^{-2}), and k is apparent rate constant (cm s^{-1}). D was calculated as 1.77×10^{-5} cm^2 s^{-1}, and v was obtained from literature to be as 0.0126 cm^2 s^{-1}, respectively [82], According to the Eq. (4.9), plot of j^{-1} values versus $\omega^{-1/2}$ should show linearity for the data are selected in mix-controlled region (mass transport controlled + kinetically controlled) on linear sweep voltammograms. Considering mix-controlled region between -0.4 and -0.30 V as seen in **Figure 4.14**, plotted lines were shown in **Figure 4.22** for Au rotating disc electrode. From this on, the slope and intercepts have been used to calculate transferred electron number (n) and apparent rate constant (k), respectively.

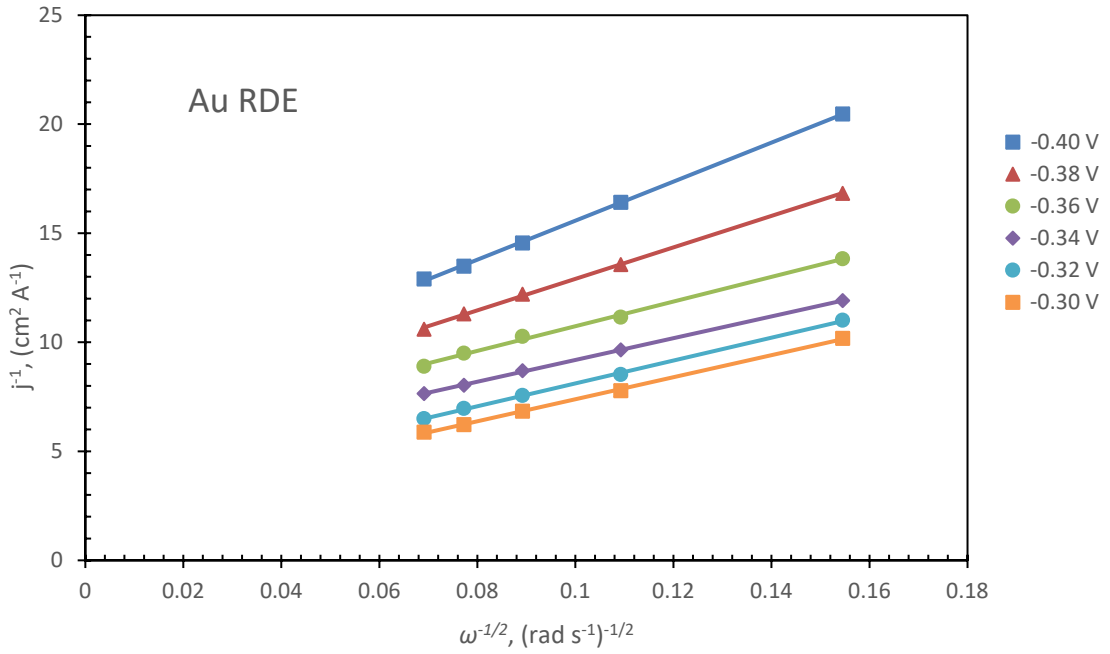

Figure 4.22: Koutecky-Levich plot of Au rotating disc electrode between -0.40 V and -0.30 V, Counter electrode: Pt; electrolyte: 0.03 M $NaBH_4$ + 2 M NaOH; scan rate: 10 mV s^{-1}; at 20 °C (±1 °C)

In theory, transferred electron numbers must be in a range between 0 and $8e^-$ per BH_4^- ion according to Eq. (4.10).

$$BH_4^- + xOH^- \rightarrow BO_2^- + (x-2)H_2O + (4-(0.5)x)H_2 + xe^- \quad (4.10)$$

Calculated kinetic parameters, n and k, using calculated value of diffusion coefficient number, D, were shown in

Table 4.6. Calculated *n* number at -0.4 V vs SCE was 4.4, but when the potential increase to -0.34 V, *n* value reached to 7.8 which is close to theoretical transferred electron number for direct oxidation of borohydride, in agreement with the value reported by by Bard and co-workers [84]. Close to mix-controlled and mass transport control region border, such as at -0.34 V, average number of electrons exchanged reached to a maximum value of 7.8. At higher voltage than -0.30 V, calculated transferred electron number led to a decrease to around 5.5 higher. The main reason for this drop in exchanged electron number is due to deviation from Koutecky-Levich equation which is valid only for mix-controlled region. In **Appendix A**, transferred electron number and apparent rate constant were provided between -0.40 and 0.20 V interval for further examination. However, calculated transferred electron numbers in mix-controlled region were similar with those of Cheng and Scott's which were reported as 4.03 at 0 V and 8.60 at 0.6 V *vs* Hg/HgO reference electrode obtained using a rotating Au disc electrode and deploying 0.27 M $NaBH_4$ in 2.5 M NaOH [30].

In terms of apparent rate constant, calculated *k* values were less than those of Cheng and Scott results, but in agreement with Santos and Sequeire [30], [82]. In both studies Au disc electrode was used, but determination method for k were different. Apart from that, Cheng and Scott used only one concentration value in determination of k, 1.32 M $NaBH_4$ in 2.5 M NaOH, yet Santos and Sequeire measured k for different borohydride concentration, ranging between 0.03 M and 0.12 M $NaBH_4$ in 2 M NaOH supporting electrolyte. In the study of Santos and Sequeire, the apparent rate constant was reported to be between 0.0289 and 0.0591 cm s^{-1} in a potential range of -0.2 an 0.2 V *vs* SCE, considering the experiments results conducted with 0.03 M $NaBH_4$ in 2 M NaOH.

Table 4.6: Obtained kinetic parameters from borohydride oxidation on Au rotating disk electrode for using calculated D value.

Potential, V	n	Standard deviation	k (cm s^{-1})	Standard deviation
-0.40	4.4	0.2	0.012	0.005
-0.38	5.5	0.1	0.011	0.005
-0.36	7.3	0.1	0.010	0.005
-0.34	7.8	0.1	0.011	0.005
-0.32	7.9	0.2	0.014	0.005
-0.30	8.0	0.2	0.018	0.001

Besides Au rotating disc electrode, developed Au_aNi_b/TiNT-C electrocatalyst were tested in oxidation of borohydride to obtain diffusion coefficient number, D, number of electrons exchanged, n, and apparent rate constant, k, were measured. The same procedure was followed

in determination of D, k, and n for composite catalyst as for done Au rotating disc electrode. Obtained diffusion coefficient numbers, D, in the case of developed Au_{100}/TiNT-C and gold-nickel bimetallic catalysts (Au_aNi_b/TiNT-C), calculated D values were smaller than those of Au disc electrode. The difference in D values between the Au rotating disc electrode and the developed electrocatalyst for borohydride diffusion may result from a couple of reasons. First, the addition of nafion into texture of developed catalysts to bind the catalyst ink onto glassy carbon electrode surface might prevent catalyst surface from fully interacting with the electrolyte. This may reduce the transfer of borohydride ions to the electrode surface, resulting in less electroactive species reaching to the electrode surface, thereby causing smaller D values. Second, the rough surface of the working electrode, which is composed of a catalyst-coated glassy carbon disc electrode, may cause deviations in the D values for the developed electrocatalysts, resulting in smaller D values. These D values could be apparent diffusion coefficient number. However, diffusion coefficient number can only change by changing sodium borohydride concentration or supporting electrolyte concentration. Due to this fact, calculated D value for Au disc electrode was chosen and used for all calculations.

Table 4.7 shows calculated exchanged number of electrons, n, and apparent rate constant, k in different potentials range for Au disc electrode, Au_{100}/TiNT-C, $Au_{80}Ni_{20}$/TiNT-C, $Au_{60}Ni_{40}$/TiNT-C, $Au_{40}Ni_{60}$/TiNT-C, and $Au_{20}Ni_{80}$/TiNT-C. Different potential range was selected to calculate n and k values due to appearance range of mix-controlled region on LSV voltammograms for Au disc electrode and other developed catalysts. In the case of Au_{100}/TiNT-C, transferred electron numbers shows a similar trend with those of Au disc electrode, with only a difference in potential range. Regarding the developed co-catalysts, Au_aNi_b/TiNT-C, transferred electron numbers appear to be close the theoretical $8e^-$ in the investigated voltage range at mix-controlled region on LSV curves. For instance, at -0.10 V calculated transferred electron numbers as follow: 5.9, 7.9, 8.9, 7.6, and 7.8 for Au_{100}/TiNT-C, $Au_{80}Ni_{20}$/TiNT-C, $Au_{60}Ni_{40}$/TiNT-C, $Au_{40}Ni_{60}$/TiNT-C, and $Au_{20}Ni_{80}$/TiNT-C, respectively. At some potential, calculated n values tend to be higher than theoretical value of $8e^-$. This may result from side reactions, e.g. oxygen evolution, and blockage of electrode surface by adsorbed intermediates, such as BH_3 or B_2H_6, which cause superimposed oxidation currents [30], [31].

In terms of calculated apparent rate constant values, k, there is a comparable difference between monometallic Au_{100}/TiNT-C and Au_aNi_b/TiNT-C co-catalysts. For instance, calculated k values were 0.003, 0.006, 0.009, 0.007, and 0.006 cm s^{-1}, at 0 V for Au_{100}/TiNT-C, $Au_{80}Ni_{20}$/TiNT-C, $Au_{60}Ni_{40}$/TiNT-C, $Au_{40}Ni_{60}$/TiNT-C, and $Au_{20}Ni_{80}$/TiNT-C, respectively.

These results show that k values of prepared co-catalysts are higher than the value of Au_{100}/TiNT-C. These increase in apparent rate constant supports that catalytic activities improve when nickel is used as co-catalyst with gold decorated on titanate nanotubes.

Table 4.7: Calculated number of electrons exchanged, n, and apparent kinetic rate constant, k at different voltage range.

Catalyst	Potential, V	n	Standard deviation	k (cm s^{-1})	Standard deviation
Au disc electrode	-0.40	4.4	0.2	0.012	0.005
	-0.38	5.5	0.1	0.011	0.005
	-0.36	7.3	0.1	0.010	0.006
	-0.34	7.8	0.1	0.011	0.005
	-0.32	7.9	0.2	0.014	0.005
	-0.30	8.0	0.2	0.018	0.001
Au_{100}/TiNT-C	-0.30	1.6	0.2	0.003	0.001
	-0.25	2.4	0.2	0.003	0.001
	-0.20	3.6	0.4	0.003	0.001
	-0.15	4.8	0.7	0.003	0.001
	-0.10	5.9	1.0	0.003	0.002
	-0.05	6.9	1.2	0.003	0.001
	0.00	7.6	1.4	0.003	0.001
	0.05	7.8	1.4	0.003	0.001
	0.10	8.0	1.4	0.003	0.002
$Au_{80}Ni_{20}$/TiNT-C	-0.30	8.5	2.4	0.001	0.001
	-0.25	7.3	2.3	0.002	0.001
	-0.20	7.1	2.8	0.003	0.001
	-0.15	7.6	3.0	0.003	0.001
	-0.10	7.9	3.2	0.004	0.001
	-0.05	7.8	3.0	0.005	0.002
	0.00	8.0	2.6	0.006	0.002
	0.05	8.1	2.4	0.007	0.002
	0.10	8.5	2.1	0.007	0.002
$Au_{60}Ni_{40}$/TiNT-C	-0.30	8.9	3.5	0.002	0.001
	-0.25	7.9	2.2	0.003	0.001
	-0.20	8.5	1.3	0.004	0.002
	-0.15	8.6	1.6	0.005	0.002
	-0.10	8.9	1.8	0.006	0.002
	-0.05	9.1	1.8	0.007	0.002
	0.00	9.1	1.7	0.009	0.003
	0.05	9.0	1.4	0.009	0.003
	0.10	8.8	1.3	0.011	0.003

Catalyst	Potential, V	n	Standard deviation	k (cm s^{-1})	Standard deviation
$Au_{40}Ni_{60}$/TiNT-C	-0.30	5.4	0.2	0.001	
	-0.25	6.6	0.3	0.002	0.000
	-0.20	7.3	0.4	0.003	0.001
	-0.15	7.5	0.4	0.004	0.001
	-0.10	7.6	0.2	0.005	0.001
	-0.05	7.6	0.4	0.007	0.001
	0.00	7.7	0.7	0.007	0.001
	0.05	7.6	0.6	0.008	0.001
	0.10	7.8	0.5	0.007	0.002
$Au_{20}Ni_{80}$/TiNT-C	-0.30	7.6	1.3	0.001	0.000
	-0.25	7.5	1.4	0.002	0.000
	-0.20	7.1	1.7	0.003	0.000
	-0.15	7.4	1.3	0.004	0.001
	-0.10	7.8	1.3	0.005	0.001
	-0.05	8.3	1.4	0.005	0.001
	0.00	8.3	1.4	0.006	0.001
	0.05	8.3	1.5	0.007	0.001
	0.10	9.8	1.1	0.005	0.001

4.2.4 Chronoamperometry

The electroactivity of the catalysts for BH_4^- oxidation can be further understood using chronoamperometry test [43]. Chronoamperometric curves were recorded by applying constant voltages. For each catalyst, these constant voltages were chosen as where current densities reached a peak on LSV curves as seen in **Figure 4.17**. These voltages were as follow for each catalyst, Au_{100}/TiNT-C at 0.15 V, $Au_{80}Ni_{20}$/TiNT-C at 0.04 V, $Au_{60}Ni_{40}$/TiNT-C at 0.08 V, $Au_{40}Ni_{60}$/TiNT-C at 0.07 V, and $Au_{20}Ni_{80}$/TiNT-C at 0.08 V with respect to a KCl saturated calomel electrode (SCE). In terms of chronoamperometric measurements, catalytic activities of developed Au-Ni cocatalysts can be seen on **Figure 4.23.** These measurements were recorded in 0.03 M $NaBH_4$ + 2 M NaOH solution, at ω = 0 rpm, 22 ºC, at the applied voltages mentioned before.

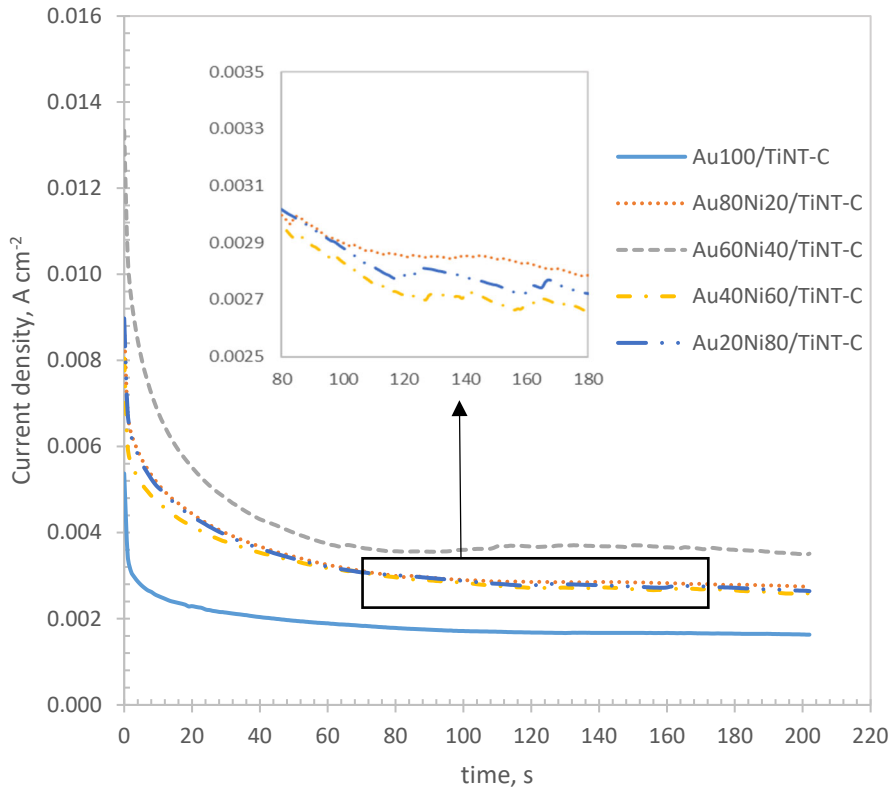

Figure 4.23: Chronoamperometry curves of borohydride ions oxidation on glassy carbon rotating disc electrode (RDE) coated with Au_{100}/TiNT-C, $Au_{80}Ni_{20}$/TiNT-C, $Au_{60}Ni_{40}$/TiNT-C, $Au_{40}Ni_{60}$/TiNT-C, and $Au_{20}Ni_{80}$/TiNT-C catalysts at 0.15 V, 0.04 V, 0.08 V, 0.07 V, and 0.08 V *vs.* SCE in 0.03 M $NaBH_4$ + 2 M NaOH solution, ω = 0 rpm, at 22 ºC.

Due to diffusion control, there is a rapid decrease in current density with time in all studied catalysts as it can be seen on **Figure 4.23**. Owing to the absence of stirring in the solution and no rotation of the rotating disc electrode (no stimulated convection), mass transport of borohydride to the electrode surface via convection was kept to a minimum and its effect on the current decrease was disregarded. Current density decrease rate over time is faster on Au_{100}/TiNT-C then all the other Au-Ni bimetallic catalysts. After 200 seconds, $Au_{60}Ni_{40}$/TiNT-C shows the highest current density (0.0035 A cm^{-2}), and Au_{100}/TiNT-C shows the lowest current densitity (0.0016 A cm^{-2}). $Au_{80}Ni_{20}$/TiNT-C, $Au_{40}Ni_{60}$/TiNT-C, and $Au_{20}Ni_{80}$/TiNT-C show a similar current density, ca. 0.0028 A cm^{-2}. Under the same conditions, the current density of all four Au-Ni/TiNT-C electrodes is superior to that of the Au_{100}/TiNT-C electrode. The Au-Ni/TiNT-C electrodes exhibit the highest current density, suggesting it may possess the greatest electrocatalytic activity.

Results obtained with chronoamperometry experiments can be used to calculate number of electrons exchanged, *n*, by means of Cottrell equation given by Eq. (4.11).

$$i = \frac{nFAC_b D^{\frac{1}{2}}}{\pi^{\frac{1}{2}} t^{\frac{1}{2}}} \quad (4.11)$$

Here, i is current density (A cm^{-2}), n is transferred electron number, F is Faraday constant (96485 C mol^{-1}), C_b is bulk concentration of borohydride (mol cm^{-3}), D is diffusion coefficient for borohydride ions (1.77×10^{-5} cm^2 s^{-1}), π is constant (3.14), and t is time (in second).

By plotting i versus $t^{-1/2}$ between 5 and 30 seconds, electrons of exchanged in borohydride oxidation reaction was calculated from the slope of the plot. **Figure 4.24** shows i - $t^{-1/2}$ plots of Au_{100}/TiNT-C, $Au_{80}Ni_{20}$/TiNT-C, $Au_{60}Ni_{40}$/TiNT-C, $Au_{40}Ni_{60}$/TiNT-C, and $Au_{20}Ni_{80}$/TiNT-C.

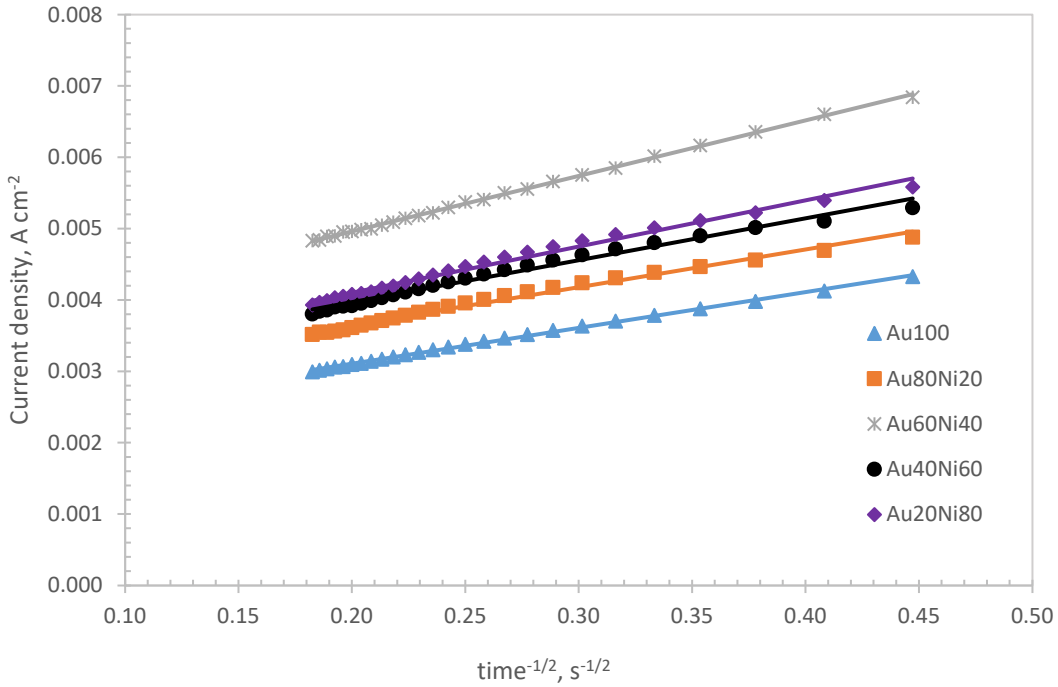

Figure 4.24: i – $t^{-1/2}$ plot of Au_{100}/TiNT-C, $Au_{80}Ni_{20}$/TiNT-C, $Au_{60}Ni_{40}$/TiNT-C, $Au_{40}Ni_{60}$/TiNT-C, and $Au_{20}Ni_{80}$/TiNT-C.

Number of electrons exchanged which calculated by means of Cottrell equation is shown in **Table 4.8**. Transferred electron numbers on Au_{100}/TiNT-C $Au_{80}Ni_{20}$/TiNT-C and $Au_{40}Ni_{60}$/TiNT-C close to the theoretical $8e^-$ value. This can be ascribed that there is not considerable hydrolysis takes place on electrode surface and borohydride ions mostly undergone the oxidation route. However, number of electrons exchanged are higher than theoretical $8e^-$ transfer on $Au_{60}Ni_{40}$/TiNT-C and $Au_{20}Ni_{80}$/TiNT-C. These unexpected results may result from two main reasons: first is experimental faults and second is complex oxidation route of borohydride ions with multiple electron transfer. To minimize experimental error,

experiments were repeated several times. However, results were similar tendency with the repeated experiment.

Table 4.8: Calculated transferred electron numbers by means of Cottrell equation

Catalyst	Potential, V	n	Standard deviation
Au_{100}/TiNT-C	0.15	7.3	0.3
$Au_{80}Ni_{20}$/TiNT-C	0.04	7.7	0.8
$Au_{60}Ni_{40}$/TiNT-C	0.08	11.3	2.2
$Au_{40}Ni_{60}$/TiNT-C	0.07	7.8	0.3
$Au_{20}Ni_{80}$/TiNT-C	0.08	9.4	0.5

Table 4.9 shows transferred electron number reported in the literature. He and co-workers, prepared different bimetallic catalyst alloyed with gold on carbon support, annotated as Au-Fe/C, Au-Co/C, Au-Ni/C, Au-Cu/C [43]. With the molar ratio between Au-Ni as seen in **Table 4.9**, transferred electron number was reported as to be 6.8. In another study, Duan and co-workers, reported the transferred electron numbers as 4.92, 5.79, 6.58, and 5.64 for the following catalysts: Au_{100}/C, $Ni_{33}Au_{67}$/C, $Ni_{50}Au_{50}$/C, and $Ni_{67}Au_{33}$/C, respectively. When these transferred electron numbers compared to the current study results of Au_{100}/TiNT-C, $Au_{80}Ni_{20}$/TiNT-C, $Au_{60}Ni_{40}$/TiNT-C, $Au_{40}Ni_{60}$/TiNT-C, and $Au_{20}Ni_{80}$/TiNT-C catalysts, it can be suggested that Au-Ni/TiNT-C catalysts have better catalytic activities towards oxidation of borohydride.

Table 4.9: reported transferred electron numbers by different catalysts reported in the literature.

Ref.	Catalyst	n
[43]	$Au_{58}Ni_{42}$/C	6.8
[85]	Au_{100}/C	4.92
	$Ni_{33}Au_{67}$/C	5.79
	$Ni_{50}Au_{50}$/C	6.58
	$Ni_{67}Au_{33}$/C	5.64
[86]	$Ni_{95}Ce_5$	1
	$Ni_{90}Ce_{10}$	1
[52]	1 g Ni pasted on 2×2.5 Ni foam	4

4.3 Conclusion

To the best knowledge of author, deposition of nickel and co-deposition of gold-nickel on titanate nanotubes by ion-exchange deposition-reduction method was carried out for the first time and tested for borohydride oxidation. Results revealed that maximum deposition of nickel and gold were found to be around 2.1 and 17.3 wt. %, respectively. Even though, nickel

deposition is limited at low percentage, it has a considerable improvement on electrocatalytic activity of the developed gold-nickel co-catalysts in borohydride oxidation. Due to low deposition of nickel on titanate nanotubes, total metal loading was kept at 4 wt. % to reach targeted atomic ratio of gold and nickel in bimetallic catalyst composition deposited on titanate nanotubes. These targeted atomic ratios for gold:nickel were as follow: 100:0, 80:20, 60:40, 40:60, and 20:80 for the catalysts Au_{100}/TiNT, $Au_{80}Ni_{20}$/TiNT, $Au_{60}Ni_{40}$/TiNT, $Au_{40}Ni_{60}$/TiNT, and $Au_{20}Ni_{80}$/TiNT, respectively. After addition of nafion and carbon black to the catalyst texture, total metal loading dropped to 2.51 wt. %.

Cyclic voltammograms of developed Au_{100}/TiNT-C and Au-Ni/TiNT-C co-catalysts show only one oxidation peak on forward scan related to direct oxidation of borohydride. On reverse scan, another oxidation peak was observed linked to the oxidation of adsorbed intermediates such as BH_3OH^-.

Linear sweep voltammetry characterisation of developed catalysts in borohydride oxidation revealed that developed Au-Ni/TiNT-C co-catalysts outperformed those of monometallic Au_{100}/TiNT-C performance. In terms of maximum current generation in borohydride oxidation, $Au_{80}Ni_{20}$/TiNT-C demonstrates superior performance among the Au-Ni/TiNT-C co-catalysts. When comparing the peak current performance of $Au_{80}Ni_{20}$/TiNT-C, $Au_{60}Ni_{40}$/TiNT-C, $Au_{40}Ni_{60}$/TiNT-C, and $Au_{20}Ni_{80}$/TiNT-C with that of Au_{100}/TiNT-C at 2000 rpm, the co-catalysts demonstrate improvements in percentage of 122.0, 111.3, 116.5, and 79.5, respectively. In other words, all co-catalysts exhibit a minimum 80 percent increase in catalytic activity. These improvements make nickel a preferable co-catalyst candidate with gold decorated on titanate nanotubes, reducing gold usage in catalyst texture while improving catalytic activities for borohydride oxidation.

Diffusion coefficient number, D, was calculated for Au rotating disc electrode as to be 1.77×10^{-5} cm^2 s^{-1}. Calculated diffusion coefficient number, D, for Au disc electrode and developed catalysts were compared. The results indicate that D values of developed catalysts for borohydride diffusion were smaller than those of calculated Au disc electrode.

The n and k values were calculated using different potential ranges for the Au disc electrode and other developed catalysts due to the appearance range of the mix-controlled region on LSV voltammograms. The transferred electron numbers for Au_{100}/TiNT-C showed a similar trend to those of the Au disc electrode, except for a difference in potential range. The transferred electron numbers for the developed co-catalysts, Au-Ni/TiNT-C, were found to be close to the

theoretical 8e- in the investigated voltage range at the mix-controlled region on LSV curves. For example, at -0.10 V, the calculated transferred electron numbers were 5.9, 7.9, 8.9, 7.6, and 7.8 for Au_{100}/TiNT-C, $Au_{80}Ni_{20}$/TiNT-C, $Au_{60}Ni_{40}$/TiNT-C, $Au_{40}Ni_{60}$/TiNT-C, and $Au_{20}Ni_{80}$/TiNT-C, respectively.

The calculated apparent rate constant values, k, show a comparable difference between monometallic Au_{100}/TiNT-C and Au-Ni/TiNT-C co-catalysts. For example, at 0 V, the calculated k values for Au_{100}/TiNT-C, $Au_{80}Ni_{20}$/TiNT-C, $Au_{60}Ni_{40}$/TiNT-C, $Au_{40}Ni_{60}$/TiNT-C, and $Au_{20}Ni_{80}$/TiNT-C were 0.003, 0.006, 0.009, 0.007, and 0.006 cm s^{-1}, respectively. These results indicate that the k values of the prepared co-catalysts are higher than that of Au_{100} /TiNT-C. This increase in apparent rate constant supports the idea that catalytic activities improve when nickel is used as a co-catalyst with gold decorated on titanate nanotubes.

Chronoamperometry results show that $Au_{60}Ni_{40}$/TiNT-C has better stability in borohydride oxidation test. Au_{100}/TiNT-C shows the lowest stability among the developed catalysts. The order of stability for all catalysts as follows: $Au_{60}Ni_{40}$/TiNT-C > $Au_{80}Ni_{20}$/TiNT-C > $Au_{20}Ni_{80}$/TiNT -C > $Au_{40}Ni_{60}$/TiNT-C > Au_{100}/TiNT-C.

Chapter 5: ELECTROCATALITIC OXIDATION OF BOROHYDRIDE BY GOLD-COBALT COMPOSITE CATALYSTS

5.1 Quantitative Analysis: Metal Deposition Determination

5.1.1 Cobalt Deposition on Titanate Nanotubes

First, for cobalt deposition on titanate nanotubes, 9 different standard solution of triethylenediamine cobalt (II) nitrate $[Co(en)_3](NO_3)_2$ were prepared to measure absorbance of these solution and plot calibration curve. In **Figure 5.1**, light absorbance tendency of these standard solution can be seen between 190 and 700 nm wavelength. The light absorbance of $[Co(en)_3](NO_3)_2$ solutions reach a peak at around 355 nm, and these peak absorbance values were used to generate calibration curve as shown in **Figure 5.2**. From this calibration curve, extinction-coefficient found to be 2079 L cm^{-1} mol^{-1} for cobalt solution. This enables to detect even the smaller concentration changes in determination of cobalt adsorption process.

Second, 7 different deposition experiments were carried out to determine cobalt deposition on titanate nanotubes as shown in **Table 5.1**. These experiments were conducted using solution with 25 mL volume and 0.5 g titanate nanotubes in each solution. By knowing volume of the solution, added titanate nanotubes mass, initial and remaining metal concentration after deposition takes place, the relative amount of deposited metal complex, *a*, adsorbed cobalt

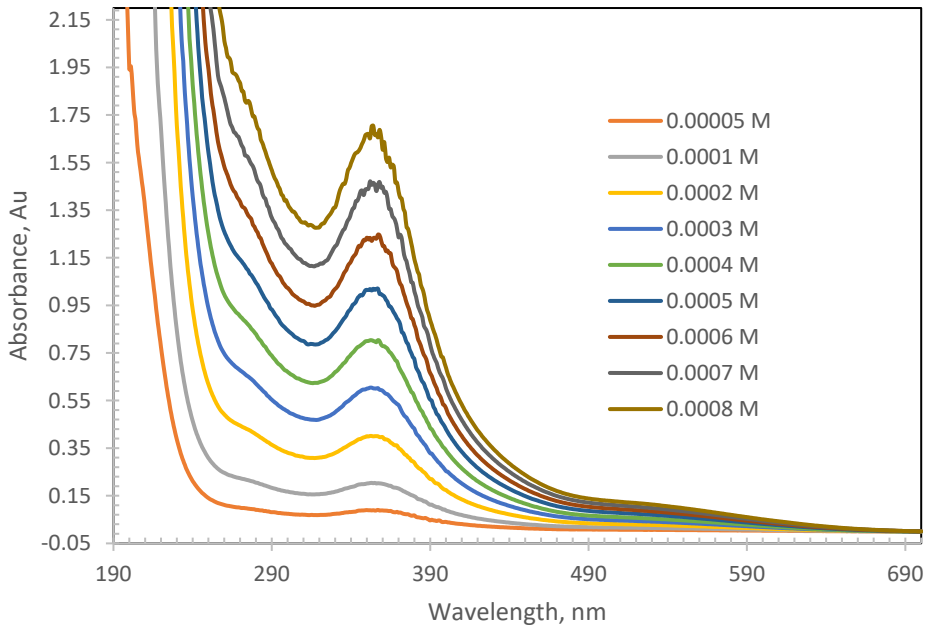

Figure 5.1: Absorbance spectrum of triethylenediamine cobalt (II) nitrate $[Co(en)_3](NO_3)_2$ solutions measured at 22 °C

mass and weight percentages can be calculated. The relative amount of deposited metal complex *a* [mol(M)×mol $(TiO_2)^{-1}$] can be determined by the following formula:

$$a = \frac{80 \times (C_0 - C^*) \times V}{m} \quad (5.1)$$

Here m is mass of added TiO_2 nanotubes powder. Calculating *a* value can be beneficial to understand how many mol metal can be adsorbed by per mol of titanate nanotubes powder from the solution. Considering **Table 5.1** and **Figure 5.3**, it can be clearly seen that $[Co(en)_3]^{2+}_{(aq)}$ cations adsorbed on titanate nanotubes almost entirely at lower concentration than 8 mmol L^{-1}. As illustrated on **Figure 5.3**, increase of adsorbed $[Co(en)_3]^{2+}_{(aq)}$ is slows down after 8 mmol L^{-1}. Calculated weight percentage of adsorbed cobalt at 32 mmol L^{-1} is 3.65. All the data collected from colorimetric measurements is included in **Table 5.1**.

Adsorbed cobalt mass can be calculated using with Eq. ((5.2).

$$m\,(cobalt) = (C_0 - C^*) \times MW(cobalt) \times V \quad (5.2)$$

Here *m* is mass of adsorbed cobalt, and *MW* is molecular weight of the cobalt, C_o initial and C^* remaining concentrations, and V is the volume of the solution where adsorption take place. Considering the added titanate nanotubes powder mass in the studied solution, it allows us to determine weight percentage of the metal adsorbed on titanate nanotubes powder added to the solution. This can be calculated with the formula as shown below:

$$adsorbed\ metal\ wt.\% = \frac{m\,(metal)}{m\,(metal) + m(TiNT)} \times 100 \quad (5.3)$$

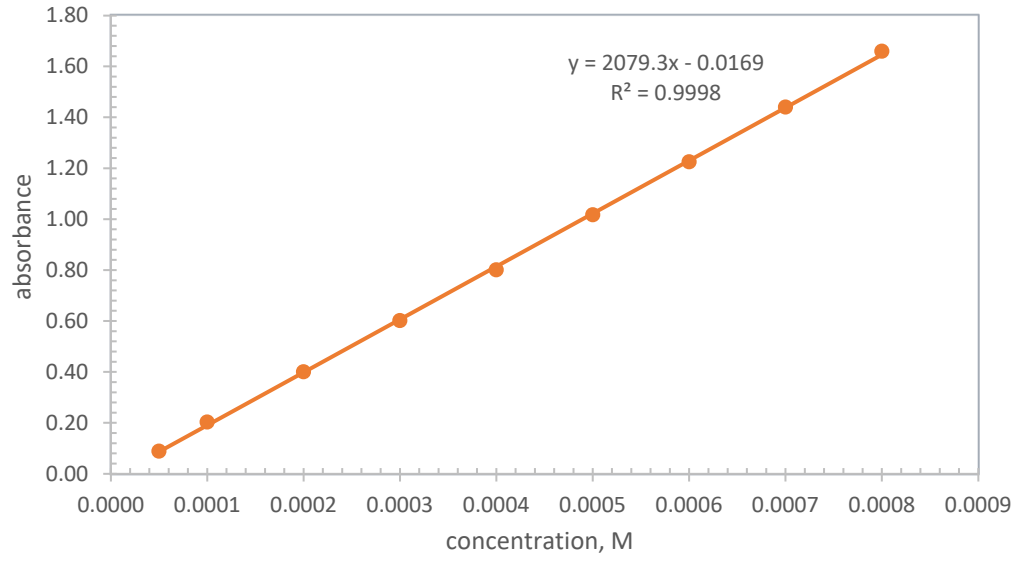

Figure 5.2: Calibration curve obtained at 355 nm for triethylenediamine cobalt (II) nitrate $[Co(en)_3](NO_3)_2$ solutions.

Table 5.1: Initial and remaining concentration of $[Co(en)_3]^{2+}$ ions with the data calculated based on these two measurements.

Initial $[Co(en)_3]^{2+}_{(aq)}$ concentration, mmol L^{-1}, C_o	Remaining $[Co(en)_3]^{2+}_{(aq)}$ concentration, mmol L^{-1}, C^*	Ion-exchange molar ratio / mol (Co) mol^{-1} (TiNT), a	wt. %
2	0.02	0.008	0.58
4	0.04	0.016	1.15
6	0.01	0.024	1.73
8	0.03	0.032	2.29
12	2.53	0.038	2.71
16	5.73	0.041	2.92
32	19.20	0.051	3.65

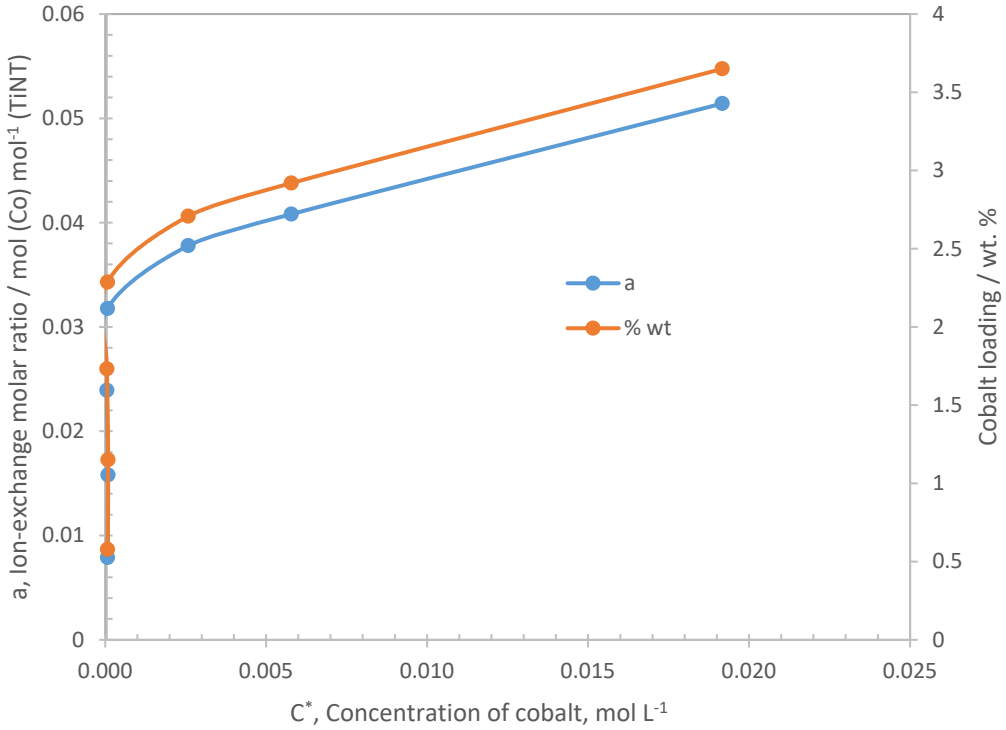

Figure 5.3: Isotherm of $[Co(en)_3]^{2+}_{(aq)}$ cation adsorption on titanate nanotubes in water suspension at 20 °C (±1 °C) and responding wt. % cobalt loading.

When Adsorption of gold, nickel, and cobalt on titanate nanotubes are compared at 32 mmol L^{-1}, gold has better adsorption with 15.15 wt. % while nickel has 1.66 wt. % and cobalt has 3.65 wt. %. At this concentration cobalt shows better adsorption capability than nickel.

5.1.2 Co-deposition of Gold-cobalt (Au-Co)

To calculate weight percentage of adsorbed cobalt, a value provided by Eq. (3.1) were converted into g (metal) g^{-1} (TiO2) as expressed with Eq. (4.3):

$$a\,[g\ (metal)\ g^{-1}\ (TiO_2)] = a \times \frac{MW_{metal}}{MW_{TiO_2}} \tag{5.4}$$

After converting 'a' value into g (metal) g^{-1} (TiO2) for all the studied concentrations, weight percentage of adsorbed metal were calculated by Eq. (4.4):

$$wt.\% = \frac{g_{metal}}{g_{TiO_2} + g_{metal}} \times 100 \tag{5.5}$$

Exploiting initial concentration versus weight percentage of adsorbed metal, the correlation between adsorbed metal percentage and its required initial concentration to reach this percentage were provided as function of natural logarithm as seen in and **Figure 4.9** for gold and **Figure 5.4** for cobalt. Intended a final 4 wt. % catalyst loadings were determined with different molar ratios of metals on titanate nanotubes surface. In **Table 5.2**, required metal weight percentages for the intended molar ratio of gold:cobalt was provided. To obtain the weight percentage of each metal shown in **Table 5.2**, required amount of metal solutions were determined by using functions provided in **Figure 4.9** and **Figure 5.4**. For instance, to get a Au:Co weight percentages ratio of (3.72):(0.28) out of 4 wt. % catalyst loading on 1 g TiNTs, which corresponds a 80:20 Au:Ni molar ratio, it was calculated that 1.89 mL of $HAuCI_4$ solution from its 0.1 M stock solution and 0.81 mL of $Co(NO_3)_2$ from its 0.1 M stock solution are required.

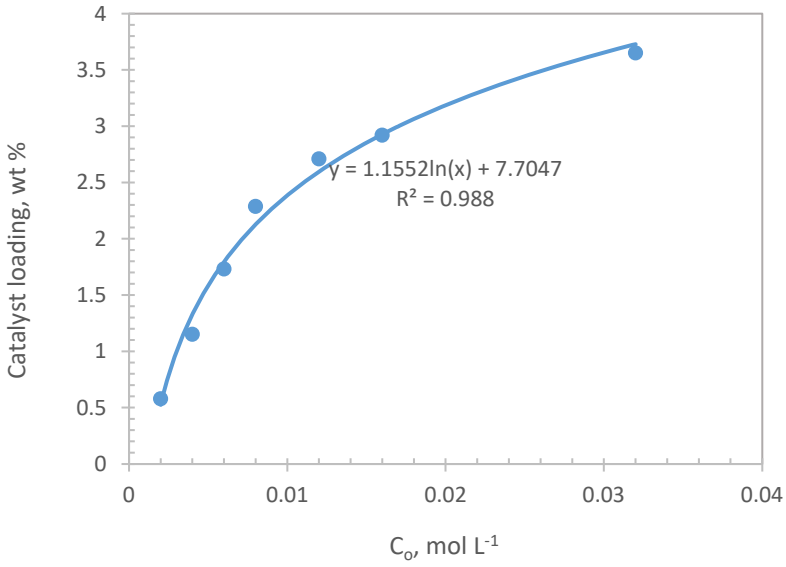

Figure 5.4: Correlation of Catalyst loading (wt. %)-initial concentration of $Co(en)_3]^{2+}{}_{(aq)}$

Table 5.2: Calculated molar ratios between gold and cobalt with a total catalyst loading on TiNT

	Molar ratio of Au:Co, %		Weight to weight percentage of Au:Co, wt. %		
Catalyst	Au	Co	Au	Co	Total
Au_{100}/TiNT	100	0	4	0	4
$Au_{80}Co_{20}$/TiNT	80	20	3.72	0.28	4
$Au_{60}Co_{40}$/TiNT	60	40	3.33	0.67	4
$Au_{40}Co_{60}$/TiNT	40	60	2.75	1.25	4
$Au_{20}Co_{80}$/TiNT	20	80	1.80	2.20	4

5.2 Electrochemical Measurements

Cyclic voltammetry (CV), linear sweep voltammetry (LSV), and chronoamperometry (CA) were used to evaluate electrocatalytic activities of developed catalysts in reaction of borohydride oxidation.

5.2.1 Cyclic Voltammetry

Cyclic voltammogram of Au_{100}/TiNT-C and $Au_{40}Co_{60}$/TiNT-C can be seen in **Figure 5.5** and **Figure 5.6**, respectively. When the voltammograms of Au_{100}/TiNT-C and $Au_{40}Co_{60}$/TiNT-C are examined, a similar distinctive broad oxidation peak (a_2) can be seen on the forward scan with those of $Au_{40}Ni_{60}$/TiNT-C. These peaks formed at around +0.10 V for Au_{100}/TiNT-C and -0.15 V for $Au_{40}Co_{60}$/TiNT-C, shifting 0.25 V to more negative potentials which makes $Au_{40}Co_{60}$/TiNT-C preferable over Au_{100}/TiNT-C for direct oxidation of borohydride. Appearance place of these peaks on CV curves are mainly attributed to direct oxidation of borohydride as shown in Eq. (4.7) [16], [78]. In terms of peak current density, Au_{100}/TiNT-C and $Au_{40}Co_{60}$/TiNT-C show a similar value, 5.8 and 6.2 mA cm^{-2}, respectively. The is only 6 % improvement in the favour of $Au_{40}Co_{60}$/TiNT-C.

Another important distinguishing feature on these two figures is that current increase on $Au_{40}Co_{60}$/TiNT-C catalyst starts at around -0.7 V which is 0.20 V more negative potential than those of Au_{100}/TiNT-C catalyst. This shows that combining gold with cobalt improve catalytic activities of the developed catalysts. The other CV curves which obtained for $Au_{80}Co_{20}$/TiNT-C, $Au_{60}Co_{40}$/TiNT-C, $Au_{20}Co_{80}$/TiNT-C were provided in **Appendix B**.

$$BH_4^- + 8OH^- \rightarrow BO_2^- + 6H_2O + 8e^- \quad E^0_{anode} = -1.24\,V\ vs.\,SHE \tag{5.6}$$

.

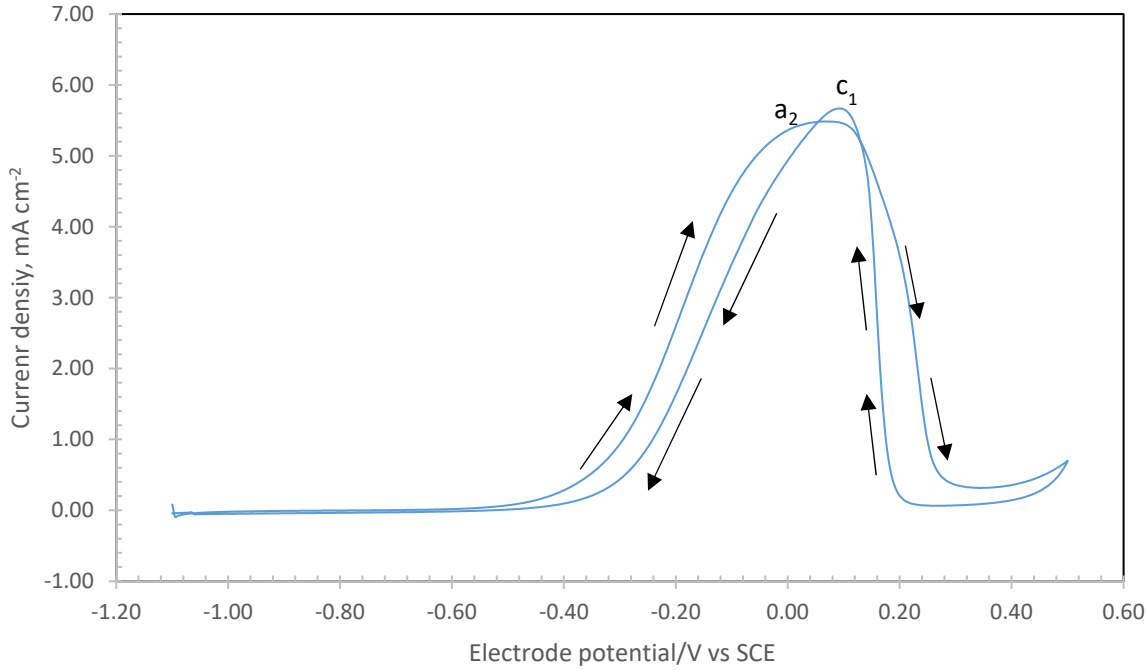

Figure 5.5: CV curve of Au_{100}/TiNT-C electrode. Counter electrode: Pt; electrolyte: 0.03 M $NaBH_4$ + 2 M NaOH; scan rate:10 mV s^{-1}; disc rotation 400 rpm; at ambient temperature (20 °C ±1)

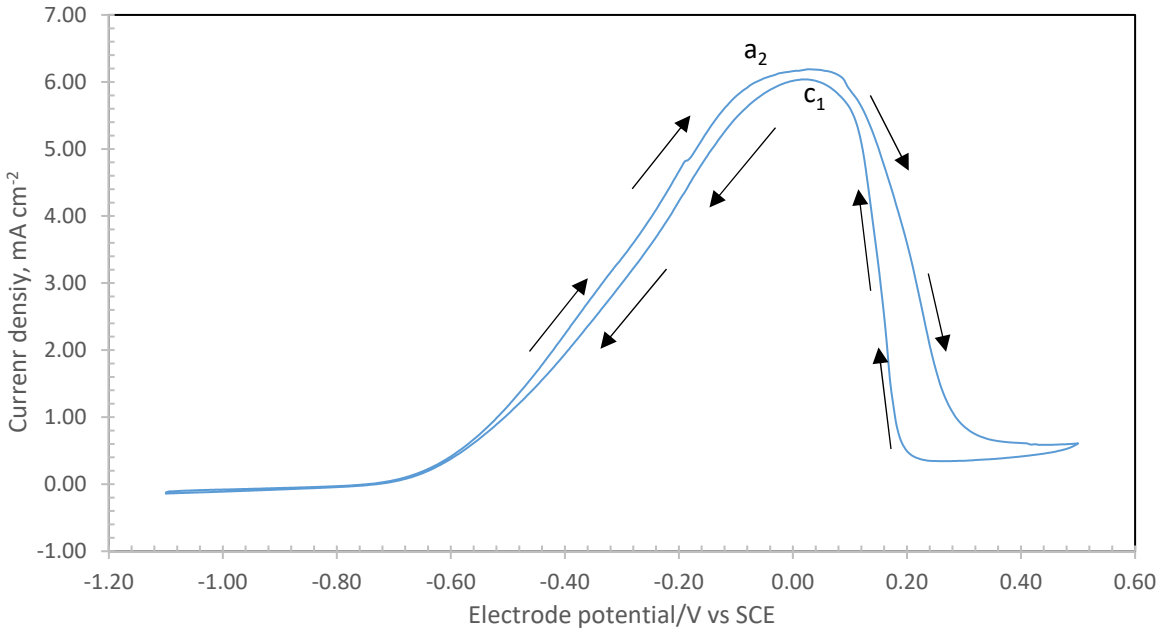

Figure 5.6: CV curve of $Au_{40}Co_{60}$/TiNT-C electrode. Counter electrode: Pt; electrolyte: 0.03 M $NaBH_4$ + 2 M NaOH; scan rate:10 mV s^{-1}; disc rotation 400 rpm; at ambient temperature (20 °C ±1)

5.2.2 Linear Sweep Voltammetry

At five different rotation rates, the polarization curves of Au_{100}/TiNT-C catalyst coated glassy carbon disc electrodes are displayed in **Figure 5.7**. Comparing this figure to the linear sweep voltammograms of the Au rotating disc electrode presented in **Figure 4.14** reveals a comparable trend in terms of where peak currents appear on the voltammograms. Possibly due to a lower gold loading, the oxidation reaction initiates at a voltage slightly more positive on Au_{100}/TiNT-C (around -0.5 V).

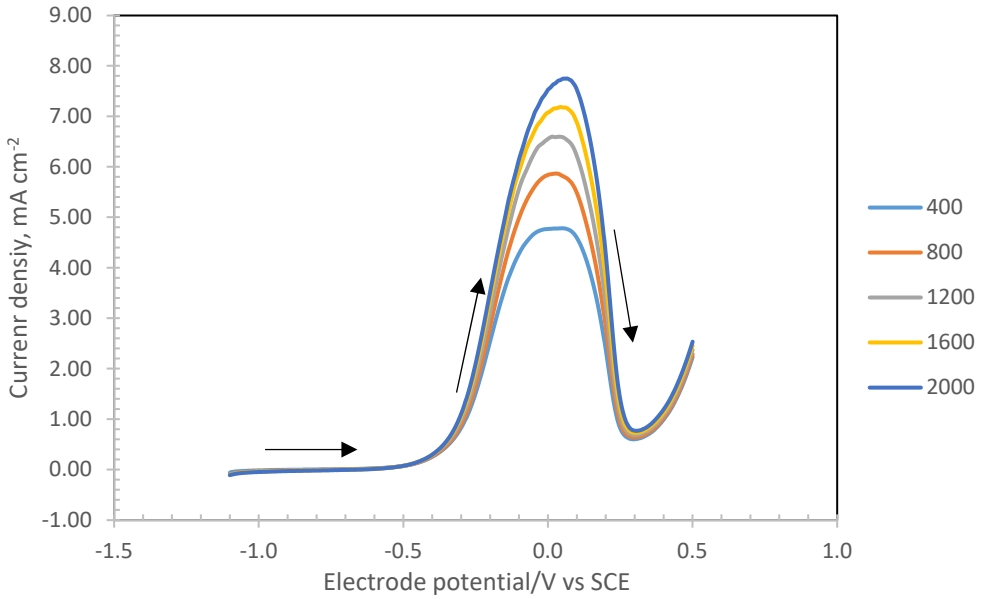

Figure 5.7: Linear sweep voltammograms (LSV) of Au_{100}/TiNT-C coated glassy carbon disc electrode at different rotation rates. Counter electrode: Pt; electrolyte: 0.03 M $NaBH_4$ + 2 M NaOH; scan rate:10 mV s^{-1}; at 20 °C (±1 °C)

Nevertheless, the start of borohydride oxidation occurs at approximately -0.7 V when gold is combined with cobalt, which corresponds to more negative the potential then of gold rotating disc electrode. **Figure 5.8**, which was acquired for an $Au_{40}Co_{60}$/TiNT-C coated on glassy carbon disc electrode, illustrates this alteration clearly. This could be interpreted as the catalytic improvement resulted from combining gold with cobalt.

Comparison of peak current densities obtained of Au_{100}/TiNT-C, $Au_{80}Co_{20}$/TiNT-C, $Au_{60}Co_{40}$/TiNT-C, $Au_{40}Co_{60}$/TiNT-C, and $Au_{20}Co_{80}$/TiNT-C at 2000 rpm is shown in **Figure 5.9**. This comparison shows that there is limited improvement in peak current densities. For instance, $Au_{80}Co_{20}$/TiNT-C shows 18.6 % higher peak current density compared to Au_{100}/TiNT-C. Au_{100}/TiNT-C, $Au_{60}Co_{40}$/TiNT-C, and $Au_{40}Co_{60}$/TiNT-C show similar peak current densities. $Au_{20}Co_{80}$/TiNT-C has the lowest peak current density being 6.72 mA cm^{-2}. However, when gold contend reduced and cobalt content increased in the developed catalysts,

current density increase starts at more negative potential. Especially, $Au_{40}Co_{60}$/TiNT-C and $Au_{20}Co_{80}$/TiNT-C curves on **Figure 5.9** show this shift clearly. **Table 5.3** illustrates catalyst loading and percentages with resulting current densities. LSV of $Au_{80}Co_{20}$/TiNT-C, $Au_{60}Co_{40}$/TiNT-C, and $Au_{20}Co_{80}$/TiNT-C can be found in **Appendix B**.

Table 5.3: Maximum current densities at 2000 rpm and Au mass-based current density comparison of developed Au_{100}/TiNT-C and Au-Co/TiNT-C catalysts.

Catalyst	Weight percentage of Au (wt. % Au)	Au loading mg cm^{-2}	Weight percentage of Co (wt. % Co)	Co loading mg cm^{-2}	Max. current density at 2000 rpm, mA cm^{-2}	Au mass based current density mA mg^{-1}
Au_{100}/TiNT-C	2.51	0.051	0	0.00	7.72	154.71
$Au_{80}Co_{20}$/TiNT-C	2.33	0.047	0.18	0.004	9.36	199.15
$Au_{60}Co_{40}$/TiNT-C	2.09	0.042	0.42	0.009	7.50	178.57
$Au_{40}Co_{60}$/TiNT-C	1.72	0.035	0.79	0.016	7.89	225.43
$Au_{20}Co_{80}$/TiNT-C	1.13	0.023	1.38	0.028	6.72	292.17

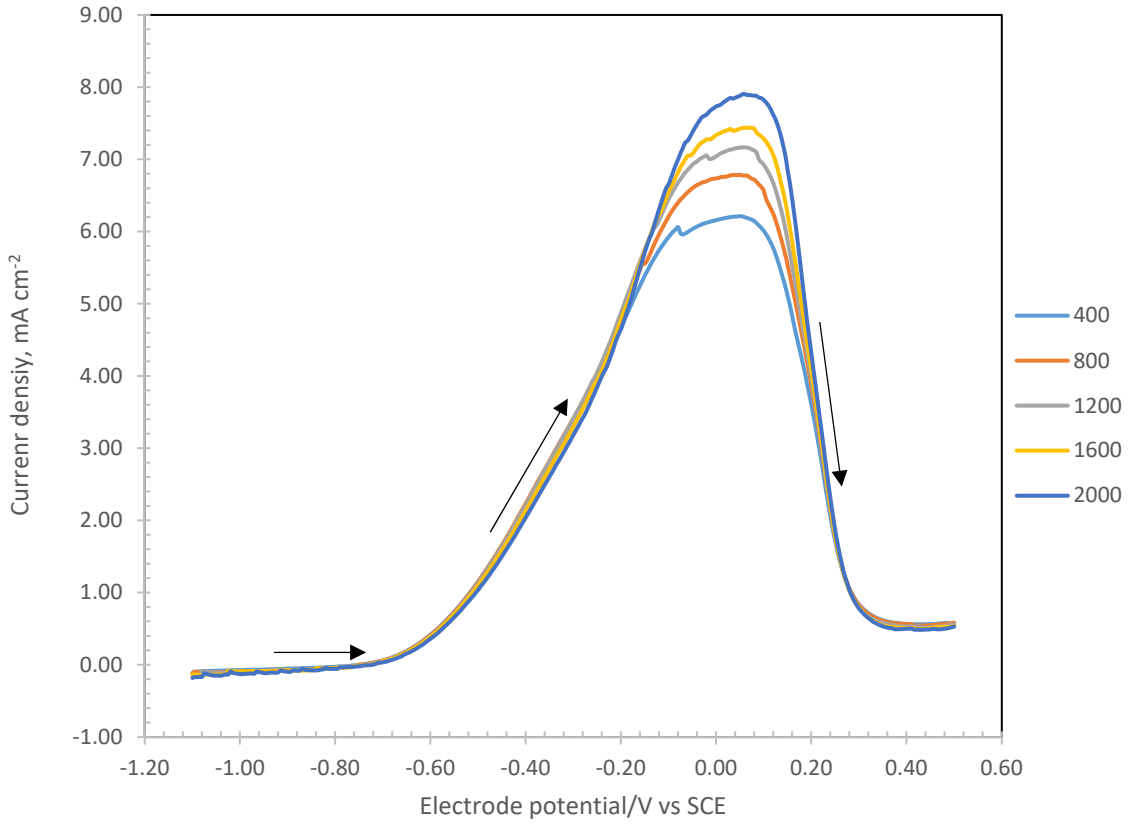

Figure 5.8: Linear sweep voltammograms of $Au_{40}Co_{60}$/TNT-C coated glassy carbon disc electrode at different rotation rates. Counter electrode: Pt; electrolyte: 0.03 M $NaBH_4$ + 2 M NaOH; scan rate:10 mV s^{-1}; at 20 °C (±1 °C)

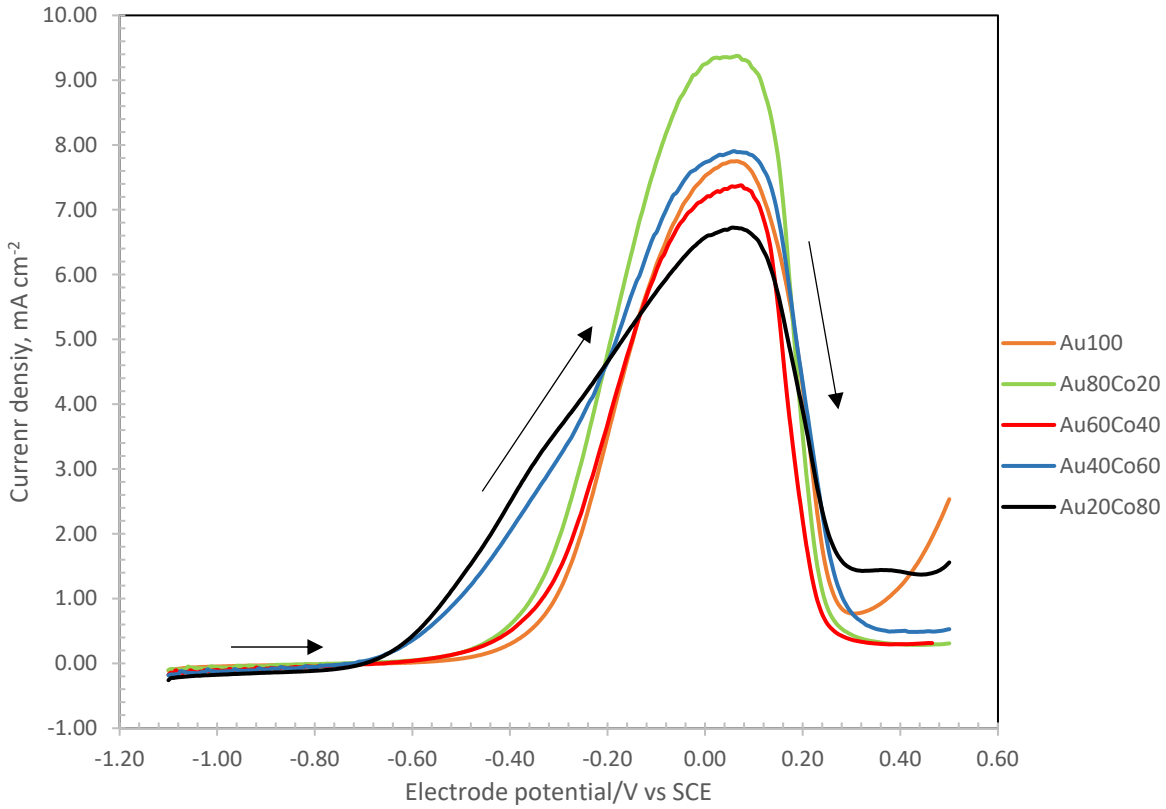

Figure 5.9: Comparison of linear sweep voltammogram peak current densities measured for Au_{100}/TiNT-C, $Au_{80}Co_{20}$/TiNT-C, $Au_{60}Co_{40}$/TiNT-C, $Au_{40}Co_{60}$/TiNT-C, and $Au_{20}Co_{80}$/TiNT-C at 2000 rpm. Counter electrode: Pt; electrolyte: 0.03 M $NaBH_4$ + 2 M NaOH; scan rate:10 mV s^{-1}; at 20 ºC (±1 ºC)

5.2.3 Determination of D, *k*, and *n*

The Levich equation given by Eq.(5.7) was utilized in determination of diffusion coefficient, D, for developed gold-cobalt catalyst in borohydride oxidation at the limiting current potential of 0.05 V.[30].

$$I_L = -0.62nFAD^{\frac{2}{3}}C_b v^{-\frac{1}{6}}\omega^{1/2} \quad (5.7)$$

Where, I_L is limiting current (A cm^{-2}), n is transferred electron number (n was assumed to be 8), A is geometric area of working electrode (cm^2), F is Faraday constant (96485 C mol^{-1}), D is diffusion coefficient of the electro active species (cm^2 s^{-1}), C_b is bulk concentration of borohydride (mol cm^{-3}), v is kinematic viscosity of the solution (cm^2 s^{-1}), and ω is the angular velocity of the rotating disc (radians s^{-1}). **Figure 5.10** illustrates Levich plot of $Au_{40}Co_{60}$/TiNT-C used to calculate diffusion coefficient, D. In the case of developed Au_{100}/TiNT-C and gold-cobalt bimetallic catalysts (Au-Co/TiNT-C), calculated D values were smaller than those of Au disc electrode. This could be due to rough surface of working electrode which composed of catalyst coated glassy carbon disc electrode.

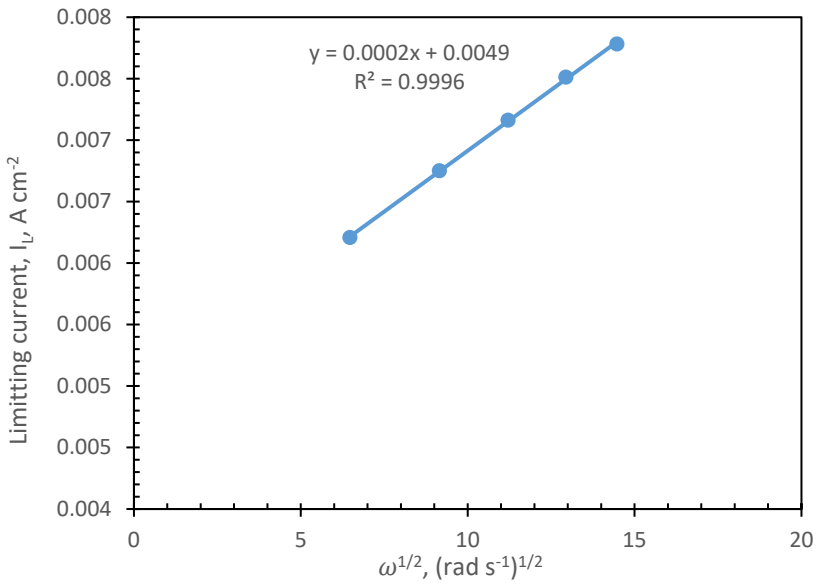

Figure 5.10: Levich plot of $Au_{40}Co_{60}$/TiNT-C generated at a limiting current measured at 0.05 V *vs* SCE and based on five different rotation speed, 400, 800, 1200, 1600, and 2000 rpm. Counter electrode: Pt; electrolyte: 0.03 M $NaBH_4$ + 2 M NaOH; scan rate:10 mV s^{-1}; at 20 °C (±1 °C)

The Koutecky-Levich equation, Eq. (5.8)[32], was employed to determine both the transferred electron number, n, and the apparent rate constant, k.

$$\frac{1}{j} = \frac{1}{nFkC_b} + \frac{1}{0.62nFD^{2/3}C_b v^{-1/6}\omega^{1/2}} \quad (5.8)$$

Where, j is disc current density (A cm^{-2}), and k is apparent rate constant (cm s^{-1}). D was calculated as 1.77×10^{-5} cm^2 s^{-1}, and v was obtained from literature to be as 0.0126 cm^2 s^{-1}, respectively [82], According to the Eq. (5.8), plot of j^{-1} values versus $\omega^{-1/2}$ should show linearity for the data are selected in mix-controlled region (mass transport controlled + kinetically controlled) on linear sweep voltammograms. **Figure 5.11** shows Koutecky-Levich plot of $Au_{40}Co_{60}$/TiNT-C used in determination of k and n. Koutecky-Levich plot of $Au_{80}Co_{20}$/TiNT-C, $Au_{60}Co_{40}$/TiNT-C, and $Au_{20}Co_{80}$/TiNT-C can be found in **Appendix B**.

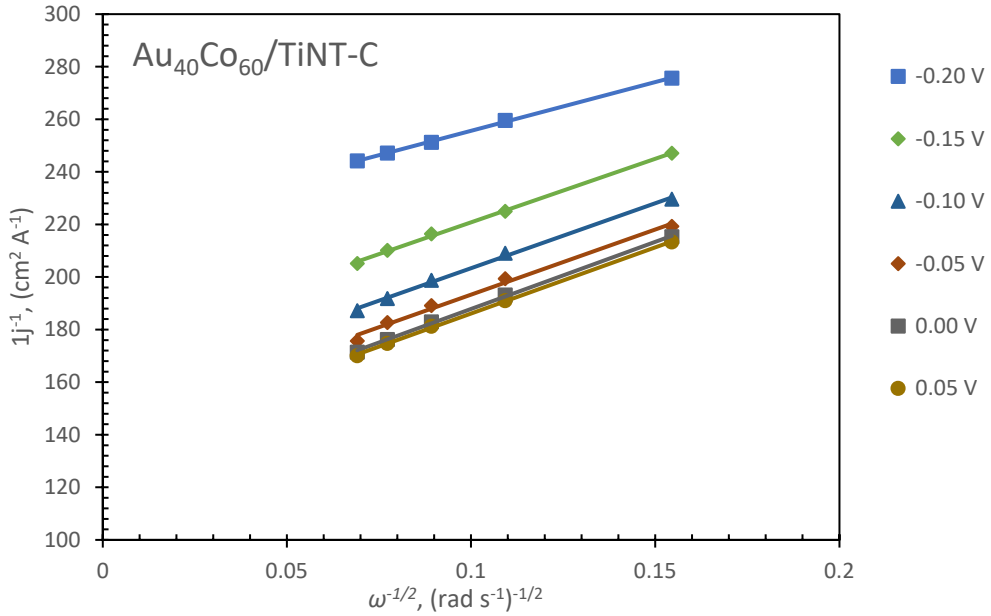

Figure 5.11: Koutecky-Levich plot of $Au_{40}Co_{60}$/TiNT-C between -0.20 V and 010 V, Counter electrode: Pt; electrolyte: 0.03 M $NaBH_4$ + 2 M NaOH; scan rate: 10 mV s^{-1}; at 20 ºC (±1 ºC)

In theory, transferred electron numbers must be in a range between 0 and 8e^- per BH_4^- ion according to Eq. (5.8).

$$BH_4^- + xOH^- \rightarrow BO_2^- + (x-2)H_2O + (4-(0.5)x)H_2 + xe^- \quad (5.9)$$

Table 5.4 shows calculated exchanged number of electrons, n, and apparent rate constant, k in different potentials range for Au disc electrode, Au_{100}/TiNT-C, $Au_{80}Co_{20}$/TiNT-C, $Au_{60}Co_{40}$/TiNT-C, $Au_{40}Co_{60}$/TiNT-C, and $Au_{20}Co_{80}$/TiNT-C. Different potential range was selected to calculate n and k values due to appearance range of mix-controlled region on LSV voltammograms for Au disc electrode and other developed catalysts differ from each other. Regarding the developed composite catalysts, Au-Co/TiNT-C, transferred electron numbers appear to be smaller or larger than theoretical 8e^- in the investigated voltage range. This may result from side reactions, e.g. oxygen evolution, and blockage of electrode surface by adsorbed intermediates, such as BH_3 or B_2H_6, which cause superimposed oxidation currents [30], [31]. Transferred electron numbers, n, at -0.10 V are calculated to be 6.9, 5.7, 8.9, and 5.5 for $Au_{80}Co_{20}$/TiNT-C, $Au_{60}Co_{40}$/TiNT-C, $Au_{40}Co_{60}$/TiNT-C, and $Au_{20}Co_{80}$/TiNT-C, respectively. In terms of faradic efficiency, $Au_{80}Co_{20}$/TiNT-C and $Au_{40}Co_{60}$/TiNT-C show better performance than $Au_{60}Co_{40}$/TiNT-C and $Au_{20}Co_{80}$/TiNT-C.

In terms of calculated apparent rate constant values, k, there is a comparable difference between monometallic Au_{100}/TiNT-C and bimetallic Au_aCo_b/TiNT-C catalysts. For instance, calculated k values were 0.003, 0.006, 0.007, 0.003, and 0.002 cm s^{-1}, at 0 V for Au_{100}/TiNT-C, $Au_{80}Co_{20}$/TiNT-C, $Au_{60}Co_{40}$/TiNT-C, $Au_{40}Co_{60}$/TiNT-C, and $Au_{20}Co_{80}$/TiNT-C, respectively. These results demonstrate that $Au_{60}Co_{40}$/TiNT-C and $Au_{40}Co_{60}$/TiNT-C have highest k values provided **Table 5.3**. In other words, the highest maximum current density belongs to the catalyst which has the highest k value. These results confirm that combining gold with cobalt improves reaction kinetics towards borohydride oxidation.

Table 5.4: Calculated number of electrons exchanged, n, and apparent kinetic rate constant, k at different voltage range.

Catalyst	Potential, V	n	Standard deviation	k (cm s^{-1})	Standard deviation
Au disc electrode	-0.40	4.4	0.2	0.012	0.005
	-0.38	5.5	0.1	0.011	0.005
	-0.36	7.3	0.1	0.010	0.006
	-0.34	7.8	0.1	0.011	0.005
	-0.32	7.9	0.2	0.014	0.005
	-0.30	8.0	0.2	0.018	0.001
Au_{100}/TiNT-C	-0.20	3.6	0.4	0.003	0.001
	-0.15	4.8	0.7	0.003	0.001
	-0.10	5.9	1.0	0.003	0.002
	-0.05	6.9	1.2	0.003	0.001
	0.00	7.6	1.4	0.003	0.001
	0.05	7.8	1.4	0.003	0.001
$Au_{80}Co_{20}$/TiNT-C	-0.20	7.1	1.0	0.003	0.0000
	-0.15	7.9	1.0	0.003	0.0003
	-0.10	8.0	0.8	0.004	0.0004
	-0.05	8.1	1.0	0.005	0.0004
	0.00	7.6	0.9	0.006	0.0004
	0.05	7.6	1.0	0.006	0.0005
$Au_{60}Co_{40}$/TiNT-C	-0.20	6.1	0.1	0.003	0.0004
	-0.15	6.4	0.3	0.004	0.0001
	-0.10	6.5	0.6	0.004	0.0003
	-0.05	5.9	0.5	0.005	0.0002
	0.00	5.7	0.4	0.006	0.0000
	0.05	5.7	0.4	0.006	0.0000
$Au_{40}Co_{60}$/TiNT-C	-0.20	10.5	0.2	0.001	0.0004
	-0.15	8.1	0.7	0.002	0.0004
	-0.10	7.9	0.9	0.002	0.0004
	-0.05	7.9	0.8	0.002	0.0003
	0.00	7.7	0.8	0.003	0.0005
	0.05	7.8	0.7	0.003	0.0006
$Au_{20}Co_{80}$/TiNT-C	-0.20	6.0	1.3	0.003	0.0007
	-0.15	5.9	1.6	0.004	0.0008
	-0.10	6.2	2.2	0.004	0.0009
	-0.05	6.8	01.9	0.004	0.0009
	0.00	7.3	1.5	0.004	0.0010
	0.05	7.6	1.4	0.004	0.0011

5.2.4 Chronoamperometry

The electrocatalytic activity and stability of electrocatalyst can be effectively evaluated using the Chronoamperometry technique [43], [87]. Due to these reasons, developed Au-Co/TiNT-C catalysts were evaluated by chronoamperometry test. Chronoamperometry curves were obtained applying constant voltage and monitoring current versus time. Applied constant voltage was 0.05 V *vs* SCE for all Au-Co/TiNT-C catalysts. Recorded CA curves can be seen in **Figure 5.12**. From this figure, it can be understood that $Au_{60}Co_{40}$/TiNT-C, and $Au_{40}Co_{60}$/TiNT-C shows similar catalytic activity and stability after 200 seconds observation period. It is also clear that these two catalysts outperform those of Au_{100}/TiNT-C, $Au_{80}Co_{20}$/TiNT-C, and $Au_{20}Co_{80}$/TiNT-C. The last three catalysts aforementioned here follow similar tendency in terms of current density drop over time on CV curve.

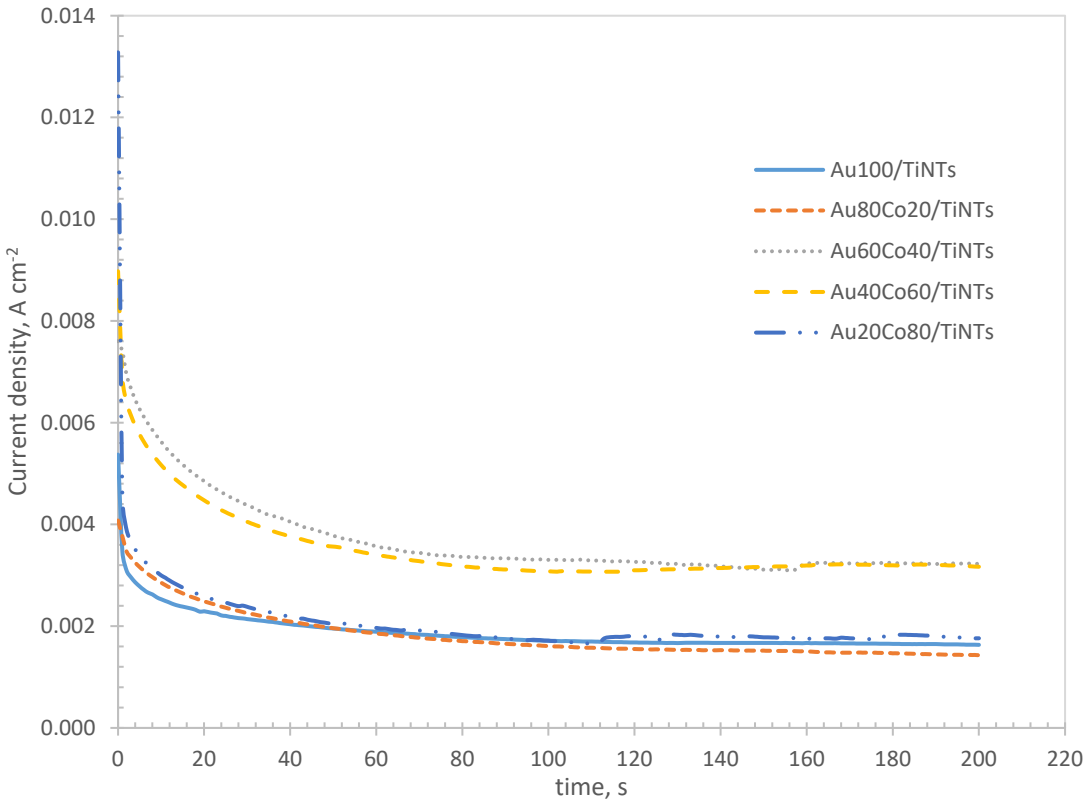

Figure 5.12: Chronoamperometry curves of borohydride ions oxidation on glassy carbon rotating disc electrode (RDE) coated with Au_{100}/TiNT-C, $Au_{80}Co_{20}$/TiNT, $Au_{60}Co_{40}$/TiNT-C, $Au_{40}Co_{60}$/TiNT-C, and $Au_{20}Co_{80}$/TiNT-C catalysts in 0.03 M $NaBH_4$ + 2 M NaOH solution, ω = 0 rpm, at 22 ºC.

After 200 seconds, current density generation of studied catalysts were as follow: 1.6, 1.4, 3.2, 3.1, and 1.7 mA cm^{-2} for Au_{100}/TiNT-C, $Au_{80}Co_{20}$/TiNT-C, $Au_{60}Co_{40}$/TiNT-C, $Au_{40}Co_{60}$/TiNT-C, and $Au_{20}Co_{80}$/TiNT-C, respectively.

Using Cottrell equation given by Eq. (5.10), transferred electron number, n, was calculated for the developed Au-Co/TiNT-C catalyst for borohydride oxidation. To do this, $i - t^{-1/2}$ plot of Au_{100}/TiNT-C, $Au_{80}Co_{20}$/TiNT-C, $Au_{60}Co_{40}$/TiNT-C, $Au_{40}Co_{60}$/TiNT-C, and $Au_{20}Co_{80}$/TiNT-C were plotted as shown in **Figure 5.13**. After then, n values were calculated using slope of these plots. These calculated n values are represented in **Table 5.5**.

$$i = \frac{nFAC_b D^{\frac{1}{2}}}{\pi^{\frac{1}{2}} t^{\frac{1}{2}}} \tag{5.10}$$

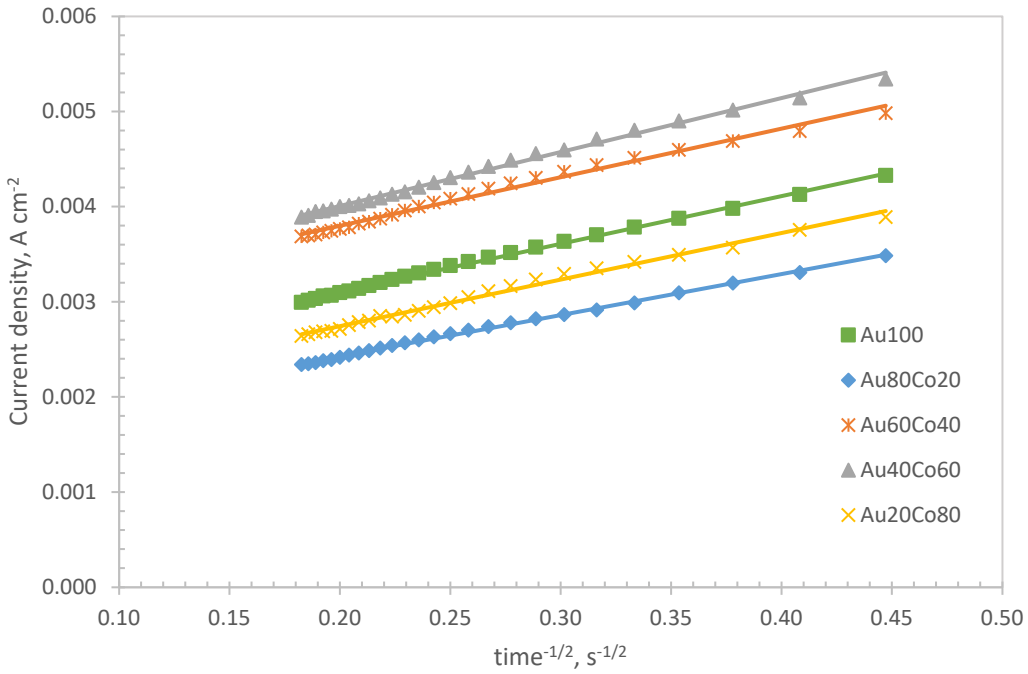

Figure 5.13: $i - t^{-1/2}$ plot of Au_{100}/TiNT-C, $Au_{80}Co_{20}$/TiNT-C, $Au_{60}Co_{40}$/TiNT-C, $Au_{40}Co_{60}$/TiNT-C, and $Au_{20}Co_{80}$/TiNT-C

Table 5.5: Calculated transferred electron numbers by means of Cottrell equation

Catalyst	Potential, V	n	Standard deviation
Au_{100}/TiNT-C	0.15	7.3	0.3
$Au_{80}Co_{20}$/TiNT-C	0.05	6.2	0.5
$Au_{60}Co_{40}$/TiNT-C	0.05	7.4	0.7
$Au_{40}Co_{60}$/TiNT-C	0.05	8.3	1.3
$Au_{40}Co_{60}$/TiNT-C	0.05	7.1	0.8

5.3 Conclusion

For the first time, the ion-exchange deposition-reduction method was utilized to deposit cobalt and co-deposit gold-cobalt onto titanate nanotubes. Subsequently, these developed catalysts were tested for their ability to oxidize borohydride. It was discovered from the results that the highest amount of cobalt deposition was approximately 3.65 wt. % in the studied concentration range. Despite the limited deposition of cobalt at a low percentage, the electrocatalytic activity of the developed gold-cobalt co-catalysts in borohydride oxidation shows a significant improvement.

Similar to the developed Au_{100}/TiNT-C and Au-Ni/TiNT-C co-catalysts, the cyclic voltammograms of the developed Au-Co/TiNT-C co-catalysts exhibit a single oxidation peak during the forward scan, which is associated with the direct oxidation of borohydride. During the reverse scan, an additional oxidation peak is observed, indicating the oxidation of adsorbed intermediates like BH_3OH^-.

The characterization of developed catalysts in borohydride oxidation using linear sweep voltammetry showed that the developed Au-Co/TiNT-C co-catalysts exhibited certain enhancements in comparison to the performance of monometallic Au_{100}/TiNT-C. Among the co-catalysts of Au-Co/TiNT-C, $Au_{80}Co_{20}$/TiNT-C exhibits exceptional performance in terms of maximum current generation in borohydride oxidation with an improvement of 21 percent compared to Au_{100}/TiNT-C.

Comparing calculated diffusion coefficient number, D, of developed Au-Co/TiNT-C with those of Au rotating disc electrode, it was found that D values for Au-Co/TiNT-C catalysts are smaller.

Different potential ranges were used to calculate the n and k values for the Au disc electrode and developed Au-Co/TiNT-C catalysts. This was necessary because the appearance range of the mix-controlled region on LSV voltammograms varied. The transferred electron numbers for the developed co-catalysts, Au-Co/TiNT-C, were close to the theoretical $8e^-$ in the investigated voltage range at the mix-controlled region on LSV curves. For instance, at -0.10 V, the calculated transferred electron numbers were 5.9, 8.0, 6.5, 7.9, and 6.2 for Au_{100}/TiNT-C, $Au_{80}Co_{20}$/TiNT-C, $Au_{60}Co_{40}$/TiNT-C, $Au_{40}Co_{60}$/TiNT-C, and $Au_{20}Co_{80}$/TiNT-C, respectively.

The calculated values for the apparent rate constant, k, demonstrate a significant difference between monometallic Au_{100}/TiNT-C and Au-Co/TiNT-C co-catalysts. For instance, at 0 V, the calculated k values for Au_{100}/TiNT-C, $Au_{80}Co_{20}$/TiNT-C, $Au_{60}Co_{40}$/TiNT-C, $Au_{40}Co_{60}$/TiNT-C, and $Au_{20}Co_{80}$/TiNT-C were 0.003, 0.006, 0.006, 0.003, and 0.004 cm s^{-1}, respectively. These findings suggest that the prepared co-catalysts have higher k values compared to Au_{100}/TiNT-C. This increase in apparent rate constant supports the notion that incorporating cobalt as a co-catalyst with gold on titanate nanotubes enhances catalytic activities.

After 200 seconds of stability test conducted with chronoamperometry technique, both $Au_{60}Co_{40}$/TiNT-C and $Au_{40}Co_{60}$/TiNT-C exhibit comparable catalytic activity and stability. Chronoamperometry results show that Au_{100}/TiNT-C, $Au_{80}Co_{20}$/TiNT-C, and $Au_{20}Co_{80}$/TiNT-C have similar performance in terms of stability in borohydride oxidation test, but their performance was less than those of $Au_{60}Co_{40}$/TiNT-C and $Au_{40}Co_{60}$/TiNT-C. Catalytic activity and stability order for all catalysts is as follows: $Au_{60}Co_{40}$/TiNT-C > $Au_{40}Co_{60}$/TiNT-C > $Au_{20}Co_{80}$/TiNT-C > Au_{100}/TiNT-C > $Au_{80}Co_{20}$/TiNT-C.

Chapter 6: ELECTROCATALITIC OXIDATION OF BOROHYDRIDE BY GOLD-COPPER COMPOSITE CATALYSTS

6.1 Quantitative Analysis: Metal Deposition Determination

6.1.1 Copper Deposition on Titanate Nanotubes

Eight standard solutions -raging between 0.005 and 0.040 Molar- of diethylenediamine copper (II) nitrate $[Cu(en)_2](NO_3)_2$ were prepared to measure their absorbance and plot a calibration curve for copper deposition on titanate nanotubes. **Figure 6.1** shows the light absorbance trend of these standard solutions in the wavelength range of 390 to 700 nm. **Figure 6.2** illustrates the calibration curve generated using the peak absorbance values of $[Cu(en)_2](NO_3)_2$ solutions, which were observed to occur at approximately 545 nm. The copper solution was found to have an extinction coefficient of 52 L cm^{-1} mol^{-1} based on the calibration curve.

Then, 6 experiments conducted to ascertain the deposition of copper on titanate nanotubes as displayed in **Table 6.1**. Each solution used in these experiments contained 0.5 g of titanate nanotubes and had a volume of 25 mL. The calculation of the relative amount of deposited metal complex, *a*, adsorbed copper mass and weight percentages, can be achieved by determining the volume of the solution, added titanate nanotubes mass, initial and remaining metal concentration after deposition occurs. The formula used to determine the relative amount of deposited metal complex a [mol(M) mol $(TiO2)^{-1}$] is given by Eq. (6.1).

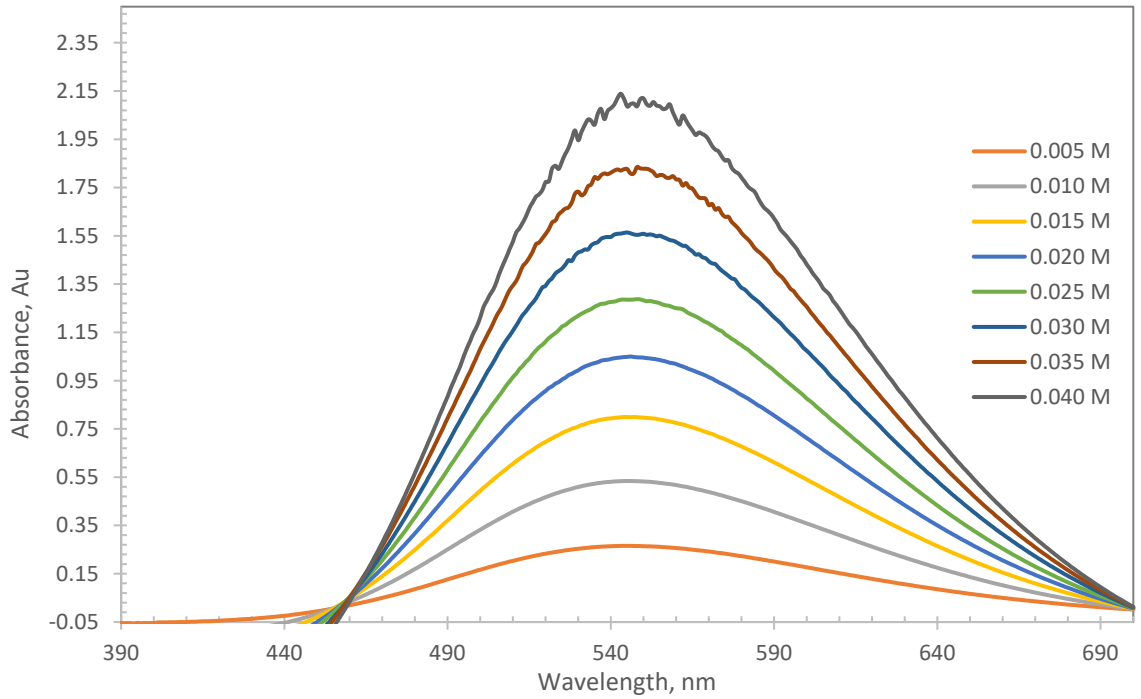

Figure 6.1: Absorbance spectrum of diethylenediamine copper (II) nitrate $[Co(en)_2](NO_3)_2$ solutions measured at 22 °C

$$a = \frac{80 \times (C_0 - C^*) \times V}{m} \tag{6.1}$$

Here, the mass of TiO_2 nanotubes powder added in the solution is represented by m. To determine the amount of metal that can be absorbed by each mole of titanate nanotubes powder from the solution is advantages for deciding catalyst loading. Based on the information provided by **Table 6.1**, it is evident that $[Cu(en)_2]^{2+}_{(aq)}$ cations adhere to titanate nanotubes from the solution at a very high rate below the concentration of 16 mmol L^{-1}. After this concentration, adsorption rate of $[Cu(en)_2]^{2+}_{(aq)}$ cations reaches to equilibrium. This is demonstrated in **Figure 6.3**. Maximum adsorbed cupper on titanate nanotubes was found to be 4.0 wt. % for 64 mmol L^{-1}.

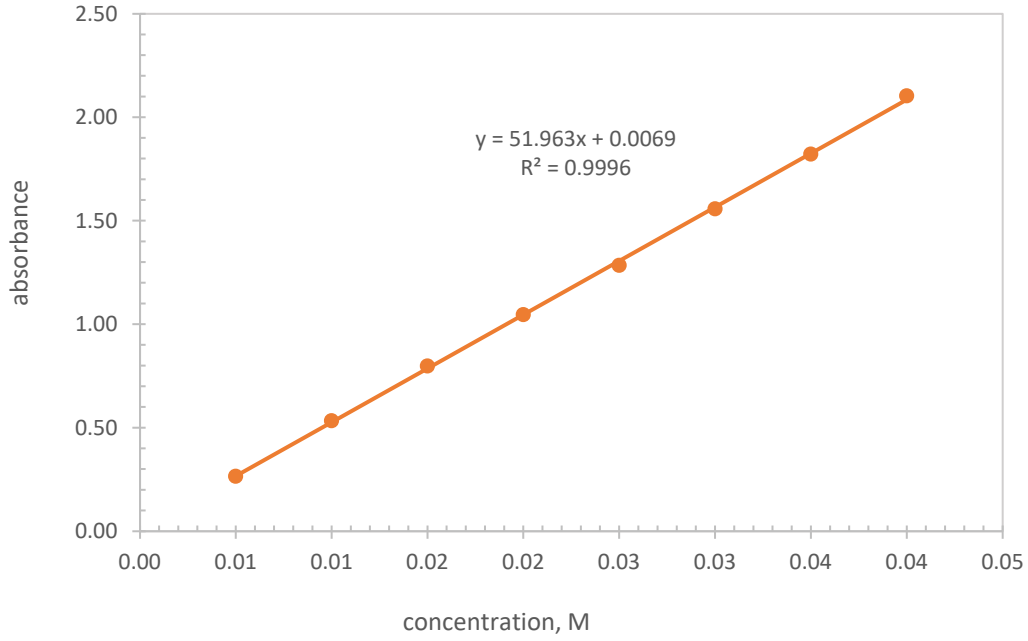

Figure 6.2: Calibration curve obtained at 545 nm for diethylenediamine copper (II) nitrate $[Cu(en)_2](NO_3)_2$ solutions.

Eq. (6.2) is used to calculate adsorbed mass of copper from solution on titanate nanotubes surface.

$$m\,(copper) = (C_0 - C^*) \times MW\,(copper) \times V \tag{6.2}$$

Here m is mass of adsorbed cobalt, and MW is molecular weight of the cobalt, C_o initial and C^* remaining concentrations, and V is the volume of the solution where adsorption take place. Considering the mass of titanate nanotubes powder added to the solution, we can ascertain the weight percentage of metal that has been adsorbed onto it. Eq. (6.3) can be utilized to calculate this percentage.

$$adsorbed\ metal\ wt.\% = \frac{m\,(metal)}{m\,(metal) + m(TiNT)} \times 100 \tag{6.3}$$

Table 6.1: Initial and remaining concentration of $[Cu(en)_2]^{2+}$ ions with the data calculated based on these two measurements.

Initial $[Co(en)2]^{2+}_{(aq)}$ concentration, mmol L^{-1}, C_o	Remaining $[Co(en)2]^{2+}_{(aq)}$ concentration, mmol L^{-1}, C^*	Ion-exchange molar ratio / mol (Co) mol^{-1} (TiNT), a	wt. %
4	0.6	0.014	1.07
8	0.7	0.029	2.27
12	3.5	0.034	2.91
16	6.0	0.040	3.06
32	20.8	0.045	3.44

64	50.8	0.052	4.00

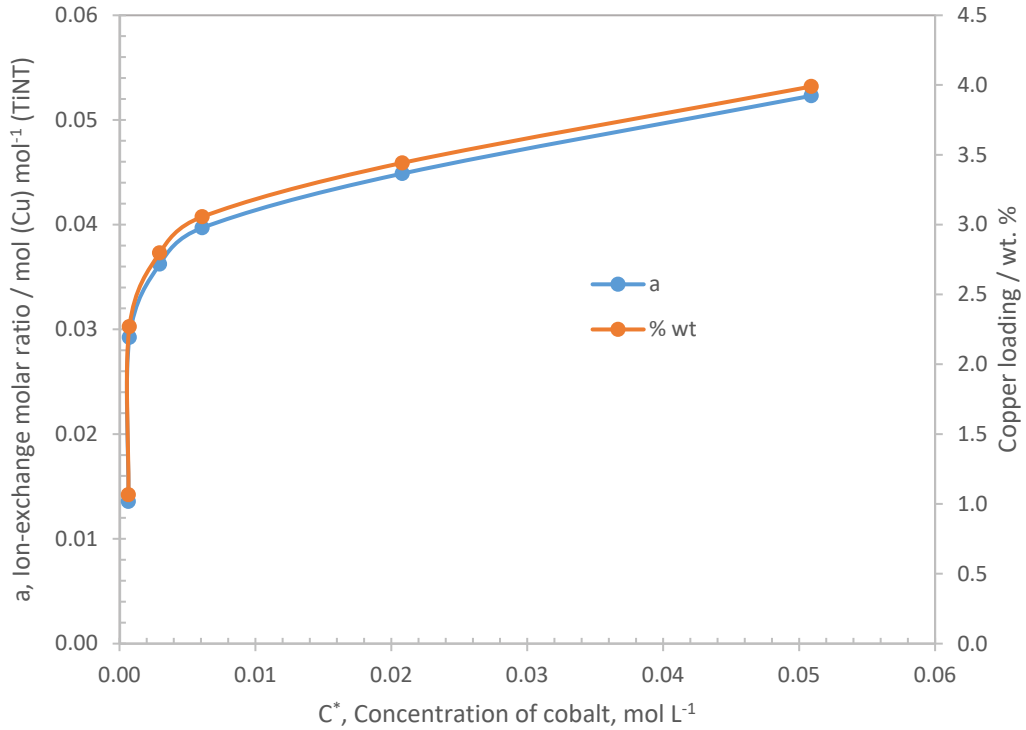

Figure 6.3: Isotherm of $[Cu(en)_2]^{2+}_{(aq)}$ cation adsorption on titanate nanotubes in water suspension at 20 °C (±1 °C) and responding wt. % copper loading.

6.1.2 Co-deposition of Gold-copper (Au-Co)

Determination of weight percentage of adsorbed copper is carried out by converting *a* value provided by Eq. (6.1) into g (metal) g^{-1} (TiO2) as given by Eq. (6.6)

$$a\ [g\ (metal)\ g^{-1}\ (TiO_2)] = a \times \frac{MW_{metal}}{MW_{TiO_2}} \tag{6.4}$$

Eq. (6.7) was used to calculate the weight percentage of adsorbed metal after converting the value into g (metal) g^{-1}(TiO2) for all the concentrations studied.

$$wt.\% = \frac{g_{metal}}{g_{TiO_2} + g_{metal}} \times 100 \tag{6.5}$$

The relationship between the percentage of adsorbed metal and its initial concentration required to achieve this percentage was determined by examining the exploitation of initial concentration versus weight percentage of adsorbed metal. This correlation was represented as a function of the natural logarithm, as depicted in **Figure 4.9** for gold and **Figure 6.4** for copper. Different molar ratios of metals were used to determine the intended final 4 wt. % catalyst loadings on the surface of titanate nanotubes. **Table 6.2** provided the necessary metal

weight percentages for the desired molar ratio of gold to copper. The weight percentage of each metal in **Table 6.2** was obtained by determining the required amount of metal solutions using the functions provided in **Figure 4.9** for gold and **Figure 6.4** for copper. For example, to achieve a weight percentage ratio of (1.75):(2.25) for Au:Cu in a 4 wt. % catalyst loading on 1 g TiNTs, which corresponds to an 20:80 of Au:Cu molar ratio, it was calculated that 1.28 mL of $HAuCI_4$ solution from its 0.1 M stock solution and 4.67 mL of $Cu(NO_3)_2$ from its 0.1 M stock solution are needed.

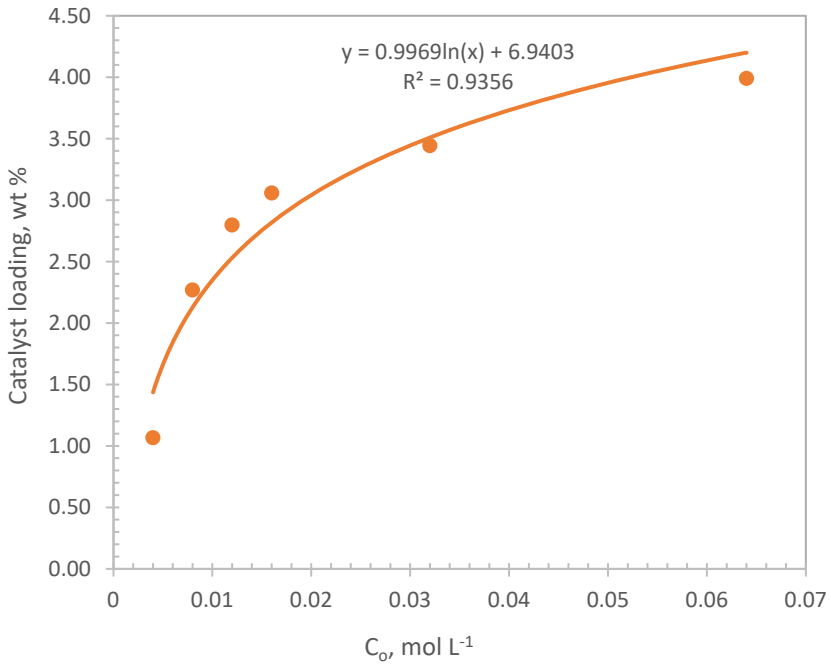

Figure 6.4: Correlation of Catalyst loading (wt. %)-initial concentration of $Cu[(en)_2]^{2+}_{(aq)}$

Table 6.2: Calculated molar ratios between gold and copper with a total catalyst loading on TiNTs

	Molar ratio of Au:Cu, %		Weight to weight percentage of Au:Cu, wt. %		
Catalyst	Au	Cu	Au	Cu	Total
Au_{100}/TiNT	100	0	4	0	4
$Au_{80}Cu_{20}$/TiNT	80	20	3.70	0.30	4
$Au_{60}Cu_{40}$/TiNT	60	40	3.29	0.71	4
$Au_{40}Cu_{60}$/TiNT	40	60	2.70	1.30	4
$Au_{20}Cu_{80}$/TiNT	20	80	1.75	2.25	4

6.2 Electrochemical Measurements

The electrocatalytic activities of the developed Au-Cu/TiNT-C catalysts were assessed in the borohydride oxidation reaction using cyclic voltammetry (CV), linear sweep voltammetry (LSV), and chronoamperometry (CA).

6.2.1 Cyclic Voltammetry

Cyclic voltammetry (CV) results of developed Au-Cu/TiNT-C catalysts reveal that there is no substantial contribution of copper used with gold. CV curve of Au_{100}/TiNT and $Au_{40}Co_{60}$/TiNT-C are provided in **Figure 6.5** and **Figure 6.6**. It can be clearly seen from these figures that maximum current density obtained with Au_{100}/TiNT-C is nearly 3 times higher than $Au_{40}Co_{60}$/TiNT-C. These results contradict with Behmenyar and Akin results conducted using carbon-supported Pd and bimetallic Pd-Cu anode catalysts [21]. This contradiction may result from different synergetic effect of Au-Cu and Pd-Cu. However, Au_{100}/TiNT-C and $Au_{40}Co_{60}$/TiNT-C show similar oxidation pattern peaks on CV curves. The rest of the CV curves obtained for $Au_{80}Cu_{20}$/TiNT-C, $Au_{60}Cu_{40}$/TiNT-C, $Au_{20}Cu_{80}$/TiNT-C were provided in **Appendix C**.

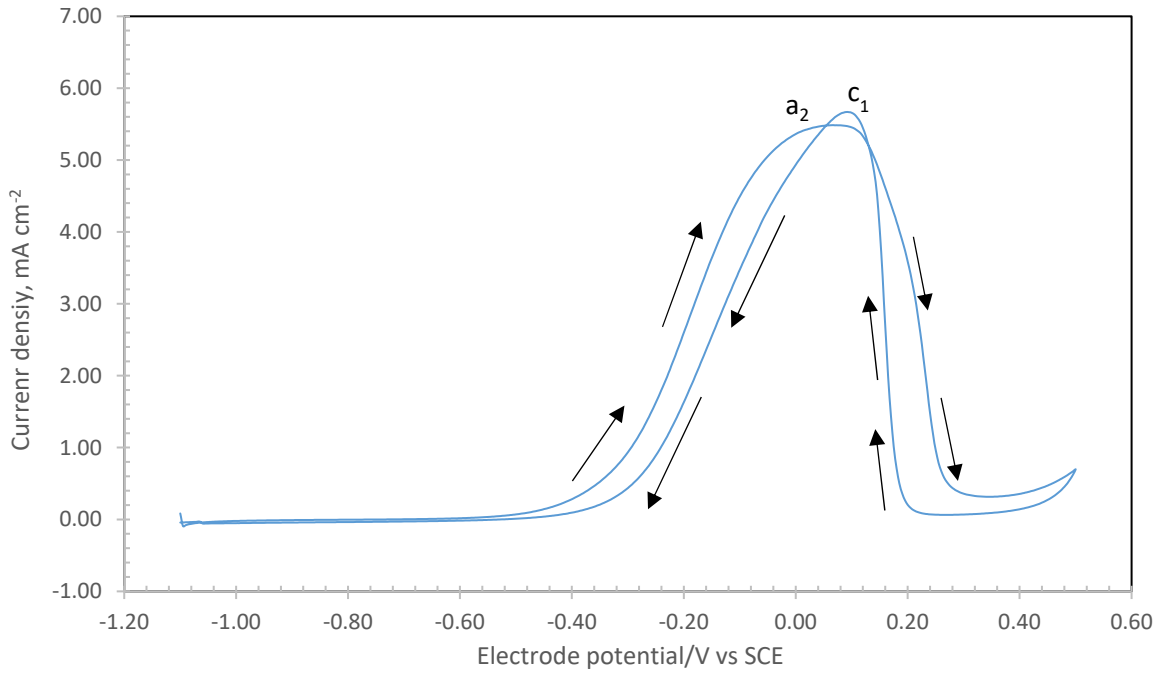

Figure 6.5: CV curve of Au_{100}/TiNT-C electrode. Counter electrode: Pt; electrolyte: 0.03 M $NaBH_4$ + 2 M NaOH; scan rate:10 mV s^{-1}; disc rotation 400 rpm; at ambient temperature (20 °C ±1)

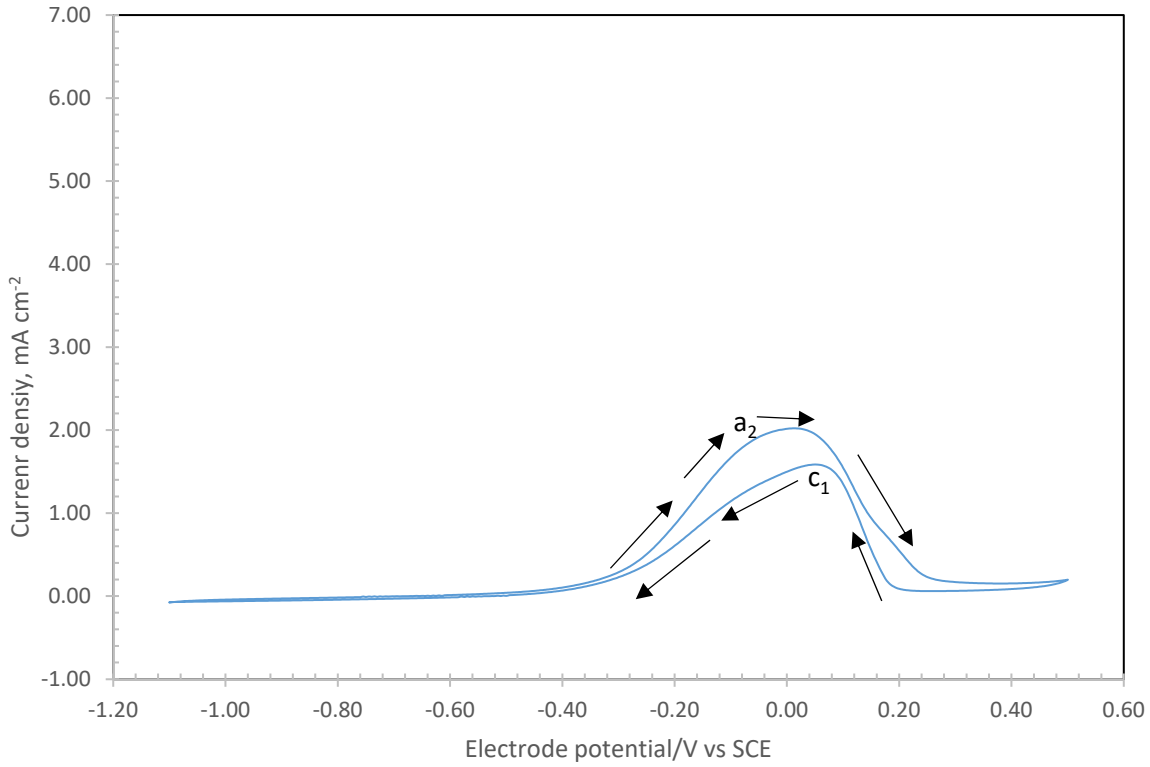

Figure 6.6: CV curve of $Au_{40}Cu_{60}$/TiNT-C electrode. Counter electrode: Pt; electrolyte: 0.03 M $NaBH_4$ + 2 M NaOH; scan rate:10 mV s^{-1}; disc rotation 400 rpm; at ambient temperature (20 °C ±1)

6.2.2 Linear Sweep Voltammetry

Linear sweep voltammetry measurements were carried out for $Au_{80}Cu_{20}$/TiNT-C, $Au_{60}Cu_{40}$/TiNT-C, $Au_{40}Cu_{60}$/TiNT-C, and $Au_{20}Cu_{80}$/TiNT-C in 0.03 M $NaBH_4$ + 2 M NaOH. Obtained results show that there is limited improvement for borohydride oxidation when gold and copper mixed catalysts used. For instance, LSV curves of Au_{100}/TiNT-C shows better performance than $Au_{40}Cu_{60}$/TiNT-C as demonstrated in **Figure 6.7** and **Figure 6.8**. LSV of $Au_{80}Cu_{20}$/TiNT-C $Au_{60}Cu_{40}$/TiNT-C, and $Au_{20}Cu_{80}$/TiNT-C can be found in **Appendix C**. Electrocatalytic worsening of $Au_{40}Cu_{60}$/TiNT-C is probably resulted from passivation of copper metal with the reaction of hydroxide ions [88]. Eq. (6.6) shows this passivation reaction:

$$Cu_{(s)} + OH^-_{(aq)} \rightarrow Cu(OH)_{2(s)} \quad (6.6)$$

Peak current densities of Au_{100}/TiNT-C, $Au_{80}Cu_{20}$/TiNT-C, $Au_{60}Cu_{40}$/TiNT-C, $Au_{40}Cu_{60}$/TiNT-C, and $Au_{20}Cu_{80}$/TiNT-C measured at 2000 rpm are compared as shown in **Figure 6.9**. This comparison indicates that peak currents of Au_{100}/TiNT-C, $Au_{80}Cu_{20}$/TiNT-C, and $Au_{60}Cu_{40}$/TiNT-C are close to each other, being 7.72, 7.86, and 7.40 mA cm^{-2}, respectively. $Au_{40}Cu_{60}$/TiNT-C shows the poorest peak current density with a value of 5.68 mA cm^{-2}. This value is 26 percent less than those of Au_{100}/TiNT-C peak current. **Figure 6.9** also demonstrates that current density increase starts at slightly more positive potentials (at -0.40 V) with copper

addition in the catalysts texture for Au-Cu/TiNT-C catalysts. Even if this shift is limited to a 0.10 V, it may indicate poor catalytic activities of Au-Cu/TiNT-C catalysts in borohydride oxidation.

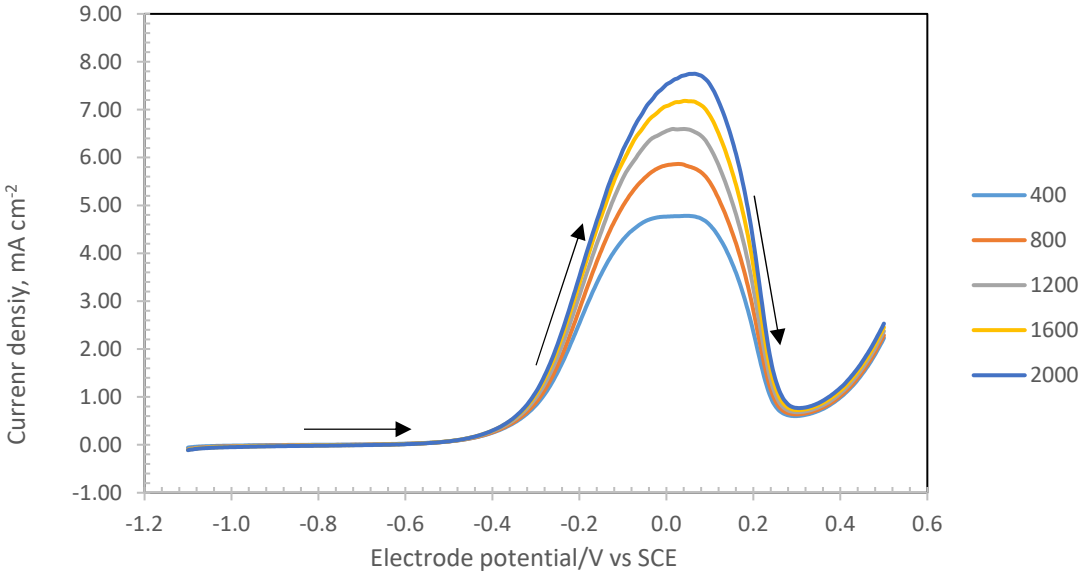

Figure 6.7: Linear sweep voltammograms (LSV) of Au_{100}/TiNT-C coated glassy carbon disc electrode at different rotation rates. Counter electrode: Pt; electrolyte: 0.03 M $NaBH_4$ + 2 M NaOH; scan rate:10 mV s^{-1}; at 20 °C (±1 °C)

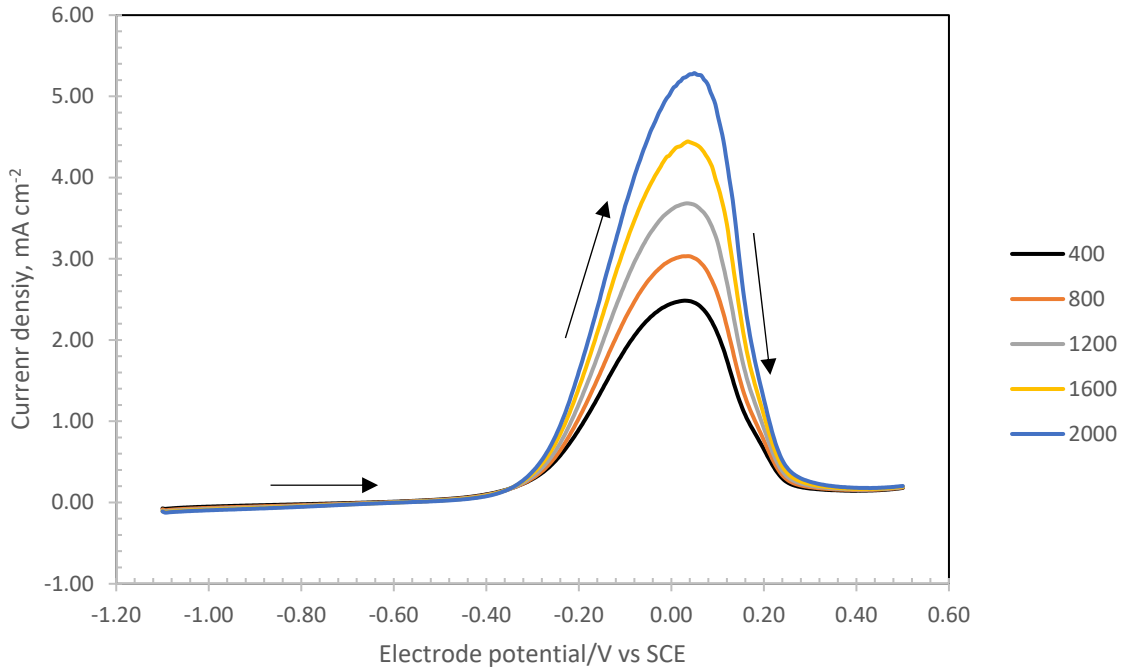

Figure 6.8: Linear sweep voltammograms (LSV) of $Au_{40}Cu_{60}$/TiNT-C coated glassy carbon disc electrode at different rotation rates. Counter electrode: Pt; electrolyte: 0.03 M $NaBH_4$ + 2 M NaOH; scan rate:10 mV s^{-1}; at 20 °C (±1 °C)

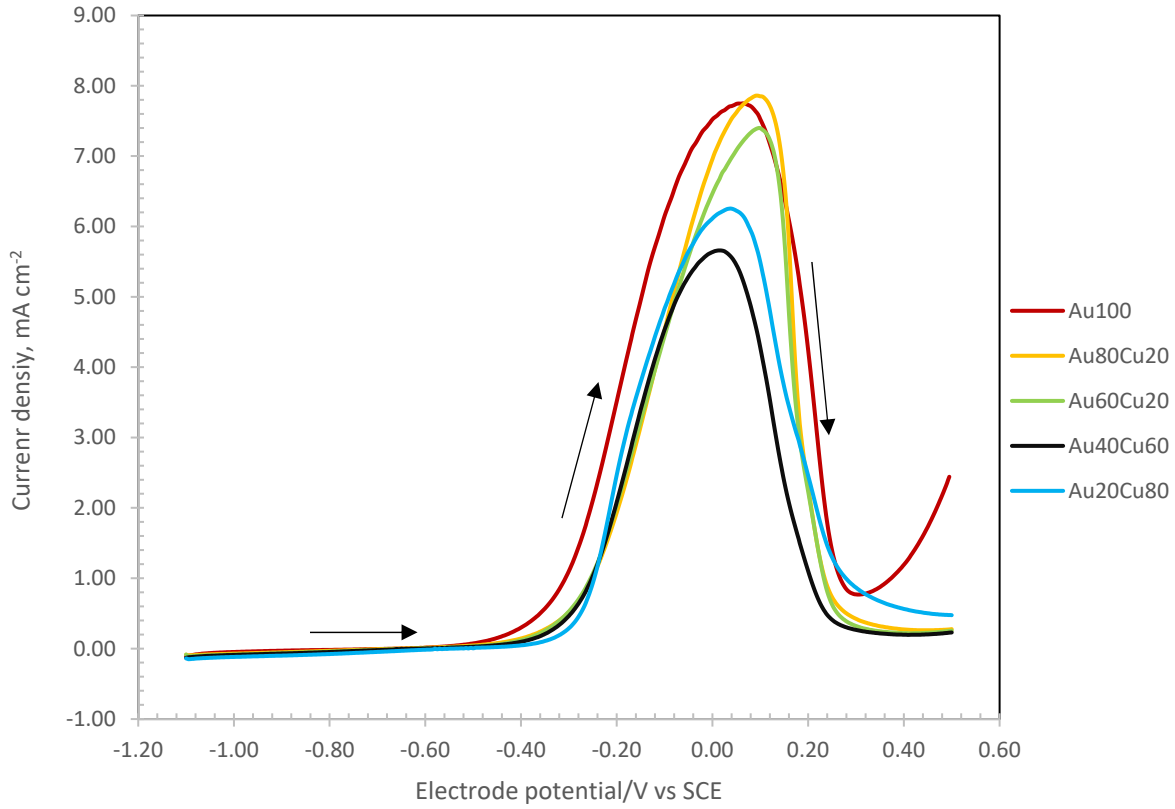

Figure 6.9: Comparison of linear sweep voltammogram peak current densities measured for Au_{100}/TiNT-C, $Au_{80}Cu_{20}$/TiNT-C, $Au_{60}Cu_{40}$/TiNT-C, $Au_{40}Cu_{60}$/TiNT-C, and $Au_{20}Cu_{80}$/TiNT-C at 2000 rpm. Counter electrode: Pt; electrolyte: 0.03 M $NaBH_4$ + 2 M NaOH; scan rate:10 mV s^{-1}; at 20 ºC (±1 ºC)

Weight percentages, maximum current densities at 2000 rpm, metal loading for each metal and maximum current density generated per mg Au are given in **Table 6.3** for the developed Au/TiNT-C and Au-Cu/TiNT-C catalysts. Considering this table, current density generated per mg Au is increased from 154.71 to 176.19 mA cm^{-2} by lowering the Au loading from 0.051 to 0.042 mg cm^{-2}. In other words, when Au loading decrease by 17.6 percent and corresponding current density increase by 14 percent. However, further reduction in Au loading from 0.042 to 0.035 mg cm^{-2} lead to a fall in current density from 176.19 to 162.29 mA cm^{-2}. Surprisingly, when gold loading continues to decline from 0.035 to 0.023 mg cm^{-2}, gold-based current density increases from 162.29 to 277.39 mA cm^{-2}. When Au_{100}/TiNT-C and $Au_{20}Cu_{80}$/TiNT-C catalysts are compared, current density per mg Au rises from 154.71 to 277.39 mA cm^{-2} with Au loading degreasing from 0.051 to 0.023 mg cm^{-2}. It can be concluded that maximum current density per mg Au increases 79 percent when Au loading decreases 55 percent.

Based on Au weight percentage and corresponding maximum current densities obtained for Au_{100}/TiNT-C, $Au_{80}Cu_{20}$/TiNT-C, $Au_{60}Cu_{40}$/TiNT-C, $Au_{40}Cu_{60}$/TiNT-C, and $Au_{20}Cu_{80}$/TiNT-C as seen **Table 6.3**, **Figure 6.10**was plotted to visualize relation between the developed Au-Cu/TiNT-C catalyst and peak current densities. From this figure, it can be clearly seen that

there is a decrease trend in current densities. These result shows that the is no improvement when gold and copper co-catalyst used for borohydride oxidation.

Table 6.3: Maximum current densities at 2000 rpm and Au mass-based current density comparison of developed Au_{100}/TiNT-C and Au-Cu/TiNT-C catalysts.

Catalyst	Weight percentage of Au (wt. % Au)	Au loading mg cm^{-2}	Weight percentage of Cu (wt. % Cu)	Cu loading mg cm^{-2}	Max. current density at 2000 rpm, mA cm^{-2}	Au mass based current density mA mg^{-1}
Au_{100}/TiNT-C	2.51	0.051	0	0.00	7.89	154.71
$Au_{80}Cu_{20}$/TiNT-C	2.33	0.047	0.18	0.004	7.86	167.23
$Au_{60}Cu_{40}$/TiNT-C	2.09	0.042	0.42	0.009	7.40	176.19
$Au_{40}Cu_{60}$/TiNT-C	1.72	0.035	0.79	0.016	5.68	162.29
$Au_{20}Cu_{80}$/TiNT-C	1.13	0.023	1.38	0.028	6.38	277.39

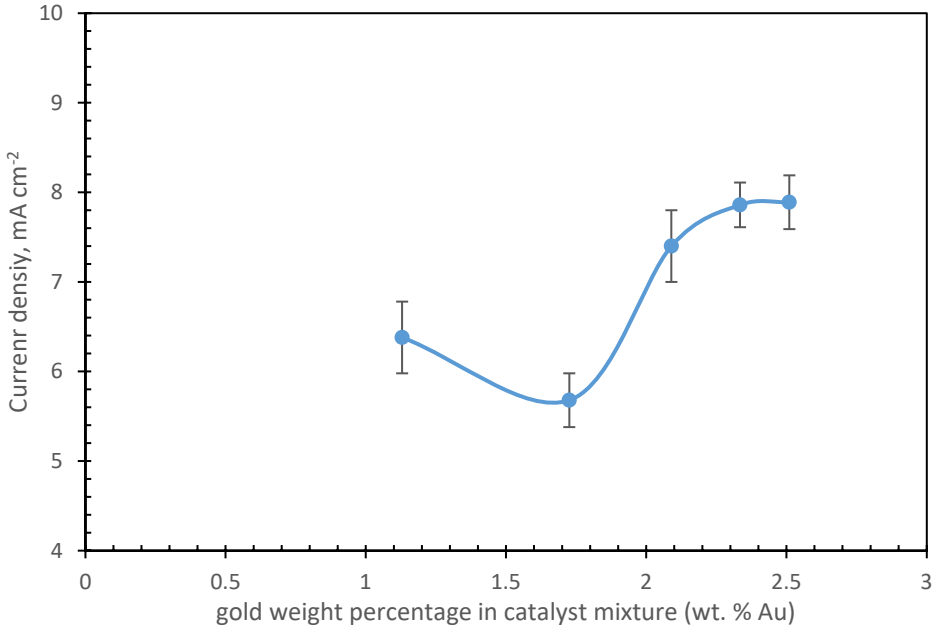

Figure 6.10: Comparison of maximum current densities versus gold weight percentage in the catalyst mixture for the developed catalysts: Au_{100}/TiNT-C, $Au_{80}Cu_{20}$/TiNT-C, $Au_{60}Cu_{40}$/TiNT-C, $Au_{40}Cu_{60}$/TiNT-C, and $Au_{20}Cu_{80}$/TiNT-C, obtained at 2000 rpm.

6.2.3 Determination of D, *k*, and *n*

Determination of diffusion coefficient number, D, is carried out by using the Levich equation given by Eq.(6.7) at the limiting current potential for developed Au-Cu/TiNT-C catalysts [30].

$$I_L = -0.62nFAD^{\frac{2}{3}}C_b v^{-\frac{1}{6}}\omega^{1/2} \quad (6.7)$$

Where, I_L is limiting current (A cm^{-2}), n is transferred electron number (n was assumed to be 8), A is geometric area of working electrode (cm^2), F is Faraday constant (96485 C mol^{-1}), D is diffusion coefficient of the electro active species (cm^2 s^{-1}), C_b is bulk concentration of

borohydride (mol cm^{-3}), v is kinematic viscosity of the solution (cm^2 s^{-1}), and ω is the angular velocity of the rotating disc (radians s^{-1}). Levich plot of $Au_{40}Cu_{60}$/TiNT-C is shown in **Figure 6.11**, which used to calculate D. Calculated D values for Au rotating disc electrode, Au_{100}/TiNT-C, and developed Au-Cu/TiNT-C are compared. D values of developed Au-Cu/TiNT catalysts are two times smaller than those of Au rotating disc electrode. Differentiation in D values is believed resulted from rough surface of rotating disc electrode after coating developed catalyst ink. This may lead to a deviation from Levich equation, which requires polished and smoot surface of rotating disc electrode to obtain reliable results.

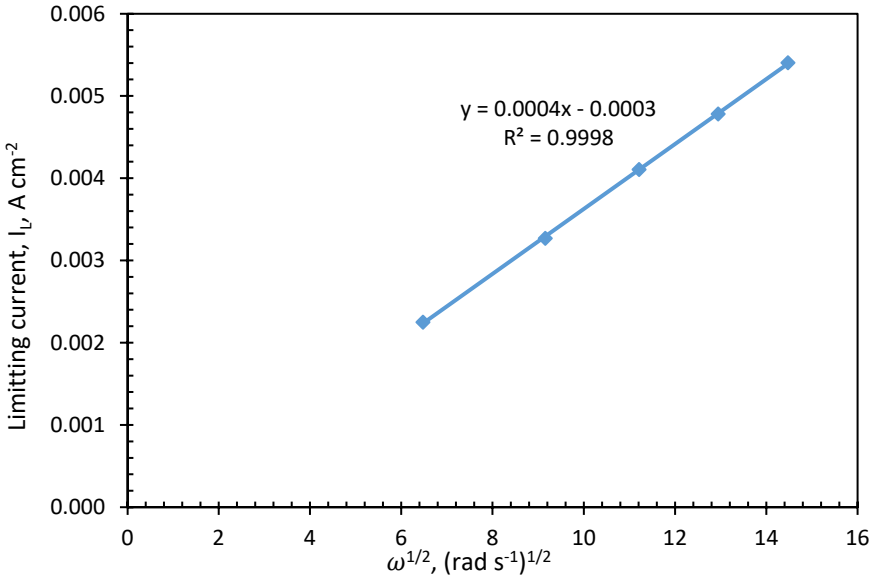

Figure 6.11: Levich plot of $Au_{40}Cu_{60}$/TiNT generated at a limiting current measured at 0.05 V *vs* SCE and based on five different rotation speed, 400, 800, 1200, 1600, and 2000 rpm. Counter electrode: Pt; electrolyte: 0.03 M $NaBH_4$ + 2 M NaOH; scan rate:10 mV s^{-1}; at 20 ºC (±1 ºC)

To calculate transferred electron number, n, and apparent rate constant, k, the Koutecky-Levich equation is used as given by Eq.(6.8) [32].

$$\frac{1}{j} = \frac{1}{nFkC_b} + \frac{1}{0.62nFD^{2/3}C_b v^{-1/6}\omega^{1/2}} \tag{6.8}$$

Where, j is disc current density (A cm^{-2}), and k is apparent rate constant (cm s^{-1}). D was calculated as 1.77×10^{-5} cm^2 s^{-1}, and v was obtained from literature to be as 0.0126 cm^2 s^{-1}, respectively [32], [82]. By plotting j^{-1} values versus $\omega^{-1/2}$ obtained for developed Au-Cu/TiNT-C catalysts at five different rotation speeds, n can be calculated from the slope and k can be calculated from intercept of j^{-1} versus $\omega^{-1/2}$ plots. **Figure 6.12** shows j^{-1} versus $\omega^{-1/2}$ plot of $Au_{40}Cu_{60}$/TiNT-C. j^{-1} versus $\omega^{-1/2}$ plots for $Au_{80}Cu_{20}$/TiNT-C, $Au_{60}Cu_{40}$/TiNT-C, and $Au_{20}Cu_{80}$/TiNT-C can be found in **Appendix C**. Calculated transferred electron number and apparent rate constant, k, are given in **Table 6.4**, using the Koutecky-Levich equation.

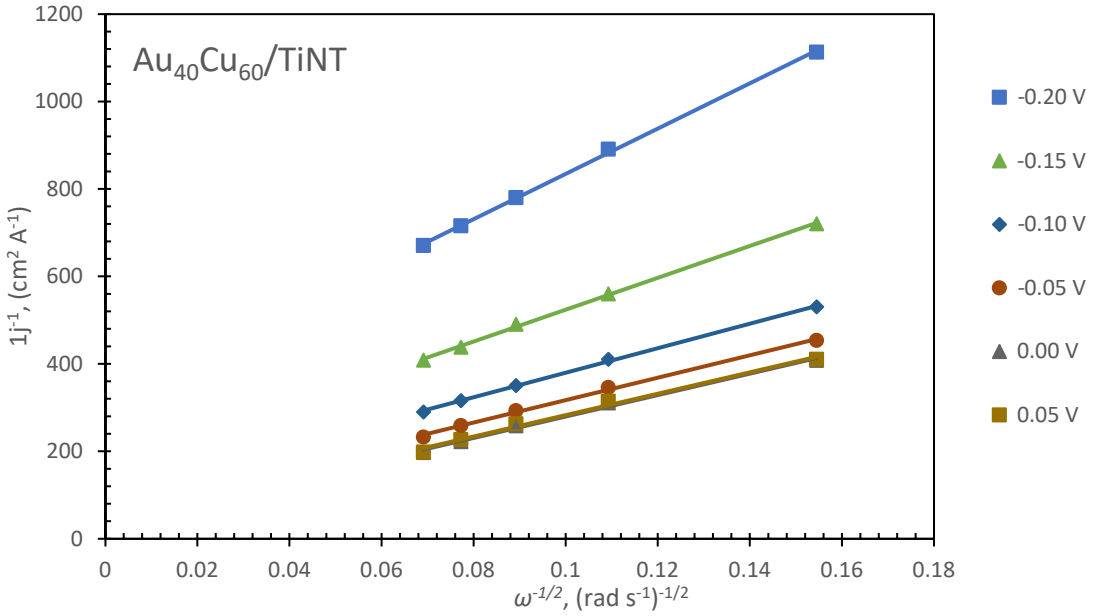

Figure 6.12: j^{-1} versus $\omega^{-1/2}$ plot of $Au_{40}Cu_{60}$/TiNT-C between -0.20 V and 0.05 V, Counter electrode: Pt; electrolyte: 0.03 M $NaBH_4$ + 2 M NaOH; scan rate: 10 mV s^{-1}; at 20 ºC (±1 ºC)

As can be seen on **Table 6.4**, transferred electron numbers tend to decrease in parallel with gold reduction and copper increase in catalyst texture. For instance, n values for developed catalysts at a potential of -0.05 V versus SCE are 6.9, 5.4, 4.8, 1.5, and 1.9 for Au_{100}/TiNT-C, $Au_{80}Cu_{20}$/TiNT-C, $Au_{60}Cu_{40}$/TiNT-C, $Au_{40}Cu_{60}$/TiNT-C, and $Au_{20}Cu_{80}$/TiNT-C, respectively. Mixing copper with gold leads to decrease in catalyst performance. It can be concluded that faradic efficiency of developed Au-Cu/TiNT-C catalysts is lower than Au_{100}/TiNT. This makes copper unfavourable catalyst to use with gold deposited on titanate nanotubes for borohydride oxidation.

The potential had a significant impact on the rate constant values. Apparent rate constant, k, generally increased by increase of potential. When the k values are compared, $Au_{20}Cu_{80}$/TiNT-C and $Au_{60}Cu_{40}$/TiNT-C show similar trend with those of Au-Ni/TiNT-C and Au-Co/TiNT-C co-catalysts. However, $Au_{40}Cu_{60}$/TiNT-C and $Au_{20}Cu_{80}$/TiNT-C have significantly large k values. This may result from effect of side reaction such as oxidation od adsorbed intermediates BH_3 and B_2H_6.

Table 6.4: Calculated number of electrons exchanged, n, and apparent kinetic rate constant, k at different voltage range.

Catalyst	Potential, V	n	Standard deviation	k (cm s^{-1})	Standard deviation
Au disc electrode	-0.40	4.4	0.2	0.012	0.005
	-0.38	5.5	0.1	0.011	0.005
	-0.36	7.3	0.1	0.010	0.006
	-0.34	7.8	0.1	0.011	0.005
	-0.32	7.9	0.2	0.014	0.005
	-0.30	8.0	0.2	0.018	0.001
Au_{100}/TiNT-C	-0.20	3.6	0.4	0.003	0.001
	-0.15	4.8	0.7	0.003	0.001
	-0.10	5.9	1.0	0.003	0.002
	-0.05	6.9	1.2	0.003	0.001
	0.00	7.6	1.4	0.003	0.001
	0.05	7.8	1.4	0.003	0.001
$Au_{80}Cu_{20}$/TiNT-C	-0.20	2.0	0.3	0.004	0.0024
	-0.15	3.8	0.9	0.006	0.0007
	-0.10	4.7	0.6	0.006	0.0005
	-0.05	5.4	0.8	0.008	0.0001
	0.00	5.7	0.9	0.009	0.0005
	0.05	5.8	1.0	0.009	0.0005
$Au_{60}Cu_{40}$/TiNT-C	-0.20	2.9	0.6	0.003	0.0003
	-0.15	3.9	0.7	0.004	0.0004
	-0.10	4.8	0.7	0.004	0.0005
	-0.05	4.8	0.6	0.006	0.0002
	0.00	4.8	0.4	0.007	0.0005
	0.05	4.8	0.3	0.008	0.0006
$Au_{40}Cu_{60}$/TiNT-C	-0.20	0.8	0.1	0.012	0.0004
	-0.15	1.1	0.1	0.020	0.0006
	-0.10	1.4	0.2	0.025	0.0006
	-0.05	1.5	0.2	0.037	0.0005
	0.00	1.6	0.2	0.062	0.0005
	0.05	1.6	0.2	0.056	0.0005
$Au_{20}Cu_{80}$/TiNT-C	-0.20	0.8	0.0	0.025	0.0071
	-0.15	1.3	0.1	0.029	0.0075
	-0.10	1.7	0.1	0.026	0.0037
	-0.05	1.9	0.2	0.033	0.0032
	0.00	2.0	0.2	0.036	0.0017
	0.05	2.1	0.2	0.036	0.0072

6.2.4 Chronoamperometry

The electroactivity and stability of catalysts for BH_4^- oxidation can be studied in greater depth using chronoamperometry tests [43]. These tests were conducted in a solution containing 0.03 M $NaBH_4$ and 2 M NaOH, under specific conditions such as no rotation (0 rpm) and a temperature of 22 ºC. During these tests, constant voltage is applied and chronoamperometric curves are recorded. The chosen constant voltage corresponds to the peak current densities observed on the linear sweep voltammetry (LSV) curves, being 0.05 V vs SCE. **Figure 6.13** illustrates the catalytic activities of the developed Au-Cu/TiNT-C and Au100/TiNT-C cocatalysts in chronoamperometric measurements.

The visualization of these measurements provides valuable insights into the electrochemical behaviour of the Au-Cu/TiNT-C cocatalysts. By examining **Figure 6.13** in details, additional information regarding the stability and efficiency of these catalysts can be obtained for borohydride oxidation. $Au_{80}Cu_{20}$/TiNT-C and $Au_{60}Cu_{40}$/TiNT-C provide higher current density than Au_{100}/TiNT-C. On the other hand, $Au_{40}Cu_{60}$/TiNT-C and $Au_{20}Cu_{80}$/TiNT-C generates less current density than Au_{100}/TiNT-C at the same conditions. When chronoamperometry curves of $Au_{80}Cu_{20}$/TiNT-C and $Au_{60}Cu_{40}$/TiNT-C are compared, current decrease on $Au_{60}Cu_{40}$/TiNT-C is slower than $Au_{80}Cu_{20}$/TiNT-C. However, $Au_{80}Cu_{20}$/TiNT-C gives more stable current density after 200 seconds. End of 200 seconds test period showed on **Figure 6.13**, current density generation of catalysts were as follow: 1.63, 2.22, 2.03, 0.41, and 0.23 mA cm^{-2} for following order of catalysts Au_{100}/TiNT-C, $Au_{80}Cu_{20}$/TiNT-C, $Au_{60}Cu_{40}$/TiNT-C, $Au_{40}Cu_{60}$/TiNT-C, and $Au_{20}Cu_{80}$/TiNT-C.

These chronoamperometric stability tests exhibit that using a molar ratio above 60:40 (Au:Cu) between gold and copper gives more stable results. Below than a molar ratio 40:60 between Au:Cu gives detrimental results in current generation.

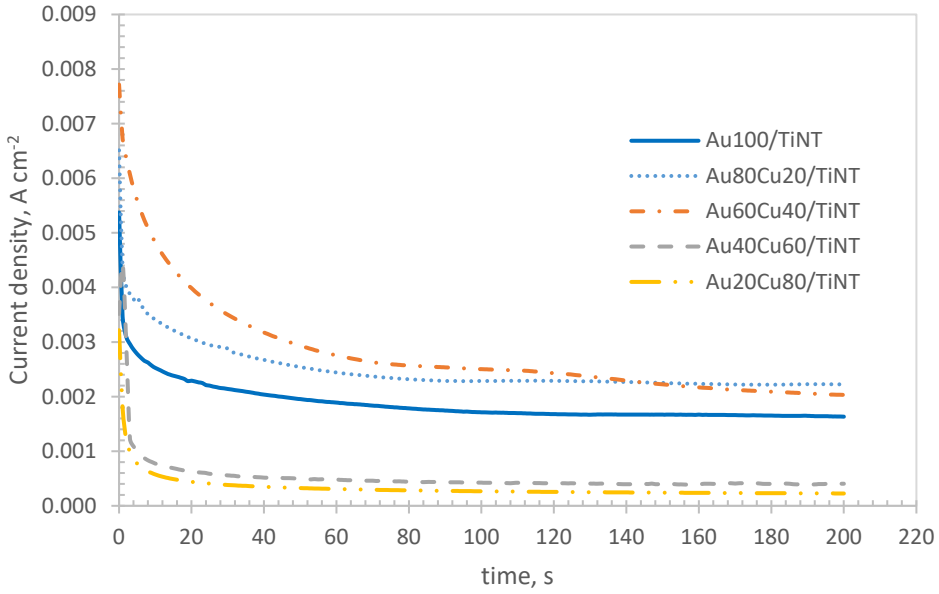

Figure 6.13: Chronoamperometry curves of borohydride ions oxidation on glassy carbon rotating disc electrode (RDE) coated with Au_{100}/TiNT-C, $Au_{80}Cu_{20}$/TiNT-C, $Au_{60}Cu_{40}$/TiNT-C, $Au_{40}Cu_{60}$/TiNT-C, and $Au_{20}Cu_{80}$/TiNT-C catalysts in 0.03 M $NaBH_4$ + 2 M NaOH solution, ω = 0 rpm, at 22 °C.

Chronoamperometry technique can be used to estimate transferred electron numbers for an electrocatalytic reaction. In this respect, Cottrell equation, given by Eq. (6.9), was employed to calculate the number of electrons exchanged, n, using results obtained from chronoamperometry experiments.

$$i = \frac{nFAC_b D^{\frac{1}{2}}}{\pi^{\frac{1}{2}} t^{\frac{1}{2}}} \tag{6.9}$$

Here, i is current density (A cm^{-2}), n is transferred electron number, F is Faraday constant (96485 C mol^{-1}), C_b is bulk concentration of borohydride (mol cm^{-3}), D is diffusion coefficient for borohydride ions (1.77×10^{-5} cm^2 s^{-1}), π is constant (3.14), and t is time (in second).

By plotting the current density against the reciprocal of the square of time within the range of 5 to 30 seconds, the number of electrons exchanged in the borohydride oxidation reaction can be determined from the slope of the plot. **Figure 6.14** illustrates $i - t^{-1/2}$ plots of Au_{100}/TiNT-C, $Au_{80}Cu_{20}$/TiNT-C, $Au_{60}Cu_{40}$/TiNT-C, $Au_{40}Cu_{60}$/TiNT-C, and $Au_{20}Cu_{80}$/TiNT-C developed catalysts.

Calculated transferred electron numbers can be found in **Table 6.5** for Au_{100}/TiNT-C, $Au_{80}Cu_{20}$/TiNT-C, $Au_{60}Cu_{40}$/TiNT-C, $Au_{40}Cu_{60}$/TiNT-C, and $Au_{20}Cu_{80}$/TiNT-C.

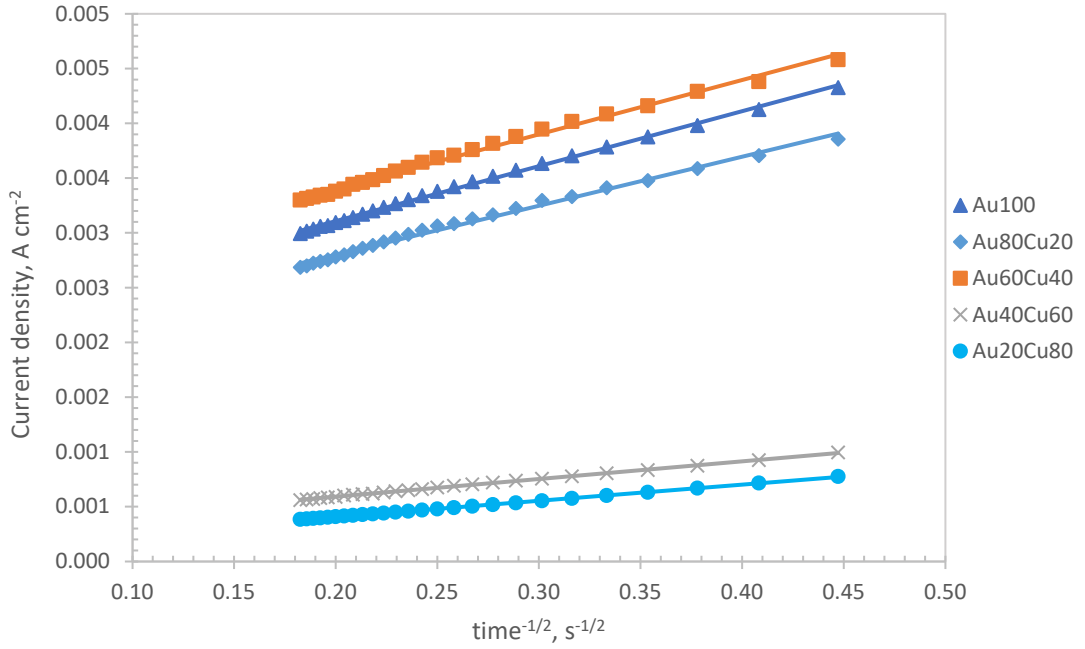

Figure 6.14: $i - t^{-1/2}$ plot of Au_{100}/TiNT-C, $Au_{80}Cu_{20}$/TiNT-C, $Au_{60}Cu_{40}$/TiNT-C, $Au_{40}Cu_{60}$/TiNT-C, and $Au_{20}Cu_{80}$/TiNT-C

Table 6.5: Calculated transferred electron numbers by means of Cottrell equation

Catalyst	Potential, V	n	Standard deviation
Au_{100}/TiNT-C	0.05	7.3	0.3
$Au_{80}Cu_{20}$/TiNT-C	0.05	6.5	0.5
$Au_{60}Cu_{40}$/TiNT-C	0.05	7.3	0.3
$Au_{40}Cu_{60}$/TiNT-C	0.05	2.3	0.2
$Au_{40}Cu_{60}$/TiNT-C	0.05	2.2	0.2

6.3 Conclusion

Copper and gold-copper were deposited onto titanate nanotubes using the ion-exchange deposition-reduction method, which was a novel approach. The findings revealed that the maximum amount of copper deposition within the tested concentration range was around 4.00 wt. %. The resulting catalysts were then evaluated for their effectiveness in oxidizing borohydride.

The cyclic voltammograms of the developed Au-Cu/TiNT-C co-catalysts show a single oxidation peak during the forward scan, similar to the developed Au_{100}/TiNT-C, Au-Ni/TiNT-C, and Au-Co/TiNT-C co-catalysts. This peak is linked to the direct oxidation of borohydride. On the reverse scan, an extra oxidation peak is observed, indicating the oxidation of adsorbed intermediates such as BH_3OH^-.

Linear sweep voltammetry was used to characterize the developed catalysts in borohydride oxidation. The results indicated that the performance of the developed Au-Cu TiNT-C co-catalysts was inferior to that of the monometallic Au_{100}/TiNT-C catalyst. Among the co-catalysts, $Au_{80}Cu_{20}$/TiNT-C exhibits similar performance in terms of maximum current generation in borohydride oxidation compared to Au_{100}/TiNT-C. When the percentage of copper was increased further in developed co-catalyst texture, maximum current density reduced to lower values.

The comparison of the calculated diffusion coefficient number, D, for the developed Au-Cu/TiNT-C with that of the Au rotating disc electrode revealed that the D values for Au-Cu/TiNT-C catalysts are smaller than of those Au rotating disc electrode.

To calculate the n and k values for the Au disc electrode and developed Au-Cu/TiNT-C catalysts, different potential ranges were utilized. This was necessary due to the varying appearance range of the mix-controlled region on LSV voltammograms. The transferred electron numbers for the developed Au-Cu/TiNT-C co-catalysts were smaller than the theoretical $8e^-$ within the investigated voltage range at the mix-controlled region on LSV curves. For example, at -0.10 V, the calculated transferred electron numbers were 5.9, 4.7, 4.8, 1.4, and 1.7 for Au_{100}/TiNT-C, $Au_{80}Cu_{20}$/TiNT-C, $Au_{60}Cu_{40}$/TiNT-C, $Au_{40}Cu_{60}$/TiNT-C, and $Au_{20}Cu_{80}$/TiNT-C respectively.

The rate constant values were greatly influenced by the potential. Generally, an increase in potential led to an increase in the apparent rate constant, k. When comparing the k values, it was observed that $Au_{20}Cu_{80}$/TiNT-C and $Au_{60}Cu_{40}$/TiNT-C followed a similar trend to that of Au-Ni/TiNT-C and Au-Co/TiNT-C co-catalysts. However, $Au_{40}Cu_{60}$/TiNT-C and $Au_{20}Cu_{80}$/TiNT-C exhibited significantly higher k values. This could be attributed to the impact of side reactions, such as the oxidation of adsorbed intermediates BH_3 and B_2H_6.

In terms of stability and efficiency, the catalysts $Au_{80}Cu_{20}$/TiNT-C and $Au_{60}Cu_{40}$/TiNT-C exhibit greater current density compared to Au_{100}/TiNT-C. Conversely, $Au_{40}Cu_{60}$/TiNT-C and $Au_{20}Cu_{80}$/TiNT-C produce lower current density than Au_{100}/TiNT-C under identical conditions. At the end of the 200-second test period, the catalysts generated current densities in the following order: 1.63, 2.22, 2.03, 0.41, and 0.23 mA cm^{-2} for the catalysts Au_{100}/TiNT-C, $Au_{80}Cu_{20}$/TiNT-C, $Au_{60}Cu_{40}$/TiNT-C, $Au_{40}Cu_{60}$/TiNT-C, and $Au_{20}Cu_{80}$/TiNT-C, respectively.

Chapter 7: REVIEW OF VARIOUS CO-CATALYST WITH GOLD (M-Au_{100}/TiNT) FOR BOROHYDRIDE OXIDATION

In this chapter it was aimed to give detailed explanation and pre-tested results for potential cocatalysts to use with gold in borohydride oxidation. These tested metals were nickel, cobalt, copper, iron, bismuth, and lead.

First, glassy carbon electrode (GC) was coated with Au_{100}/TiNT-C ink and left to dry overnight. Following that, four different concentrations were prepared for each metal. Au_{100}/TiNT-C catalyst coated glassy carbon disc electrode was submerged to a metal solution, starting with lowest concentration (0.001 M). Then it was taken out, rinsed with water, and directly submerged to 0.2 M $NaBH_4$ solution to reduce adsorbed metal ions. Leftover $NaBH_4$ solution was rinsed with water before testing prepared catalyst. A fresh coating was used for each concentration. Catalytic activities of prepared catalyst tested in a three-electrode cell by linear sweep voltammetry at 400 rpm rotation rate in 0.03 M $NaBH_4$ + 2 M NaOH solution. Each test was repeated 3 times prior to report for reliable results. For each metal these steps were repeated at four different concentrations. An illustration of the preparing method of catalysts mentioned under this chapter is shown in **Figure 7.1**.

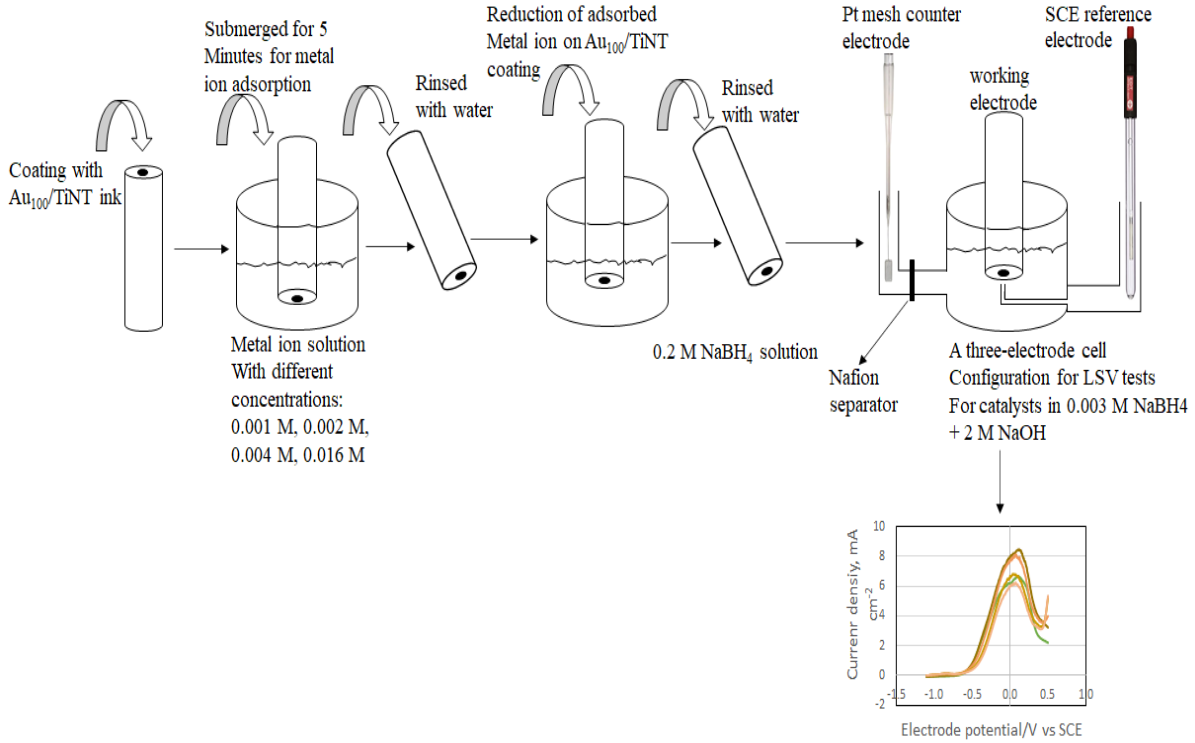

Figure 7.1: Schematic illustration of catalyst preparation for pre-tested metals adsorbed on Au_{100}/TiNT-C coated GC for borohydride oxidation.

7.1 Nickel (Ni)

Four different concentration of $Ni(NO_3)_{2(aq)}$ were prepared to conduct LSV test. These concentrations were 0.001, 0.002, 0.004, and 0.016 M $Ni(NO_3)_{2(aq)}$. A brief explanation for preparation of nickel adsorbed Au_{100}/TiNT-C catalyst as denoted Ni_c-Au_{100}/TiNT-C can be seen in **Figure 7.1**. Following denotation were used for adsorption of Ni at different concentrations: Ni_{c1}-Au_{100}/TiNT-C for 0.001 M, Ni_{c2}-Au_{100}/TiNT-C for 0.002 M, Ni_{c3}-Au_{100}/TiNT-C for 0.004 M, and Ni_{c4}-Au_{100}/TiNT-C for 0.016 M.

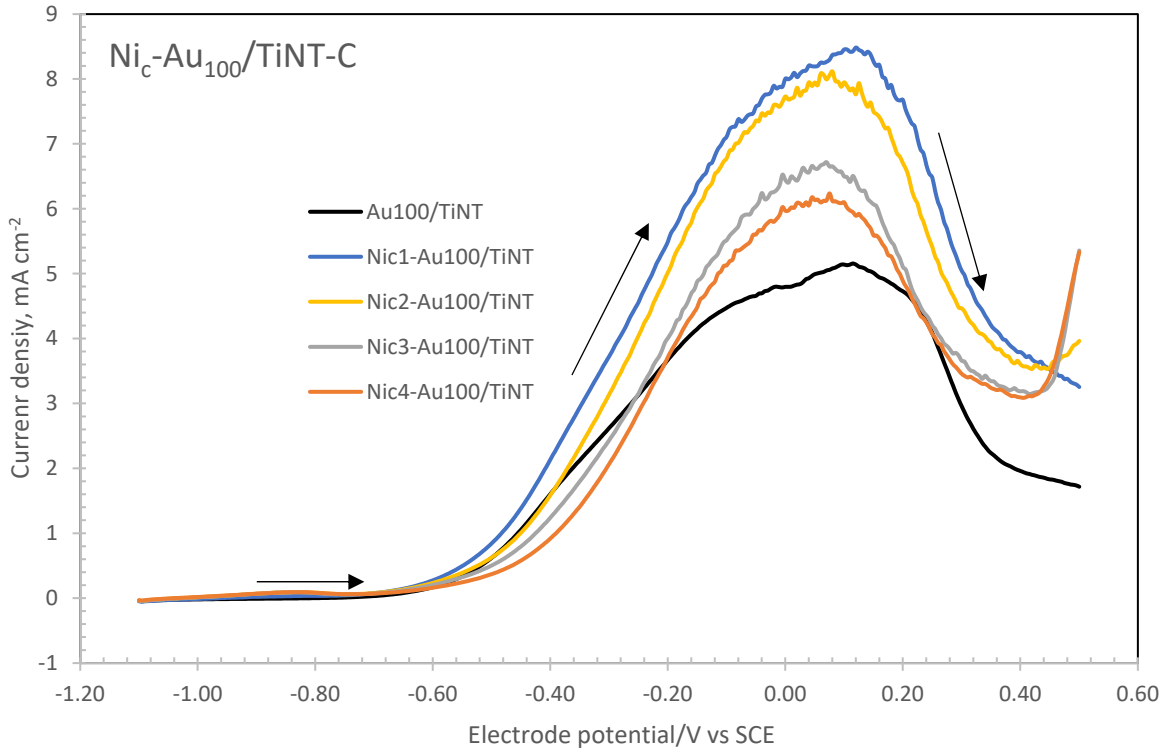

Figure 7.2: Linear Au_{100}/TiNT-C, and Ni_{c4}-Au_{100}/TiNT-C at 400 rpm rotation rate. Counter electrode: Pt; electrolyte: 0.03 M $NaBH_4$ + 2 M NaOH; scan rate:10 mV s^{-1}; at 20 °C (±1 °C)sweep voltammetry of Au_{100}/TiNT-C, Ni_{c1}-Au_{100}/TiNT-C, Ni_{c2}-Au_{100}/TiNT-C, Ni_{c3}-

Linear sweep voltammetry of developed catalysts is illustrated in **Figure 7.2**. Measured maximum current densities for Au_{100}/TiNT-C, Ni_{c1}-Au_{100}/TiNT-C, Ni_{c2}-Au_{100}/TiNT-C, Ni_{c3}-Au_{100}/TiNT-C, and Ni_{c4}-Au_{100}/TiNT-C were 5.2, 8.5, 8, 6.7, and 6.1 mA cm^{-2}, respectively. As can be seen that Au_{100}/TiNT-C catalyst provides the lowest maximum current density. When Au_{100}/TiNT-C catalyst ink coated GC electrode soaked in 0.001 M $Ni(NO_3)_{2(aq)}$ solution and following the steps as provided **Figure 7.1**, maximum current density increased to 8.5 mA cm^{-2} conducted by Ni_{c1}-Au_{100}/TiNT-C catalyst. This proves that adsorbed Ni on Au_{100}/TiNT-C improves catalytic activities for borohydride oxidation. However, when higher concentration of $Ni(NO_3)_{2(aq)}$ are used for Ni adsorption on Au_{100}/TiNT-C maximum current density tends

to decrease. This may cause from blockage of active sites Au nano particles on Au_{100}/TiNT-C by Ni nanoparticles, preventing borohydride ions intact to Au nano particles. It can be concluded that combining Ni with Au on titanate nanotubes catalyst support enhances catalytic activities towards borohydride oxidation at lower $Ni(NO_3)_{2(aq)}$ concentration.

7.2 Cobalt (Co)

To conduct the LSV test, four different concentrations of $Co(NO_3)_{2(aq)}$ were prepared. These concentrations were 0.001 M, 0.002 M, 0.004 M, and 0.016 M $Co(NO3)_{2(aq)}$. **Figure 7.1** provides a brief explanation for the preparation of the cobalt adsorbed Au_{100}/TiNT-C catalyst, referred to as Co_c-Au_{100}/TiNT-C. The denotations used for adsorption of Co at different concentrations are as follows: Co_{c1}-Au_{100}/TiNT-C for 0.001 M, Co_{c2}-Au_{100}/TiNT-C for 0.002 M, Co_{c3}-Au_{100}/TiNT-C for 0.004 M, and Co_{c4}-Au_{100}/TiNT-C for 0.016 M.

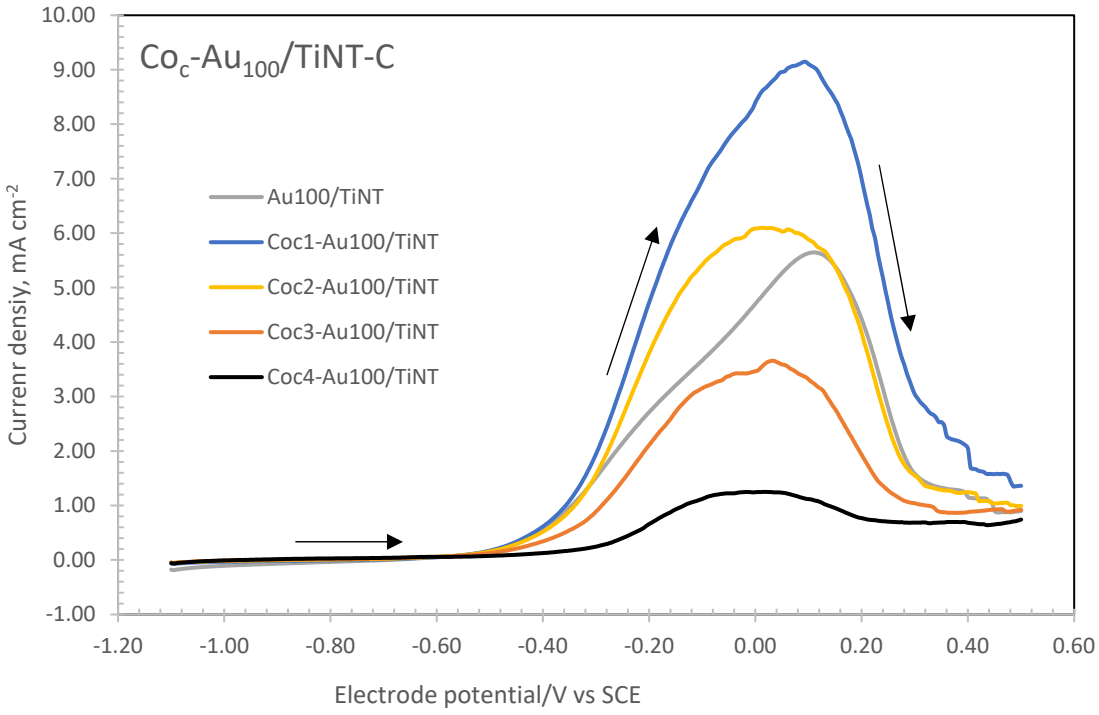

Figure 7.3: Linear sweep voltammetry of Au_{100}/TiNT-C, Co_{c1}-Au_{100}/TiNT-C, Co_{c2}-Au_{100}/TiNT-C, Co_{c3}-Au_{100}/TiNT-C, and Co_{c4}-Au_{100}/TiNT-C at 400 rpm rotation rate. Counter electrode: Pt; electrolyte: 0.03 M $NaBH_4$ + 2 M NaOH; scan rate:10 mV s^{-1}; at 20 ºC (±1 ºC)

Figure 7.3 demonstrates the linear sweep voltammetry of developed catalysts. The measured maximum current densities for different catalysts, namely Au_{100}/TiNT-C, Co_{c1}-Au_{100}/TiNT-C, Co_{c2}-Au_{100}/TiNT-C, Co_{c3}-Au_{100}/TiNT-C, and Co_{c4}-Au_{100}/TiNT-C, were 5.6, 9.2, 6.1, 3.6, and 1.2 mA cm^{-2}, respectively. Upon coating the GC electrode with Au_{100}/TiNT-C catalyst ink and immersing it in a 0.001 M $Co(NO_3)_{2(aq)}$ solution following the steps shown in **Figure 7.1**, the

maximum current density increased to 9.2 mA cm^{-2} with the Co_{c1}-Au_{100}/TiNT-C catalyst. This indicates that the presence of adsorbed Co on Au_{100}/TiNT-C enhances catalytic activities for borohydride oxidation. However, when higher concentrations of $Co(NO_3)_{2(aq)}$ are utilized for Co adsorption on Au_{100}/TiNT-C, the maximum current density tends to decrease. While Au_{100}/TiNT-C and Co_{c2}-Au_{100}/TiNT-C provide a similar maximum current density, Co_{c3}-Au_{100}/TiNT-C, and Co_{c4}-Au_{100}/TiNT-C yield less maximum current density. Once again, this deterioration in current density may result from the obstruction of active sites for Au nano particles at higher $Co(NO_3)_{2(aq)}$. Therefore, using lower concentration of $Co(NO_3)_{2(aq)}$ for adrsorption of Co on Au_{100}/TiNT-C might be beneficial for borohydride oxidation, by preventing blockage of active sites of Au nano particles.

7.3 Copper (Cu)

In order to perform the LSV test, four different concentrations of $Cu(NO_3)_{2(aq)}$ were prepared. These concentrations included 0.001 M, 0.002 M, 0.004 M, and 0.016 M $Cu(NO_3)_{2(aq)}$. **Figure 7.1** provides a brief explanation of how the copper adsorbed Au_{100}/TiNT-C catalyst, shown as Cu_c-Au_{100}/TiNT-C, was prepared. The designations used for the adsorption of Cu at various concentrations are as follows: Cu_{c1}-Au_{100}/TiNT-C for 0.001 M, Cu_{c2}-Au_{100}/TiNT-C for 0.002 M, Cu_{c3}-Au_{100}/TiNT-C for 0.004 M, and Cu_{c4}-Au_{100}/TiNT-C for 0.016 M.

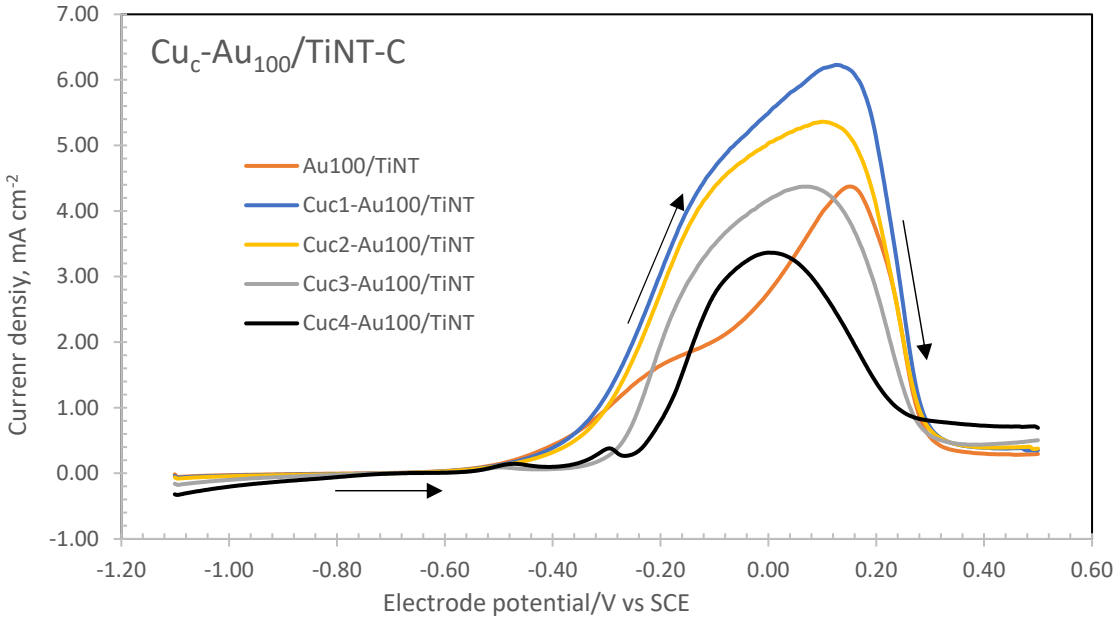

Figure 7.4: Linear sweep voltammetry of Au_{100}/TiNT-C, Cu_{c1}-Au_{100}/TiNT-C, Cu_{c2}-Au_{100}/TiNT-C, Cu_{c3}-Au_{100}/TiNT-C, and Cu_{c4}-Au_{100}/TiNT-C at 400 rpm rotation rate. Counter electrode: Pt; electrolyte: 0.03 M $NaBH_4$ + 2 M NaOH; scan rate:10 mV s^{-1}; at 20 ºC (±1 ºC)

The linear sweep voltammetry of developed catalysts is shown in **Figure 7.4**. The maximum current densities for different catalysts, namely Au_{100}/TiNT-C, Cu_{c1}-Au_{100}/TiNT-C, Cu_{c2}-Au_{100}/TiNT-C, Cu_{c3}-Au_{100}/TiNT-C, and Cu_{c4}-Au_{100}/TiNT-C, were measured as 4.5, 6.3, 5.3, 4.6, and 3.3 mA cm^{-2}, respectively. By coating the GC electrode with Au_{100}/TiNT-C catalyst ink and immersing it in a 0.001 M $Co(NO_3)_{2(aq)}$ solution following the steps illustrated in **Figure 7.1**, the maximum current density increased to 6.3 mA cm^{-2} with the Cu_{c1}-Au_{100}/TiNT-C catalyst. This suggests that the presence of adsorbed Cu on Au_{100}/TiNT-C enhances catalytic activities for borohydride oxidation. However, using higher concentrations of $Cu(NO_3)_{2(aq)}$ for Cu adsorption on Au_{100}/TiNT-C tends to result in a decrease in maximum current density.

7.4 Iron (Fe)

Four different concentrations of $Fe(SO_4)_{2(aq)}$ were prepared for the LSV test, which included 0.001 M, 0.002 M, 0.004 M, and 0.016 M $Fe(SO_4)_{2(aq)}$. **Figure 7.1** explains the preparation of the iron adsorbed Au_{100}/TiNT-C catalyst, referred to as Fe_c-Au_{100}/TiNT-C. The designations for the adsorption of Fe at different concentrations are as follows: Fe_{c1}-Au_{100}/TiNT-C for 0.001 M, Fe_{c2}-Au_{100}/TiNT-C for 0.002 M, Fe_{c3}-Au_{100}/TiNT-C for 0.004 M, and Fe_{c4}-Au_{100}/TiNT-C for 0.016 M.

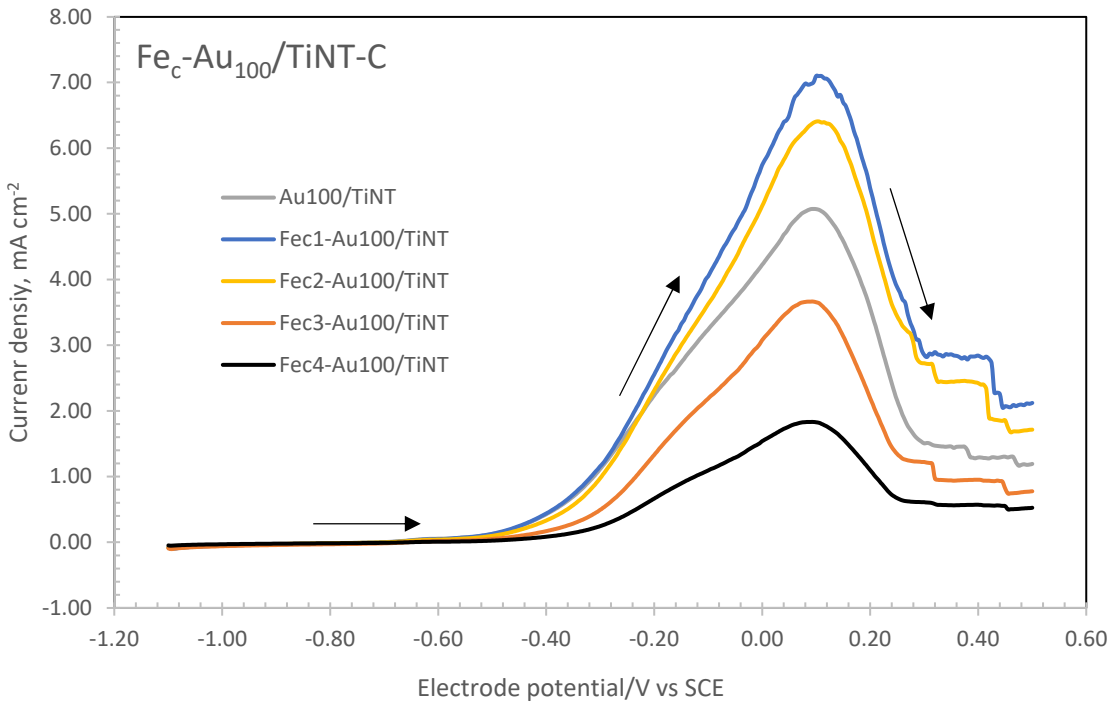

Figure 7.5: Linear sweep voltammetry of Au_{100}/TiNT-C, Fe_{c1}-Au_{100}/TiNT-C, Fe_{c2}-Au_{100}/TiNT-C, Fe_{c3}-Au_{100}/TiNT-C, and Fe_{c4}-Au_{100}/TiNT-C at 400 rpm rotation rate. Counter electrode: Pt; electrolyte: 0.03 M $NaBH_4$ + 2 M NaOH; scan rate:10 mV s^{-1}; at 20 °C (±1 °C)

Figure 7.5 displays the linear sweep voltammetry results of various catalysts, including Au_{100}/TiNT-C, Fe_{c1}-Au_{100}/TiNT-C, Fe_{c2}-Au_{100}/TiNT-C, Fe_{c3}-Au_{100}/TiNT-C, and Fe_{c4}-Au_{100}/TiNT-C. The maximum current densities for these catalysts were measured as 5.1, 7.1, 6.4, 3.9, and 1.8 mA cm^{-2}, respectively. Coating the GC electrode with Au_{100}/TiNT-C catalyst ink and immersing it in a 0.001 M $Fe(SO_4)_{2(aq)}$ solution following the steps illustrated in **Figure 7.1** resulted in an increase in maximum current density to 7.1 mA cm^{-2} with the Fe_{c1}-Au_{100}/TiNT-C catalyst. This indicates that the presence of adsorbed Fe on Au_{100}/TiNT-C enhances catalytic activities for borohydride oxidation. However, using higher concentrations of $Fe(SO_4)_{2(aq)}$ for Fe adsorption on Au_{100}/TiNT-C tends to lead to a decrease in maximum current density from 7.1 to 1.8 mA cm^{-2} when concentration of the submerged $Fe(SO_4)_{2(aq)}$ solution increase from 0.001 to 0.016 M.

7.5 Bismuth (Bi)

For the LSV test, $Bi(NO_3)_{3(aq)}$ solutions were prepared in four different concentrations: 0.001 M, 0.002 M, 0.004 M, and 0.016 M. **Figure 7.1** provides an explanation of how the Bi_c-Au_{100}/TiNT catalyst, which is the bismuth adsorbed Au_{100}/TiNT-C catalyst, was prepared. The designations for the adsorption of Bi at different concentrations are Bi_{c1}-Au_{100}/TiNT-C for 0.001 M, Bi_{c2}-Au_{100}/TiNT-C for 0.002 M, Bi_{c3}-Au_{100}/TiNT-C for 0.004 M, and Bi_{c4}-Au_{100}/TiNT-C for 0.016 M.

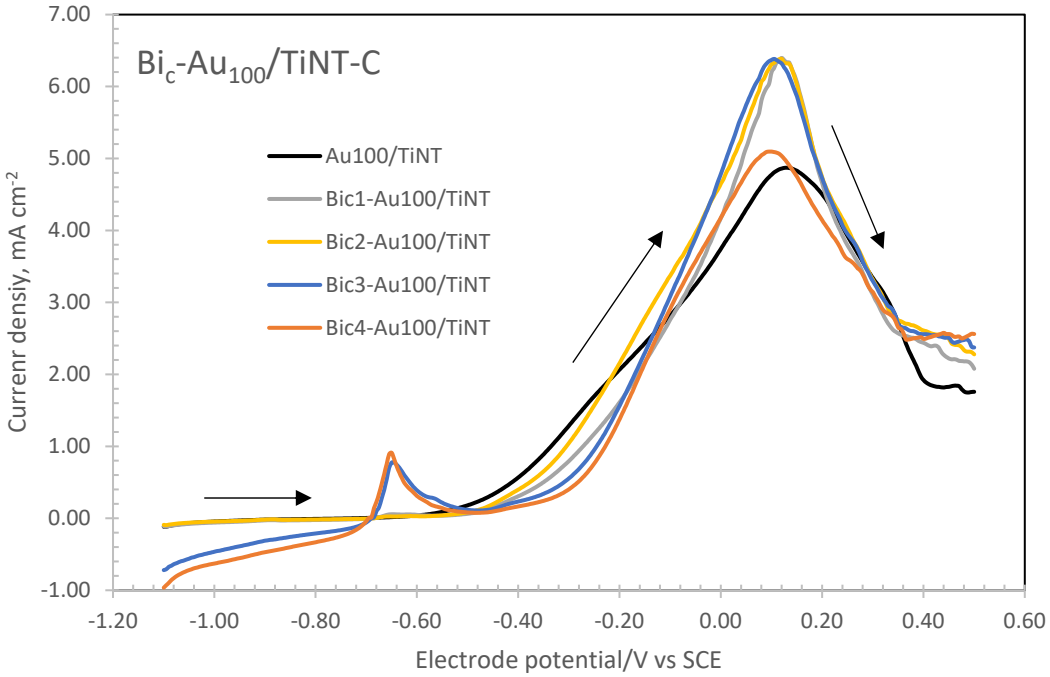

Figure 7.6: Linear sweep voltammetry of Au_{100}/TiNT-C, Bi_{c1}-Au_{100}/TiNT-C, Bi_{c2}-Au_{100}/TiNT-C, Bi_{c3}-Au_{100}/TiNT-C, and Bi_{c4}-Au_{100}/TiNT-C at 400 rpm rotation rate. Counter electrode: Pt; electrolyte: 0.03 M $NaBH_4$ + 2 M NaOH; scan rate:10 mV s^{-1}; at 20 ºC (±1 ºC)

In **Figure 7.6**, the results of linear sweep voltammetry for different catalysts are shown. These catalysts include Au_{100}/TiNT-C, Bi_{c1}-Au_{100}/TiNT-C, Bi_{c2}-Au_{100}/TiNT-C, Bi_{c3}-Au_{100}/TiNT-C, and Bi_{c4}-Au_{100}/TiNT-C. The maximum current densities for Bi_{c1}-Au_{100}/TiNT-C, Bi_{c2}-Au_{100}/TiNT-C, and Bi_{c3}-Au_{100}/TiNT-C catalysts were measured as nearly the same being 6.4 mA cm^{-2}, while the maximum current densities for Au_{100}/TiNT-C and Bi_{c4}-Au_{100}/TiNT-C were measured 4.8 and 5.2 mA cm^{-2}, respectively.

Coating the GC electrode with Au_{100}/TiNT-C catalyst ink and immersing it in a 0.001 M $Bi(NO_3)_{3(aq)}$ solution following the steps shown in **Figure 7.1** resulted in an increase in maximum current density to 6.4 mA cm^{-2} with the Bi_{c1}-Au_{100}/TiNT-C catalyst. This indicates that the presence of adsorbed Bi on Au_{100}/TiNT enhances catalytic activities for borohydride oxidation. When 0.002 M and 0.004 M $Bi(NO_3)_{3(aq)}$ solutions were used for Bi adsorption on Au_{100}/TiNT-C catalyst ink coated GC electrode, measured maximum current density stayed at 6.4 mA cm^{-2} as it was measured value for Bi_{c1}-Au_{100}/TiNT-C. This is probably resulted from saturation of surface with adsorbed Bi^{3+} ions at 0.001 M concentration. This might indicate that adsorption of Bi^{3+} ions on titanate nanotube surface is limited with small amount. However, the maximum current density fell to 5.2 mA cm^{-2} with Bi_{c4}-Au_{100}/TiNT-C catalyst when the concentration rises from 0.004 to 0.016 M. This decrease in maximum current density suggests

that more Bi^{3+} ions are forced to adsorbed on the catalyst surface with the increase of concentration, causing Au nanoparticles coverage and preventing their contact to borohydride ions.

7.6 Lead (Pb)

In order to carry out the LSV test, four concentrations of $Pb(NO_3)_{2(aq)}$ solution were prepared. These concentrations included 0.001 M, 0.002 M, 0.004 M, and 0.016 M $Pb(NO_3)_{2(aq)}$. **Figure 7.1** provides a brief explanation of how the Pb_c-Au_{100}/TiNT-C catalyst, which is the lead adsorbed Au_{100}/TiNT-C catalyst, was prepared. The abbreviations used for the adsorption of Pb at different concentrations are as follows: Pb_{c1}-Au_{100}/TiNT-C for 0.001 M, Pb_{c2}-Au_{100}/TiNT-C for 0.002 M, Pb_{c3}-Au_{100}/TiNT-C for 0.004 M, and Pb_{c4}-Au_{100}/TiNT-C for 0.016 M.

Figure 7.7 depicts the linear sweep voltammetry results of developed catalysts. The measured maximum current densities for Au_{100}/TiNT-C, Pb_{c1}-Au_{100}/TiNT-C, Pb_{c2}-Au_{100}/TiNT-C, Pb_{c3}-Au_{100}/TiNT-C, and Pb_{c4}-Au_{100}/TiNT-C were 6.3, 4.8, 4.0, 3.6, and 2.3 mA cm^{-2}, respectively. It is clearly seen that the Au_{100}/TiNT-C catalyst exhibits the highest maximum current density. By coating the Au_{100}/TiNT-C catalyst ink on a GC electrode and immersing it in a 0.001 M $Pb(NO_3)_{2(aq)}$ solution following the steps shown in **Figure 7.1**, the maximum current density decreased from 6.3 to 4.8 mA cm^{-2} with the Pb_{c1}-Au_{100}/TiNT-C catalyst. This demonstrates that the presence of adsorbed Pb on Au_{100}/TiNT-C worsening the catalytic activity for borohydride oxidation. It is important to note that the maximum current density continues to decrease when higher concentrations of $Pb(NO_3)_{2(aq)}$ are used for Pb adsorption on Au_{100}/TiNT-C. It can be concluded Pb acts as inhibitor for borohydride oxidation when it is presence in catalyst texture.

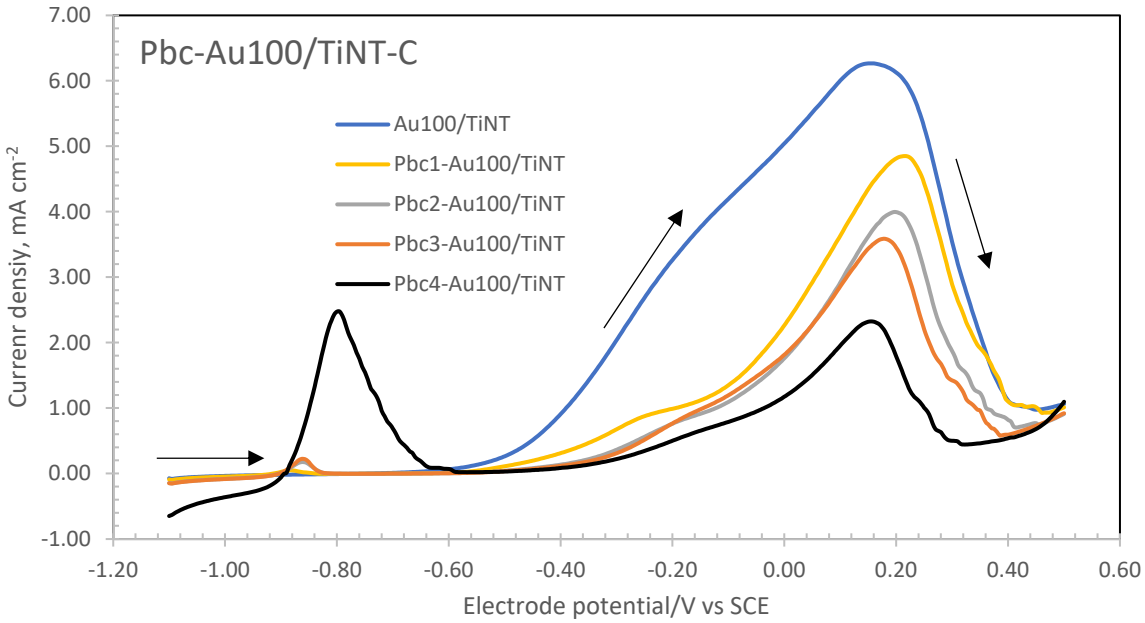

Figure 7.7: Linear sweep voltammetry of Au_{100}/TiNT-C, Pb_{c1}-Au_{100}/TiNT-C, Pb_{c2}-Au_{100}/TiNT-C, Pb_{c3}-Au_{100}/TiNT-C, and Pb_{c4}-Au_{100}/TiNT-C at 400 rpm rotation rate. Counter electrode: Pt; electrolyte: 0.03 M $NaBH_4$ + 2 M NaOH; scan rate:10 mV s^{-1}; at 20 ºC (±1 ºC)

Chapter 8: CONCLUSION

The study will be concluded in this chapter by summarizing the significant research findings in relation to the research aims and questions, along with their value and contribution. Additionally, the study's limitations will be reviewed, and suggestions for future research opportunities will be proposed.

Fuel cells, particularly direct borohydride fuel cells, potentially offer a more efficient way to convert stored chemical energy into electricity compared to traditional methods. These cells do not require combustion or mechanical converters like turbines. Sodium borohydride fuel cell, a promising device for electricity generation which is predominantly reliant on fossil fuels, can be used for small or medium-scale power applications such as portable devices, remote power systems, or power backup. The use of sodium borohydride in an aqueous solution for these kind of fuel cells simplifies fuel handling, making the design process easier from an engineering standpoint. However, the commercialization of direct borohydride fuel cells is hindered by challenges related to anode catalyst development. These challenges include the hydrolysis of borohydride, the high cost of anode catalysts due to their reliance on noble metals, issues with fuel crossover, and concerns about the stability of the anode catalyst.

8.1 Synthesis of Titanate Nanotubes

Titanate nanotubes synthesized by wet chemical method was chosen as the catalyst support due to its unique properties. First, titanate nanotubes has good stability in highly acidic or basic mediums. This virtue of titanate nanotubes is essential for direct borohydride fuel cell, which operates at a pH of over 12. Second, titanate nanotubes has high specific surface area per unit weight (252 m^2 g^{-1}). This characteristic makes titanate nanotubes a good catalyst substrate for active catalyst dispersion on the catalyst support and provides an efficient utilization of deposited active catalysts per weight during cell operation. Third, strong interaction between titanate nanotubes and active catalysts nanoparticles. This property ensures an evenly distribution of active catalyst nanoparticles on titanate nanotubes and prevents agglomeration of active catalyst nanoparticles. Forth, abundance of titanium oxide makes it cost-effective catalyst support. Due to this, the catalyst cost can be reduced to a certain level.

Titanate nanotubes were synthesized by wet chemical method from anatase grade of TiO_2. This synthesized titanate nanotubes was used as substrate for active catalyst nano particles. A

detailed explanation of the process was provided under section **3.4**. Following that deposition of metals onto titanate nanotubes were conducted.

8.2 Deposition of Gold, Nickel, Cobalt, and Cupper on Titanate Nanotubes

Deposition of gold, nickel, cobalt, and copper onto titanate nanotubes was carried out using the ion-exchange deposition-reduction method separately. In this method, ethylenediamine was used as a catalytic agent to enhance the adsorption of metal ions on titanate nanotubes. Colorimetric analysis was employed to determine the quantity of adsorbed metal on titanate nanotubes. Briefly, the absorbance of standard solutions for each metal was measured using UV-visible spectroscopy, and the absorbance spectrum of metal solutions was recorded between 190 and 700 nm, reaching characteristic peak values for each solution in the studied spectrum range. These distinctive peak values appeared on absorbance spectrum for each metal solution were chosen in determination of calibration curve. The peak absorbance values used were 305 nm for $[Au(en)_2]CI_3$, 545 nm for $[Ni(en)_3](NO_3)_2$, 355 nm for $[Co(en)_3](NO_3)_2$, and 545 nm for $[Cu(en)_2](NO_3)_2$ metal solutions, respectively. Obtained calibration curves for the mentioned metal solution were used to determine remaining metal solution after deposition of each metal on titanate nanotubes. Considering the volume of solutions, initial concentration, remaining concentration, and the amount of titanate nanotubes added to each solution, the adsorbed metal mass on titanate nanotubes was calculated quantitively.

After deposition of studied metals on titanate nanotube, findings show that maximum deposition of gold, nickel, cobalt, and copper on titanate nanotubes were as 17.28, 2.11, 3.65, 4.00 in weight percentage, respectively. Here, most distinctive result belongs to gold deposition on titanate nanotubes, outperforming other metal deposition at least 4 time. In this method, adsorption isotherms of each metal were obtained. Later, these isotherms were used to generate coloration between catalyst loading and initial concentration of metal solutions. Using this coloration between initial concentration and adsorbed metal loading, gold-metal composite catalysts namely Au-Ni/TiNT, Au-Co/TiNT, and Au-Cu/TiNT were synthesized at different molar ratios on titanate nanotubes surface with a total 4 percent (in weight) metal loading. To the best knowledge of the author, this deposition method was used to decorate titanate nanotube surface by the mentioned metals for the first time. Later, these synthesized composited catalysts were tested in borohydride oxidation by cyclic voltammetry (CV), linear sweep voltammetry (LSV), and chronoamperometry (CA).

8.3 Electrochemical Characterization of Developed Catalysts

8.3.1 Cyclic Voltammetry

Cyclic voltammetry was used to investigate the oxidation pattern of borohydride on both forward and backward scans. This investigation was carried out using an Au rotating disc electrode, a Pt rotating disc electrode, and glassy carbon electrodes coated with the developed electrocatalyst ink within a potential range between -1.1 and +0.5 V *vs* SCE.

Research employing a Pt disc electrode has demonstrated that the oxidation of borohydride on Pt follows a complex pathway involving multiple electron transfer steps, resulting in the appearance of multiple oxidation peaks on the cyclic voltammetry curve. A sharp peak detected near -1 V on the forward scan is associated with H_2 oxidation originating from borohydride dissociation on the Pt electrode. A broad peak was observed on forward scan around -0.15 V *vs* SCE, which is linked to direct oxidation of borohydride. On the other hand, only one peak appeared on reverse scan at -0.38 V, which is proposed to be direct oxidation of borohydride or the oxidation of adsorbed intermediates, such as BH_3OH^-.

Studies conducting an Au disc electrode has showed three distinctive oxidation peaks on the cyclic voltammogram. The first peak was observed at -0.40 V *vs* SCE was associated with direct oxidation of borohydride. In contrast to the Pt rotating disc electrode, the Au rotating disc CV curve does not show an oxidation peak at around -0.8 V, which is typically linked to H_2 oxidation originated from borohydride hydrolysis. The second peak appeared at +0.25 V *vs* SCE associated with oxidation of adsorbed intermediates, such as BH_3OH^-.

The results of the cyclic voltammetry experiments conducted with developed Au_{100}/TiNT-C, Au-Ni/TiNT-C, Au-Co/TiNT-C, and Au-Cu/TiNT-C catalysts revealed that only one broad oxidation peak appeared on cyclic voltammetry curve, which is associated with the direct oxidation of borohydride starting at around -0.45 V *vs* SCE during the forward scan. This finding supports the idea that developed electrocatalyst show minimal activity or no activity for unwanted borohydride hydrolysis. However, during the reverse scan, an additional oxidation peak is observed at +0.20 V *vs* SCE, similar to those of Au disc electrode, which is attributed to the oxidation of adsorbed intermediates like BH_3OH^-.

8.3.2 Linear Sweep Voltammetry

Linear sweep voltammetry findings indicate that the addition of nickel and cobalt to the catalysts texture with gold improves the electrocatalytic activities of developed catalysts. In contrast, addition of copper worsens catalytic activities of the catalysts. Catalytic performance

of Au-Ni/TiNT-C catalysts in borohydride oxidation outperforms those of Au-Co/TiNT-C, and Au-Cu/TiNT-C catalysts. Among the Au-Ni/TiNT-C catalysts, superior performance is demonstrated by $Au_{80}Ni_{20}$/TiNT-C. Using linear sweep voltammetry, diffusion coefficient number, D, and kinetic parameters such as transferred electron numbers, *n*, and apparent rate constant, *k*, were determined.

Using gold rotating disc electrode, diffusion coefficient number, D, obtained as 1.77×10^{-5} cm^2 s^{-1} for borohydride ions in 2 M NaOH solution. Calculated D values for developed catalyst namely Au-Ni/TiNT-C, Au-Co/TiNT-C, and Au-Cu/TiNT-C were 2.18×10^{-6}, 1.01×10^{-6}, and 1.56×10^{-6}, 1.77×10^{-5} cm^2 s^{-1}, respectively.

Transferred electron numbers calculated for Au-Ni/TiNT-C for borohydride oxidation were close to theoretical $8e^-$. For instance, these obtained electron numbers at -0.15 V *vs* SCE were 7.6, 8.6, 7.5, and 7.5 for $Au_{80}Ni_{20}$/TiNT-C, $Au_{60}Ni_{40}$/TiNT-C, $Au_{40}Ni_{60}$/TiNT-C, and $Au_{20}Ni_{80}$/TiNT-C, respectively. In terms of Au-Co/TiNT-C catalysts, number of electrons exchanged in borohydride oxidation at the same potential mentioned before found to be as 7.9, 6.4, 8.1, and 5.9 for the following order of catalysts $Au_{80}Co_{20}$/TiNT-C, $Au_{60}Co_{40}$/TiNT-C, $Au_{40}Co_{60}$/TiNT-C, and $Au_{20}Co_{80}$/TiNT-C. As it can be understood from these transferred electron numbers, some of Au-Co/TiNT-C catalysts have low faradic efficiency, providing low number of electrons exchanged especially $Au_{60}Co_{40}$/TiNT-C and $Au_{20}Co_{80}$/TiNT-C. When it comes to Au-Cu/TiNT-C catalysts, transferred electron numbers in borohydride oxidation at -0.15 V *vs* SCE were 3.8, 3.9, 1.1, and 1.3 for $Au_{80}Cu_{20}$/TiNT-C, $Au_{60}Cu_{40}$/TiNT-C, $Au_{40}Cu_{60}$/TiNT-C, and $Au_{20}Cu_{80}$/TiNT-C, respectively. These results show that Au-Cu/TiNT-C catalysts show poor catalytic performance by providing low electrons of exchanged in borohydride oxidation.

Apparent rate constant, *k,* was calculated from the data collected linear sweep voltammetry measurements. For Au_{100}/TiNT-C, the rate constant was obtained as 0.003 cm s^{-1} being the same at all potential values. On the other hand, *k* values varied depending on the potential for Au-Ni/TiNT-C, Au-Co/TiNT-C, and Au-Cu/TiNT-C catalysts. **Table 4.7**, **Table 5.4**, and **Table 6.4** can be examined to see all calculated *k* values at different potentials for these catalysts. However, apparent rate constant, *k*, was higher obtained for Au-Ni/TiNT-C and Au-Co/TiNT-C catalysts, suggesting that catalytic activities improved compared to Au_{100}/TiNT-C catalyst. Au-Cu/TiNT-C catalysts have similar k values with those of Au-Ni/TiNT-C and Au-

Co/TiNT-C catalysts for $Au_{80}Cu_{20}$/TiNT-C and $Au_{60}Cu_{40}$/TiNT-C, but $Au_{40}Cu_{60}$/TiNT-C and $Au_{20}Cu_{80}$/TiNT-C catalysts have unreasonably high k values.

8.3.3 Chronoamperometry

Chronoamperometry was another method which used to evaluate catalytic activities of the developed catalysts. Chronoamperometric measurements of the catalysts were carried out applying constant voltage chosen as peak current potential and recording corresponding current for 200 seconds test period. End of this measurement period, all Au-Ni/TiNT-C catalysts show better stability generating higher current densities than to Au_{100}/TiNT-C catalyst. Additionally, some of Au-Co/TiNT-C catalysts namely $Au_{60}Co_{40}$/TiNT-C and $Au_{40}Co_{60}$/TiNT-C also showed better stability than Au_{100}/TiNT-C catalyst. $Au_{80}Co_{20}$/TiNT-C and $Au_{20}Co_{80}$/TiNT-C exhibited similar stability with Au_{100}/TiNT-C.

8.4 Limitations and Suggested Future Works

Low adsorption of nickel, cobalt, and copper metals on titanate nanotubes surface limits full potential of utilization of composite catalysts in borohydride oxidation. Surface structure of titanate nanotubes might be improved for more metal deposition on it. Thereby, catalytic activities of developed composite catalysts improve for borohydride oxidation. Au-Ni/TiNT-C and Au-Co/TiNT-C composite catalysts reveal that using gold with these two metals improve catalytic activities towards borohydride oxidation. If further improvement is done for more metal deposition on titanate nanotubes, it has a potential to be utilized as anode catalyst in direct borohydride fuel cell.

Being in the highest oxidation state, most metal oxides exhibit poor electrical conductivity. Another important factor to consider is that the electrical conductivity of titanium oxide is considerably low, limiting the full potential of the developed electrocatalyst in borohydride oxidation. To increase electrical conductivity and overcome to this limitation, active metal decorated titanate nanotubes was mixed with carbon black. This method improved electrical conductivity to a certain level. However, maximum current densities of developed catalysts in borohydride oxidation were still not in an acceptable range to be considered as commercial value. There are different methods to change electrical conductivity of titanium oxide. In this respect, sub-stoichiometric form of titanium oxide, or metal doped titanium oxide might be considered to increase electrical conductivity of titanium oxide. In sub-stoichiometric method, oxygen vacancies are obtained in titanium oxide structure, and can be shown as Ti_nO_{2n-1} formula. These oxygen vacancies in the titanium oxide structure can lower the band gap for

electrons and thus increase electrical conductivity of titanium oxide. Metal dopped titanium oxide reported that this method improves electrical conductivity of titanium oxide to a certain level. In this method, mostly niobium (Nb) metal used as doped metal to titanium oxide structure. These two methods can be considered for future projects to increase titanate nanotube electrical conductivity of titanate nanotubes to obtain higher maximum current densities for borohydride oxidation.

A complete fuel cell setup is suggested to test performance of developed Au-Ni/TiNT-C, and Au-Co/TiNT-C catalysts. In this regard, the catalyst ink can be applied on carbon clothes or 3-D porous substrates such as nickel or titanium metal to prepare anode catalyst for borohydride oxidation. Based on the literature research, suggested anolyte composition for sodium borohydride and sodium hydroxide concentration can be selected as 1 M $NaBH_4$ and 3 M NaOH, respectively. At the cathode compartment, commercially available Pt decorated carbon clothes can be used as cathode catalyst for oxygen reduction. Hydrogen peroxide is suggested as catholyte with a composition of 2 M H_2O_2 and 0.5 M H_2SO_4. This complete cell test might have importance if considerable power output is achieved.

Chapter 9: Appendix

9.1 Appendix A: additional graphs, tables, and information for CV, LSV, and Koutecky-Levich plots used to calculate *n* and *k* values for Au-Ni/TiNT

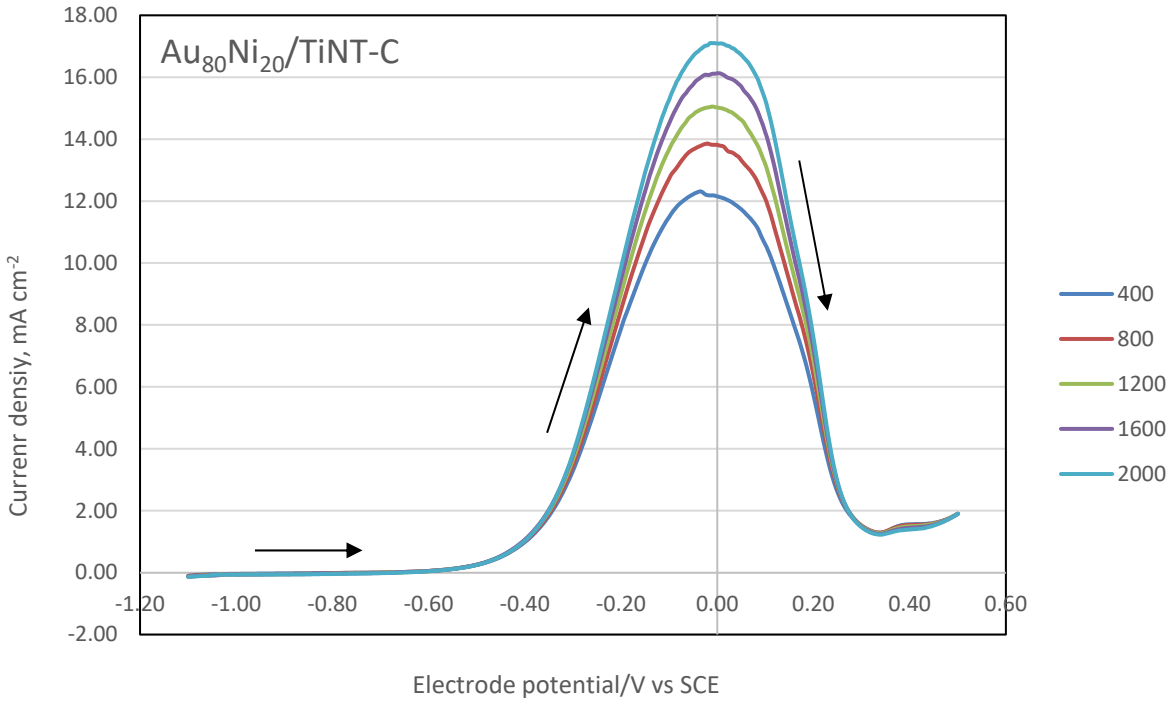

Figure 9.1: Linear sweep voltammograms (LSV) of $Au_{80}Ni_{20}$/TNT-C coated glassy carbon disc electrode at different rotation rates. Counter electrode: Pt; electrolyte: 0.03 M $NaBH_4$ + 2 M NaOH; scan rate:10 mV s^{-1}; at 20 ºC (±1 ºC)

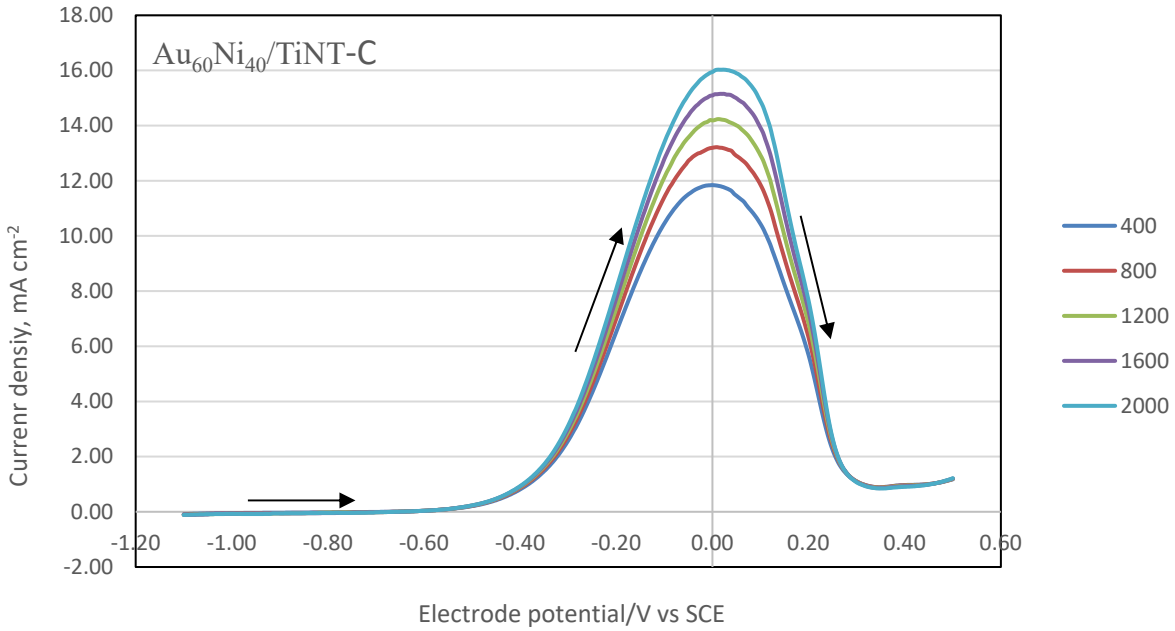

Figure 9.2: Linear sweep voltammograms (LSV) of $Au_{60}Ni_{40}$/TNT-C coated glassy carbon disc electrode at different rotation rates. Counter electrode: Pt; electrolyte: 0.03 M $NaBH_4$ + 2 M NaOH; scan rate:10 mV s^{-1}; at 20 ºC (±1 ºC)

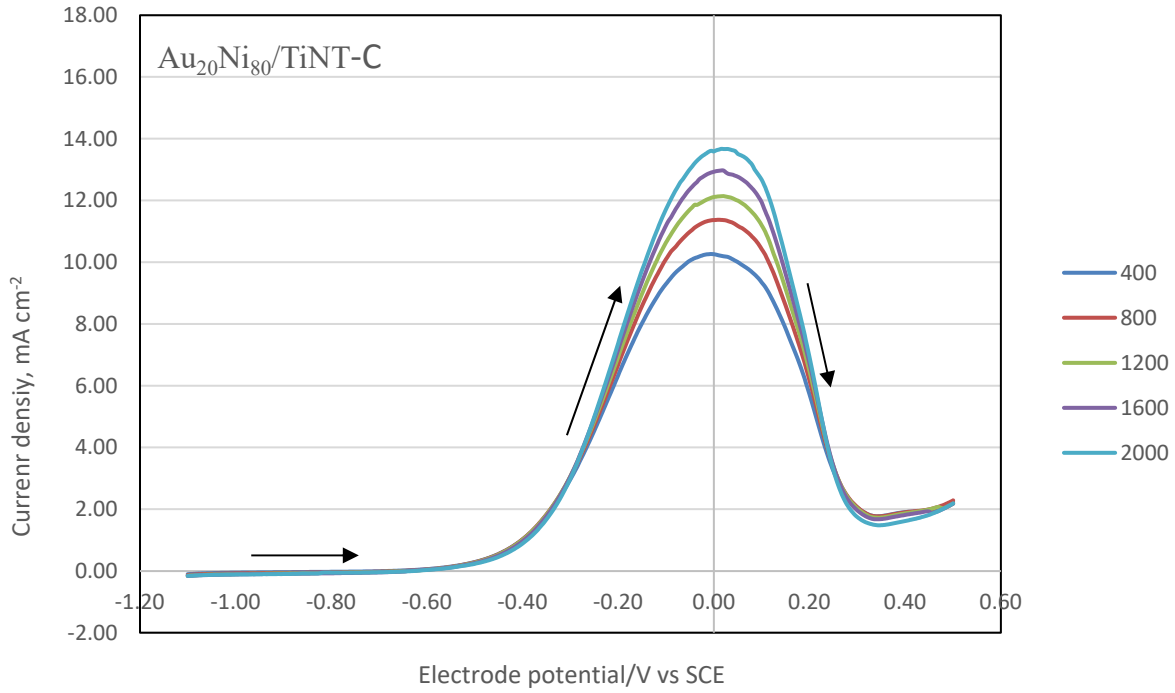

Figure 9.3: Linear sweep voltammograms (LSV) of $Au_{20}Ni_{80}$/TiNT-C coated glassy carbon disc electrode at different rotation rates. Counter electrode: Pt; electrolyte: 0.03 M $NaBH_4$ + 2 M NaOH; scan rate:10 mV s^{-1}; at 20 ºC (±1 ºC)

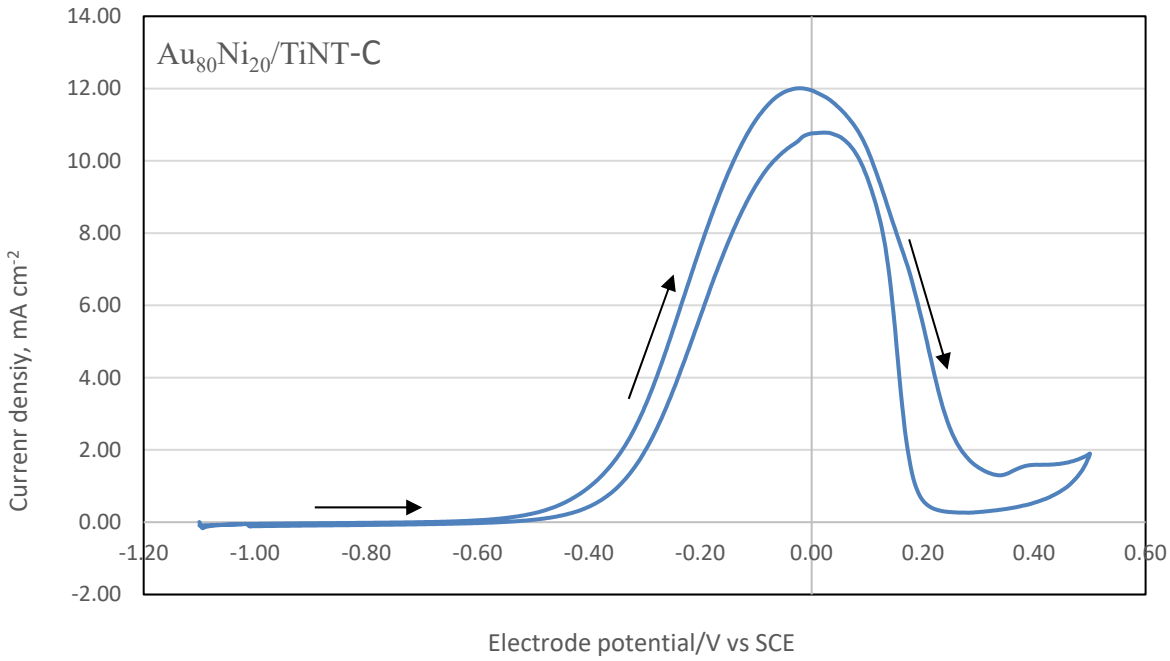

Figure 9.4: CV curve of $Au_{80}Ni_{20}$/TiNT-C electrode. Counter electrode: Pt; electrolyte: 0.03 M $NaBH_4$ + 2 M NaOH; scan rate:10 mV s^{-1}; disc rotation 400 rpm; at ambient temperature (20 ^oC ±1)

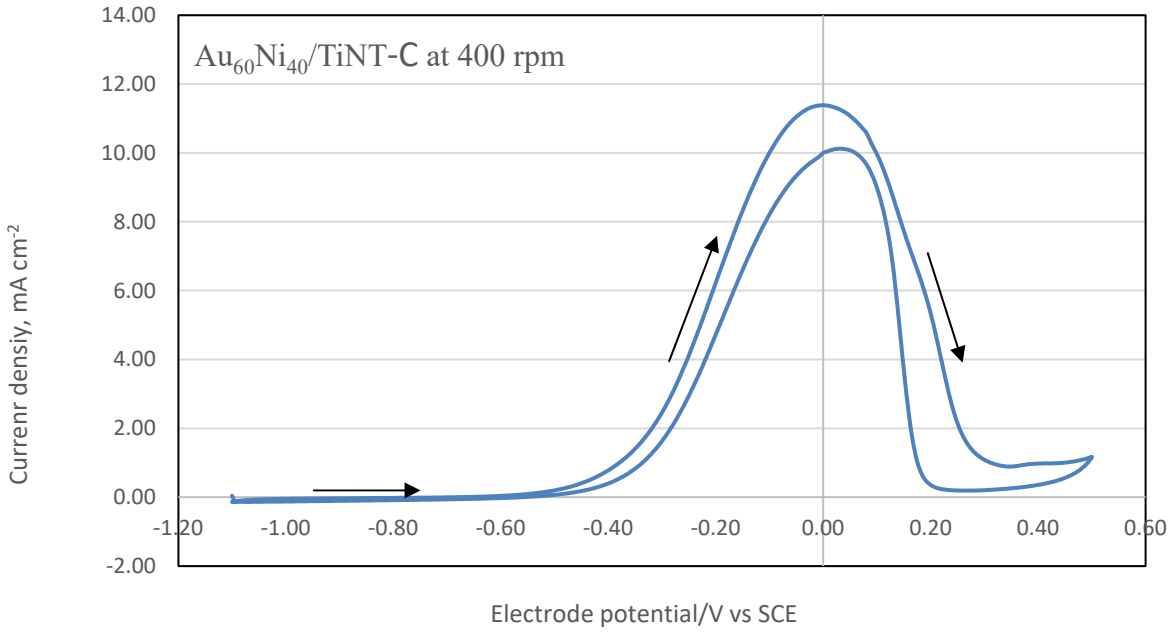

Figure 9.5: CV curve of $Au_{60}Ni_{40}$/TiNT-C electrode. Counter electrode: Pt; electrolyte: 0.03 M $NaBH_4$ + 2 M NaOH; scan rate:10 mV s^{-1}; disc rotation 400 rpm; at ambient temperature (20 ^oC ±1)

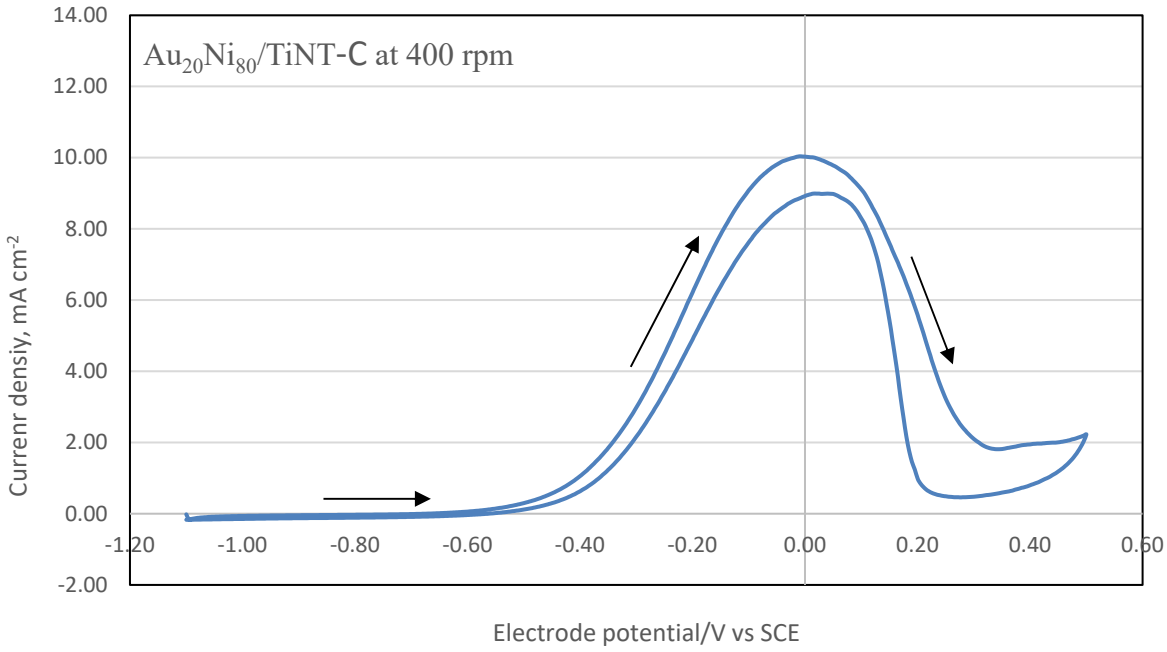

Figure 9.6: CV curve of $Au_{20}Ni_{80}$/TiNT-C electrode. Counter electrode: Pt; electrolyte: 0.03 M $NaBH_4$ + 2 M NaOH; scan rate:10 mV s^{-1}; disc rotation 400 rpm; at ambient temperature (20 ºC ±1)

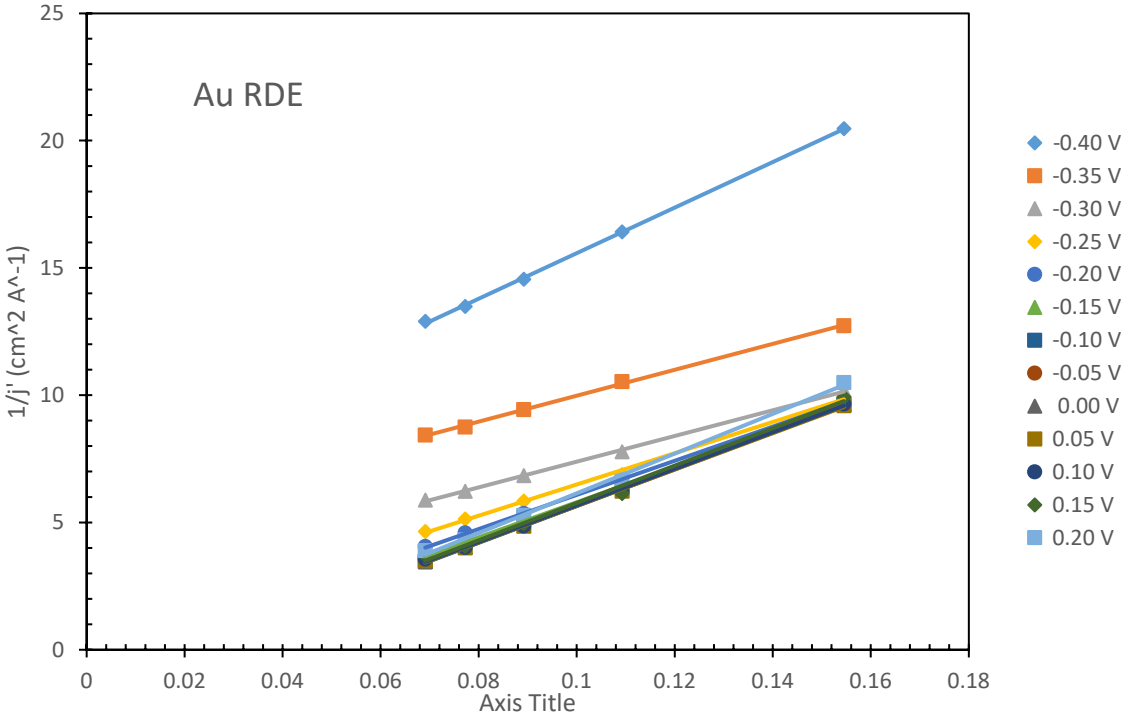

Figure 9.7: Koutecky-Levich plot of Au rotating disc electrode between -0.4 V and 0.2 V, Counter electrode: Pt; electrolyte: 0.03 M $NaBH_4$ + 2 M NaOH; scan rate:10 mV s^{-1}; at 20 ºC (±1 ºC)

Table 9.1: Obtained kinetic parameters from borohydride oxidation on Au disc electrode, using calculated D value.

Potential, V	n	k (cm s^{-1})
-0.40	4.4	0.012
-0.35	7.4	0.011
-0.30	8.0	0.018
-0.25	6.5	0.151
-0.20	5.9	-0.094
-0.15	5.7	-0.055
-0.10	5.5	-0.040
-0.05	5.5	-0.042
0.00	5.5	-0.040
0.05	5.5	-0.042
0.10	5.5	-0.042
0.15	5.4	-0.041
0.20	5.1	-0.041

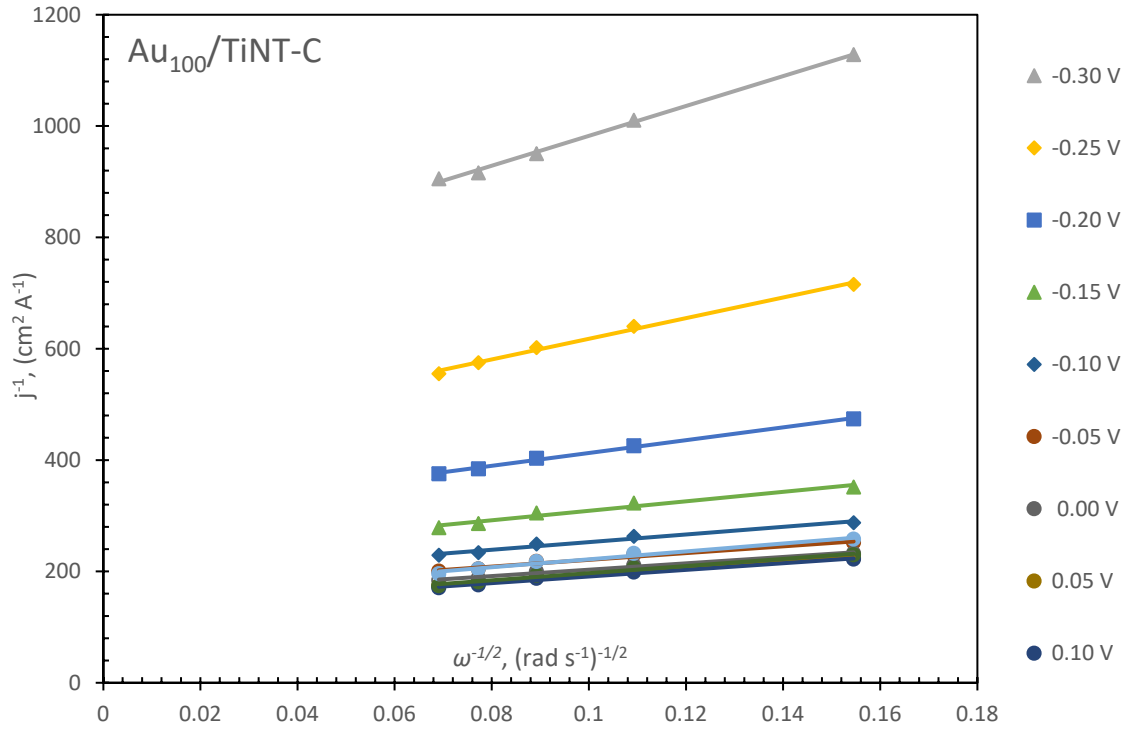

Figure 9.8: Koutecky-Levich plot of Au_{100}/TiNT-C electrode between -0.30 V and 0.10 V, Counter electrode: Pt; electrolyte: 0.03 M $NaBH_4$ + 2 M NaOH; scan rate:10 mV s^{-1}; at 20 ºC (±1 ºC)

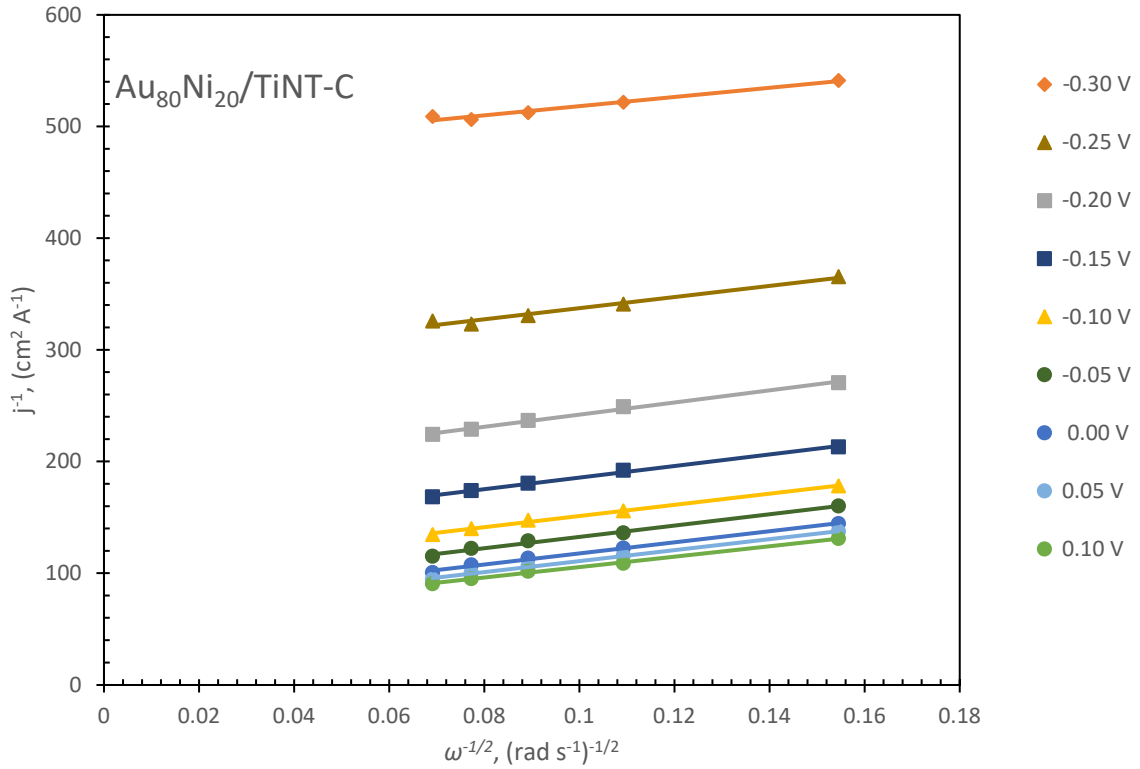

Figure 9.9: Koutecky-Levich plot of $Au_{80}Ni_{20}$/TiNT-C electrode between -0.30 V and 0.10 V, Counter electrode: Pt; electrolyte: 0.03 M $NaBH_4$ + 2 M NaOH; scan rate:10 mV s^{-1}; at 20 ºC (±1 ºC)

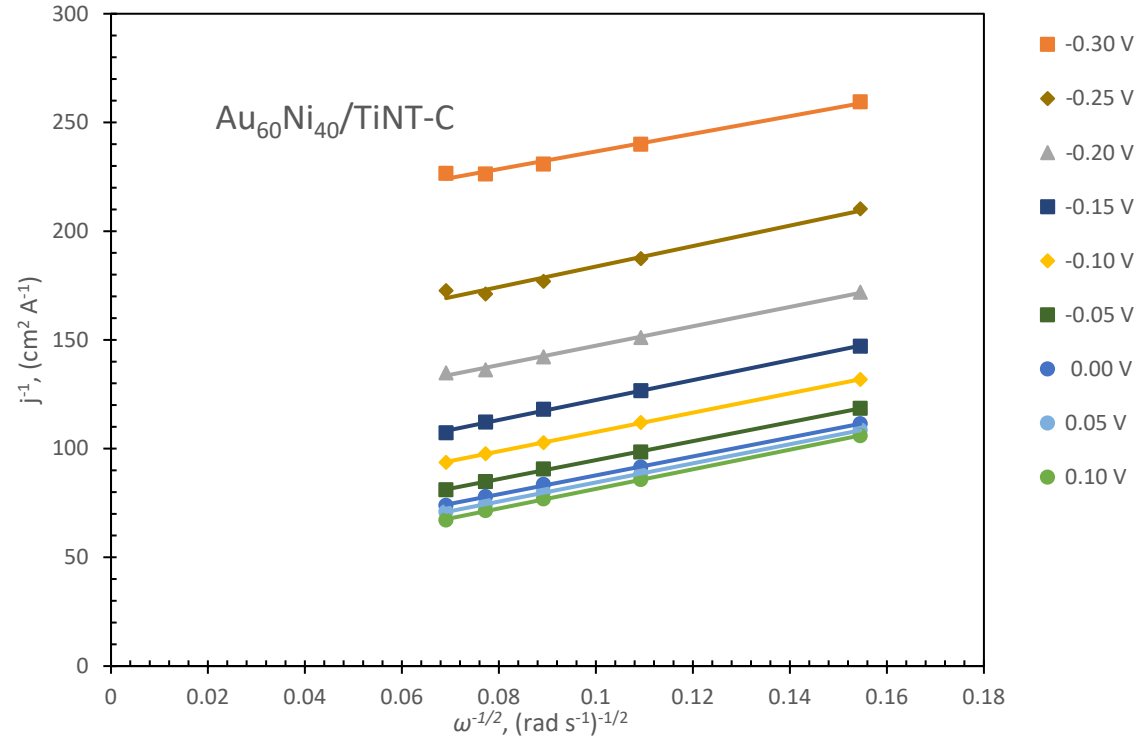

Figure 9.10: Koutecky-Levich plot of $Au_{60}Ni_{40}$/TiNT-C electrode between -0.30 V and 0.10 V, Counter electrode: Pt; electrolyte: 0.03 M $NaBH_4$ + 2 M NaOH; scan rate:10 mV s^{-1}; at 20 ºC (±1 ºC)

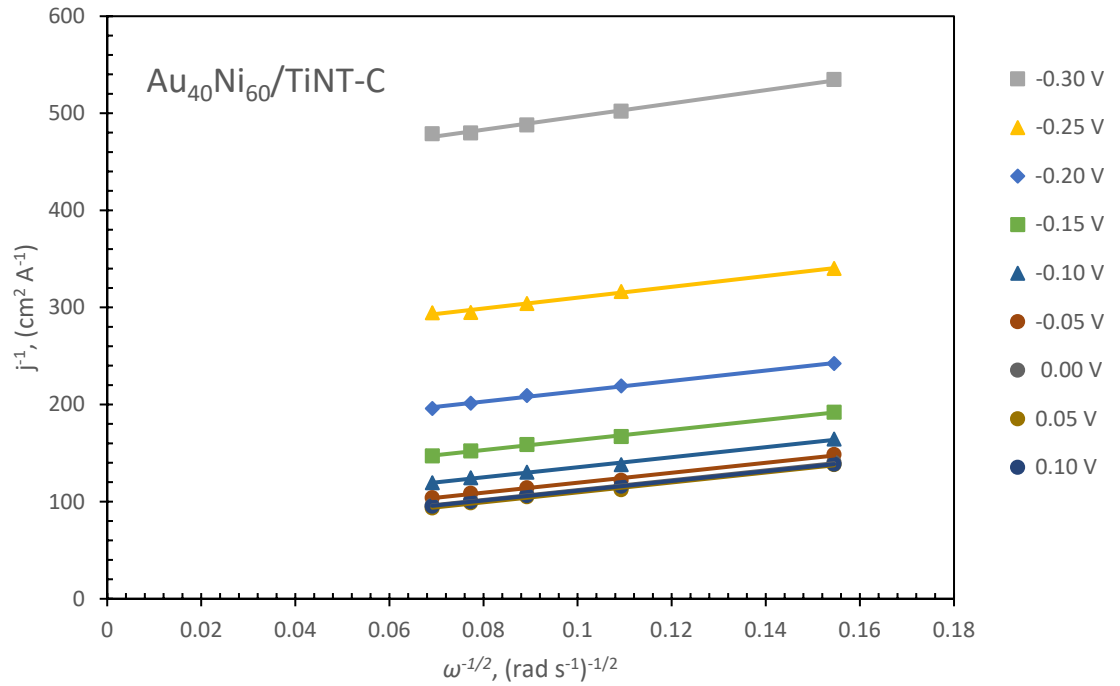

Figure 9.11: Koutecky-Levich plot of $Au_{40}Ni_{60}$/TiNT-C electrode between -0.30 V and 0.10 V, Counter electrode: Pt; electrolyte: 0.03 M $NaBH_4$ + 2 M NaOH; scan rate:10 mV s^{-1}; at 20 ºC (±1 ºC)

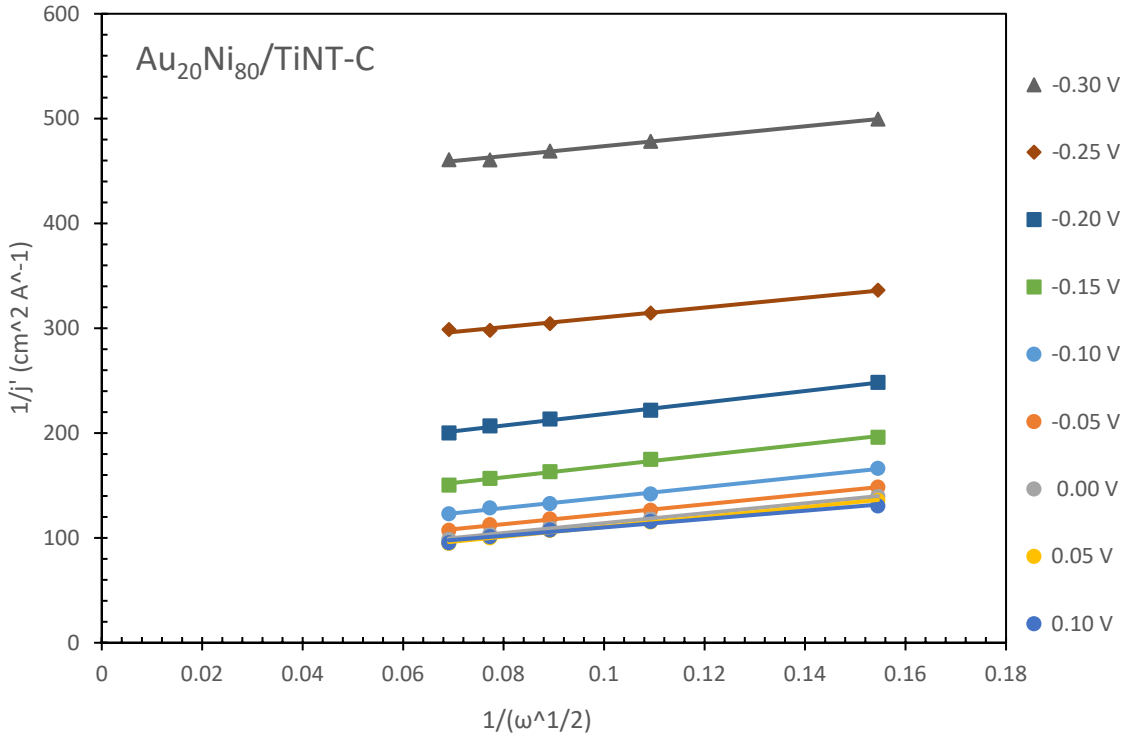

Figure 9.12: Koutecky-Levich plot of $Au_{20}Ni_{80}$/TiNT-C electrode between -0.30 V and 0.10 V, Counter electrode: Pt; electrolyte: 0.03 M $NaBH_4$ + 2 M NaOH; scan rate:10 mV s^{-1}; at 20 ºC (±1 ºC)

9.2 Appendix B: additional graphs, tables, and information for CV, LSV, and Koutecky-Levich plots used to calculate *n* and *k* values for Au-Co/TiNT

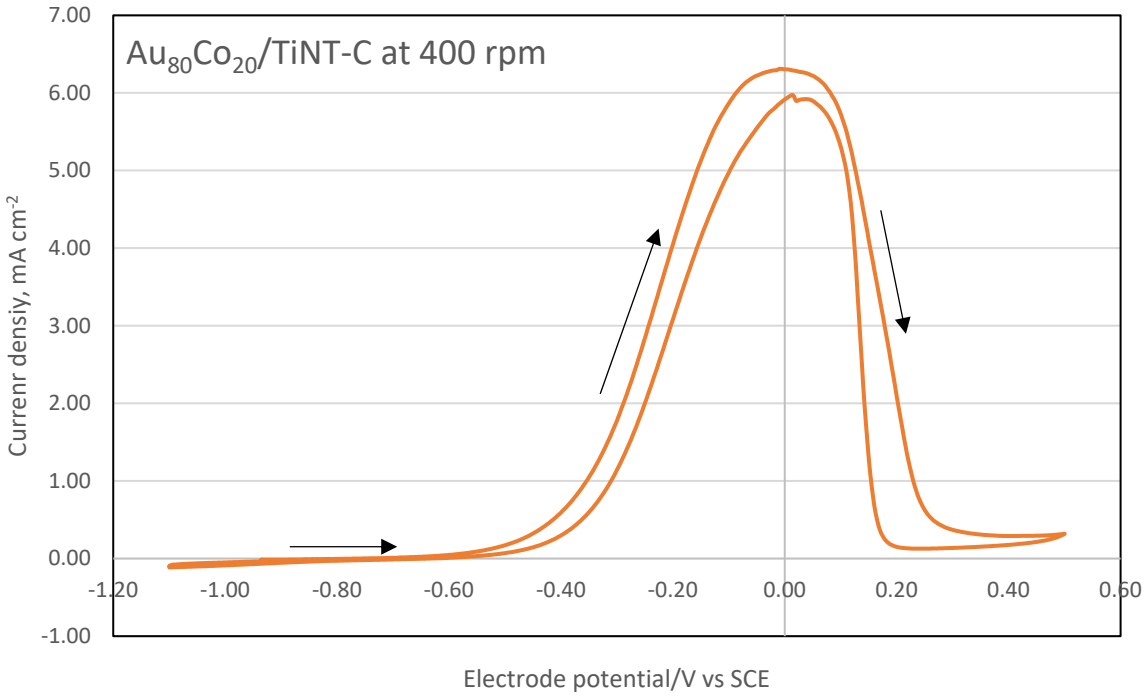

Figure 9.13: CV curve of $Au_{80}Co_{20}$/TiNT-C electrode. Counter electrode: Pt; electrolyte: 0.03 M $NaBH_4$ + 2 M NaOH; scan rate:10 mV s^{-1}; disc rotation 400 rpm; at ambient temperature (20 ºC ±1)

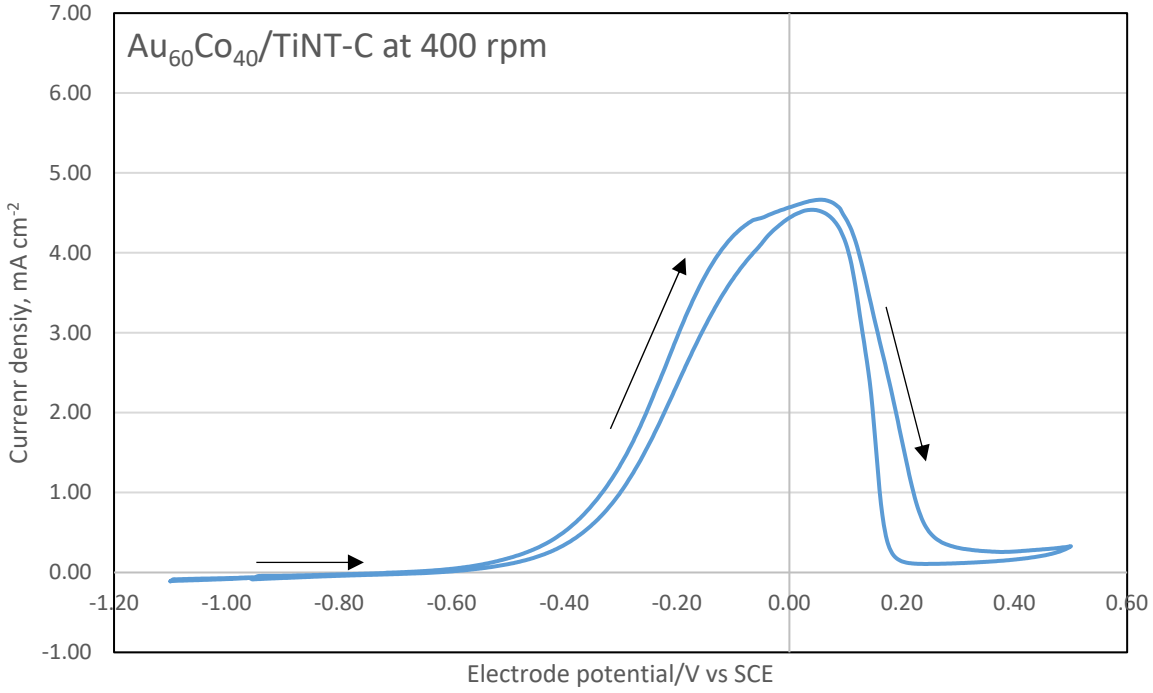

Figure 9.14: CV curve of $Au_{60}Co_{40}$/TiNT-C electrode. Counter electrode: Pt; electrolyte: 0.03 M $NaBH_4$ + 2 M NaOH; scan rate:10 mV s^{-1}; disc rotation 400 rpm; at ambient temperature (20 ºC ±1)

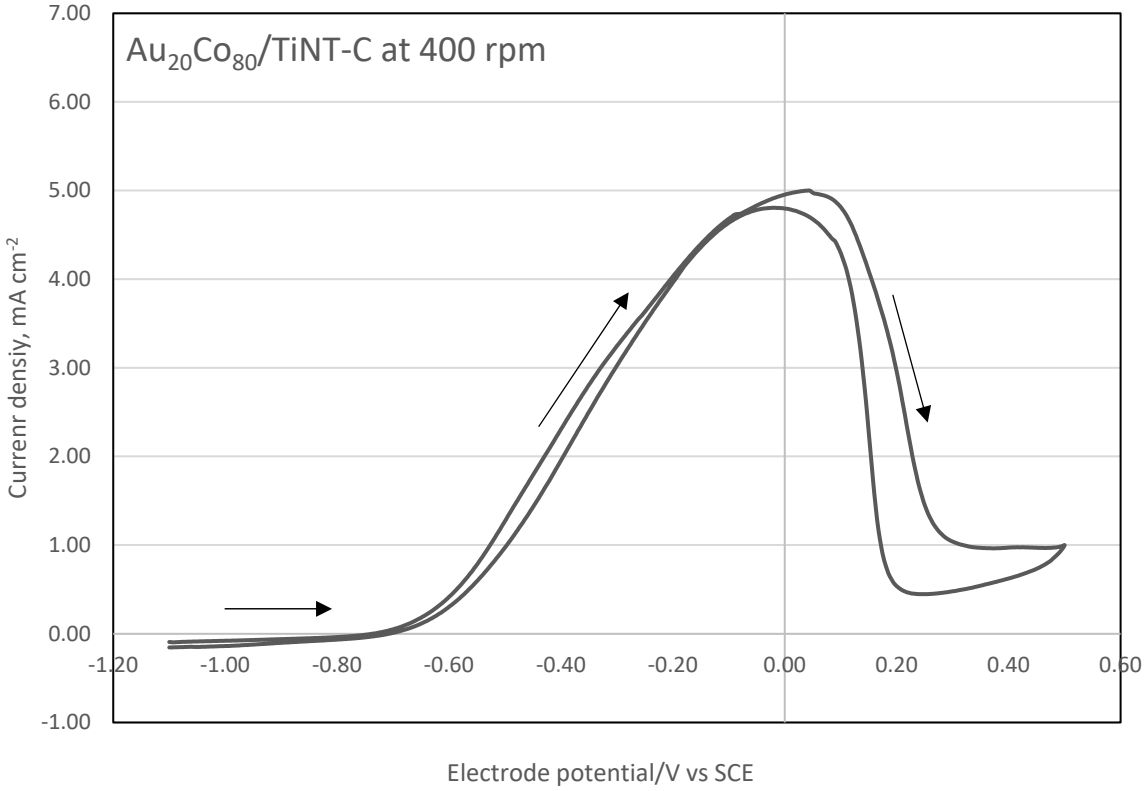

Figure 9.15: CV curve of $Au_{20}Co_{80}$/TiNT-C electrode. Counter electrode: Pt; electrolyte: 0.03 M $NaBH_4$ + 2 M NaOH; scan rate:10 mV s^{-1}; disc rotation 400 rpm; at ambient temperature (20 ^oC ±1)

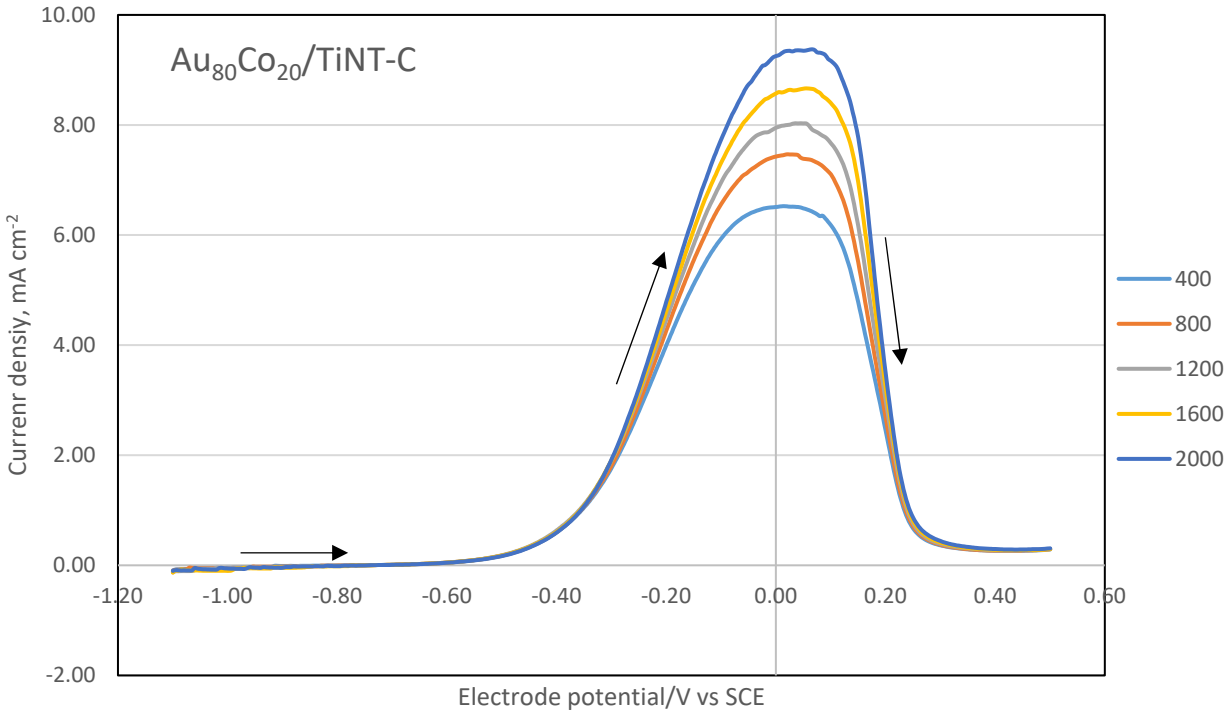

Figure 9.16: Linear sweep voltammograms of $Au_{80}Co_{20}$/TNT-C coated glassy carbon disc electrode at different rotation rates. Counter electrode: Pt; electrolyte: 0.03 M $NaBH_4$ + 2 M NaOH; scan rate:10 mV s^{-1}; at 20 ºC (±1 ºC)

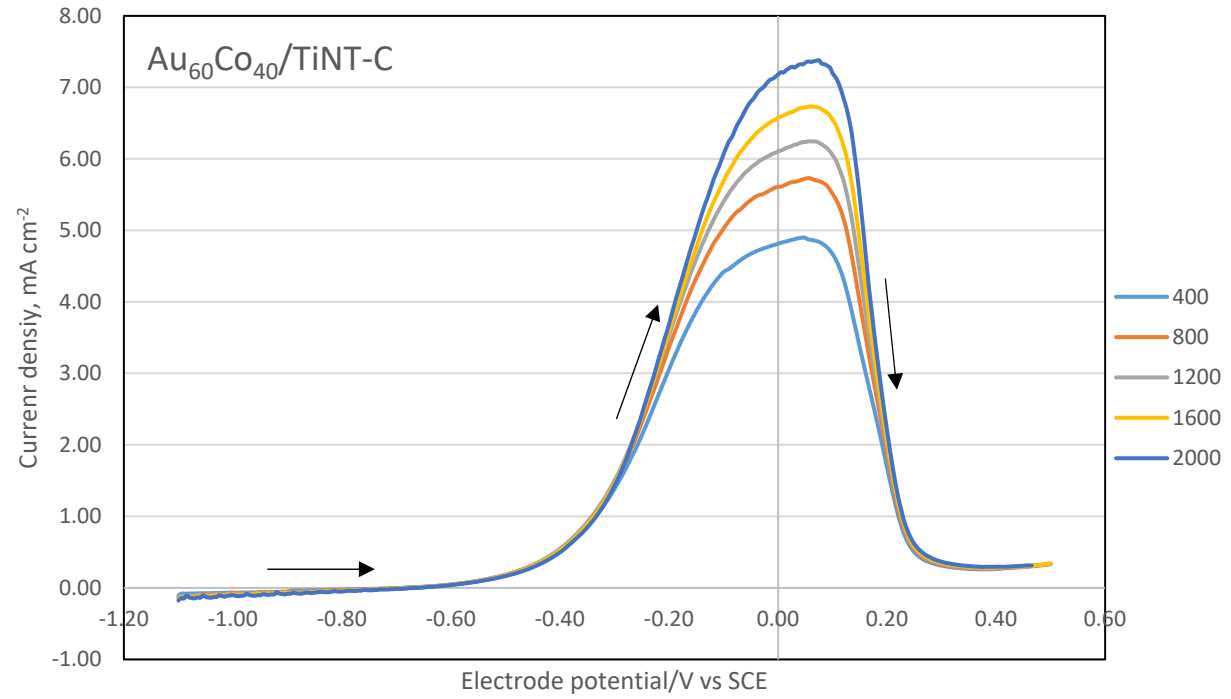

Figure 9.17: Linear sweep voltammograms of $Au_{60}Co_{40}$/TNT-C coated glassy carbon disc electrode at different rotation rates. Counter electrode: Pt; electrolyte: 0.03 M $NaBH_4$ + 2 M NaOH; scan rate:10 mV s^{-1}; at 20 ºC (±1 ºC)

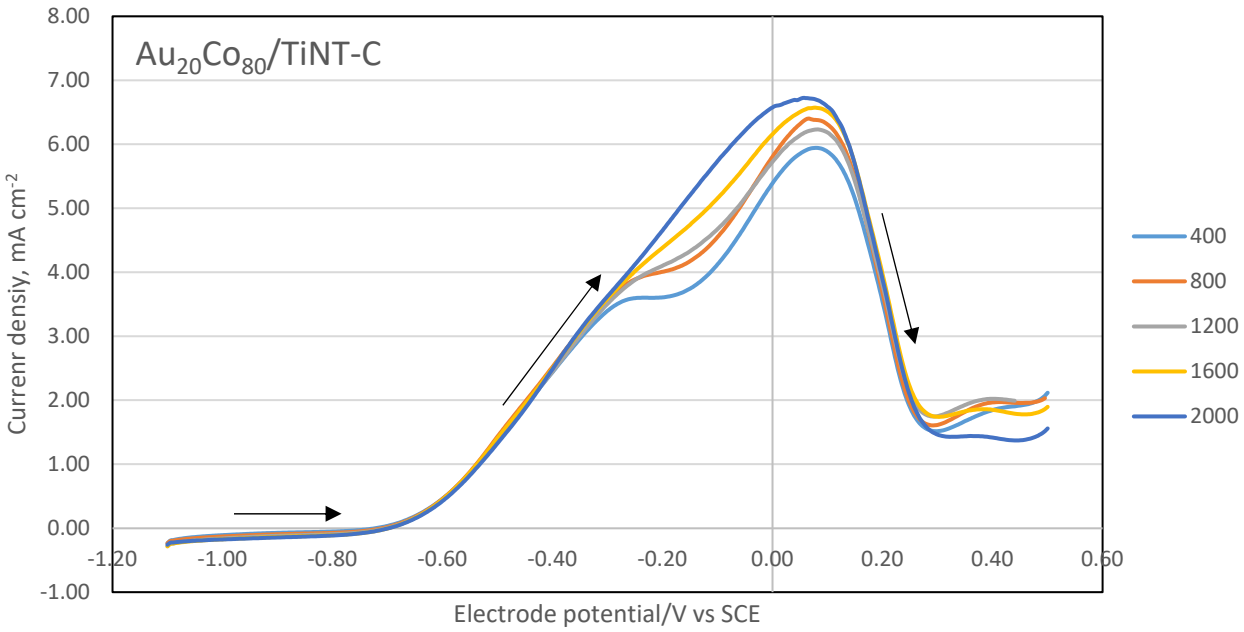

Figure 9.18: Linear sweep voltammograms of $Au_{20}Co_{80}$/TNT-C coated glassy carbon disc electrode at different rotation rates. Counter electrode: Pt; electrolyte: 0.03 M $NaBH_4$ + 2 M NaOH; scan rate:10 mV s^{-1}; at 20 ºC (±1 ºC)

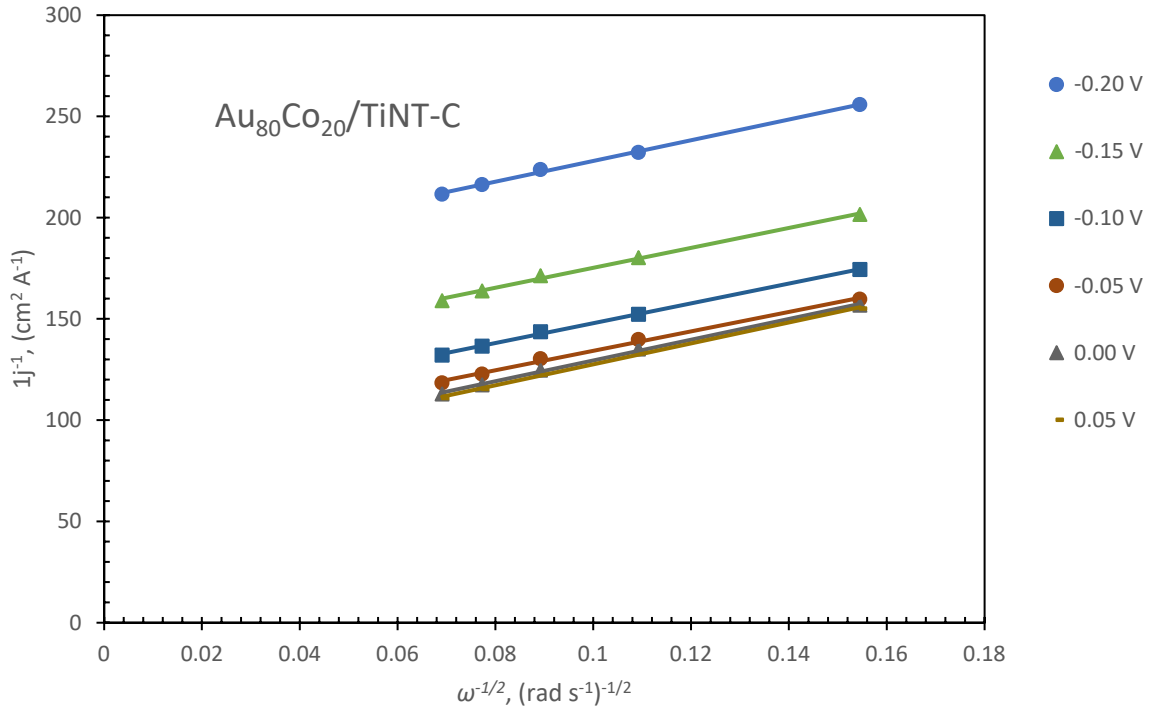

Figure 9.19: Koutecky-Levich plot of $Au_{80}Co_{20}$/TiNT-C between -0.20 V and 0.10 V, Counter electrode: Pt; electrolyte: 0.03 M $NaBH_4$ + 2 M NaOH; scan rate: 10 mV s^{-1}; at 20 ºC (±1 ºC)

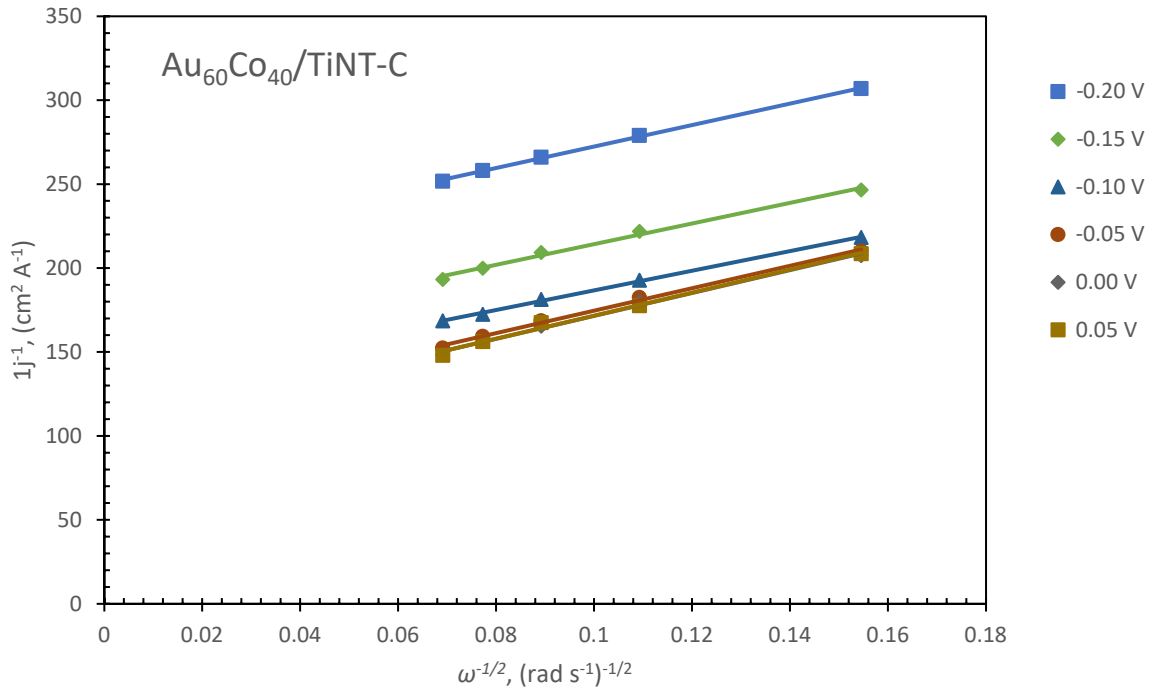

Figure 9.20: Koutecky-Levich plot of $Au_{60}Co_{40}$/TiNT-C between -0.20 V and 0.10 V, Counter electrode: Pt; electrolyte: 0.03 M $NaBH_4$ + 2 M NaOH; scan rate: 10 mV s^{-1}; at 20 ºC (±1 ºC)

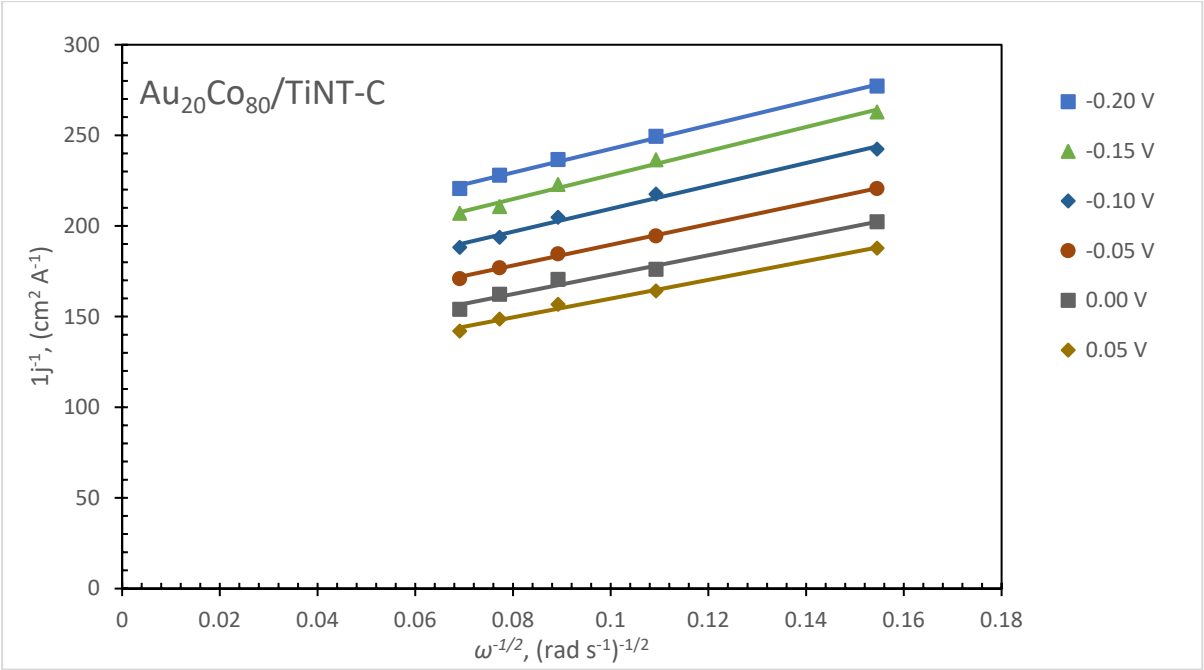

Figure 9.21: Koutecky-Levich plot of $Au_{20}Co_{80}$/TiNT-C between -0.20 V and 0.10 V, Counter electrode: Pt; electrolyte: 0.03 M $NaBH_4$ + 2 M NaOH; scan rate: 10 mV s^{-1}; at 20 ºC (±1 ºC)

9.3 Appendix C: additional graphs, tables, and information for CV, LSV, and Koutecky-Levich plots used to calculate *n* and *k* values for Au-Cu/TiNT

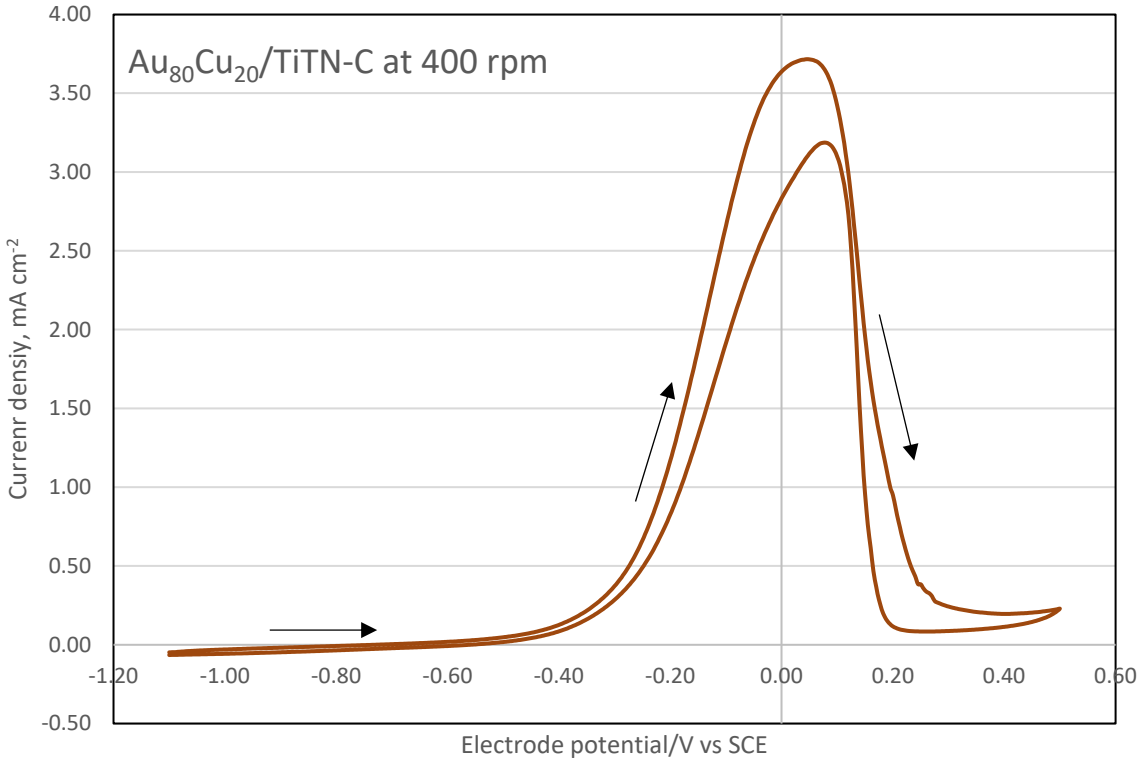

Figure 9.22: CV curve of $Au_{80}Cu_{20}$/TiNT-C electrode. Counter electrode: Pt; electrolyte: 0.03 M $NaBH_4$ + 2 M NaOH; scan rate:10 mV s^{-1}; disc rotation 400 rpm; at ambient temperature (20 ^oC ±1)

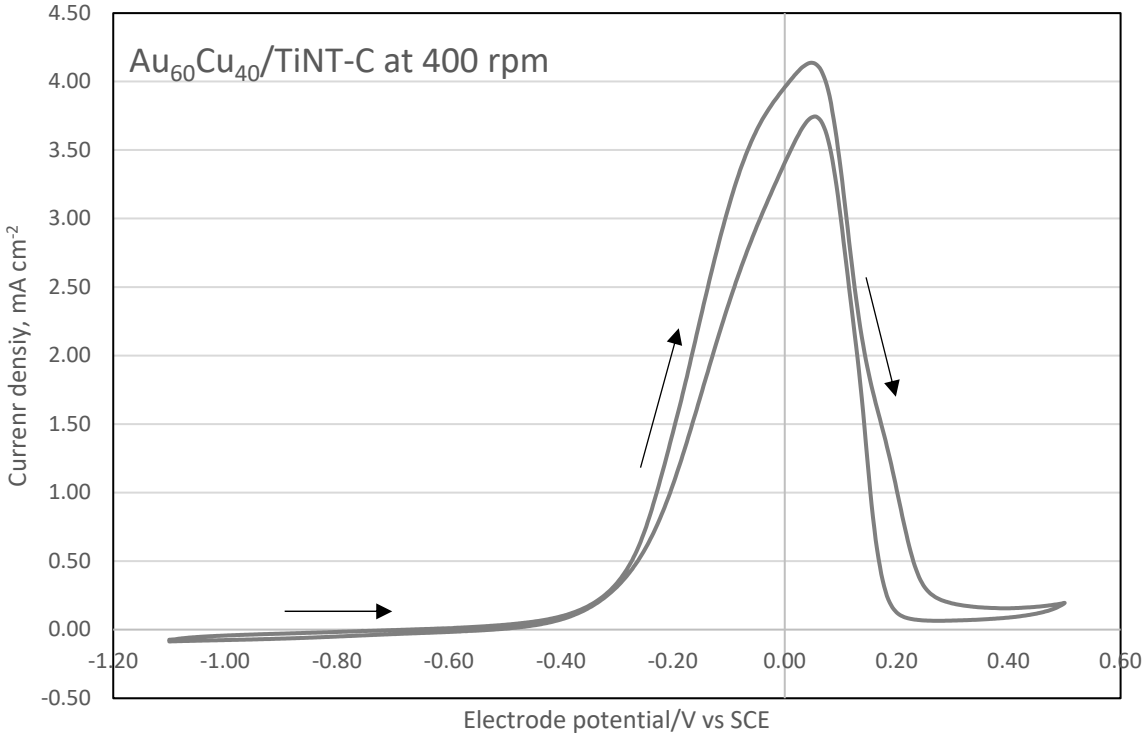

Figure 9.23: CV curve of $Au_{60}Cu_{40}$/TiNT-C electrode. Counter electrode: Pt; electrolyte: 0.03 M $NaBH_4$ + 2 M NaOH; scan rate:10 mV s^{-1}; disc rotation 400 rpm; at ambient temperature (20 ^oC ±1)

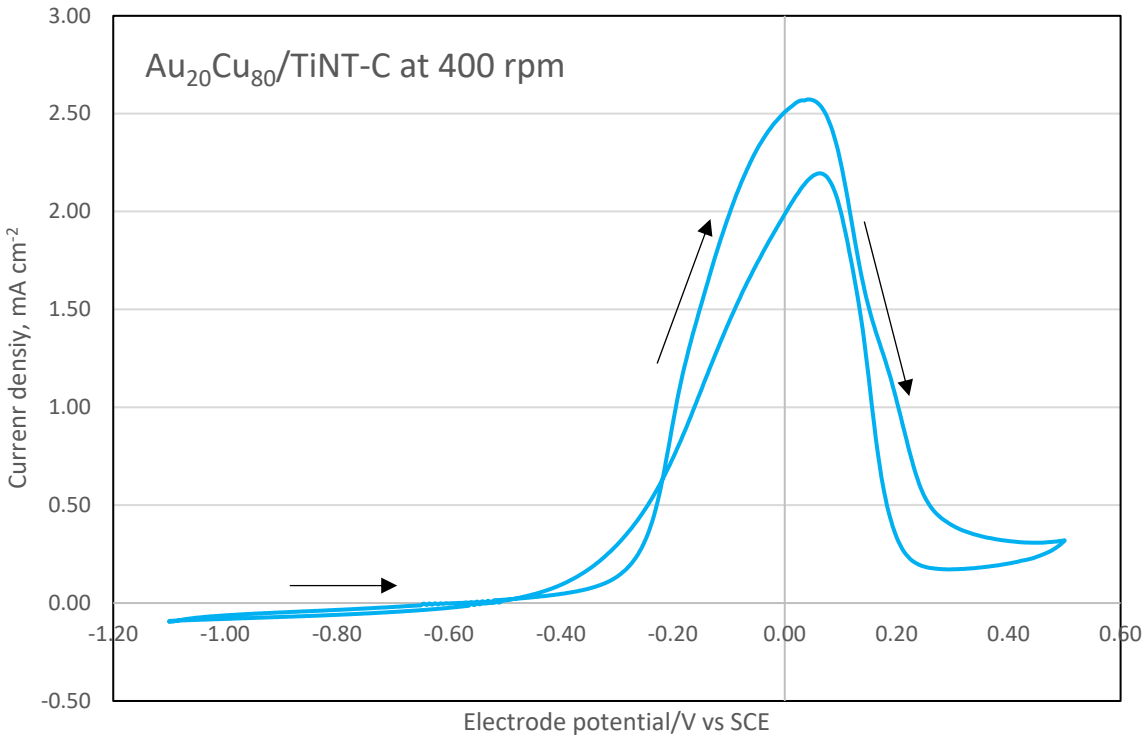

Figure 9.24: CV curve of $Au_{20}Cu_{80}$/TiNT-C electrode. Counter electrode: Pt; electrolyte: 0.03 M $NaBH_4$ + 2 M NaOH; scan rate:10 mV s^{-1}; disc rotation 400 rpm; at ambient temperature (20 ^oC ±1)

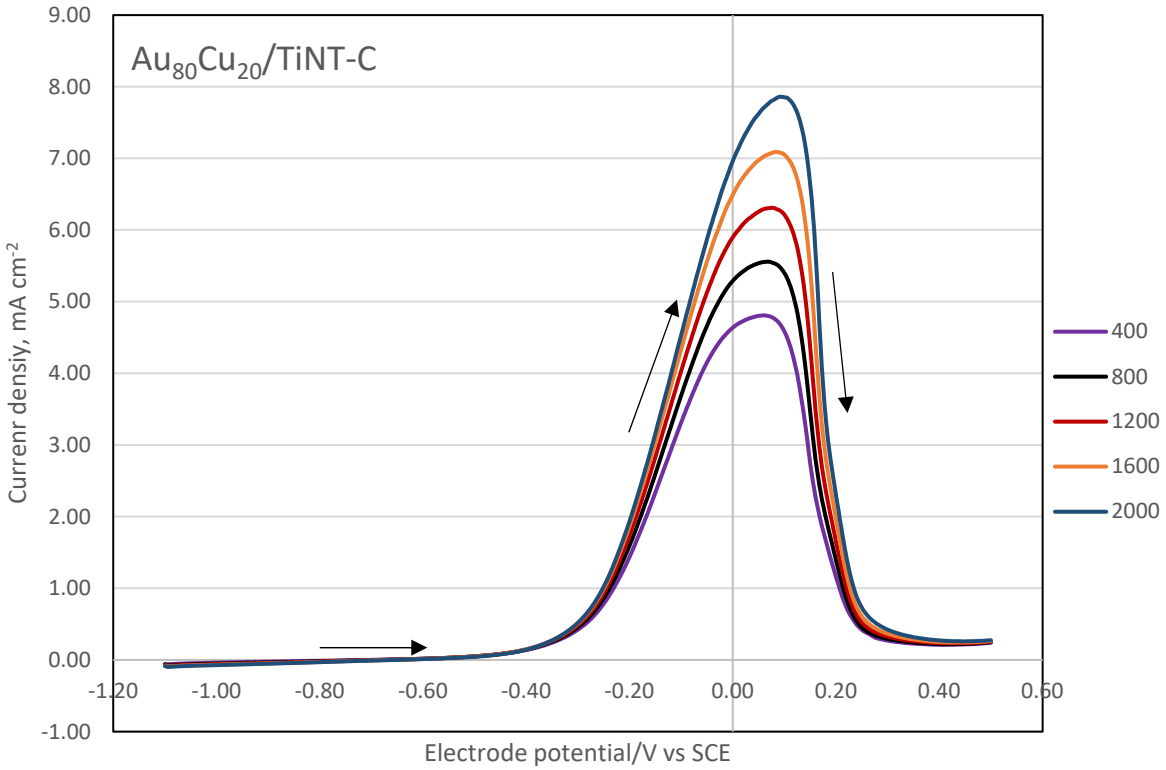

Figure 9.25: Linear sweep voltammograms of $Au_{80}Co_{20}$/TNT-C coated glassy carbon disc electrode at different rotation rates. Counter electrode: Pt; electrolyte: 0.03 M $NaBH_4$ + 2 M NaOH; scan rate:10 mV s^{-1}; at 20 ºC (±1 ºC)

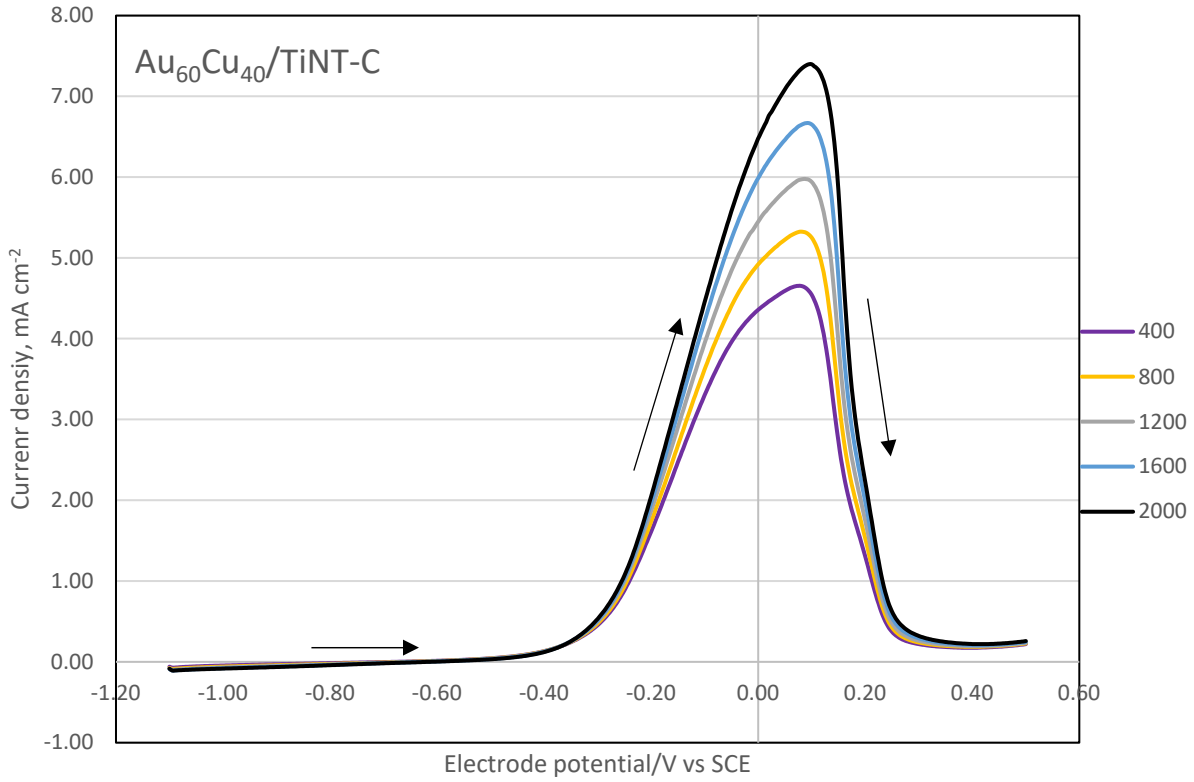

Figure 9.26: Linear sweep voltammograms of $Au_{60}Co_{40}$/TNT-C coated glassy carbon disc electrode at different rotation rates. Counter electrode: Pt; electrolyte: 0.03 M $NaBH_4$ + 2 M NaOH; scan rate:10 mV s^{-1}; at 20 ºC (±1 ºC)

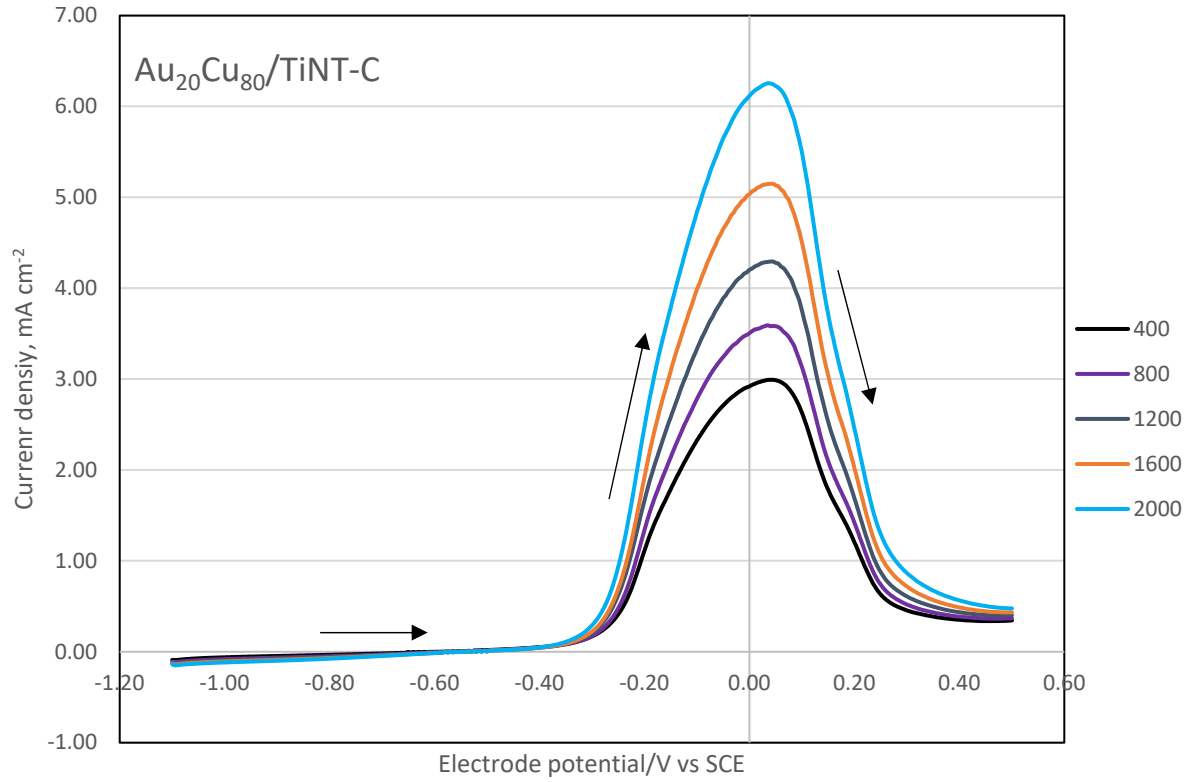

Figure 9.27: Linear sweep voltammograms of $Au_{20}Co_{80}$/TNT-C coated glassy carbon disc electrode at different rotation rates. Counter electrode: Pt; electrolyte: 0.03 M $NaBH_4$ + 2 M NaOH; scan rate:10 mV s^{-1}; at 20 ºC (±1 ºC)

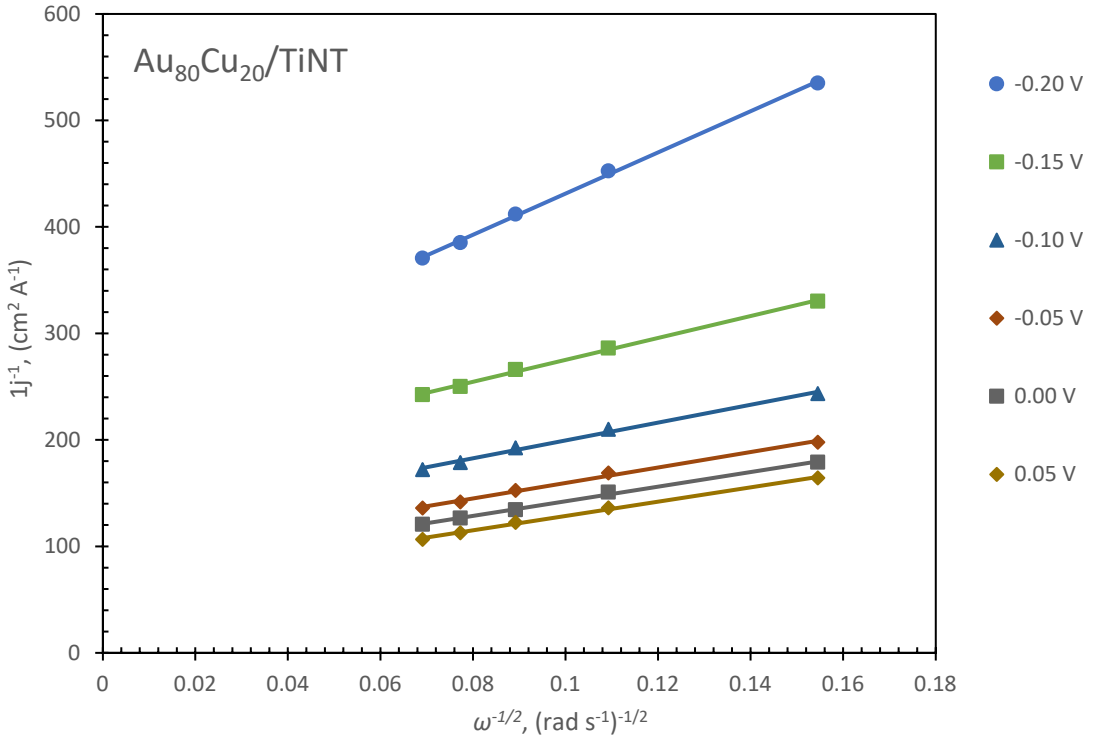

Figure 9.28: j^{-1} versus $\omega^{-1/2}$ plot of $Au_{80}Cu_{20}$/TiNT-C between -0.20 V and 0.05 V, Counter electrode: Pt; electrolyte: 0.03 M $NaBH_4$ + 2 M NaOH; scan rate: 10 mV s^{-1}; at 20 ºC (±1 ºC)

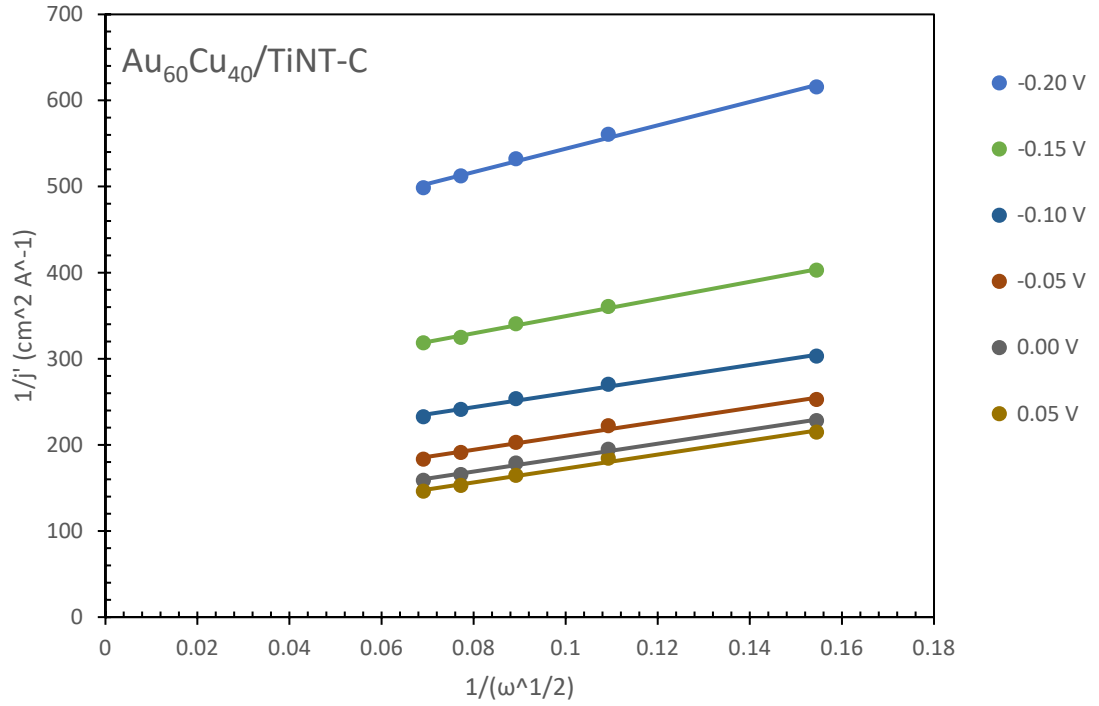

Figure 9.29: j^{-1} versus $\omega^{-1/2}$ plot of $Au_{60}Cu_{40}$/TiNT-C between -0.20 V and 0.05 V, Counter electrode: Pt; electrolyte: 0.03 M $NaBH_4$ + 2 M NaOH; scan rate: 10 mV s^{-1}; at 20 ºC (±1 ºC)

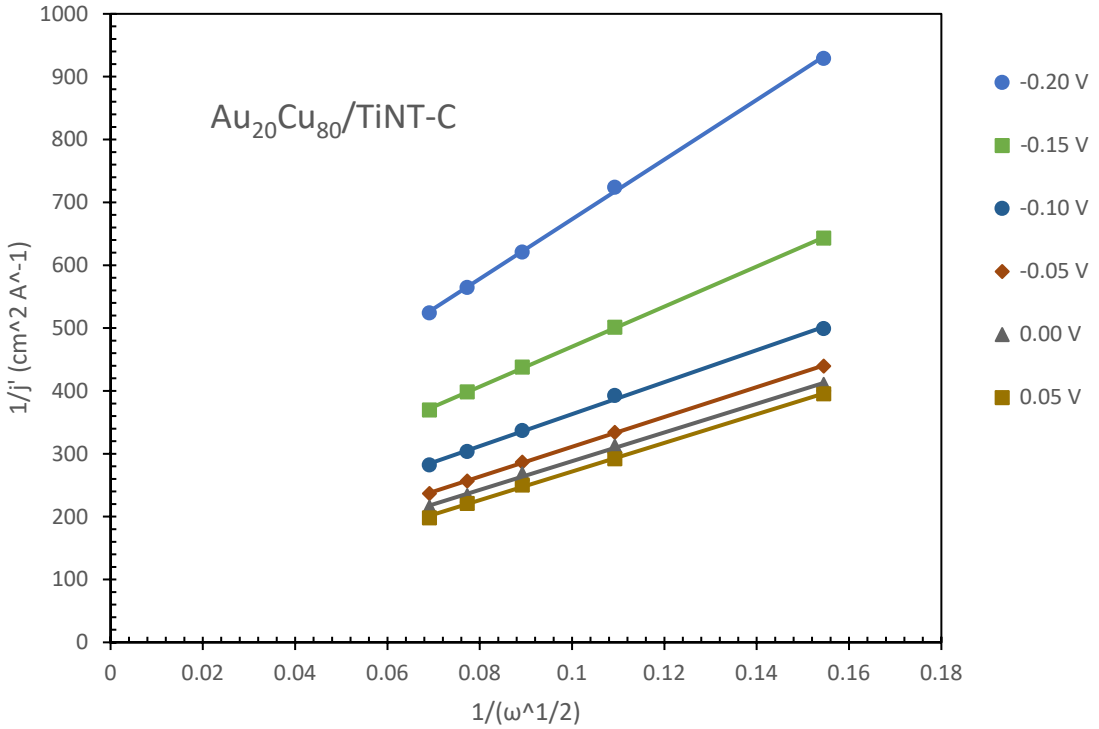

Figure 9.30: j^{-1} versus $\omega^{-1/2}$ plot of $Au_{20}Cu_{80}$/TiNT-C between -0.20 V and 0.05 V, Counter electrode: Pt; electrolyte: 0.03 M $NaBH_4$ + 2 M NaOH; scan rate: 10 mV s^{-1}; at 20 ºC (±1 ºC)

References

[1] T. M. I. Mahlia, T. J. Saktisahdan, A. Jannifar, M. H. Hasan, and H. S. C. Matseelar, "A review of available methods and development on energy storage; Technology update," *Renewable and Sustainable Energy Reviews*. 2014. doi: 10.1016/j.rser.2014.01.068.

[2] L. H. Rude *et al.*, "Tailoring properties of borohydrides for hydrogen storage: A review," *Physica Status Solidi (A) Applications and Materials Science*, vol. 208, no. 8, pp. 1754–1773, 2011, doi: 10.1002/pssa.201001214.

[3] U. Eberle, M. Felderhoff, and F. Schüth, "Chemical and physical solutions for hydrogen storage," *Angewandte Chemie - International Edition*, vol. 48, no. 36, pp. 6608–6630, 2009, doi: 10.1002/anie.200806293.

[4] J. Andersson and S. Gronkvist, "Large-scale storage of hydrogen," *Int J Hydrogen Energy*, vol. 44, no. 23, pp. 11901–11919, 2019, doi: 10.1016/j.ijhydene.2019.03.063.

[5] I. Merino-Jiménez, C. Ponce De León, A. A. Shah, and F. C. Walsh, "Developments in direct borohydride fuel cells and remaining challenges," *J Power Sources*, vol. 219, pp. 339–357, 2012, doi: 10.1016/j.jpowsour.2012.06.091.

[6] J. Ma, N. A. Choudhury, and Y. Sahai, "A comprehensive review of direct borohydride fuel cells," *Renewable and Sustainable Energy Reviews*, vol. 14, no. 1, pp. 183–199, Jan. 2010, doi: 10.1016/j.rser.2009.08.002.

[7] C. P. de Leon, F. C. Walsh, D. Pletcher, D. J. Browning, and J. B. Lakeman, "Direct borohydride fuel cells," *J Power Sources*, vol. 155, no. 2, pp. 172–181, 2006, doi: 10.1016/j.jpowsour.2006.01.011.

[8] S. Uhm, H. J. Lee, and J. Lee, "Understanding underlying processes in formic acid fuel cells," *Physical Chemistry Chemical Physics*, vol. 11, no. 41, pp. 9326–9336, 2009, doi: 10.1039/b909525j.

[9] X. Yu and P. G. Pickup, "Recent advances in direct formic acid fuel cells (DFAFC)," *J Power Sources*, vol. 182, no. 1, pp. 124–132, 2008, doi: 10.1016/j.jpowsour.2008.03.075.

[10] B. C. Ong, S. K. Kamarudin, and S. Basri, "Direct liquid fuel cells: A review," *Int J Hydrogen Energy*, vol. 42, no. 15, pp. 10142–10157, 2017, doi: 10.1016/j.ijhydene.2017.01.117.

[11] Z. Zhang, J. Liu, J. Gu, L. Su, and L. Cheng, "An overview of metal oxide materials as electrocatalysts and supports for polymer electrolyte fuel cells," *Energy Environ Sci*, vol. 7, no. 8, pp. 2535–2558, 2014, doi: 10.1039/c3ee43886d.

[12] M. Indig and R. Snyder, “Sodium borohydride, an interesting anodic fuel,” *J Electrochem Soc*, pp. 1104–1106, 1962.

[13] S. C. Amendola, P. Onnerud, M. T. Kelly, P. J. Petillo, S. L. Sharp-goldman, and M. Binder, “Short communication A novel high power density borohydride-air cell,” *J Power Sources*, pp. 130–133, 1999.

[14] L. Yi *et al.*, “Electrochemical oxidation of sodium borohydride on carbon supported Pt-Zn nanoparticle bimetallic catalyst and its implications to direct borohydride-hydrogen peroxide fuel cell,” *Electrochim Acta*, vol. 158, pp. 209–218, 2015, doi: 10.1016/j.electacta.2015.01.111.

[15] P. He, X. Wang, P. Fu, H. Wang, and L. Yi, “The studies of performance of the Au electrode modified by Zn as the anode electrocatalyst of direct borohydride fuel cell,” *Int J Hydrogen Energy*, vol. 36, no. 15, pp. 8857–8863, 2011, doi: 10.1016/j.ijhydene.2011.04.128.

[16] D. M. F. Santos and C. A. C. Sequeira, “Zinc Anode for Direct Borohydride Fuel Cells,” *J Electrochem Soc*, vol. 157, no. 1, p. B13, 2009, doi: 10.1149/1.3247540.

[17] F. Pei *et al.*, “Performance of supported Au-Co alloy as the anode catalyst of direct borohydride-hydrogen peroxide fuel cell,” *Int J Hydrogen Energy*, vol. 35, no. 15, pp. 8136–8142, 2010, doi: 10.1016/j.ijhydene.2010.01.016.

[18] B. H. Liu, Z. P. Li, K. Arai, and S. Suda, “Performance improvement of a micro borohydride fuel cell operating at ambient conditions,” *Electrochim Acta*, vol. 50, no. 18, pp. 3719–3725, 2005, doi: 10.1016/j.electacta.2005.01.018.

[19] D. M. F. Santos *et al.*, “ AuCo/TiO 2 -NTs Anode Catalysts for Direct Borohydride Fuel Cells ,” *J Electrochem Soc*, vol. 163, no. 14, pp. F1553–F1557, 2016, doi: 10.1149/2.0891614jes.

[20] J. Liu *et al.*, “Investigation of nanoporous carbon supported palladium-zinc nanocomposites as anode catalysts for direct borohydride-hydrogen peroxide fuel cell,” *Int J Hydrogen Energy*, vol. 40, no. 23, pp. 7301–7307, 2015, doi: 10.1016/j.ijhydene.2015.04.047.

[21] G. Behmenyar and A. N. Akin, “Investigation of carbon supported Pd-Cu nanoparticles as anode catalysts for direct borohydride fuel cell,” *J Power Sources*, vol. 249, pp. 239–246, 2014, doi: 10.1016/j.jpowsour.2013.10.063.

[22] H. Cheng, K. Scott, and K. Lovell, “Material aspects of the design and operation of direct borohydride fuel cells,” *Fuel Cells*, vol. 6, no. 5, pp. 367–375, 2006, doi: 10.1002/fuce.200500260.

[23] R. X. Feng, H. Dong, Y. D. Wang, X. P. Ai, Y. L. Cao, and H. X. Yang, "A simple and high efficient direct borohydride fuel cell with MnO 2-catalyzed cathode," *Electrochem commun*, vol. 7, no. 4, pp. 449–452, 2005, doi: 10.1016/j.elecom.2005.02.023.

[24] C. Grimmer *et al.*, "Carbon Supported Nanocrystalline Manganese Oxide: Surpassing Platinum as Oxygen Reduction Catalyst in Direct Borohydride Fuel Cells," *J Electrochem Soc*, vol. 163, no. 8, pp. F885–F890, 2016, doi: 10.1149/2.1091608jes.

[25] E. Gyenge, M. Atwan, and D. Northwood, "Electrocatalysis of Borohydride Oxidation on Colloidal Pt and Pt-Alloys (Pt-Ir, Pt-Ni, and Pt-Au) and Application for Direct Borohydride Fuel Cell Anodes," *J Electrochem Soc*, vol. 153, no. 1, p. A150, 2005, doi: 10.1149/1.2131831.

[26] B. H. Liu, Z. P. Li, and S. Suda, "Electrocatalysts for the anodic oxidation of borohydrides," *Electrochim Acta*, vol. 49, no. 19, pp. 3097–3105, 2004, doi: 10.1016/j.electacta.2004.02.023.

[27] G. Braesch, A. Bonnefont, V. Martin, E. R. Savinova, and M. Chatenet, "Borohydride oxidation reaction mechanisms and poisoning effects on Au, Pt and Pd bulk electrodes: From model (low) to direct borohydride fuel cell operating (high) concentrations," *Electrochim Acta*, vol. 273, pp. 483–494, 2018, doi: 10.1016/j.electacta.2018.04.068.

[28] C. Louis, "Chemical Preparation of Supported Bimetallic Catalysts. Gold-Based Bimetallic, a Case Study," *Catalysts*, vol. 6, no. 8, p. 110, 2016, doi: 10.3390/catal6080110.

[29] J. A. Gardiner and J. W. Collat, "Kinetics of the Stepwise Hydrolysis of Tetrahydroborate Ion," *J Am Chem Soc*, vol. 87, no. 8, pp. 1692–1700, 1965, doi: 10.1021/ja01086a013.

[30] H. Cheng and K. Scott, "Determination of kinetic parameters for borohydride oxidation on a rotating Au disk electrode," *Electrochim Acta*, vol. 51, no. 17, pp. 3429–3433, 2006, doi: 10.1016/j.electacta.2005.09.038.

[31] E. Gyenge, "Electrooxidation of borohydride on platinum and gold electrodes: Implications for direct borohydride fuel cells," *Electrochim Acta*, vol. 49, no. 6, pp. 965–978, 2004, doi: 10.1016/j.electacta.2003.10.008.

[32] D. A. Finkelstein, N. Da Mota, J. L. Cohen, and H. D. Abruña, "Rotating disk electrode (RDE) investigation of BH4- and BH3OH-electro-oxidation at Pt and Au: Implications for BH 4- fuel cells," *Journal of Physical Chemistry C*, vol. 113, no. 45, pp. 19700–19712, 2009, doi: 10.1021/jp900933c.

[33] M. V. Mirkin, H. Yang, and A. J. Bard, “Borohydride Oxidation at a Gold Electrode,” *J Electrochem Soc*, vol. 139, no. 8, pp. 2212–2217, 1992, doi: 10.1149/1.2221204.

[34] J. Larminie, *Fuel Cell Systems Explained*, SecoLarmin. Chichester, West Sussex: J. Wiley, 2003.

[35] B. H. Liu and S. Suda, “Hydrogen storage alloys as the anode materials of the direct borohydride fuel cell,” *J Alloys Compd*, vol. 454, no. 1–2, pp. 280–285, 2008, doi: 10.1016/j.jallcom.2006.12.034.

[36] C. G. Morales-Guio, L. A. Stern, and X. Hu, “Nanostructured hydrotreating catalysts for electrochemical hydrogen evolution,” *Chem Soc Rev*, vol. 43, no. 18, pp. 6555–6569, 2014, doi: 10.1039/c3cs60468c.

[37] H. Çelikkan, M. Şahin, M. L. Aksu, and T. Nejat Veziroğlu, “The investigation of the electrooxidation of sodium borohydride on various metal electrodes in aqueous basic solutions,” *Int J Hydrogen Energy*, vol. 32, no. 5, pp. 588–593, 2007, doi: 10.1016/j.ijhydene.2006.06.065.

[38] P. Y. Olu, N. Job, and M. Chatenet, “Evaluation of anode (electro)catalytic materials for the direct borohydride fuel cell: Methods and benchmarks,” *J Power Sources*, vol. 327, pp. 235–257, 2016, doi: 10.1016/j.jpowsour.2016.07.041.

[39] M. Chatenet, F. Micoud, I. Roche, and E. Chainet, “Kinetics of sodium borohydride direct oxidation and oxygen reduction in sodium hydroxide electrolyte. Part I. BH4- electro-oxidation on Au and Ag catalysts,” *Electrochim Acta*, vol. 51, no. 25, pp. 5459–5467, 2006, doi: 10.1016/j.electacta.2006.02.015.

[40] M. Chatenet, F. H. B. Lima, and E. A. Ticianelli, “Gold is not a Faradaic-Efficient Borohydride Oxidation Electrocatalyst: An Online Electrochemical Mass Spectrometry Study,” *J Electrochem Soc*, vol. 157, no. 5, p. B697, 2010, doi: 10.1149/1.3328179.

[41] H. Cheng, K. Scott, and K. Lovell, “Material Aspects of the Design and Operation of Direct Borohydride Fuel Cells,” *Fuel Cells*, vol. 6, no. 5, pp. 367–375, 2006, doi: 10.1002/fuce.200500260.

[42] M. Haruta, “Catalysis of gold nanoparticles deposited on metal oxides,” *Cattech*, vol. 6, no. 3, pp. 102–115, 2002, doi: 10.1023/A:1020181423055.

[43] P. He, X. Wang, Y. Liu, X. Liu, and L. Yi, “Comparison of electrocatalytic activity of carbon-supported Au-M (M = Fe, Co, Ni, Cu and Zn) bimetallic nanoparticles for direct borohydride fuel cells,” *Int J Hydrogen Energy*, vol. 37, no. 16, pp. 11984–11993, 2012, doi: 10.1016/j.ijhydene.2012.05.054.

[44] L. Yi *et al.*, “High activity of Au-Cu/C electrocatalyst as anodic catalyst for direct borohydride-hydrogen peroxide fuel cell,” *Int J Hydrogen Energy*, vol. 36, no. 24, pp. 15775–15782, 2011, doi: 10.1016/j.ijhydene.2011.09.019.

[45] X. Geng, H. Zhang, Y. Ma, and H. Zhong, “Borohydride electrochemical oxidation on carbon-supported Pt-modified Au nanoparticles,” *J Power Sources*, vol. 195, no. 6, pp. 1583–1588, 2010, doi: 10.1016/j.jpowsour.2009.09.036.

[46] C. Celik, F. G. Boyaci San, and H. I. Sarac, “Effects of operation conditions on direct borohydride fuel cell performance,” *J Power Sources*, vol. 185, no. 1, pp. 197–201, 2008, doi: 10.1016/j.jpowsour.2008.06.066.

[47] C. P. De León *et al.*, “A direct borohydride – peroxide fuel cell using a Pd / Ir alloy coated microfibrous carbon cathode,” *Electrochem commun*, vol. 10, no. 10, pp. 1610–1613, 2008, doi: 10.1016/j.elecom.2008.08.006.

[48] M. Chatenet, F. Micoud, I. Roche, E. Chainet, and J. Vondrák, “Kinetics of sodium borohydride direct oxidation and oxygen reduction in sodium hydroxide electrolyte. Part II. O2 reduction,” *Electrochim Acta*, vol. 51, no. 25, pp. 5452–5458, 2006, doi: 10.1016/j.electacta.2006.02.014.

[49] E. Sanlı, H. Çelikkan, B. Z. Uysal, and M. L. Aksu, “Anodic behavior ofAg metal electrode in direct borohydride fuel cells,” *Int J Hydrogen Energy*, vol. 31, no. 13, pp. 1920–1924, 2006, doi: 10.1016/j.ijhydene.2006.04.003.

[50] R. X. Feng, H. Dong, Y. L. Cao, X. P. Ai, and H. X. Yang, “Agni-catalyzed anode for direct borohydride fuel cells,” *Int J Hydrogen Energy*, vol. 32, no. 17, pp. 4544–4549, 2007, doi: 10.1016/j.ijhydene.2007.08.001.

[51] K. Wang and L. Z. Juntao Lu, “A current-decomposition study of the borohydride oxidation reaction at Ni electrodes,” *Journal of Physical Chemistry C*, vol. 111, no. 20, pp. 7456–7462, 2007, doi: 10.1021/jp0710483.

[52] B. H. Liu, Z. P. Li, and S. Suda, “Anodic Oxidation of Alkali Borohydrides Catalyzed by Nickel,” *J Electrochem Soc*, vol. 150, no. 3, p. A398, 2003, doi: 10.1149/1.1553785.

[53] B. Hong, Z. Peng, and S. Suda, “Short communication A study on performance stability of the passive direct borohydride fuel cell,” *J Power Sources*, vol. 185, no. 2, pp. 1257–1261, 2008, doi: 10.1016/j.jpowsour.2008.08.063.

[54] P. He *et al.*, “Investigation of carbon supported Au-Ni bimetallic nanoparticles as electrocatalyst for direct borohydride fuel cell,” *J Power Sources*, vol. 196, no. 3, pp. 1042–1047, 2011, doi: 10.1016/j.jpowsour.2010.08.037.

[55] P. He, X. Wang, Y. Liu, L. Yi, and X. Liu, “Reverse micelle synthesis of AuNi alloy as electrocatalyst of borohydride oxidation,” *Int J Hydrogen Energy*, vol. 37, no. 2, pp. 1254–1262, 2012, doi: 10.1016/j.ijhydene.2011.09.144.

[56] F. Yang, K. Cheng, G. Wang, and D. Cao, “Preparation of Au nanosheets supported on Ni foam and its electrocatalytic performance towards NaBH4 oxidation,” *Electrochim Acta*, vol. 159, pp. 111–115, 2015, doi: 10.1016/j.electacta.2015.01.171.

[57] R. Jamard, A. Latour, J. Salomon, P. Capron, and A. Martinent-Beaumont, “Study of fuel efficiency in a direct borohydride fuel cell,” *J Power Sources*, vol. 176, no. 1, pp. 287–292, 2008, doi: 10.1016/j.jpowsour.2007.10.036.

[58] M. Martins *et al.*, “PtNi supported on binary metal oxides: Potential bifunctional electrocatalysts for low-temperature fuel cells?,” *Appl Surf Sci*, vol. 428, pp. 31–40, 2018, doi: 10.1016/j.apsusc.2017.09.132.

[59] P. Y. Olu, N. Job, and M. Chatenet, “Evaluation of anode (electro)catalytic materials for the direct borohydride fuel cell: Methods and benchmarks,” *J Power Sources*, vol. 327, pp. 235–257, 2016, doi: 10.1016/j.jpowsour.2016.07.041.

[60] M. Martins *et al.*, “Mn2O3-MO (MO = ZrO2, V2O5, WO3) supported PtNi nanoparticles: Designing stable and efficient electrocatalysts for oxygen reduction and borohydride oxidation,” *Microporous and Mesoporous Materials*, vol. 273, no. July 2018, pp. 286–293, 2019, doi: 10.1016/j.micromeso.2018.07.022.

[61] M. Martins *et al.*, “Bimetallic PdM (M = Fe, Ag, Au) alloy nanoparticles assembled on reduced graphene oxide as catalysts for direct borohydride fuel cells,” *J Alloys Compd*, vol. 718, pp. 204–214, 2017, doi: 10.1016/j.jallcom.2017.05.058.

[62] K. T. Park, U. H. Jung, S. U. Jeong, and S. H. Kim, “Influence of anode diffusion layer properties on performance of direct borohydride fuel cell,” *J Power Sources*, vol. 162, no. 1, pp. 192–197, 2006, doi: 10.1016/j.jpowsour.2006.07.040.

[63] B. H. Liu, Z. P. Li, and S. Suda, “Development of high-performance planar borohydride fuel cell modules for portable applications,” *J Power Sources*, vol. 175, no. 1, pp. 226–231, 2008, doi: 10.1016/j.jpowsour.2007.09.047.

[64] J. H. Kim *et al.*, “Carbon-supported and unsupported Pt anodes for direct borohydride liquid fuel cells,” *J Electrochem Soc*, vol. 151, no. 7, pp. 1039–1043, 2004, doi: 10.1149/1.1756351.

[65] N. A. Choudhury, R. K. Raman, S. Sampath, and A. K. Shukla, “An alkaline direct borohydride fuel cell with hydrogen peroxide as oxidant,” *J Power Sources*, vol. 143, no. 1–2, pp. 1–8, 2005, doi: 10.1016/j.jpowsour.2004.08.059.

[66] F. G. Boyaci San, O. Okur, Ç. Iyigün Karadağ, I. Isik-Gulsac, and E. Okumuş, "Evaluation of operating conditions on DBFC (direct borohydride fuel cell) performance with PtRu anode catalyst by response surface method," *Energy*, vol. 71, pp. 160–169, 2014, doi: 10.1016/j.energy.2014.04.037.

[67] H. Cheng and K. Scott, "Influence of operation conditions on direct borohydride fuel cell performance," *J Power Sources*, vol. 160, no. 1, pp. 407–412, 2006, doi: 10.1016/j.jpowsour.2006.01.097.

[68] J. I. Martins, M. C. Nunes, R. Koch, L. Martins, and M. Bazzaoui, "Electrochemical oxidation of borohydride on platinum electrodes: The influence of thiourea in direct fuel cells," *Electrochim Acta*, vol. 52, no. 23, pp. 6443–6449, 2007, doi: 10.1016/j.electacta.2007.04.066.

[69] N. A. Choudhury, J. Ma, and Y. Sahai, "High performance and eco-friendly chitosan hydrogel membrane electrolytes for direct borohydride fuel cells," *J Power Sources*, vol. 210, pp. 358–365, 2012, doi: 10.1016/j.jpowsour.2012.03.013.

[70] U. B. Demirci, "Direct borohydride fuel cell: Main issues met by the membrane-electrodes-assembly and potential solutions," *J Power Sources*, vol. 172, no. 2, pp. 676–687, 2007, doi: 10.1016/j.jpowsour.2007.05.009.

[71] N. A. Choudhury, J. Ma, and Y. Sahai, "High performance and eco-friendly chitosan hydrogel membrane electrolytes for direct borohydride fuel cells," *J Power Sources*, vol. 210, pp. 358–365, 2012, doi: 10.1016/j.jpowsour.2012.03.013.

[72] V. Tripković *et al.*, "Metal Oxide-Supported Platinum Overlayers as Proton-Exchange Membrane Fuel Cell Cathodes," *ChemCatChem*, vol. 4, no. 2, pp. 228–235, 2012, doi: 10.1002/cctc.201100308.

[73] C. Subban *et al.*, "Catalyst supports for polymer electrolyte fuel cells," *Philosophical Transactions of the Royal Society A: Mathematical, Physical and Engineering Sciences*, vol. 368, no. 1923, pp. 3243–3253, 2010, doi: 10.1098/rsta.2010.0116.

[74] D. V. Bavykin, V. N. Parmon, A. A. Lapkin, and F. C. Walsh, "The effect of hydrothermal conditions on the mesoporous structure of TiO2 nanotubes," *J Mater Chem*, vol. 14, no. 22, pp. 3370–3377, 2004, doi: 10.1039/b406378c.

[75] S. J. Tauster, S. C. Fung, and R. L. Garten, "Strong Metal-Support Interactions. Group 8 Noble Metals Supported on TiO2," *J Am Chem Soc*, vol. 100, no. 1, pp. 170–175, 1978, doi: 10.1021/ja00469a029.

[76] C. P. de León, F. C. Walsh, A. Rose, J. B. Lakeman, D. J. Browning, and R. W. Reeve, "A direct borohydride-Acid peroxide fuel cell," *J Power Sources*, vol. 164, no. 2, pp. 441–448, 2007, doi: 10.1016/j.jpowsour.2006.10.069.

[77] A. Wolf and F. Schüth, "A systematic study of the synthesis conditions for the preparation of highly active gold catalysts," *Appl Catal A Gen*, vol. 226, no. 1–2, pp. 1–13, 2002, doi: 10.1016/S0926-860X(01)00772-4.

[78] C. Ponce-de-León, D. V. Bavykin, and F. C. Walsh, "The oxidation of borohydride ion at titanate nanotube supported gold electrodes," *Electrochem commun*, vol. 8, no. 10, pp. 1655–1660, 2006, doi: 10.1016/j.elecom.2006.07.031.

[79] D. V. Bavykin, A. A. Lapkin, P. K. Plucinski, L. Torrente-Murciano, J. M. Friedrich, and F. C. Walsh, "Deposition of Pt, Pd, Ru and Au on the surfaces of titanate nanotubes," *Top Catal*, vol. 39, no. 3–4, pp. 151–160, 2006, doi: 10.1007/s11244-006-0051-4.

[80] R. Zanella, S. Giorgio, C. R. Henry, and C. Louis, "Alternative methods for the preparation of gold nanoparticles supported on TiO2," *Journal of Physical Chemistry B*, vol. 106, no. 31, pp. 7634–7642, 2002, doi: 10.1021/jp0144810.

[81] B. Kasemo, S. Johansson, H. Persson, P. Thormählen, and V. P. Zhdanov, "Catalysis in the nm-regime: Manufacturing of supported model catalysts and theoretical studies of the reaction kinetics," *Top Catal*, vol. 13, no. 1–2, pp. 43–53, 2000, doi: 10.1023/a:1009024603803.

[82] D. M. F. Santos and C. A. C. Sequeira, "Determination of Kinetic and Diffusional Parameters for Sodium Borohydride Oxidation on Gold Electrodes," *J Electrochem Soc*, vol. 156, no. 5, p. F67, 2009, doi: 10.1149/1.3082371.

[83] A. A. Abahussain, C. P. de Leon, and F. C. Walsh, "Mass-Transfer Measurements at Porous 3D Pt-Ir/Ti Electrodes in a Direct Borohydride Fuel Cell," *J Electrochem Soc*, vol. 165, no. 3, pp. F198–F206, 2018, doi: 10.1149/2.0751803jes.

[84] G. Denuault, M. V. Mirkin, and A. J. Bard, "Direct determination of diffusion coefficients by chronoamperometry at microdisk electrodes," *Journal of Electroanalytical Chemistry*, vol. 308, no. 1–2, pp. 27–38, 1991, doi: 10.1016/0022-0728(91)85056-U.

[85] D. Duan *et al.*, "The effective carbon supported core-shell structure of Ni@Au catalysts for electro-oxidation of borohydride," *Int J Hydrogen Energy*, vol. 40, no. 1, pp. 488–500, 2015, doi: 10.1016/j.ijhydene.2014.10.101.

[86] D. M. F. Santos, B. Šljukić, L. Amaral, D. Macciò, A. Saccone, and C. A. C. Sequeira, “Nickel and Nickel-Cerium Alloy Anodes for Direct Borohydride Fuel Cells,” *J Electrochem Soc*, vol. 161, no. 5, pp. F594–F599, 2014, doi: 10.1149/2.023405jes.

[87] L. Yi, L. Liu, X. Wang, X. Liu, W. Yi, and X. Wang, “Carbon-supported Pt-Co nanoparticles as anode catalyst for direct borohydride-hydrogen peroxide fuel cell: Electrocatalysis and fuel cell performance,” *J Power Sources*, vol. 224, no. 17, pp. 6–12, 2013, doi: 10.1016/j.jpowsour.2012.09.082.

[88] A. M. Castro, L. De Medina, S. L. Marchiano, and A. J. Arvi’a, “The potentiodynamic behaviour of copper in NaOH solutions,” 1978.